# Steady-State Analysis and Optimal Power Routing of Standalone Unbalanced Hybrid AC/DC Microgrids

by

Mahmoud Ahmed Allam Sayed Alsanbawy

A thesis
presented to the University of Waterloo
in fulfillment of the
thesis requirement for the degree of
Doctor of Philosophy
in
Electrical and Computer Engineering

Waterloo, Ontario, Canada, 2018

**Examining Committee Membership**

The following served on the Examining Committee for this thesis. The decision of the Examining Committee is by majority vote.

| | |
|---|---|
| External Examiner: | Amirnaser Yazdani<br>Professor, Electrical, Computer and Biomedical Engineering,<br>Ryerson University |
| Supervisor: | Mehrdad Kazerani<br>Professor, Electrical and Computer Engineering,<br>University of Waterloo |
| Internal Member: | Magdy Salama<br>Professor, Electrical and Computer Engineering,<br>University of Waterloo |
| Internal Member: | Ramadan El-Shatshat<br>Lecturer, Electrical and Computer Engineering,<br>University of Waterloo |
| Internal-External Member: | Gordon Savage<br>Professor, Systems Design Engineering,<br>University of Waterloo |

I hereby declare that I am the sole author of this thesis. This is a true copy of the thesis, including any required final revisions, as accepted by my examiners.

I understand that my thesis may be made electronically available to the public.

**Abstract**

The concept of ac microgrids was introduced to integrate distributed generators (DGs) and loads within one entity that can operate autonomously or connected to a utility grid. Furthermore, dc microgrids have received increasing attention as a potential solution to deliver power from DGs to modern dc loads with reduced conversion stages. Moreover, hybrid ac/dc microgrids have been introduced as a paradigm combining the benefits of the two types of microgrids by interconnecting them through interlinking converters (ICs).

Steady-state analysis is essential for planning and operation studies of electrical power systems. However, conventional analysis approaches cannot be applied to hybrid ac/dc microgrids due to their distinctive features, such as droop characteristics, lack of a slack bus, and coupling between the ac and dc variables. Additionally, the unbalanced nature of ac microgrids adds to the complexity of modeling and analysis in such networks. Therefore, this thesis is focused on developing steady-state modeling and analysis framework for standalone unbalanced hybrid ac/dc microgrids.

First, a steady-state analysis tool for unbalanced hybrid ac/dc microgrids is developed. The ac subgrid's components are modeled in phase coordinates. Furthermore, the dc subgrid's components are modeled and the coupling between the ac and dc variables is formulated. The models of the various system elements are incorporated into a unified power flow formulation, which is solved using a Newton-Trust Region (NTR) method. The developed power flow algorithm is verified through comparisons with time-domain simulations of test microgrids. The analysis tool is used to analyze a larger hybrid ac/dc microgrid through case studies. The case studies shed light on some challenges of these microgrids, namely, imposed limitations on microgrid loadability due to unbalanced ac subgrid's loading, effect of IC settings on microgrid operation, and trade-off between proportional loading of the ac and dc subgrids and proportional power-transfer sharing among ICs.

Second, based on the identified microgrid loadability limitation of unbalanced microgrids, a novel adaptive power routing (APR) scheme is proposed to maximize the microgrid loadability. The proposed scheme allows independent control of active and reactive powers flowing through IC phases, so that power can be routed among the ac subgrid's phases. The DPR scheme is integrated into an optimal power flow (OPF) formulation with the objective of minimizing load shedding. A supervisory controller is proposed to solve the OPF problem by adjusting the DG and IC settings. Several case studies are conducted to show the ineffectiveness of conventional supervisory controllers in resolving the loadability issue, and to verify the success of the proposed controller in solving the problem.

Third, a power flow approach based on sequence component analysis of the ac microgrid's elements is adopted for faster convergence and improved modeling accuracy as

compared to conventional approaches in phase coordinates. This approach breaks down the system model into positive-, negative-, and zero-sequence subsystems that can be solved in parallel for enhanced performance. The positive-sequence power flow is solved using a Newton-Raphson (NR) method, while the negative- and zero-sequence voltages are obtained by solving linear complex equations. The approach is verified through comparisons with time-domain simulations. In addition, the algorithm is utilized to investigate the operation of droop-controlled DGs in larger-scale isochronous unbalanced ac microgrids, and to examine its limit-enforcement abilities at the same time. The algorithm demonstrates significant improvements in terms of accuracy and convergence time when compared against the conventional NTR-based approach in phase coordinates.

Finally, the power flow approach developed in the third part is extended to include the IC's and dc subgrid's models so that it can be applied to hybrid ac/dc microgrids. A power flow algorithm is proposed to solve the ac and dc power flows independently in a sequential manner, while maintaining the correlation between the two. The algorithm is verified through comparisons with time-domain models of test hybrid microgrids. Case studies are introduced to test the algorithm's effectiveness in enforcing the DG and IC limits in the power flow solution under various conditions. The algorithm also shows enhanced accuracy and solution speed with respect to the tool developed in the first stage.

**Acknowledgements**

First and foremost, I would like to thank God whose guidance has led me this far.

My sincerest gratitude goes to my advisor, Professor Mehrdad Kazerani, for his professional guidance, valuable advice, continual support and encouragement shown throughout the period of my PhD study. My appreciation and thanks are also extended to my PhD committee members: Professor Magdy Salama, Professor Ramadan El-Shatshat, and Professor Gordon Savage. Thanks are also due to my external examiner, Professor Amirnaser Yazdani, for coming from Ryerson University to referee this thesis.

My parents, Mr. Ahmed Allam and Mrs. Hanaa Salama, and my aunt, Fatema Salama, always receive my deepest thanks, and endless appreciation. My research would not have been possible without their help, constant support and encouragement, and their blessed wishes and prayers.

I wish also to thank my colleagues and friends, Amr Said, Marten Pape, Zuher Alnasir, and Elham Karimi, whose fruitful discussions and support inspired me during my PhD.

Last but not least, I would like to express my sincere gratitude to my former advisor, Professor Mostafa Marei, for his guidance through my MSc study at Ain Shams University, and for his support and recommendation to start my PhD at University of Waterloo.

## Dedication

*To my beloved parents, Ahmed and Hanaa, and my aunt, Fatema, in recognition of your endless love, support, and encouragement.*

# Table of Contents

# List of Tables

# List of Figures

# List of Abbreviations

| | |
|---|---|
| **APR** | Adaptive Power Routing. |
| **BESS** | Battery Energy Storage System. |
| **CC-VSC** | Current-Controlled Voltage Source Converter. |
| **CHP** | Combined Heat and Power. |
| **DER** | Distributed Energy Resource. |
| **DG** | Distributed Generation. |
| **EIDG** | Electronically-Interfaced Distributed Generator. |
| **EMF** | Electromotive Force. |
| **ESS** | Energy Storage System. |
| **FC** | Fuel Cell. |
| **GRG** | Generalized Reduced Gradient. |
| **IC** | Interlinking Converter. |
| **LIB** | Limit-Induced Bifurcation. |
| **MGCC** | Microgrid Central Controller. |
| **MPPT** | Maximum Power Point Tracking. |
| **MT** | Micro-Turbine. |
| **MTDC** | Multi-Terminal DC. |

**NR** Newton Raphson.
**NTR** Newton-Trust Region.

**OPF** Optimal Power Flow.

**PCC** Point of Common Coupling.
**PE** Power Electronics.
**PEV** Plug-in Electric Vehicles.
**PI** Proportional-Integral.
**PLL** Phase-Locked Loop.
**PR** Proportional-Resonant.
**PV** Photo-Voltaic.

**RER** Renewable Energy Resources.

**SGDG** Synchronous Generator-based Distributed Generator.
**SNB** Saddle-Node Bifurcation.

**VC-VSC** Voltage-Controlled Voltage Source Converter.
**VSC** Voltage Source Converter.
**VSD** Variable Speed Drive.

**WT** Wind Turbine.

# List of Symbols

| | |
|---|---|
| $B^{012}_{i,j}$ | Shunt admittance matrix of a feeder connecting nodes $i$ and $j$ in per-unit (sequence components). |
| $G_{ij}$ | The conductance matrix elements between dc buses $i$ and $j$ in per-unit. |
| $I_{ac,IC,l}$ | Interlinking converter's balanced output current magnitude at the ac side in per-unit. |
| $I^{x}_{ac,IC,l}$ | Interlinking converter's phase current magnitude in per-unit at the ac side where $x \in \{a, b, c\}$. |
| $I^{012}_{ac,L,i}$ | AC load's sequence current components in per-unit. |
| $I^{012}_{ac,ii}$ | Shunt admittance currents of a feeder connecting nodes $i$ and $j$ at node $i$ in per-unit (sequence components). |
| $I^{012}_{ac,ij}$ | Series admittance currents of a feeder connecting nodes $i$ and $j$ in per-unit (sequence components). |
| $I^{abc}_{ac,ij}$ | Three phase currents in a feeder connecting nodes $i$ and $j$ in per-unit (phase coordinates). |
| $I_{dc,G,i}$ | DC DG's output current in per-unit. |
| $I^{0}_{dc,L,i}$ | DC load rated current in per-unit. |
| $J_{ac}$ | AC Jacobian matrix. |
| $J_{dc}$ | DC Jacobian matrix. |
| $K^{x}_{pf,i}$ | Load active power-frequency constant. |
| $K^{x}_{qf,i}$ | Load reactive power-frequency constant. |
| $N_{IC}$ | Number of interlinking converters. |
| $N_{ac,DG}$ | The total number of AC DGs. |
| $N_{ac,F}$ | The total number of AC feeders. |

| | |
|---|---|
| $N_{ac,L}$ | The total number of AC loads. |
| $N_{ac}$ | Number of ac nodes. |
| $N_{dc}$ | Number of dc nodes. |
| $P_{IC,loss,l}$ | Interlinking converter's total active power losses in per-unit. |
| $P^{x}_{IC,loss,l}$ | Interlinking converter's phase active power losses in per-unit. |
| $P_{ac,G,i}$ | AC DG's active power output in per-unit. |
| $P^{1}_{ac,G,i}$ | AC DG's positive-sequence active power output in per-unit. |
| $P^{max}_{ac,G,i}$ | AC DG's active power capacity in per-unit. |
| $P_{ac,IC,l}$ | Interlinking converter's active power at the ac side in per-unit. |
| $P^{1}_{ac,IC,l}$ | Interlinking converter's positive-sequence active power at the ac side in per-unit. |
| $P^{0,x}_{ac,L,base,i}$ | Base active power of ac load of phase $x$ at node $i$ in per-unit. |
| $P^{0,x}_{ac,L,i}$ | The nominal value of the load phase active power in per-unit at node $i$ where $x \in \{a,b,c\}$ for Y-loads and $x \in \{ab,bc,ca\}$ for $\Delta$-loads (phase coordinates). |
| $P^{1}_{ac,L,i}$ | AC load's positive-sequence active power in per-unit. |
| $P^{x}_{ac,L,i}$ | AC load phase active power in per-unit at node $i$ where $x \in \{a,b,c\}$ for Y-loads and $x \in \{ab,bc,ca\}$ for $\Delta$-loads (phase coordinates). |
| $P^{1}_{ac,i}$ | Injected positive-sequence active power at node $i$ in per-unit. |
| $P^{x}_{ac,i}$ | Injected active power of each phase where $x \in \{a,b,c\}$ at node $i$ in per-unit (phase coordinates). |
| $P_{ac,loss,k}$ | AC feeder active power losses in per-unit. |
| $P_{dc,G,i}$ | DC DG's output power in per-unit. |
| $P_{dc,IC,l}$ | Interlinking converter's power at the dc side in per-unit. |
| $P^{0}_{dc,L,i}$ | DC load rated power in per-unit. |
| $P_{dc,i}$ | DC power injected at bus $i$ in per-unit. |
| $Q_{ac,G,i}$ | AC DG's reactive power output in per-unit. |
| $Q^{1}_{ac,G,i}$ | AC DG's positive-sequence reactive power output in per-unit. |
| $Q^{max}_{ac,G,i}$ | AC DG's reactive power capacity in per-unit. |
| $Q_{ac,IC,l}$ | Interlinking converter's reactive power in per-unit. |

| | |
|---|---|
| $Q^{1}_{ac,IC,l}$ | Interlinking converter's positive-sequence reactive power at the ac side in per-unit. |
| $Q^{0,x}_{ac,L,base,i}$ | Base reactive power of ac load of phase $x$ at node $i$ in per-unit. |
| $Q^{0,x}_{ac,L,i}$ | The nominal value of the load phase reactive power in per-unit at node $i$ where $x \in \{a,b,c\}$ for Y-loads and $x \in \{ab,bc,ca\}$ for $\Delta$-loads (phase coordinates). |
| $Q^{1}_{ac,L,i}$ | AC load's positive-sequence active power in per-unit. |
| $Q^{x}_{ac,L,i}$ | AC load phase reactive power in per-unit at node $i$ where $x \in \{a,b,c\}$ for Y-loads and $x \in \{ab,bc,ca\}$ for $\Delta$-loads (phase coordinates). |
| $Q^{1}_{ac,i}$ | Injected positive-sequence reactive power at node $i$ in per-unit. |
| $Q^{x}_{ac,i}$ | Injected reactive power of each phase where $x \in \{a,b,c\}$ at node $i$ in per-unit (phase coordinates). |
| $Q_{ac,loss,k}$ | AC feeder reactive power losses in per-unit. |
| $S^{max}_{IC,l}$ | Interlinking converter's apparent power capacity in per-unit. |
| $S^{ph,max}_{ac,G,i}$ | The AC DG's phase apparent-power capacity in per-unit. |
| $S^{x}_{ac,G,i}$ | The AC DG's output phase apparent-power in per-unit. |
| $S_{ac,L,base,i}$ | Base complex power of ac load at node $i$ in per-unit. |
| $S_{ac,L,i}$ | Actual complex power of ac load at node $i$ in per-unit. |
| $S^{x}_{ac,L,j}$ | The phase apparent power demand of the $j^{th}$ ac load. |
| $S^{abc}_{ac,i}$ | Injected three phase complex power at node $i$ in per-unit (phase coordinates). |
| $S^{x}_{ac,loss,k}$ | The phase apparent power loss of the $k^{th}$ ac distribution feeder. |
| $T$ | Sequence component to phase coordinate transformation matrix. |
| $U_{L,i}$ | Load shedding control variable. |
| $V_{ac,0,i}$ | The AC DG's no load voltage magnitude in per-unit. |
| $V^{012}_{ac,i}$ | Sequence component voltages of node $i$ in per-unit. |
| $V^{abc}_{ac,i}$ | Three phase voltages at node $i$ in per-unit (phase coordinates). |
| $V^{abc}_{ac,j}$ | Three phase voltages at node $j$ in per-unit (phase coordinates). |
| $V_{dc,0,i}$ | The DC DG's no-load voltage in per-unit. |
| $V_{dc,i}$ | The voltage of dc bus $i$ in per-unit. |
| $V_{dc,max}$ | Maximum dc subgrid voltage in per-unit. |

| | |
|---|---|
| $V_{dc,min}$ | Minimum dc subgrid voltage in per-unit. |
| $W_{L,i}$ | Load priority factor. |
| $Y^{00}$ | Decoupled zero-sequence Y-bus matrix in per-unit. |
| $Y^{11}$ | Decoupled positive-sequence Y-bus matrix in per-unit. |
| $Y^{22}$ | Decoupled negative-sequence Y-bus matrix in per-unit. |
| $Y^{0}_{DG}$ | DG's zero-sequence admittance in per-unit. |
| $Y^{2}_{DG}$ | DG's negative-sequence admittance in per-unit. |
| $Y^{012}_{ij}$ | Series admittance matrix of a feeder connecting nodes $i$ and $j$ in per-unit (sequence components). |
| $Y^{abc}_{ij}$ | Series admittance matrix of a feeder connecting nodes $i$ and $j$ in per-unit (phase coordinates). |
| $Z^{abc}_{ij}$ | Series impedance matrix of a feeder connecting nodes $i$ and $j$ (phase coordinates). |
| $\Delta I^{012}_{ac,i-j}$ | Combined series and shunt admittance sequence component decoupling currents in per-unit. |
| $\Delta I^{012}_{ac,ij-se}$ | Series admittance sequence component decoupling currents in per-unit. |
| $\Delta I^{012}_{ac,ij-sh}$ | Shunt admittance sequence component decoupling currents in per-unit. |
| $\Delta P^{1}_{ac,i-j}$ | Positive-sequence decoupling active power component of a feeder connecting nodes $i$ and $j$ at node $i$ in per-unit. |
| $\Delta Q^{1}_{ac,i-j}$ | Positive-sequence decoupling reactive power component of a feeder connecting nodes $i$ and $j$ at node $i$ in per-unit. |
| $\Delta V_{dc,pu,l}$ | The per-unit voltage deviation of the dc subgrid as measured by the interlinking converter. |
| $\Delta\omega$ | Frequency deviation from the nominal value in per-unit. |
| $\Delta\omega_{pu}$ | The per-unit frequency deviation of the ac subgrid as measured by the interlinking converter. |
| $\alpha$ | The load active power exponent (phase coordinates). |
| $\beta$ | The load reactive power exponent (phase coordinates). |
| $\delta V_{ac,0,i}$ | AC DG's reactive power secondary control signal in per-unit. |

| | |
|---|---|
| $\delta V_{dc,0,i}$ | DC DG's secondary control signal in per-unit. |
| $\delta\omega_{0,i}$ | AC DG's active power secondary control signal in per-unit. |
| $\delta\varepsilon_p^x$ | Interlinking converter's phase active power secondary control signal in per-unit. |
| $\delta\varepsilon_q^x$ | Interlinking converter's phase reactive power secondary control signal in per-unit. |
| $\delta^{\mathbf{1}}$ | Positive-sequence voltage angle vector. |
| $\delta_i^x$ | Voltage phase angle of phase $x$ where $x \in \{a, b, c\}$ at node $i$ (phase coordinates). |
| $\delta_{I,IC,l}^x$ | Interlinking converter's output current phase angle where $x \in \{a, b, c\}$. |
| $\delta_i^1$ | Positive-sequence voltage angles at node $i$. |
| $\eta_i$ | The reciprocal of the AC DG's reactive power droop gain in per-unit. |
| $\eta_l$ | Interlinking convrter's reactive power droop gain in per-unit. |
| $\gamma_l$ | Interlinking converter's active power error coefficient in per-unit. |
| $\lambda$ | Loading factor of ac loads. |
| $\lambda_{dc}$ | Loading factor of dc loads. |
| $\mathbf{I_{ac,L}^0}$ | Zero-sequence laod current vector in per-unit. |
| $\mathbf{I_{ac,L}^2}$ | Negative-sequence load current vector in per-unit. |
| $\mathbf{\Delta I_{ac}^0}$ | Zero-sequence decoupling current vector in per-unit. |
| $\mathbf{\Delta I_{ac}^2}$ | Negative-sequence decoupling current vector in per-unit. |
| $\mu_i$ | The reciprocal of the AC DG's active power droop gain in per-unit. |
| $\mu_{ac}$ | Virtual DG's droop gain in per-unit. |
| $\omega$ | AC microgrid frequency in per-unit. |
| $\omega_{0,ac}$ | Virtual DG's no-load frequency in per-unit. |
| $\omega_{0,i}$ | The AC DG's no load frequency in per-unit. |
| $\omega_{max}$ | Maximum ac subgrid frequency in per-unit. |
| $\omega_{min}$ | Minimum ac subgrid frequency in per-unit. |
| $\theta_{ij}^{11}$ | Angle of the positive-sequence Y-bus matrix element. |
| $\theta_{ij}^{xy}$ | Admittance matrix element angle between phases $x$ and $y$ where $x, y \in \{a, b, c\}$, and between nodes $i$ and $j$ (phase coordinates). |

| | |
|---|---|
| $\varrho$ | DC load power exponent. |
| $\vartheta_{I,i}$ | The reciprocal of the droop gain for the DC DG output current in per-unit. |
| $\vartheta_{P,i}$ | The reciprocal of the droop gain for the DC DG output power in per-unit. |
| $e_{ac-dc,max}$ | The globally defined difference between $\Delta\omega_{pu}$ and $\Delta V_{dc,pu,l}$ at, or beyond, which all ICs should ideally transfer their maximum powers. |
| $e_{pu}$ | Error between the per-unit deviations of the ac subgrid frequency and the dc subgrid voltage as measured by the interlinking converter. |
| $g_{ij}$ | Conducatnce of dc feeder connecting nodes $i$ and $j$ in per-unit. |
| $k_l$ | Reciprocal of interlinking converter's active power error coefficient in per-unit. |
| $m_p$ | The AC DG's active power droop gain in per-unit. |
| $n_q$ | The AC DG's reactive power droop gain in per-unit. |
| $r_{ij}$ | Resistance of dc feeder connecting nodes $i$ and $j$ in per-unit. |
| $\lvert V_{ac,i}^{1}\rvert$ | Positive-sequence voltage magnitude at node $i$ in per-unit. |
| $\lvert V_{ac,i}^{x}\rvert$ | Voltage magnitude of phase $x$ where $x \in \{a, b, c\}$ at node $i$ in per-unit (phase coordinates). |
| $\lvert Y_{ij}^{11}\rvert$ | Magnitude of the positive-sequence Y-bus matrix element in per-unit. |
| $\lvert Y_{ij}^{xy}\rvert$ | Admittance matrix element magnitude in per-unit between phases $x$ and $y$ where $x, y \in \{a, b, c\}$, and between nodes $i$ and $j$ (phase coordinates). |
| $\lvert \mathbf{V_{ac}^{0}}\rvert$ | Zero-sequence voltage magnitude vector in per-unit. |
| $\lvert \mathbf{V_{ac}^{1}}\rvert$ | Positive-sequence voltage magnitude vector in per-unit. |
| $\lvert \mathbf{V_{ac}^{2}}\rvert$ | Negative-sequence voltage magnitude vector in per-unit. |

# Chapter 1

# Introduction

## 1.1 Research Motivation

Driven by environmental concerns, electricity grids tend to become "greener"by higher penetration of renewable energy resources (RER) into existing and future grids [1], [2]. Most renewable or non-renewable energy-based distributed electricity generators and energy storage systems (ESSs) provide unregulated dc or ac power; examples of these energy sources are: photo-voltaic panels (PV), micro-turbines (MT), wind turbines (WT), fuel cells (FC), and battery energy storage systems (BESS). Therefore, waveform conditioning is a necessity to connect these energy sources to the existing electricity grids, and to provide the necessary controls. The advances in topology and control of power electronic (PE) converters in recent decades have facilitated the integration of small-scale distributed energy resources (DER), which are also known as distributed generation (DG), in distribution networks [3]–[5]. Hence, the current trend in electricity grids is toward decentralized, small-scale, local electricity generation, rather than the classical centralized scheme [6], [7]. The concept of ac microgrid was first introduced in the early 2000s as a new approach to integrate different DGs and ESSs, as well as controllable and uncontrollable loads, within a relatively small geographical area. The DG sources mainly provide electricity to the local loads; at the same time, some DGs may provide heat by the utilization of combined heat and power (CHP) generation technologies [8]. The existence of DGs close to load centers, as implied in ac microgrid concept, potentially reduces power loss in the transmission stage, and increases the cultivation of local RER and ESSs. Figure 1.1 illustrates the architecture of a simple ac microgrid [9], [10].

Although an ac microgrid should be able to operate autonomously without being con-

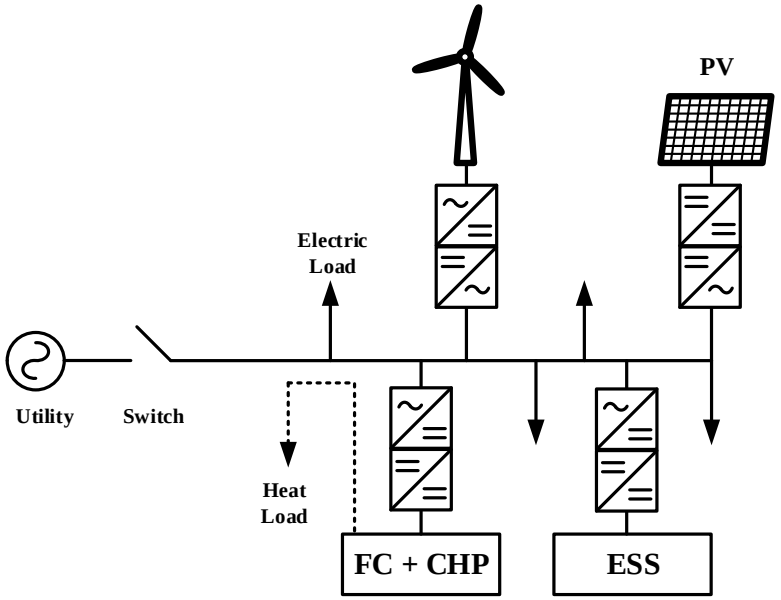


Figure 1.1: A simple ac microgrid architecture.

nected to a stiff grid, connection to a utility grid should be possible through a switch at one single point, known as the point of common coupling (PCC) [11]. Such microgrid may operate in "grid-connected" or "islanded" modes of operation. When an ac microgrid is operated in grid-connected mode, the microgrid is seen by the utility grid as a single entity, making active and reactive power trading between the main grid and the microgrid possible [12]. The microgrid is considered to be operating in islanded-mode when it operates autonomously and disconnected from the main grid. The islanding action may happen either intentionally for scheduled maintenance purposes, or accidentally in case of faults or other grid problems. Ac microgrids which do not have access to any stiff utility grid are called "isolated microgrids". Thus, ac microgrids provide a new reliability dimension by allowing autonomous operation of distribution systems in islanded mode during grid faults [13], and in isolated mode due to lack of access to bulk power systems in remote communities [14].

Moreover, the evolution and rapid growth of dc power generation, ESSs, and modern dc loads – such as variable speed drives (VSDs), plug-in electric vehicles (PEVs), and electronic devices – urge the development of dc distribution networks that outperform their conventional ac counterparts in many environmental, technical, and economic aspects [15]–[17]. Although dc power distribution has been implemented for some specific applications,

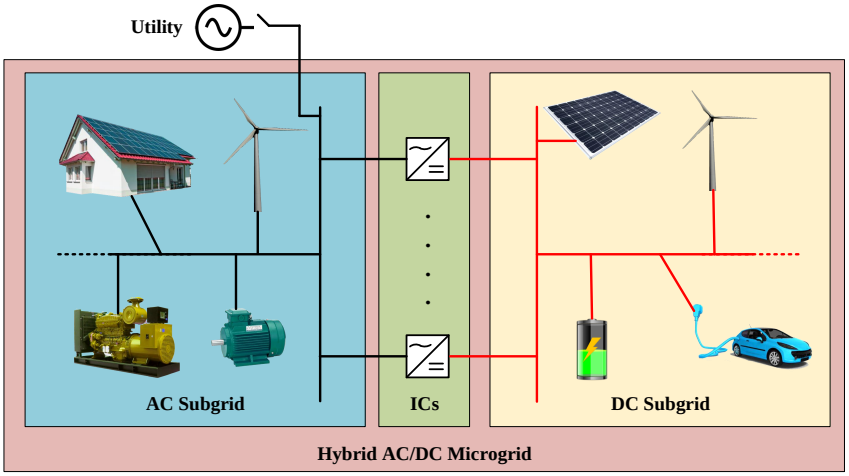


Figure 1.2: Hybrid ac/dc microgrid architecture.

such as communication and traction systems, current research is geared towards its larger scale and more flexible implementation in the form of dc microgrids. Accordingly, many projects and studies have proposed and implemented different configurations, voltage levels, and control schemes for various dc microgrid applications [18], [19].

Despite the rising potential for dc microgrids, replacing the existing ac distribution systems with dc networks is neither technically nor economically justified. Therefore, hybrid ac/dc microgrids, in which ac and dc subgrids are interfaced through interlinking converters (ICs) to form one entity, have been proposed as an optimal configuration that combines the merits of both systems [20], [21]. Incorporating ICs permits power transfer between ac and dc subgrids in the hybrid microgrid, as shown in Figure 1.2, thus leading to potential improvements to overall system reliability, security, and efficiency [13], [22].

Similar to ac microgrids, a hybrid microgrid should be able to manage the distributed energy resources and loads in the case of faults and disconnection from the main grid, operating in an islanded mode. This feature significantly increases the microgrid resilience by securing the continuity of power delivery to loads with no access to the bulk power system. Many factors affect the structure and control strategy of hybrid ac/dc microgrids, among which relative sizes of subgrids and number of ICs have stronger effects [20], [21]. On the one hand, if the hybrid microgrid contains a 'dominant' subgrid (i.e., an ac or dc subgrid of relatively larger capacity), ICs operate to regulate the power variables in the smaller subgrid. This regulation is realized by either fixing the power variables if only one IC interfaces the subgrids, or by implementing droop characteristics if multiple ICs are used [23], [24]. On the other hand, if an islanded hybrid ac/dc microgrid integrates

two subgrids with comparable sizes, ICs adopt a power sharing mode that aims for equal relative loadings for the subgrids without any communication infrastructure. For this purpose, DGs implement droop control characteristics that enable autonomous overall load-sharing among the units [13]. In the ac subgrid, DGs adapt the output frequency and voltage according to the active and reactive powers, respectively. In the dc subgrid, the units adjust their voltages based on their output power. Meanwhile, the balance between the two subgrids is maintained by the ICs, which relate the ac subgrids frequency to the dc subgrids voltage, thus resulting in variable, yet coupled, ac frequency and dc voltages [22], [25], [26]. If the subgrids are linked via a single IC, this mode is realized by equalizing the normalized frequency and voltage deviations in the ac and dc subgrids, respectively, [27]. However, if multiple ICs are employed, which is the most generic and sophisticated case, they implement droop control to proportionally share the power exchanged between the subgrids [26]. It is noteworthy that the autonomous operation of multiple droop-controlled ICs was proposed in [26], but has not been investigated so far.

Steady-state analysis is an essential step in planning and operational studies of electric power systems (e.g., reactive power planning, parameter settings, and power management) [28], [29]. These studies could be extended to include stability assessment, power sharing, optimal operation, and system loadability in islanded microgrids [30], [31]. Therefore, the development of tools that can effectively analyze the steady-state characteristics of such evolving microgrids becomes a necessity. In addition to the distinctive operational philosophies of these microgrids that have to be incorporated in the steady-state analysis studies, the unbalanced nature of ac subgrids poses further complexity on analyzing their behavior. Motivated by the aforementioned considerations, this thesis is primarily focused on developing a platform for comprehensive, computationally-efficient, and accurate steady-state analysis tools for standalone (i.e, islanded or isolated) hybrid ac/dc microgrids. The platform must provide frameworks for developing and integrating the essential steady-state DG and IC models into power flow analysis approaches. Additionally, the thesis will study uninvestigated practical operational aspects of these microgrids, such as the impact of unbalanced ac operation on the loadability of hybrid microgrids. Furthermore, the thesis will provide innovative solutions to some of the addressed operational issues. The provided analysis and discussions will open the door to different dimensions of hybrid ac/dc microgrid planning and operation studies.

## 1.2 Literature Survey

As per the motivations defined in Section 1.1, the literature survey will cover three main areas pertaining to the work developed in this thesis as follows:

1. The steady-state analysis of unbalanced ac microgrids, as an essential part of hybrid ac/dc microgrids.
2. The steady-state analysis of hybrid unbalanced ac/dc microgrids, as an extension to the analysis of ac microgrids.
3. Loadability and optimal operation of hybrid unbalanced ac/dc microgrids.

These areas are addressed thoroughly in the following subsections.

### 1.2.1 Steady-State Analysis of Unbalanced AC Microgrids

For several decades, synchronous generator-based DGs (SGDGs), such as diesel and gas generator sets, have played a vital role in powering isolated electrical distribution networks [14]. Furthermore, these generators are commonly integrated to grid-connected distribution systems to export power or to provide a stand-by source in case of the main grid's outage, thus forming an islanded microgrid. On the other hand, the enormous benefits of advanced electronically-interfaced DGs (EIDGs), such as flexibility, speed, and interfacing RERs, urge their integration into modern distribution networks. Accordingly, both types of DGs are anticipated to coexist in ac microgrids [32]. Research is ongoing on the dynamic behavior of networks that comprise the two types of DGs [33]. However, their steady-state performance has not been investigated yet.

Power-flow analysis tools play a key role in planning and operation studies of electrical power systems. At the transmission level, various power flow algorithms have been established to analyze balanced bulk power systems [34]. Some of these algorithms have been further extended to include unbalanced operation [35]. At the active distribution level, some power flow algorithms have been developed for grid-connected ac microgrids with integrated DGs, where a stiff grid acts as an ideal slack bus maintaining balanced voltages with fixed magnitude and frequency at the source node [36]. However, this analysis does not consider the integration of droop-controlled DGs, which can potentially be used in grid-connected mode to allow autonomous operation of islanded microgrids formed after an islanding event [13]. Additionally, the analysis does not account for unbalances

at the source node in case the primary source is not ideal, such as in isolated SGDG-fed microgrids.

Moreover, some approaches employ different strategies to account for microgrids' droop features. Characterized by their load-dependent voltage magnitude and frequency, droop-controlled ac microgrids differ from conventional ac systems discussed above in the following aspects:

- Droop-controlled microgrids lack a slack bus.
- The microgrid's frequency is load-dependent and therefore it is considered a power flow variable.
- The feeder and load models are frequency-dependent.

It is worth mentioning that droop-controlled microgrids lack a slack bus, since the microgrid's losses – and loads – are shared collaboratively among all droop-controlled DGs, rather than being supplied by one source as in conventional systems. However, the microgrid's frequency allows the power flow solution, because it is a global variable shared among all DGs. Altogether, these characteristics complicate the power flow problem formulation and solution, as compared to conventional distribution networks. In [37] and [23], modified Newton Raphson (NR) approaches have been introduced by providing additional mismatch equations and Jacobian matrix elements that accommodate the system's droop characteristics. Similarly, a forward-backward approach has been proposed in [38] for droop-controlled ac microgrids. Nevertheless, the application of these methods is limited to balanced ac microgrids. The authors of [39] have proposed a power flow algorithm based on a Newton-Trust Region (NTR) method to solve the unbalanced microgrid's set of frequency-dependent nonlinear equations in phase-coordinates. However, the authors have not considered SGDGs in their study, which are challenging to model in phase-coordinates, considering the machines' saliency and internal impedances [36]. Furthermore, their models ignore the influence of the interfacing transformer's delta/wye connection on the EIDG phase loading and voltage unbalances. In addition to its high computational cost, this approach does not include some aspects, such as shunt admittances of distribution feeders and delta-connected loads that commonly exist in distribution systems [40].

Based on the above-identified limitations of the power flow approaches reported in the literature, it is necessary to develop a modeling and power flow analysis framework for unbalanced ac microgrids that has the following features:

- Generic, accurate, and computationally-efficient, as compared to the reported methods,

- Integrates different DG types and various aspects of droop-controlled and isochronous unbalanced ac microgrids, which have not been considered in previous studies, and
- Can be used to investigate the operation of droop-controlled DGs in unbalanced isochronous microgrids.

### 1.2.2 Steady-State Analysis of Unbalanced Hybrid AC/DC Microgrids

As a primary steady-state analysis tool, an accurate and efficient power flow algorithm is essential for performing numerous planning and operational studies in hybrid ac/dc microgrids. Several power flow approaches have been developed for multi-terminal dc systems (MTDC); yet these algorithms are not applicable to microgrids, since MTDCs are not droop-controlled at the ac subsystem [41], [42]. A few algorithms have recently been proposed to solve the power flow of droop-controlled hybrid ac/dc microgrids. In [43], the authors have proposed a unified approach, in which a Newton-trust region (NTR) method is used to concurrently solve the power flow equations of the two subgrids. Similarly, the authors of [44] have adopted a Newton Raphson (NR) method to solve the unified set of microgrid nonlinear equations, while the authors of [45] have employed a generalized reduced gradient (GRG)-based approach that is able to work equally well for grid-connected and islanded hybrid ac/dc microgrids. Meanwhile, the sequential algorithm reported in [23] has significantly reduced the power flow computational time in comparison with the aforementioned unified methods, as it breaks down the system model into smaller decoupled sets of equations that take less time to solve. However, all the above-mentioned approaches assume balanced ac subgrids, thus limiting their application in inherently unbalanced ac distribution systems.

As explained in Section 1.2.1, the steady-state analysis of unbalanced droop-controlled ac microgrids has been performed in [39]. Nevertheless, the presented control schemes for the DGs are limited and no dc subgrids are included. Furthermore, this method assumes one model for all droop-controlled distributed generation (DG) units; therefore it does not reflect the diverse features of various DG types and configurations. Synchronous generator-based DGs (SGDGs) and electronically-interfaced DGs (EIDGs), which may coexist in the same microgrid [32], exhibit different behaviors under unbalanced loading. Furthermore, this approach does not consider the effects of transformer connections, which are commonly used to interface EIDGs to the ac network, on the system model and DG phase loadings. In addition, the power flow algorithm developed in [39] incorporates a large number of dummy variables that add significantly to the problem size and computational effort. The

relatively poor performance of such unified approach, along with the above-mentioned modeling inaccuracies, urge development of more generic, accurate, and efficient power flow approaches for standalone unbalanced hybrid ac/dc microgrids.

To date, no power flow algorithm has been proposed that addresses all operational aspects of unbalanced hybrid ac/dc microgrids, which can be summarized as follows:

- Absence of a slack bus,
- Unbalanced operation of the ac subgrid,
- Frequency and voltage variations in the ac and dc subgrids, respectively,
- Correlation between the ac frequency and dc voltage, and
- Parallel operation of droop-controlled ICs.

Therefore, it is essential to develop power flow methods for unbalanced hybrid ac/dc microgrids that:

- Consider the above-mentioned aspects of islanded hybrid microgrids altogether, which have not been addressed in the reported literature,
- Optimize the power flow formulation to reduce the number of variables and the execution times of the algorithms' subroutines for enhanced algorithm efficiency,
- Model the different types and various operational modes of the DGs and ICs to render the power flow approaches comprehensive, and
- Accurately represent parallel operation of ICs, which have been proposed in the literature, yet not discussed in any reported study.

### 1.2.3 Loadability of Hybrid Unbalanced AC/DC Microgrids

A major merit of microgrids is the ability to operate autonomously in islanded mode, thus significantly enhancing the customer service reliability during upstream disturbances. Typically, a hierarchical control scheme is adopted as a low-cost and high-reliability solution for islanded operation [46]–[48]. At the primary level, decentralized droop control eliminates the need for communication links to achieve proportional power sharing among DGs, either in ac or dc microgrids. Employing droop-controlled ICs allows autonomous power sharing

among ac and dc DGs in a hybrid paradigm, thus integrating the two subgrids into a single entity [26]. Nonetheless, since droop controllers depend solely on local measurements, different microgrid operational requirements (e.g., accurate reactive-power sharing in ac microgrids, precise load sharing in dc microgrids, voltage constraints, and maximum loadability) might not be satisfied. Therefore, a complementary microgrid central controller (MGCC) with a low-bandwidth communication infrastructure is commonly needed [49]. The MGCC adopts high-level secondary and tertiary control layers to coordinate the DGs' operation in both islanded and grid-connected modes. Various MGCCs that continually update the DG droop settings have been proposed in the literature to attain different objectives [15], [50], [51]. However, some researchers have considered offline optimal droop settings based on stochastic or probabilistic approaches, thus omitting the communication requirements [52], [53]. Although offline droop settings can be beneficial in case of absence or failure of the microgrid's communication infrastructure, communication-based droop setting approaches attain enhanced system reliability, under normal operation, as they provide real-time microgrid monitoring. Furthermore, the changes in the microgrid configuration and load distribution require continuous readjustment of the optimal DG settings.

Unbalanced loads and high penetration of single-phase DGs could impose additional challenges and constraints on islanded microgrids' operation [39]. Several studies have addressed and resolved the voltage imbalance problem arising from unbalanced loading of ac microgrid phases. Numerous autonomous and supervised control schemes have been proposed to allow for collaborative enhancement of the microgrid voltage quality as well as improving unbalanced and nonlinear load sharing among DGs [54]–[56]. However, these studies often assume moderately-loaded microgrids, and disregard the effect of load unbalances on the microgrid's maximum loading capabilities. Furthermore, reduction of distribution system unbalances has been addressed in the literature to achieve various objectives, such as enhancing system efficiency and/or reducing equipment overloading [57], [58]. Nonetheless, majority of these studies have investigated grid-connected systems rather than islanded microgrids. In islanded microgrids, the imbalance problem should be given more attention, as it can impact the microgrid loadability in addition to degrading system performance.

Self-sufficiency is a crucial factor for sustained operation of islanded microgrids. Due to the resistive nature of distribution networks, microgrid loadability is primarily restricted by the limit-induced bifurcation (LIB) criterion rather than saddle-node bifurcation (SNB) accompanied by voltage instability, which is commonly observed at the transmission level due to the excessive reactive-power losses along the transmission lines [53], [59]. However, in the literature, only balanced microgrids have been considered for loadability studies.

Despite the higher flexibility of electronically-interfaced DGs over conventional machine-based generators, they are more sensitive to over-currents. Thus, successful operation of highly unbalanced microgrids will be restricted by DG phase capacities rather than the total connected generation limits as in balanced systems.

Loadability of unbalanced ac microgrids has not yet been addressed in the literature. Furthermore, ICs are typically used only to exchange power between subgrids in a hybrid paradigm, whereas they could also provide supplementary services to either subgrid. In addition, some researchers have proposed reactive-power support to heavily loaded ac subgrids through ICs. However, reactive-power injection is limited to the condition of active-power flow in the same direction [25].

Based on the above-identified shortfalls of the work reported in the literature, a study should be conducted to achieve the goals defined below:

- Investigate the effect of unbalanced conditions on microgrid loadability,
- Extend the IC's reactive-power support that was introduced in [26] to relieve DGs on the ac side under different operational conditions, and
- Implement a control strategy at the secondary level, and integrate it into a supervisory controller that adopts a generic OPF algorithm to minimize microgrid load shedding.

## 1.3 Research Objectives

Based on the gaps identified in the literature survey of Section 1.2, the research objectives of this thesis are defined as follows:

1. Develop a steady-state analysis tool that is able to solve the power flow of droop-controlled unbalanced hybrid ac/dc microgrids. Since ac microgrids are a special form of intrinsically unbalanced distribution systems, the developed tool must incorporate the unbalanced models of the ac system components, such as unbalanced feeders and loads. The tool must also integrate the correlation between the ac and dc subgrids, through the interlinking converter models, in the hybrid ac/dc microgrid paradigm, under autonomous operation.
2. Investigate the operation of large-scale islanded hybrid ac/dc microgrid, and identify their operational limitations due to ac subgrid unbalances. The analysis must also

address other practical challenges of such microgrids, such as imperfections in the load sharing among the ac and dc subgrids, and in the proportional power sharing among interlining converters.

3. Develop an optimal power flow scheme to overcome the loading limitations imposed on the operation of islanded hybrid ac/dc microgrids due to their unbalanced nature. The developed scheme must take into consideration the droop characteristics of the microgrid. Also, it has to maintain the ac subgrid frequency and the ac and dc node voltages within their permissible limits.

4. Develop a generic, accurate, and computationally efficient modeling and power flow analysis approach for standalone unbalanced ac microgrids. The approach has to consider the different steady-state characteristics of various DG types, structures, and control schemes for better accuracy. It must also incorporate the effects of transformer connections and different unbalanced load configurations on the power flow. The DG capacity limits need to be enforced in the power flow algorithm as well. Finally, the power flow approach should be capable of analyzing the behavior of droop-controlled DGs in unbalanced isochronous ac microgrids.

5. Develop an improved modeling and power flow analysis approach for unbalanced islanded hybrid ac/dc microgrids. The approach is required to model the interlinking converters as well as the dc subgrid components in addition to the unbalanced ac subgrid elements. The correlation between the ac and dc power flow variables has to be preserved. The approach also needs to enforce the limits of all DGs and interlinking converters in the power flow solution. It is essential that the developed approach out-performs its counterparts in terms of accuracy and speed.

## 1.4 Thesis Layout

The remainder of the thesis is structured as follows:

**Chapter 2** presents the relevant theoretical background on the operational aspects of standalone ac, dc, and hybrid ac/dc microgrids. It also reviews the basic concepts of steady-state analysis of conventional power systems.

**Chapter 3** presents a steady-state analysis tool for unbalanced islanded hybrid ac/dc microgrids. The steady-state models of the various components of droop-controlled ac

and dc subgrids as well as the interlinking converters are developed in phase coordinates. The developed models are integrated into a unified power flow formulation. A Newton-Trust Region (NTR) method is adopted to solve the set of nonlinear power flow equations. The developed analysis tool is utilized to identify challenges pertaining to heavy loading as well as adjusting interlinking converter settings in such microgrids under autonomous operation.

**Chapter 4** proposes a novel adaptive power routing (APR) scheme to maximize the loadability of unbalanced hybrid ac/dc microgrids in islanded mode of operation. The APR scheme allows for independent control of the interlinking converter phases in order to relieve the stressed phases of the DGs connected to the ac subgrid. To achieve maximum microgrid loadability, a secondary controller is assumed that employs an optimal power flow approach with the objective of load shedding minimization, while maintaining the microgrid variables within limits. The optimal power flow problem is solved using an interior-point method.

**Chapter 5** presents a generic modeling and power flow analysis approach for standalone ac microgrids under both isochronous and droop modes of operation. The different microgrid components are modeled in symmetrical sequence components. To attain high modeling accuracy, different models are adopted for the various types, structures, configurations, and control schemes of DGs. The developed sequence-component models are decoupled to permit independent and parallel solution of the different sequence frames, thus resulting in significant reduction of the power flow algorithm's execution time as compared to the reported approaches.

**Chapter 6** introduces an improved modeling and power flow analysis approach for unbalanced islanded hybrid ac/dc microgrids. The ac subgrid components, as well as the ac side of the interlining converters, are modeled in symmetrical sequence components. In addition to decoupling the sequence component frames of the ac subgrid, the ac and dc subgrid power flow problems are also decoupled by introducing a virtual DG that maintains the mathematical correlation between the two subsystems. Henceforth, a Newton-Raphson-based hybrid ac/dc power flow algorithm is developed to sequentially solve the independent, yet correlated, power flow problems of the ac and dc subgrids. The proposed algorithm shows substantial improvements, in terms of accuracy and convergence time, when compared to conventional approaches.

**Chapter 7** summarizes the thesis, and presents the main thesis contributions, as well as the suggested directions for future work.

# Chapter 2

# Background Review

## 2.1 Introduction

As discussed in Chapter 1, the control and steady-state analysis of hybrid ac/dc microgrids have received increasing attention over the last few decades. In order to establish steady-state models of microgrid components, it is essential to build a comprehensive background about the structures and control strategies of such microgrids. Many hierarchical control schemes have been proposed for ac, dc, and hybrid ac/dc microgrids. Accordingly, this chapter intends to lay the background required for the conducted research through review of the structures and control strategies of the three types of microgrids. In addition, the chapter reviews some background topics required for steady-state analysis, such as power flow and optimal power flow analysis of electrical power systems.

## 2.2 Hierarchical Control of AC Microgrids

The coordination between different DGs in ac microgrids is a necessity to share the load power. Although the load sharing functionality can be realized through a centralized controller and communication infrastructure, this solution requires fast communication links which add to the cost of the system infrastructure and degrade the microgrid reliability at the same time. Therefore, the decentralized control approach was realized in the literature by introducing local decentralized controllers that are able to share the microgrid's total load among DGs based on local measurements only. This decentralized approach typically implements droop controllers for load power sharing, which have

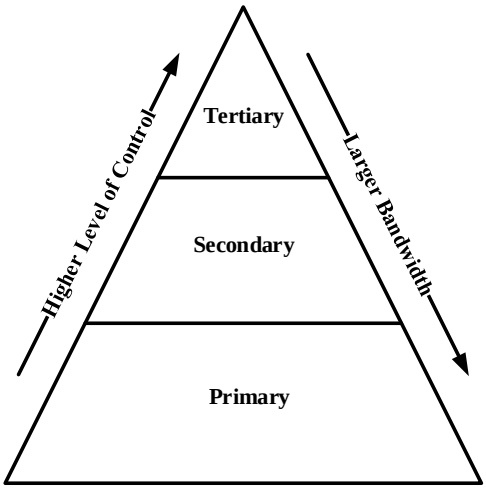


Figure 2.1: Hierarchical control structure of ac microgrids.

demonstrated fast, reliable, and stable operation. However, droop controllers normally cause deviation of microgrid frequency and voltage from their nominal values to realize the autonomous load sharing function; these deviations are considered a drawback for decentralized control of DGs. Moreover, since the decentralized controllers are based solely on their local measurements, a higher level of coordination between DGs cannot directly be implemented at that level. Therefore, a hierarchical control structure is typically used to benefit from the high reliability and low cost of decentralized controllers on the one hand, and the coordination flexibility of centralized communication-based controllers on the other hand [27], [47], [48], [60]–[64].

The hierarchical control structure of ac microgrids follows the same hierarchical scheme of conventional power systems. It typically employs primary decentralized controllers, a slow-communication-based secondary controller, and a slower higher level tertiary controller. As shown in Figure 2.1 , the higher the control level is, the smaller the controller bandwidth becomes. The following subsections illustrate the functionalities and implementation of each level of control.

### 2.2.1 Primary Control of AC Microgrids

The primary control of microgrids is mainly responsible for current and voltage shaping at the DG terminals. In addition, it regulates the power sharing among different DGs

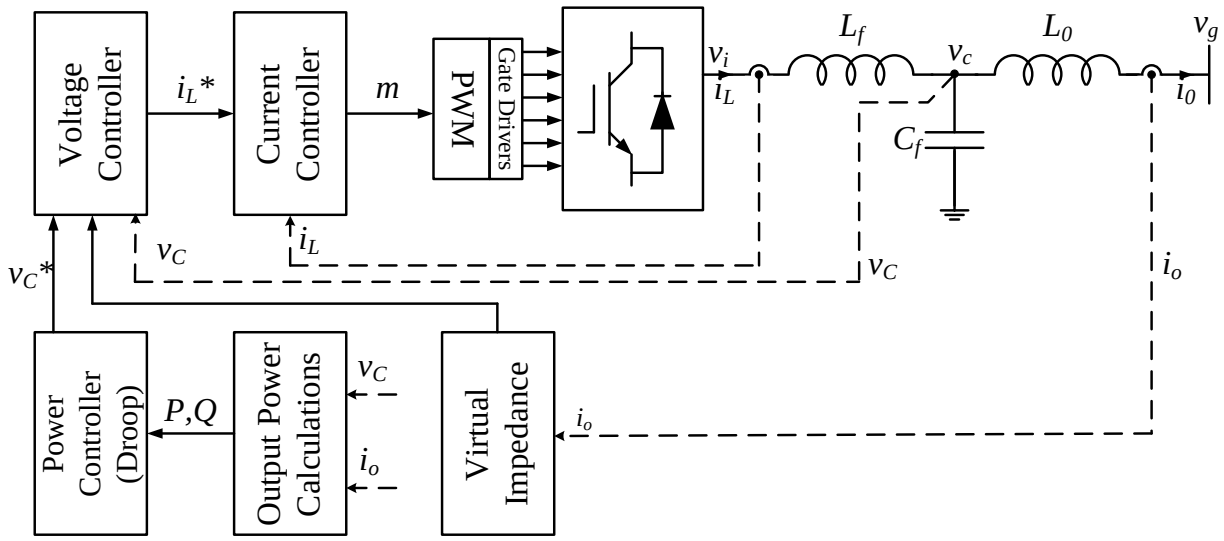


Figure 2.2: VSC primary controller.

connected to the same ac microgrid. As seen in Figure 2.2, a power-electronic-interfaced DG employs a three-phase voltage source converter (VSC) and an LC/LCL filter connected to the microgrid bus through an output impedance (i.e., cable impedance or transformer) [65], [66]. The local primary controller employs three cascaded control loops as follows: current control loop, voltage control loop, and power control loop (i.e., droop controller) [67]–[70].

### AC Current Controller

The current control loop has the largest bandwidth in the system. It is responsible for controlling the injected current by the VSC; it is also capable of limiting the output current of the VSC for protection purposes.

The current controller can be implemented using different types of controllers in different reference frames. The most commonly used controllers reported in the literature are Proportional-Integral controller (PI controller) in the *dq* synchronous reference frame and Proportional Resonant controller (PR controller) in the $\alpha\beta$ stationary reference frame.

Figure 2.3 shows the detailed structure of the current controller in *dq* reference frame. The controller consists of two linear PI-controllers to control the output filter's inductor current components $i_{Ld}$ and $i_{Lq}$. The cross-coupling terms $+i_{Ld}\omega L$ and $-i_{Lq}\omega L$ ensure full

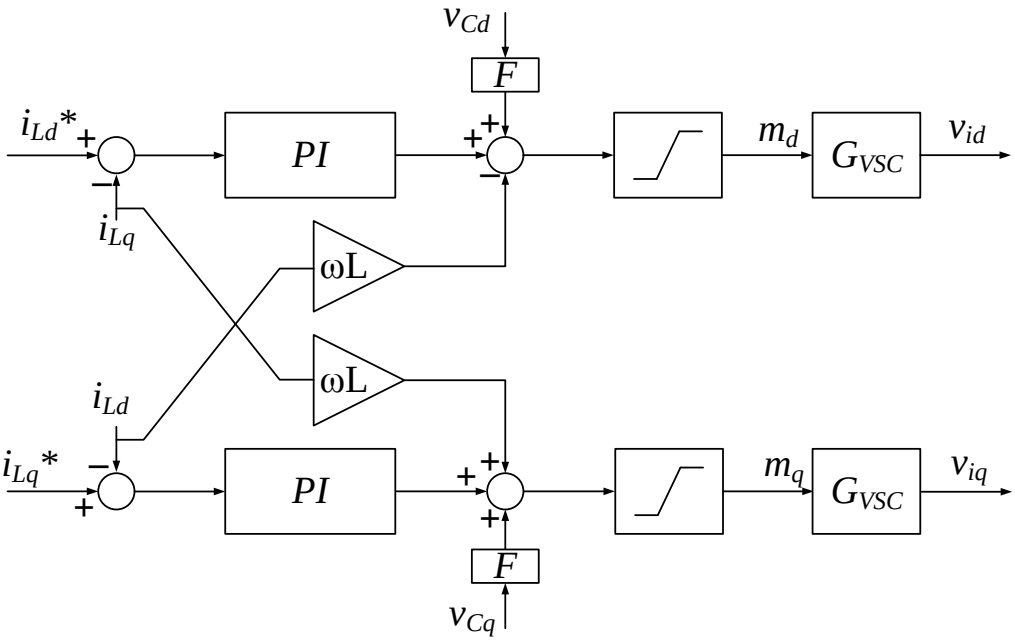


Figure 2.3: VSC current controller in dq frame.

decoupling between $i_{Ld}$ and $i_{Lq}$. In addition, the voltage feed-forward terms $v_{Cd}$ and $v_{Cq}$ are added to improve the converter start-up process and to enhance the controller disturbance rejection [71]. The main disadvantage of implementing the controllers in dq frame appears in case of the presence of unbalanced loads. To make the converter able to control unbalanced currents, an additional negative-sequence controller is required to be operated in parallel with the positive sequence controller. Moreover, for harmonic compensation when nonlinear loads are present, additional controllers – one for each harmonic frequency to be compensated for – should be implemented.

On the other hand, PR-controllers in $\alpha\beta$ frame show some advantages over PI controllers in $dq$ frame, as the PR controller is able to control both positive and negative sequence currents at the same time. Moreover, no cross-coupling terms are needed for PR controllers. Figure 2.4 shows the block diagram of the current PR controller in $\alpha\beta$ frame. The transfer function of the controller is given in (2.1). The controller also implements harmonic current compensation, as seen in the transfer function.

$$PR_I(s) = k_{pi} + \frac{k_{ri}s}{s^2 + 2\omega_c s + \omega_o^2} + \sum_{h=5,7,11,\ldots}^{n} \frac{k_{ih}s}{s^2 + 2(h\omega_c)s + (h\omega_o)^2} \tag{2.1}$$

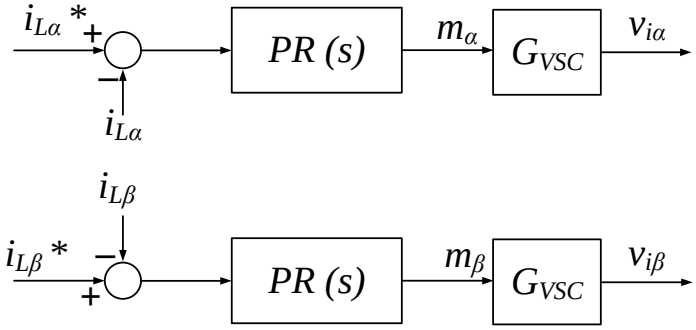


Figure 2.4: VSC current controller in $\alpha\beta$ frame.

### AC Voltage Controller

The second control loop in the cascaded control scheme of the VSC is the voltage control loop. The bandwidth of the this loop is usually designed smaller than that of the current control loop. The function of this loop is to provide reference currents to the current control loop, such that the VSC tracks the reference voltage signal. Similar to the current control loop, voltage controllers can be implemented either in $dq$ or in $\alpha\beta$ reference frames.

Figure 2.5 shows the block diagram of the voltage controller in synchronous reference frame. The controller employs two linear PI-controllers to regulate the filter capacitor voltage components. It is worth noting that the reference quadrature voltage component $v^*_{Cq}$ is set to zero. The controller also employs cross coupling terms $+v_{Cd}\,\omega C$ and $-v_{Cq}\,\omega C$ to decouple the responses of the d and q channels. In order to compensate for unbalanced and harmonic voltages, negative sequence and harmonic voltage controllers need to be implemented in parallel with the positive sequence voltage controller.

Similar to the current control loop, the voltage control loop can be realized in $\alpha\beta$ reference frame by adopting PR-controllers. Figure 2.6 and (2.2) show the block diagram and transfer function of the PR voltage controller with voltage harmonic compensation.

$$PR_V(s) = k_{pi} + \frac{k_{rv}s}{s^2 + 2\omega_c s + \omega_o^2} + \sum_{h=5,7,11,\ldots}^{n} \frac{k_{vh}s}{s^2 + 2(h\omega_c)s + (h\omega_o)^2} \tag{2.2}$$

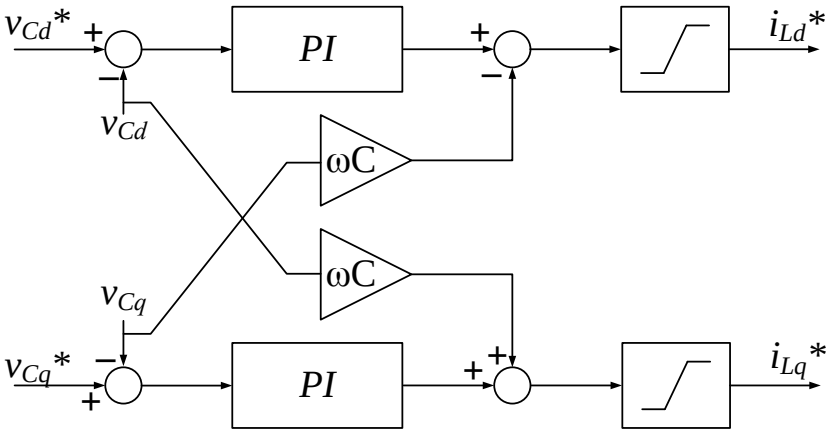


Figure 2.5: VSC voltage controller in dq frame.

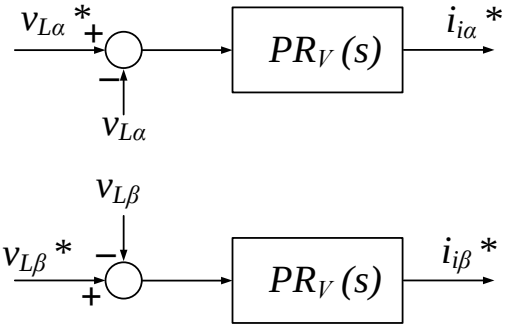


Figure 2.6: VSC voltage controller in $\alpha\beta$ frame.

### AC Power Controller

The last stage of the primary control of VSC-interfaced DGs is the power control loop (droop controller), which has the smallest bandwidth within the local controller of the DG. The power droop controller sets the voltage reference – by defining both the voltage magnitude and frequency – to the inner voltage controller based on the converter output active and reactive powers.

The active and reactive power flows between any two nodes $i$ and $j$, in a balanced ac power system, can be generally given by (2.3) and (2.4), where $\left|V_{ac,i}\right|$ and $\left|V_{ac,j}\right|$ are the voltage magnitudes at the two nodes, $R_{ij}$ and $X_{ij}$ are the line resistance and reactance respectively, and $\delta_i$ and $\delta_j$ are the voltage angles at the two nodes.

$$P_{ij} = \frac{\left|V_{ac,i}\right|}{R_{ij}^2 + X_{ij}^2}\left[R_{ij}\ \left(\left|V_{ac,i}\right| - \left|V_{ac,j}\right|\cos(\delta_i - \delta_j)\right) + X_{ij}\left|V_{ac,j}\right|\sin(\delta_i - \delta_j)\right] \tag{2.3}$$

$$Q_{ij} = \frac{\left|V_{ac,i}\right|}{R_{ij}^2 + X_{ij}^2}\left[-R_{ij}\ \left(\left|V_{ac,j}\right|\sin(\delta_i - \delta_j)\right) + X_{ij}\left(\left|V_{ac,i}\right| - \left|V_{ac,j}\right|\cos(\delta_i - \delta_j)\right)\right] \tag{2.4}$$

However, if the line impedance is heavily inductive (high X/R ratio), and the power angle $(\delta_i - \delta_j)$ is assumed small, the power flow equations can be simplified and rewritten as:

$$P_{ij} \approxeq \frac{\left|V_{ac,i}\right|\left|V_{ac,j}\right|}{X_{ij}}\sin(\delta_i - \delta_j) \approxeq \frac{\left|V_{ac,i}\right|\left|V_{ac,j}\right|}{X_{ij}}\left(\delta_i - \delta_j\right) \tag{2.5}$$

$$Q_{ij} \approxeq \frac{\left|V_{ac,i}\right|}{X_{ij}}\left(\left|V_{ac,i}\right| - \left|V_{ac,j}\right|\cos(\delta_i - \delta_j)\right) \approxeq \frac{\left|V_{ac,i}\right|^2 - \left|V_{ac,i}\right|\left|V_{ac,j}\right|}{X_{ij}} \tag{2.6}$$

As seen from (2.5) and (2.6), the active power flow is approximately proportional to the voltage angle difference, which in turn is dependent on the frequency, and the reactive power flow is approximately proportional to the node voltage magnitude. Therefore, inductive lines help in decoupling active and reactive powers.

Assuming that the line impedances in a microgrid are heavily inductive, P-$\omega$ and Q-V droop controllers can be presented. Figure 2.7 shows the P-$\omega$ and Q-V droop characteristics for both unidirectional and bidirectional schemes.

The conventional droop controllers are described mathematically by (2.7) and (2.8), where $m_p$ and $m_q$ are the droop gains, and $\omega_0$, $V_{ac,0}$, $P_{ac,0}$ and $Q_{ac,0}$ are the droop set points. It is worth mentioning that $P_{ac,G,0}$ and $Q_{ac,G,0}$ are usually set to zero, and the

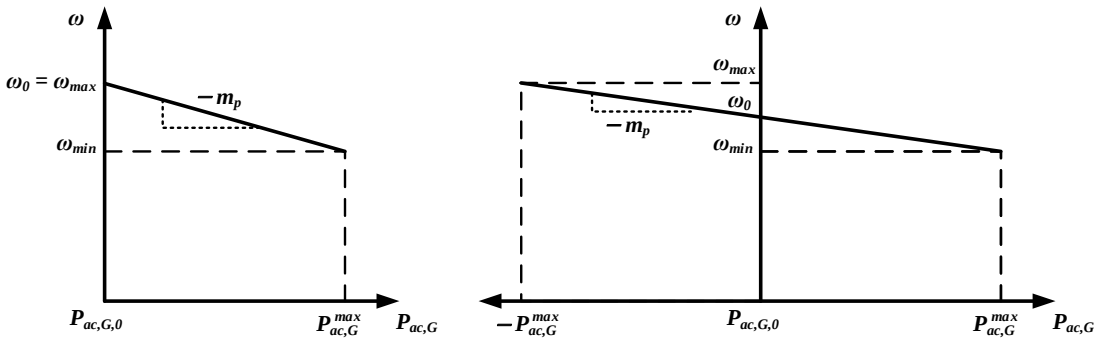


(a) P-$\omega$ droop characteristics (unidirectional)

(b) P-$\omega$ droop characteristics (bidirectional)

(c) Q-V droop characteristics (unidirectional)

(d) Q-V droop characteristics (bidirectional)

Figure 2.7: Droop Controllers

default values of the droop gains are determined based on (2.9) and (2.10). However, different droop schemes and droop controller gain settings have also been reported in the literature [53], [72]–[74].

$$\omega = \omega_{0,i} - m_{p,i}(P_{ac,G,i} - P_{ac,G,0,i}) \tag{2.7}$$

$$\left|V_{ac,i}\right| = V_{ac,0,i} - m_{q,i}(Q_{ac,G,i} - Q_{ac,G,0,i}) \tag{2.8}$$

$$m_{p,i} = \begin{cases} \dfrac{\omega_{max} - \omega_{min}}{2P^{max}_{ac,G,i}} & \dots bidirectional \\ \dfrac{\omega_{max} - \omega_{min}}{P^{max}_{ac,G,i}} & \dots unidirectional \end{cases} \tag{2.9}$$

$$m_{q,i} = \begin{cases} \dfrac{V_{ac,max} - V_{ac,min}}{2Q^{max}_{ac,G,i}} & \dots bidirectional \\ \dfrac{V_{ac,max} - V_{ac,min}}{Q^{max}_{ac,G,i}} & \dots unidirectional \end{cases} \tag{2.10}$$

In case of distribution networks, the lines are either predominantly resistive or the X/R ratio is close to one. For resistive lines, as seen in (2.11) and (2.12), the active power is approximately proportional to the voltage magnitude, whereas the reactive power is dependent on the voltage angle. Therefore, P-V and Q-$\omega$ droops can be used [75], [76].

$$P_{ij} \approxeq \frac{\left|V_{ac,i}\right|}{R_{ij}} \left(\left|V_{ac,i}\right| - \left|V_{ac,j}\right| \cos(\delta_i - \delta_j)\right) \approxeq \frac{\left|V_{ac,i}\right|^2 - \left|V_{ac,i}\right|\left|V_{ac,j}\right|}{R_{ij}} \tag{2.11}$$

$$Q_{ij} \approxeq \frac{-\left|V_{ac,i}\right|\left|V_{ac,j}\right|}{R_{ij}} \sin(\delta_i - \delta_j) \approxeq \frac{-\left|V_{ac,i}\right|\left|V_{ac,j}\right|}{R_{ij}} (\delta_i - \delta_j) \tag{2.12}$$

Considering the general case in which the line impedance cannot be approximated to be heavily inductive or resistive, the active and reactive powers cannot be assumed decoupled by nature. However, some droop control methods have been proposed to preserve the active and reactive power decoupling, in which active and reactive powers are transformed into decoupled "rotated "power components to enhance the system dynamic performance [77], [78]. Alternatively, implementation of virtual impedance is a possible solution for decoupling between active and reactive powers. Adopting an inductive virtual impedance, P-$\omega$ and Q-V droop controllers can still be used. The concept of virtual

impedance will be discussed later in this subsection. It is worth mentioning that the most commonly used droop control scheme in ac microgrids is the P-$\omega$ and Q-V despite its relatively poor dynamic performance in distribution networks, as it is compatible with droop controls of synchronous generator-based DGs. Therefore, it will be considered for the models developed in the following chapters.

Note that, in all cases, once the DG reaches its maximum output active and/or reactive powers, the inner current loop fixes the VSC's current to the limit, and the converter does not follow the voltage reference set by the droop controller(s). Thus, the DG is switched to constant-current (approximately constant-power) control rather than droop control when it injects its maximum output power(s). Furthermore, if the DG's power decreases below the capacity limit, it returns to droop operation once again. This fact is important when modeling ac DGs in steady-state, as the DG limits and modes of operation has to be taken into consideration.

### AC Virtual Impedance

Virtual impedance emulates the behavior of an actual output impedance connected to the converters terminals. It typically feeds back the converter output current to the voltage control loop through a transfer function that defines the virtual impedance elements and values. Resistive, inductive, and capacitive virtual impedances have been thoroughly discussed in the literature with the consideration of their effects on the system performance, harmonic compensation, and power sharing accuracy [79]. As discussed above, virtual impedance can reshape the output impedance of the converter, and hence it is considered a control variable that can be tuned to achieve certain transient and steady state performances. Equations (2.13) and (2.14) show an example of a virtual impedance transfer function in $dq$ frame that emulates virtual resistance $R_v$ and inductance $L_v$. This virtual impedance voltage drop is then subtracted from the reference voltage to emulate the voltage drop across the virtual line impedance. It is worth noting that implementing a virtual inductive impedance with a proper value can make the P-$\omega$ and Q-V droop characteristics valid regardless of the actual X/R ratio of the network [80]–[83].

$$V_{drop-d} = i_{od}R_v - \omega L_v i_{oq} \tag{2.13}$$

$$V_{drop-q} = i_{oq}R_v + \omega L_v i_{od} \tag{2.14}$$

### 2.2.2 Secondary Control of AC Microgrids

Despite the fact that the primary control of microgrids ensures proportional power sharing and stable operation for ac DGs, relying solely on droop controllers still has disadvantages that cannot be resolved in the primary level of control. These disadvantages can be summarized as follows:

- Deviations of the ac microgrid's voltage and frequency from their nominal values,
- Inaccurate proportional sharing of reactive power among DGs due to the differences in terminal voltages and line impedances, and
- Higher level of coordination (e.g., economic dispatch and loss minimization) not being possible at the primary control level without communication.

The secondary control level realizes functionalities that resolve the aforementioned drawbacks of primary controllers within a single microgrid. In order to minimize the infrastructure cost of the secondary controller, it utilizes small bandwidth communication links with standard communication protocols. Both centralized and decentralized secondary controllers have been addressed in the literature [51], [56], [84], [85]. However, only the centralized secondary controller approach is considered in the scope of this thesis.

#### Frequency and Voltage Regulation

One functionality of the microgrid secondary controller is frequency and voltage regulation. Measured microgrid frequency and voltage are compared with their respective nominal values, and corrective signals $\delta\omega_{0,i}$ and $\delta V_{ac,0,i}$ are generated through PI controllers as shown in Figure 2.8. These corrective signals are communicated to the primary controllers of the DGs connected to the ac microgrid to change their respective set points ($\omega_{0,i}$ and $V_{ac,0,i}$) in order to regulate the microgrid frequency and voltage to the nominal values. Figure 2.9 illustrates the frequency and voltage regulation by the secondary controller.

#### Reactive Power Sharing Correction

Since the microgrid steady state frequency is a global variable within the microgrid, the frequency regulation loop can use the measurement of the microgrid frequency at any arbitrary node, which makes the loop shown in Figure 2.8a valid under all cases. However,

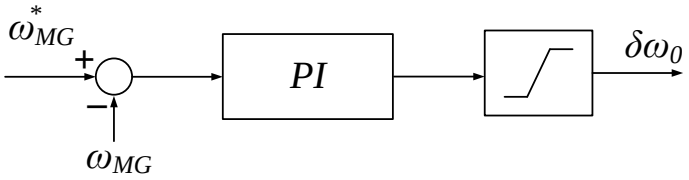


(a) Frequency regulation control loop

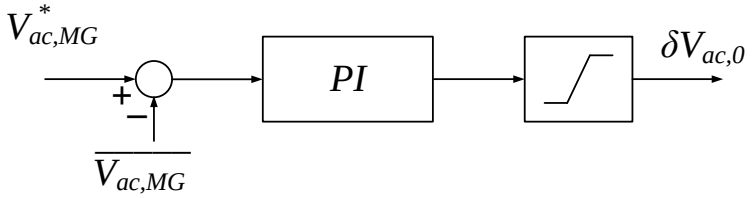


(b) Voltage regulation control loop

Figure 2.8: Implementation of secondary controller.

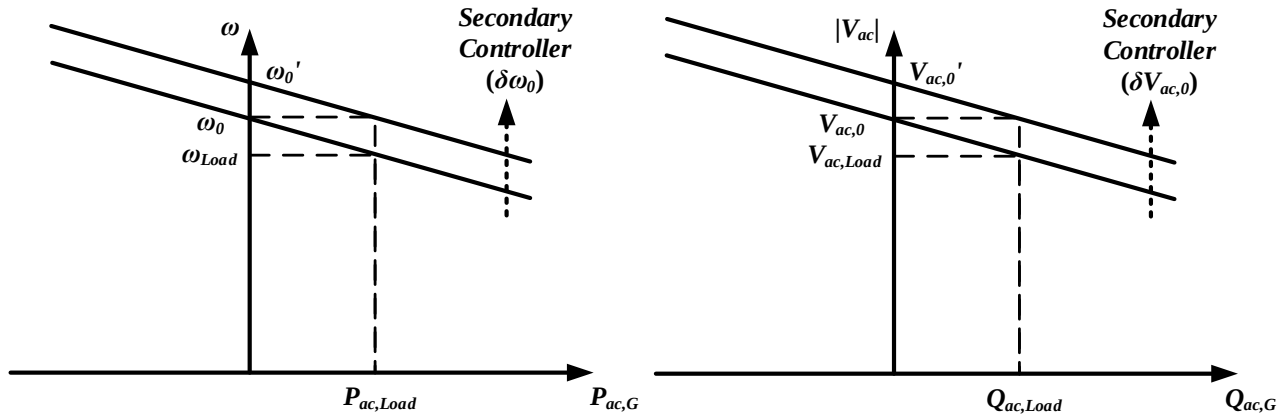


(a) Frequency regulation

(b) Voltage regulation

Figure 2.9: Secondary controller actions for frequency and voltage regulation.

since the local terminal voltage magnitudes are dissimilar for different DGs within a microgrid, the voltage regulation loop shown in Figure 2.8b should be modified. The voltage regulation loop can employ a control scheme to resolve the inaccurate proportional reactive power sharing problem of the primary controller.

The modified voltage regulation control loop is shown in Figure 2.10. In this modified loop, all the DGs within the microgrid transmit their local voltage magnitudes $V_{ac,i}$ and

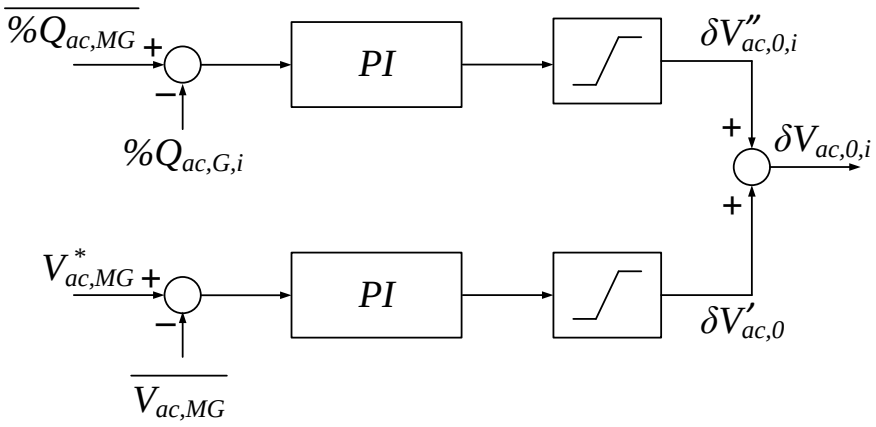


Figure 2.10: Modified voltage regulation control loop.

relative output reactive power $\%Q_{ac,G,i}$. The central secondary controller then uses (2.15) and (2.16) to calculate their respective average values $\overline{V_{ac,MG}}$ and $\overline{\%Q_{ac,MG}}$ for $N_{ac,DG}$ connected droop-controlled ac DGs. The microgrid average voltage is controlled by a PI controller to follow the nominal value, while the reactive power of each DG is controlled to follow the average reactive power generated by all DGs. The corrective signal $\delta V_{ac,0,i}$ is set differently for each DG unit to equalize the reactive power sharing and to restore the nominal microgrid voltage at the same time.

$$\overline{V_{ac,MG}} = \frac{\sum_{i=1,2...}^{N_{ac,DG}} \left|V_{ac,i}\right|}{N_{ac,DG}} \tag{2.15}$$

$$\overline{\%Q_{ac,MG}} = \frac{\sum_{i=1,2...}^{N_{ac,DG}} \%Q_{ac,G,i}}{N_{ac,DG}}, \quad \%Q_{ac,G,i} = \frac{Q_{ac,G,i}}{Q_{ac,G,i}^{max}} \tag{2.16}$$

### Optimal Microgrid Control

As highlighted before, the secondary controller could implement a control scheme to optimize the microgrid operation by attaining one or more objectives, such as economic dispatch, minimal losses, minimal emissions ... etc. In these schemes, the secondary controller sets the secondary control signals $\delta\omega_{0,i}$ and $\delta V_{ac,0,i}$ to achieve an optimal operating point according to the controller objective(s). In such case, there can be a trade-off between tightly regulating the microgrid voltage and frequency, accurate reactive power sharing

among the DGs, and achieving the optimization objective(s). Therefore, some of the objectives, such as voltage regulation, could be defined as constraints to maintain the voltage within an acceptable range rather than strictly regulating it to the nominal value.

### 2.2.3 Tertiary Control of AC Microgrids

Tertiary control is the highest level of control in the hierarchical control structure of ac microgrids. It is the slowest controller in the system and it is typically used to control the interactions between the microgrid and other entities, such as a stiff grid and/or other microgrids. The main functionalities of the tertiary controller can be summarized as follows [86]:

- Synchronize the microgrid to a stiff grid or another microgrid at the PCC,
- Control the power trading between the microgrid and other entities, and
- Implement higher-level controls/optimizations among multiple entities.

Figure 2.11 shows the main structure of the microgrid tertiary controller. As seen in the figure, the voltage measurements of both sides of the static switch (the microgrid side and the external grid side) are processed by a synchronizer which generates the synchronization signals $\delta\omega_{sync}$ and $\delta V_{ac,sync}$ to control the microgrid's voltage and frequency until the two grids are fully synchronized. After synchronization, the switch between the two grids is closed and other controllers are engaged to regulate the active and reactive power trading between the two grids as shown in Figure 2.12.

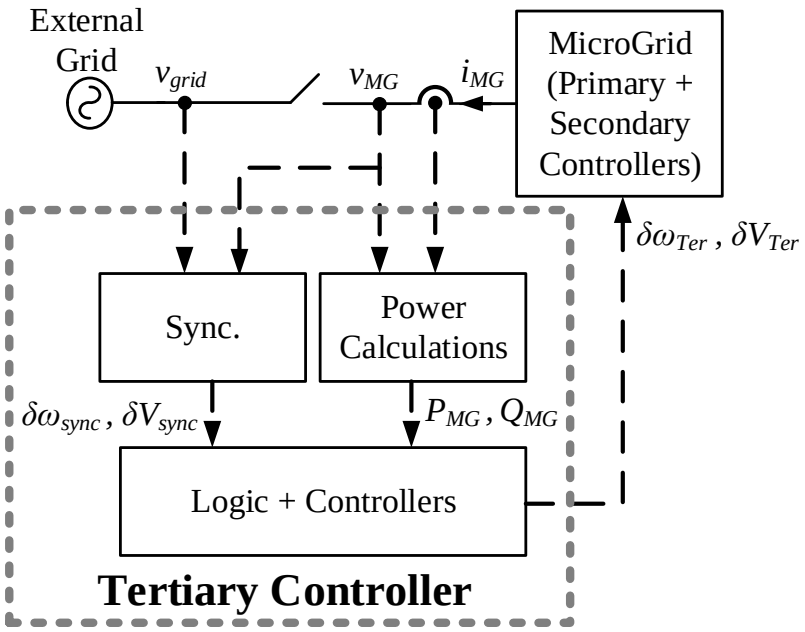


Figure 2.11: Block diagram of tertiary controller.

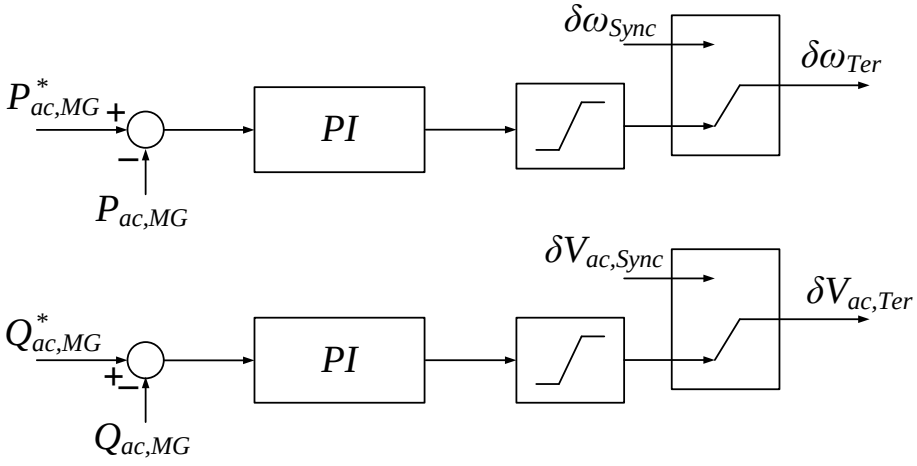


Figure 2.12: Tertiary controller structure.

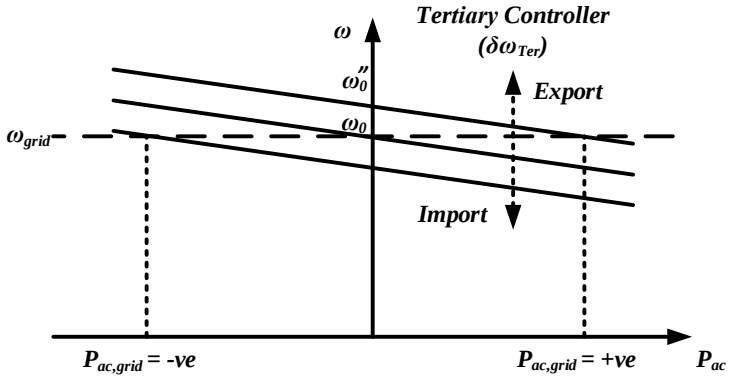


(a) Active power trading

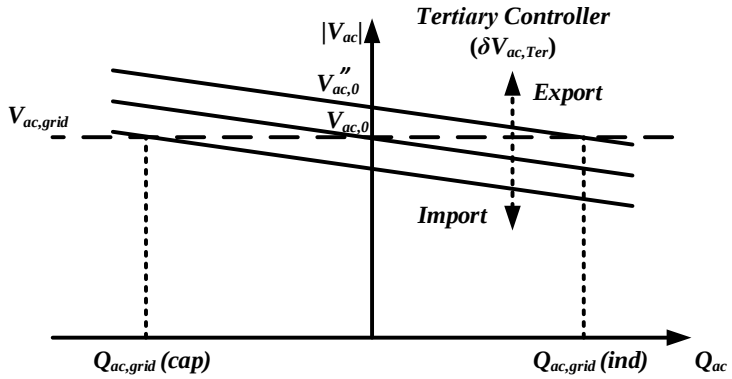


(b) Reactive power trading

Figure 2.13: Tertiary controller action for power trading between the microgrid and an external grid.

Assuming that the tie line between the two grids is predominantly inductive and the external grid voltage and frequency are fixed, the active and reactive power trading between the two grids can be controlled by controlling the microgrid frequency and voltage magnitude, respectively. Figure 2.13a shows the tertiary controller action to control the active power trading by increasing the frequency set point to export power and vice versa. Moreover, Figure 2.13b shows the influence of changing the microgrid reference voltage on the reactive power flow between the two grids. The tertiary controller signals are activated in case of connection to an external grid; otherwise, the tertiary controller output signals are set to zero.

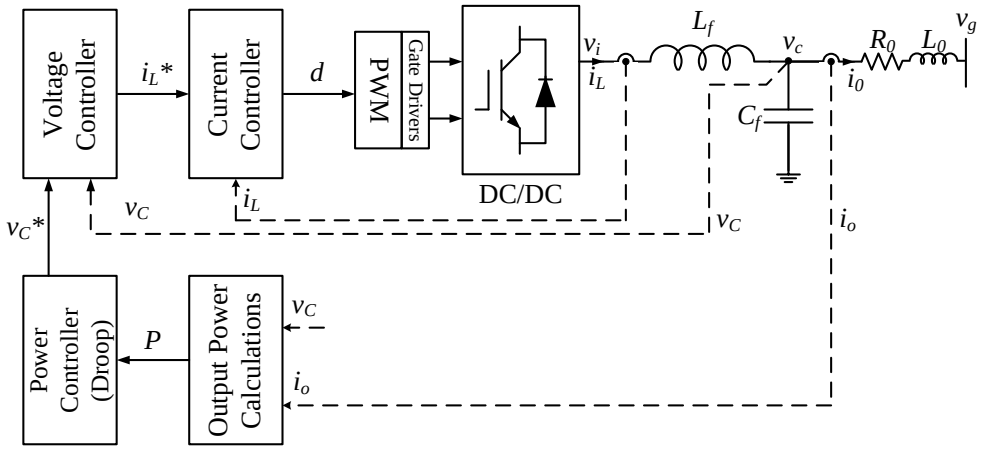


Figure 2.14: DC primary controller.

## 2.3 Hierarchical Control of DC Microgrids

DC microgrids follow the same hierarchical control structure as in ac microgrids. Primary control level typically implements droop controllers for decentralized load sharing, whereas secondary control level implements voltage regulation, load sharing corrections, and/or any higher level of optimized operation. Tertiary control level is mainly reserved for coordination (e.g., connection and power trading) with external grids [16], [87]–[94]. The three levels of control are discussed thoroughly in the following subsections.

### 2.3.1 Primary Control of DC Microgrids

DC microgrids typically employ dc/dc converters as an interface between DG sources and the dc network. Both unidirectional and bidirectional dc/dc converters can be used depending on the nature of the DG source [65], [66]. The dc/dc converter is connected to the dc bus through a low-pass LC/LCL filter. Figure 2.14 shows the primary controller of a DG source in a dc microgrid. The primary controller employs three nested control loops, namely current, voltage, and droop control loops [13], [18], [95].

#### DC Current Controller

The current control loop tightly regulates the filter inductor current and limits the converter output current in case of overloading or faults. Typically, as shown in Figure 2.15, a PI

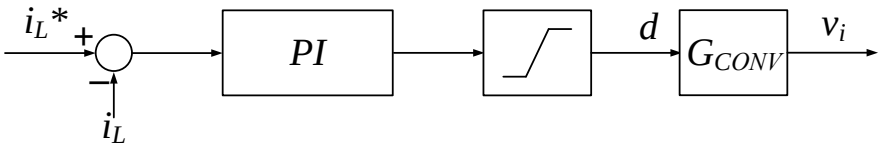


Figure 2.15: DC current controller.

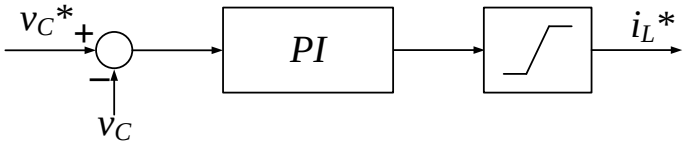


Figure 2.16: DC voltage controller.

controller is adopted to control the converter output current. The current controller gains are set to allow stable operation with the largest possible bandwidth.

### DC Voltage Controller

The second control loop is the voltage control loop, which controls the filter capacitor voltage. The voltage control loop also employs a simple PI controller to regulate the output voltage at the reference value. The controller is tuned to have a bandwidth smaller than that of the current controller, and therefore, it has a slower response, as desired. Figure 2.16 shows the structure of the voltage control loop.

### DC Power Controller

Finally, the outer loop of the primary controller is the droop controller loop. It has been reported in the literature that either current or power droops can be used in dc microgrids to allow current or power sharing between parallel DGs, respectively. However, only power droop is considered in this work, as the main focus is on hybrid ac/dc microgrids which require power sharing between the two subgrids. Similar to ac microgrids, the droop controller gain is set based on the permissible output voltage deviation, and the maximum power of the DG source. Figure 2.17 shows the droop characteristics of dc microgrids, while (2.17) and (2.18) present the mathematical relations of the droop controllers.

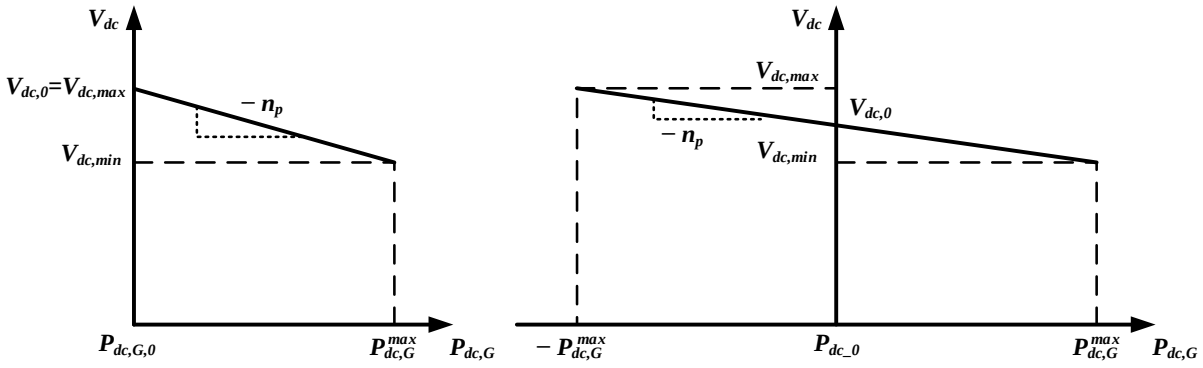


(a) P-V droop characteristics (unidirectional)

(b) P-V droop characteristics (bidirectional)

Figure 2.17: Droop controllers of DC microgrids.

$$V_{dc,i} = V_{dc,0,i} - n_p(P_{dc,G,i} - P_{dc,G,0,i}) \tag{2.17}$$

$$n_p = \begin{cases} \dfrac{V_{dc,max} - V_{dc,min}}{2P^{max}_{dc,G,i}} & \dots bidirectional \\ \dfrac{V_{dc,max} - V_{dc,min}}{P^{max}_{dc,G,i}} & \dots unidirectional \end{cases} \tag{2.18}$$

### 2.3.2 Secondary Control of DC Microgrids

The secondary control of dc microgrids utilizes slow communication links to provide a coordinated higher level of control, such as regulating the dc microgrid voltage at the nominal value, as it deviates by the action of droop controllers under varying loading conditions. Additionally, the secondary controller can be employed to compensate for the errors in power (or current) sharing among DGs in the dc microgrid. Figure 2.18 shows the secondary controller including both voltage regulation and power sharing correction functions [13], [96]. The controller collects the measurements of the output voltage and power of all droop-controlled DGs connected to the microgrid, calculates the average values of output voltage and relative output power ($\overline{V_{dc,MG}}$ and $\overline{\%P_{dc,MG}}$), and generates the corrective signal $\delta V_{dc,0,i}$. The corrective signal is fed through communication links to the corresponding droop controller [18], [19]. The secondary controller action on droop controllers is illustrated in Figure 2.19.

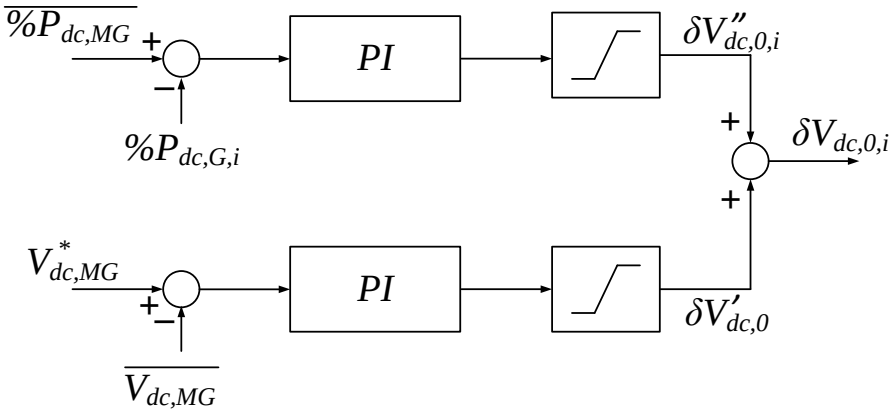


Figure 2.18: DC secondary controller with voltage regulation and power sharing correction.

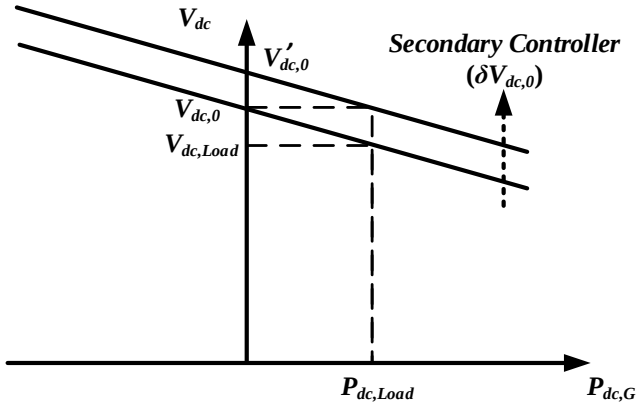


Figure 2.19: Secondary controller action on droop controllers.

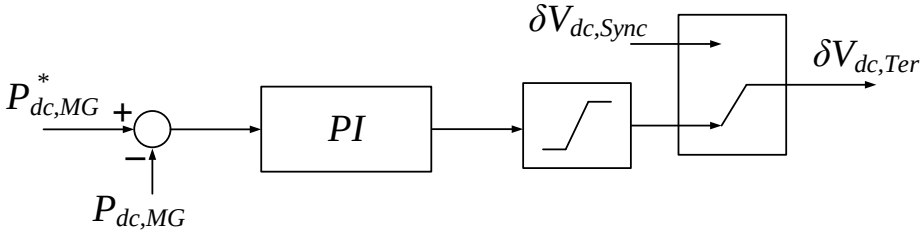


Figure 2.20: DC tertiary controller.

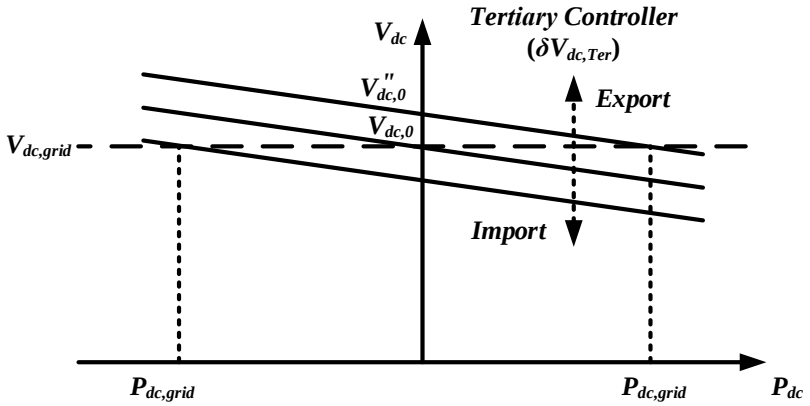


Figure 2.21: Tertiary controller action on droop controllers for power trading.

### 2.3.3 Tertiary Control of DC Microgrids

As the highest level of control hierarchy of dc microgrids, the tertiary controller is mainly dedicated to controlling the connection and power transfer with external grids [97], [98]. It may also implement a higher level of control to optimize the microgrid operation [99]. In order to avoid high currents at the moment of connection between the dc microgrid and an external entity, the control signal $\delta V_{dc,sync}$ is used to regulate the dc voltage at the PCC before the interconnecting switch is closed. As shown in Figure 2.20, after the switch closure, the control signal adjusts the microgrid voltage level to control the power flow between the microgrid and the external grid. Figure 2.21 demonstrates the tertiary controller action on the droop controllers to import/export power between the two grids.

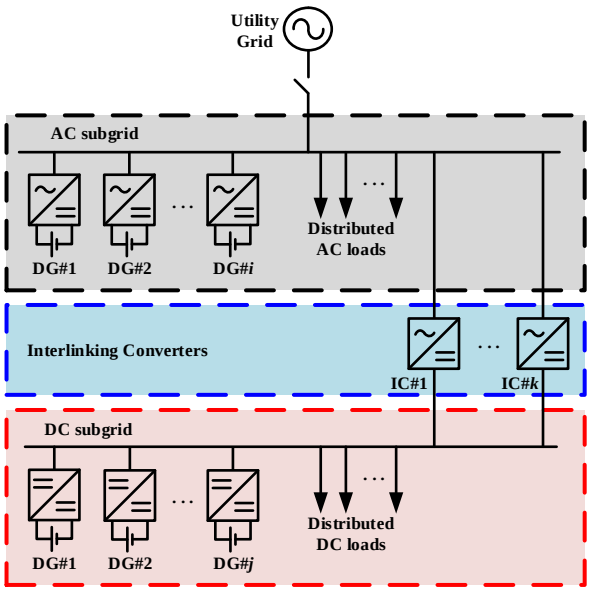


Figure 2.22: A simple structure of a hybrid ac/dc microgrid.

## 2.4 Control of Hybrid AC/DC Microgrids

The work reported in the literature on autonomous operation of hybrid ac/dc microgrids has mainly focused on primary controllers, which depend on the frequency and voltage deviations of the ac and dc subgrids to transfer power between the two subgrids [13], [22], [25], [26], [80], [96], [100]–[105]. Therefore, this section reviews the autonomous control of ICs in droop-controlled hybrid ac/dc microgrids.

Consider the structure of a Hybrid ac/dc microgrid, shown in Figure 2.22, in which one or more ICs interlink the two subgrids. The utility ac grid is defined as an infinite bus (ac source with constant balanced voltages and fixed frequency). The primary control of ICs provide the following functionalities.

1. Autonomous proportional power sharing among all the ac and dc DGs in the hybrid microgrid,

2. Autonomous proportional power-transfer sharing among ICs, and

3. Provide reactive power to the ac subgrid.

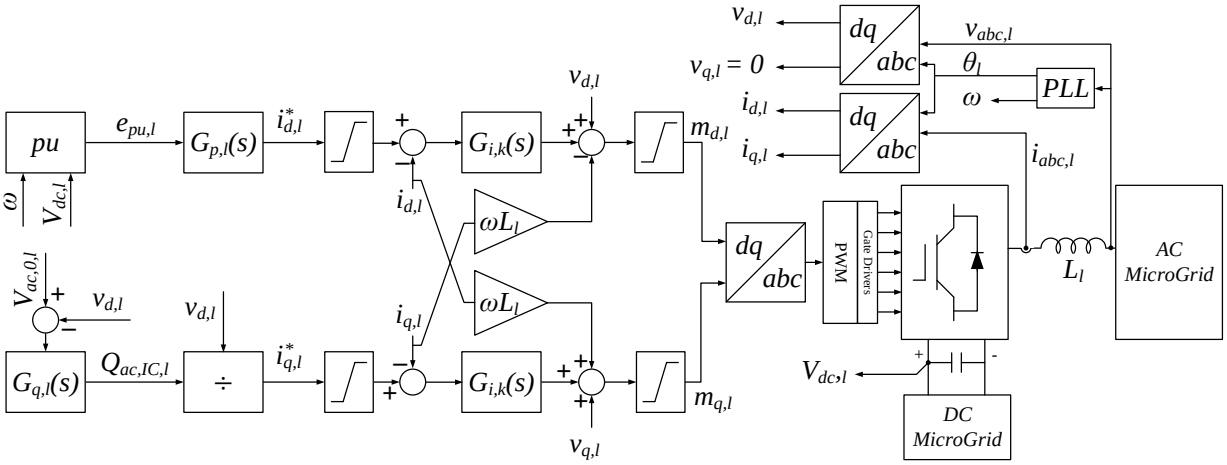


Figure 2.23: Primary controller of interlinking converters in hybrid AC/DC microgrids.

Figure 2.23 shows the primary controller of the interlinking converter $l$ of a hybrid ac/dc microgrid. The interlinking converter is a standard three-phase three-leg current-controlled VSC. The phase locked loop (PLL) synchronizes the converter with the ac subgrid, and measures the ac subgrid frequency as an input to the autonomous primary controller. The inner current controller is implemented in $dq$ synchronous reference frame utilizing two identical PI controllers defined by the transfer function $G_{i,l}(s)$ as defined by (2.19).

$$G_{i,l} = k_{pi,l} + \frac{k_{ii,l}}{s} \tag{2.19}$$

The $d$-axis reference current $i^*_{d,l}$ is set by the outer power-transfer controller to determine the amount and direction of active power-transfer between the two subgrids. On the other hand, the $q$-axis reference current $i^*_{q,l}$ follows droop characteristics to provide reactive power to the ac subgrid.

The power-transfer controller measures the local per-unit values of the ac subgrid frequency deviation and the dc subgrid voltage deviation, as described by (2.20) and (2.21). The controller calculates the per-unit error $e_{pu,l}$ given by (2.22), and processes it using the controller with the transfer function $G_{p,k}$. The definition of the power transfer controller depends on the number of ICs. If only one IC interfaces the two subgrids, the controller employs a PI controller to force the per-unit frequency and voltage deviations of the ac and dc subgrids to be equal, which ideally forces proportional load sharing between the DGs in the ac and dc subgrids. On the other hand, if multiple ICs interface the two subgrids, the utilization of PI controllers might not be the best solution, as they will cause power

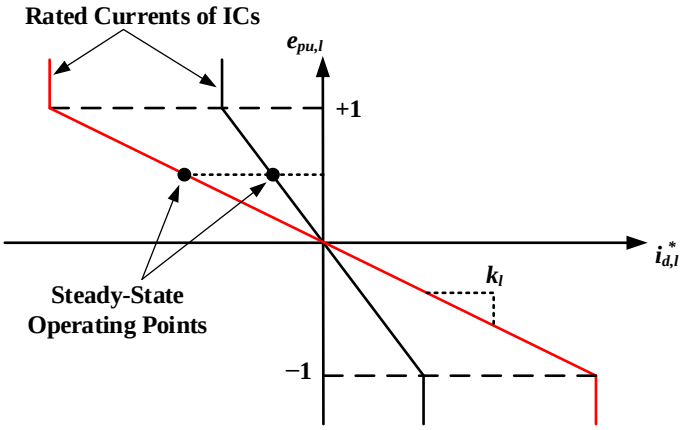


Figure 2.24: Droop controller of ICs.

deviations between the ICs depending on their initial operating conditions. Hence, droop control method can be used to share the power transfer between ICs, as shown in Figure 2.24. However, the droop controllers will not force proportional power sharing among all DGs. Moreover, poor power sharing between ICs is expected due to the different local dc voltage measurements at different IC terminals. It is worth noting that the problems associated with the droop controllers can be solved by a secondary control level through slow communication links. The mathematical formulation of the autonomous active power controller is given by (2.23). In either case, the IC injects reactive power according to the droop characteristics defined by (2.24). Note that the IC injects reactive power to the ac subgrid only if the active power flows in the same direction.

$$\Delta\omega_{pu} = \frac{\omega - (\omega_{max} + \omega_{min})/2}{(\omega_{max} - \omega_{min})/2} \tag{2.20}$$

$$\Delta V_{dc,pu} = \frac{V_{dc,l} - (V_{dc,max} + V_{dc,min})/2}{(V_{dc,max} - V_{dc,min})/2} \tag{2.21}$$

$$e_{pu,l} = \Delta\omega_{pu} - \Delta V_{dc\_pu} \tag{2.22}$$

$$G_{p,l}(s) = \begin{cases} k_{pp,l} + \dfrac{k_{ip,l}}{s} & \ldots single\ IC \\ \gamma_l & \ldots multiple\ ICs \end{cases} \tag{2.23}$$

$$G_{q,l}(s) = \begin{cases} \eta_l & if\ i^*_{d,l} \leq 0 \\ 0 & if\ i^*_{d,l} > 0 \end{cases} \tag{2.24}$$

## 2.5 Power Flow and Optimal Power Flow Analyses

Although dynamic modeling and analysis of electrical power systems is the most generic and accurate approach, as it describes the detailed dynamic and steady-state behaviors of power systems, it is impractical to implement in studies where the scope is limited to the system's steady-state behavior. The reason for this impracticality is the added complexity and computational overhead associated with the incorporation of the dynamic system model, which is unnecessary to obtain the steady-state values of the system variables. Therefore, power flow analysis is crucial for steady-state studies of electrical power systems, as it provides fast and sufficiently accurate solution for the power system variables (i.e, bus voltages, voltage angles, and generator powers). This section reviews the power flow formulation and solution methods for conventional power systems, which will be used in the next chapters as a base for power flow analysis of standalone unbalanced hybrid ac/dc microgrids.

### 2.5.1 Power-Flow Analysis of Conventional Power Systems

#### Problem Formulation

Assuming a balanced ac power system with $N_{ac}$ buses, the current injected at any bus $i$ can be given by (2.25) [106], [107].

$$I_{ac,i} = \left(V_{ac,i} - V_{ac,1}\right) y_{i1} + \left(V_{ac,i} - V_{ac,2}\right) y_{i2} + \cdots + V_{ac,i} y_{ii} + \cdots + \left(V_{ac,i} - V_{ac,N_{ac}}\right) y_{iN_{ac}} \quad (2.25)$$

In (2.25), $y_{ij}$ where $j \in \{1, 2 \ldots, N_{ac}\}$ is the line admittance between buses $i$ and $j$, and $y_{ii}$ is the shunt admittance of bus $i$. Rearranging the equation, the current can be expressed as:

$$\begin{aligned} I_{ac,i} =& (-y_{i1}) V_{ac,1} + (-y_{i2}) V_{ac,2} + \cdots + \left(y_{i1} + y_{i2} + \cdots + y_{ii} + \cdots + y_{iN_{ac}}\right) V_{ac,i} \\ &+ \cdots + (-y_{iN_{ac}}) V_{ac,N_{ac}} \end{aligned} \quad (2.26)$$

By introducing the mutual admittance $Y_{ij}$ and self admittance $Y_{ii}$ of bus $i$ as defined by (2.27) and (2.28), respectively, the injected current can be expressed as given in (2.29).

$$Y_{ij} = -y_{ij} \quad (2.27)$$

$$Y_{ii} = \left(y_{i1} + y_{i2} + \cdots + y_{ii} + \cdots + y_{iN_{ac}}\right) \quad (2.28)$$

$$\begin{aligned} I_{ac,i} &= Y_{i1} V_{ac,1} + Y_{i2} V_{ac,2} + \cdots + Y_{ii} V_{ac,i} + \cdots + Y_{iN_{ac}} V_{ac,N_{ac}} \\ &= \sum_{j=1}^{N_{ac}} Y_{ij} V_{ac,j} \end{aligned} \quad (2.29)$$

The injected active and reactive powers at bus $i$ are, subsequently, given as:

$$P_{ac,i} - jQ_{ac,i} = V_{ac,i}^{*}\, I_{ac,i} = V_{ac,i}^{*} \sum_{j=1}^{N_{ac}} Y_{ij} V_{ac,j} \tag{2.30}$$

Therefore, the active and reactive powers can be expressed in the polar form as

$$P_{ac,i} = \sum_{j=1}^{N_{ac}} \left|V_{ac,i}\right|\left|Y_{ij}\right|\left|V_{ac,j}\right| \cos\left(\theta_{ij} + \delta_j - \delta_i\right) \tag{2.31}$$

$$Q_{ac,i} = - \sum_{j=1}^{N_{ac}} \left|V_{ac,i}\right|\left|Y_{ij}\right|\left|V_{ac,j}\right| \sin\left(\theta_{ij} + \delta_j - \delta_i\right) \tag{2.32}$$

For each bus, the injected powers $P_{ac,i}$ and $Q_{ac,i}$ must satisfy the power balance equations given by:

$$P_{ac,i} = P_{ac,G,i} - P_{ac,L,i} = \sum_{j=1}^{N_{ac}} \left|V_{ac,i}\right|\left|Y_{ij}\right|\left|V_{ac,j}\right| \cos\left(\theta_{ij} + \delta_j - \delta_i\right) \tag{2.33}$$

$$Q_{ac,i} = Q_{ac,G,i} - Q_{ac,L,i} = - \sum_{j=1}^{N_{ac}} \left|V_{ac,i}\right|\left|Y_{ij}\right|\left|V_{ac,j}\right| \sin\left(\theta_{ij} + \delta_j - \delta_i\right) \tag{2.34}$$

where $P_{ac,G,i}$ and $Q_{ac,G,i}$ are the generator's specified active and reactive powers at bus $i$, respectively, and $P_{ac,L,i}$ and $Q_{ac,L,i}$ the load active and reactive powers at bus $i$, respectively.

To that end, it is important to define the types of buses that may exist in such system in order to determine the number of unknown variables. There are three types of buses as follows:

1. *Slack Bus* – Typically with a large generator connected to it. It is characterized by a constant voltage magnitude and angle, and is taken as a reference (i.e., voltage angle is zero). It provides unknown active and reactive powers to maintain the power balance in the system. Only one slack bus can be defined in the system.

2. *PV Bus* – Typically with a generator or a synchronous condenser connected to it. It is characterized by a constant voltage magnitude and specified generated active power. The voltage angle and generated reactive power are unknown.

3. *PQ Bus* – Typically a load bus, with no generators connected to it. It is characterized by constant specified active and reactive powers. The voltage magnitude and angle are unknown.

Assuming that the values and of all system loads are known, to solve for the bus voltage magnitudes and angles for a power system comprised of one slack bus, $N_{ac,PV}$ buses, and $N_{ac,PQ}$ buses, the system unknowns and equations are identified as follows:

- *Unknown Voltage Magnitudes* – The number of unknown bus voltage magnitudes is equal to $(N_{ac} - N_{ac,PV} - 1)$. Meanwhile, the number of reactive power balance equations, given by (2.34), is the same as the unknown voltage magnitudes.
- *Unknown Voltage Angles* – The number of unknown bus voltage angles is equal to $(N_{ac} - 1)$. Similarly, the number of active power balance equations, given by (2.33), is identical to that of the unknown bus voltage angles.

Therefore, the number of equations is equal to the number of unknowns, which makes obtaining the problem solution feasible.

**Problem Solution**

Various numerical/iterative methods are reported for solving the set of nonlinear power flow equations, among which, Newton-Raphson (NR) is commonly used for its good convergence characteristics [106], [107]. In this method, the mismatch equations (2.35) and (2.36) are rewritten as

$$\Gamma_{ac,P,i} = -P_{ac,G,i} + P_{ac,L,i} + \sum_{j=1}^{N_{ac}} \left|V_{ac,i}\right|\left|Y_{ij}\right|\left|V_{ac,j}\right| \cos\left(\theta_{ij} + \delta_j - \delta_i\right) \tag{2.35}$$

$$\Gamma_{ac,Q,i} = -Q_{ac,G,i} + Q_{ac,L,i} - \sum_{j=1}^{N_{ac}} \left|V_{ac,i}\right|\left|Y_{ij}\right|\left|V_{ac,j}\right| \sin\left(\theta_{ij} + \delta_j - \delta_i\right) \tag{2.36}$$

The objective is, therefore, to solve for the bus voltage magnitudes and angles, such that the power mismatches $\Gamma_{ac,P,i}$ and $\Gamma_{ac,Q,i}$ are ideally zero.

First, an initial guess for all the unknown variables is made (typically 1.0 pu for all bus voltage magnitudes and 0.0° for all the voltage angles). Based on this guess, the power

mismatches are evaluated. Second, the voltage magnitudes and angles are updated based on:

$$\begin{bmatrix} |\mathbf{V_{ac}}|_{(k+1)} \\ \delta_{(k+1)} \end{bmatrix} = \begin{bmatrix} |\mathbf{V_{ac}}|_{(k)} \\ \delta_{(k)} \end{bmatrix} - J_{ac}^{-1} \begin{bmatrix} \Gamma_{\mathbf{ac},\mathbf{P}(k)} \\ \\ \Gamma_{\mathbf{ac},\mathbf{Q}(k)} \end{bmatrix} \tag{2.37}$$

where the Jacobian matrix $J_{ac}$ is formed as

$$J_{ac} = \begin{bmatrix} \dfrac{\partial \Gamma_{\mathbf{ac},\mathbf{P}}}{\partial |\mathbf{V_{ac}}|} & \dfrac{\partial \Gamma_{\mathbf{ac},\mathbf{P}}}{\partial \delta} \\ \\ \dfrac{\partial \Gamma_{\mathbf{ac},\mathbf{Q}}}{\partial |\mathbf{V_{ac}}|} & \dfrac{\partial \Gamma_{\mathbf{ac},\mathbf{Q}}}{\partial \delta} \end{bmatrix} \tag{2.38}$$

The Jacobian matrix elements, as well as the power mismatches, are calculated at each iteration until the problem converges.

Note that although the same concepts apply to unbalanced ac systems, the problem becomes much more complicated due to the coupling between different network phases. Therefore, more attention should be paid to the formulation and solution method in order to achieve accurate and fast solution. Complete modeling and analysis of unbalanced networks will be discussed in detail in the following chapters, as the scope of this thesis is unbalanced hybrid ac/dc microgrids. It is also important to mention that, although the conventional power flow analysis approaches lay out a basis for the analysis of droop-controlled microgrids, they cannot be directly implemented in such networks, because they do not accommodate the microgrids' distinctive features. Thus, novel modeling and power flow analysis approaches need to be developed for microgrid applications.

### 2.5.2 Optimal Power-Flow Analysis

#### Problem Formulation

Optimal power flow (OPF) analysis aims at optimizing the power system operation based on one or more defined objectives while satisfying the power flow equations. Therefore, the power flow equations, given by (2.33) and (2.34), are introduced as equality constraints to the problem. Other inequality constraints can also be defined as required for proper and secure operation. Therefore, the problem is formulated as a constrained nonlinear optimization problem. The solution to the problem consists of a set of control variables, such as generator settings, load curtailment, and capacitor switching actions [108]–[115].

The general OPF formulation is represented by:

$$\min\ F \tag{2.39}$$

subject to:

$$g(z) = \quad 0 \tag{2.40}$$

$$h_{min} \leq \quad h(z) \quad \leq h_{max} \tag{2.41}$$

$$z_{min} \leq \quad z \quad \leq z_{max} \tag{2.42}$$

where $F$ is the objective function, (2.40) defines the equality constraints, (2.41) describes the set of inequality constraints, with $h_{min}$ and $h_{max}$ as the lower and upper bounds, respectively, and $z$ is the set of control variables bounded by $z_{min}$ and $z_{max}$ as the lower and upper bounds, respectively.

Conventionally, the objective function $F$ can be defined for various objectives, including but not limited to: minimum cost of operation or minimum shift from optimum, loss minimization, and minimum cost of new installed devices, such as capacitors. The equality constraints are the set of nonlinear power flow equations, given by (2.33) and (2.34). The inequality constraints represent constraints on dependent variables, such as line capacity limits and reserve margins. The set of control variables primarily include bus voltage magnitudes and angles, in addition to other state variables, such as transformer taps and capacitor switching actions. These control variables can be bounded by their physical limits, such as transformer taps and generation limits. They can also be bounded by security-based limits, rather than physical ones, such as bus voltage magnitudes and angles. Note that some of the constraints can be omitted or relaxed depending on the application.

### Problem Solution

Many OPF solution methods have been reported in the literature. Some of the reported methods are summarized below [108]–[115].

- *Gradient Methods* – Demonstrate slow convergence and often are ineffective for solving the problem when inequality constraints are introduced.
- *Newton's Method* – Exhibits fast convergence, but may encounter convergence issues when inequality constraints exist.

- *Linear Programming OPF (LPOPF)* – Handles the nonlinear objective functions and constraints by linearizion. It is fully developed and commonly used in the literature for its good convergence characteristics and its ability to handle inequality constraints.
- *Interior Point Method* – One of the most widely used methods for solving OPF problems due to its relatively fast convergence and capability to handle inequality constraints.
- *Heuristic Methods* – Many heuristic techniques have been reported in the literature for solving OPF problems, such as Genetic Algorithms and Particle Swarm. Although they are effective in solving OPF, analytic methods, such as the interior point method, are often preferred for their lower computational cost.

## 2.6 Thesis Scope and Assumptions

The complete dynamic model of a hybrid ac/dc microgrid can be derived from the detailed system components described in Sections 2.2 to 2.4. This complete model is the most generic, since it can describe both dynamic and steady-state behaviors of the system. However, developing such a detailed dynamic model for larger microgrids is cumbersome due to its high complexity. Furthermore, solving such a complicated model requires enormous memory and time, which can be impractical for larger systems. Therefore, dynamic modeling and analysis approach is typically limited to smaller systems to investigate their dynamic stability.

On the other hand, since the main goal of the analysis is to study the steady-state behavior of a microgrid, simplified steady-state models of the system components can be used for simpler modeling and faster solution of larger systems. These models ignore the system dynamics and only represent the steady-state characteristics of different system components. Although this approach is sufficient for steady-state analysis, it does not reflect the system dynamic stability, neither at the steady-state operating point nor when the system transitions from one steady-state operating point to another. The two types of analyses - dynamic and steady-state - complement one another in the sense that the dynamic analysis captures the system dynamic response and ensures dynamic system stability, while steady-state analysis provides a simple and computationally-efficient tool for fast analysis of larger systems.

It is important to mention that the scope of this thesis is limited to steady-state modeling and analysis of standalone unbalanced hybrid ac/dc microgrids. The developed frame-

work considers only the steady-state characteristics of these microgrids, which facilitates fast and accurate steady-state analysis of larger microgrids. Nonetheless, the provided analysis and results do not ensure the microgrid dynamic stability, which requires complete dynamic modeling and analysis of the system. Dynamic system modeling and analysis are beyond the scope of the thesis. Accordingly, the analysis is performed under the assumption that all microgrids under study are dynamically-stable considering:

- different microgrid configurations, loading conditions, and DG and IC controller settings,
- communication delays of supervisory controllers, and
- transitions between different stead-state operating points.

## 2.7 Summary and Discussion

This chapter presented the hierarchical control structures of ac, dc, and hybrid ac/dc microgrids. For ac and dc microgrids, the primary control level mainly regulates the power sharing among DGs connected to the same microgrid. It also employs inner current and outer voltage loops to control the output voltage and current of each DG unit. The typical autonomous decentralized power sharing scheme for microgrids utilizes droop controllers. Therefore, frequency and voltage deviations of ac microgrids, as well as voltage deviations in dc microgrids, are expected under varying loading conditions. Moreover, ac microgrids implementing Q-V droops suffer from poor reactive power sharing due to different terminal voltages and impedances of ac DGs. For the same reason, poor active power sharing among droop-controlled DGs in a dc microgrid is expected, as well.

Secondary controllers utilize slow communication links to attain one or more objectives, such as regulating the frequency and voltage of ac microgrids at their nominal values, and regulating the voltage of dc microgrids at its nominal value. Another function that can be implemented by secondary controllers is to improve the accuracy of power sharing (reactive power in ac microgrids and power in dc microgrids) among DGs connected to a microgrid. Tertiary control is the highest level of control and it typically implements small-bandwidth control loops to connect and control the power trading between a microgrid and external grids.

For hybrid ac/dc microgrids, ICs may implement different primary control schemes – depending on the number of ICs – to provide autonomous operation for the microgrid. The

main goal of the ICs' active power controller is to transfer power between the ac and dc subgrids, such that the load is ideally shared among all ac and dc DGs in proportion to their capacities. In case of a single IC, it forces the per-unit deviations of the ac frequency and the dc voltage at its terminals to be equal. For multiple ICs, they implement droop controls to share the power-transfer in proportion to their capacities; however errors are still expected due to dc voltage dissimilarities at different IC terminals.

Moreover, the chapter reviewed the basic concepts of power flow and optimal power flow analyses of conventional power systems. The problem formulation and solution methods were briefly discussed for each type of analysis. Furthermore, it was highlighted that these methods do not directly apply to steady-state analysis of standalone unbalanced hybrid ac/dc microgrids due to their distinctive operational characteristics discussed above. However, combined, the presented background about microgrid control and steady-state analysis of power systems establish an essential foundation for the steady-state analysis of hybrid ac/dc microgrids that are developed in the following chapters.

# Chapter 3

# A Steady-State Analysis Tool for Unbalanced Islanded Hybrid AC/DC Microgrids

## 3.1 Introduction

In Chapters 1 and 2, it was demonstrated that it is essential to develop comprehensive steady-state analysis tools for hybrid ac/dc microgrids to allow for accurate and fast power flow analysis of such microgrids. The developed tools must incorporate the distinctive microgrid operational features, such as droop control of the ac and dc subgrids, unbalanced ac subgrid, absence of a slack bus, correlation between ac frequency and dc voltage, and parallel operation of ICs. For that purpose, this chapter discusses different operational modes for the DGs and ICs, through extensive DG and load modeling, to solidify the performed analysis. Furthermore, the globally-convergent NTR method is adopted to solve the proposed power flow formulation. Through incorporation in benchmark networks, the proposed power flow algorithm demonstrates accurate steady-state results that match those of detailed time-domain simulations obtained in PSCAD/EMTDC environment. In addition, the power flow algorithm is utilized to address the effects of ICs' settings on DGs' and ICs' power sharing, and to inspect unbalanced loading of DG phases.

The remainder of this chapter is organized as follows. Comprehensive modeling of ac subgrid's components and power flow equations are presented in Section 3.2. Section 3.3 describes the mathematical models used to represent the dc subgrid. Section 3.4 explains the autonomous operation of ICs and their steady-state models. Section 3.5 describes the

incorporation of the presented models in a unified power flow formulation. The accuracy and significance of the developed power flow algorithm are demonstrated in Section 3.6, and Section 3.7 concludes the chapter.

## 3.2 AC Microgrid Modeling

This section addresses the mathematical models of power injection, DGs and loads in an islanded ac microgrid. Unlike conventional distribution systems, in which the frequency is constant, the DGs implement power/frequency droop characteristics to proportionally share the loads in islanded ac microgrids. Thus, the system frequency is an additional power flow variable. The effect of variable system frequency should be considered in system modeling, since it alters the network reactance. In this analysis, Carson's equations and Kron's reduction [116] are employed to represent the grounded and ungrounded three-phase wiring between any two ac buses $i$ and $j$ in a complex impedance format. Therefore, the series impedance matrix of a feeder connecting nodes $i$ and $j$, $Z_{ij}^{abc}$, is given as:

$$Z_{ij}^{abc} = \begin{bmatrix} Z_{ij}^{aa} & Z_{ij}^{ab} & Z_{ij}^{ac} \\ Z_{ij}^{ba} & Z_{ij}^{bb} & Z_{ij}^{bc} \\ Z_{ij}^{ca} & Z_{ij}^{cb} & Z_{ij}^{cc} \end{bmatrix} \tag{3.1}$$

where the diagonal matrix elements are the feeder's phase self-impedances, and off-diagonal elements phase mutual-impedances.

Accordingly, the complex branch voltages $V_{ac,i}^{abc}$ and $V_{ac,j}^{abc}$ are related to the complex branch currents $I_{ac,ij}^{abc}$ in terms of the complex branch admittance matrix, $Y_{ij}^{abc}$, as

$$I_{ac,ij}^{abc} = Y_{ij}^{abc}(V_{ac,i}^{abc} - V_{ac,j}^{abc}) \tag{3.2}$$

where

$$Y_{ij}^{abc} = {Z_{ij}^{abc}}^{-1} \tag{3.3}$$

For an arbitrary bus $i$, the injected complex power of the three phases, $S_{ac,i}^{abc}$, can be expressed as

$$S_{ac,i}^{abc} = V_{ac,i}^{abc}\left(I_{ac,i,inj}^{abc}\right)^{*} \tag{3.4}$$

where $I_{ac,i,inj}^{abc}$ is the sum of the currents of all branches connected to bus $i$. Substituting (3.2) in (3.4), the injected active and reactive powers of each phase $x \in \{a, b, c\}$ at bus $i$

, $P^x_{ac,i}$ and $Q^x_{ac,i}$,could be represented as demonstrated in (3.5) and (3.6), where $N_{ac}$ is the set of ac buses, $|V^x_{ac,i}|$ and $\delta^x_i$ are the voltage magnitude and angle at bus $i$, and $|Y^{xy}_{ij}|$ and $\theta^{xy}_{ij}$ are the magnitude and angle of bus admittance matrix entries.

$$\begin{aligned} P^x_{ac,i} = \sum_{j \in N_{ac} \setminus i} \sum_{y \in \{a,b,c\}} & \left|V^x_{ac,i}\right|\left|Y^{xy}_{ij}\right|\left|V^y_{ac,i}\right| \cos(\theta^{xy}_{ij} + \delta^y_i - \delta^x_i) \\ & - \left|V^x_{ac,i}\right|\left|Y^{xy}_{ij}\right|\left|V^y_{ac,j}\right| \cos(\theta^{xy}_{ij} + \delta^y_j - \delta^x_i) \end{aligned} \tag{3.5}$$

$$\begin{aligned} Q^x_{ac,i} = \sum_{j \in N_{ac} \setminus i} \sum_{y \in \{a,b,c\}} & \left|V^x_{ac,i}\right|\left|Y^{xy}_{ij}\right|\left|V^y_{ac,j}\right| \sin(\theta^{xy}_{ij} + \delta^y_j - \delta^x_i) \\ & - \left|V^x_{ac,i}\right|\left|Y^{xy}_{ij}\right|\left|V^y_{ac,i}\right| \sin(\theta^{xy}_{ij} + \delta^y_i - \delta^x_i) \end{aligned} \tag{3.6}$$

### 3.2.1 AC Load Modeling

Exponential ac load models presented in (3.7) and (3.8) are employed in this analysis to describe the load active and reactive powers ($P^x_{ac,L,i}$ and $Q^x_{ac,L,i}$), since they are flexible in representing load values at different frequencies and voltage levels.

$$P^x_{ac,L,i} = P^{0,x}_{ac,L,i}\left|V^x_{ac,i}\right|^{\alpha,x} (1 + K^x_{pf,i}\Delta\omega) \qquad \forall\, x \in \{a,b,c\} \tag{3.7}$$

$$Q^x_{ac,L,i} = Q^{0,x}_{ac,L,i}\left|V^x_{ac,i}\right|^{\beta,x} (1 + K^x_{qf,i}\Delta\omega) \qquad \forall\, x \in \{a,b,c\} \tag{3.8}$$

In (3.7) and (3.8), $P^{0,x}_{ac,L,i}$ and $Q^{0,x}_{ac,L,i}$ are the nominal values of the load active and reactive powers, respectively, $\alpha$ and $\beta$ are the active and reactive power exponents, $\Delta\omega$ is the frequency deviation, and $K^x_{pf,i}$ and $K^x_{qf,i}$ are constants that range from 0 to 2 and 3 to 0, respectively [117].

### 3.2.2 AC DG Modeling

It is important to mention that, in a microgrid environment, the majority of DGs are interfaced with the network via power electronic converters. Three-phase voltage source converters (VSCs) are typically adopted for this purpose. However, the implemented physical and control structures define the role and thus the model of each DG [36]. VSCs could

generally be categorized as current-controlled VSCs (CC-VSCs) and voltage-controlled VSCs (VC-VSCs). Figure 3.1a depicts the block diagram of a CC-VSC that typically incorporates an inner current loop, which can typically be implemented using either PI-controllers in dq reference frame or PR-controllers in $\alpha\beta$ reference frame. Furthermore, an outer power loop sets the reference currents to control the injected active and reactive powers to the microgrid. The CC-VSC is connected to the point of common coupling (PCC) through a large coupling inductor to suppress the switching harmonic components. A phase-locked loop (PLL) is implemented to synchronize the converter operation to the microgrid's voltage at the PCC. Since CC-VSCs are considered grid-following converters, they cannot form the grid voltage. On the other hand, Figure 3.1b demonstrates the structure and control loops of a VC-VSC operated in droop-control mode. The converter is interfaced with the microgrid through a low-pass LC filter. The output voltage is tightly controlled by nested voltage and current control loops, while the output voltage magnitude and frequency are set by the outer droop controllers. It is worth noting that the droop-controlled VC-VSCs form the grid voltage and are therefore considered grid-forming DGs [76]. Accordingly, simplified steady-state models of DGs adopting different control schemes can be represented as explained in the following subsections.

### Constant-PQ DG without imbalance compensation

This DG implements a CC-VSC in a dq reference frame. Nevertheless, as the controllers do not deal with the system unbalances, the DG output currents are not balanced and thus cannot be modeled as a current source. Hence, the power electronic converter behaves as a balanced voltage source behind the coupling inductor. Based on the active and reactive power measurements at the PCC, the voltage magnitude and phase angle are automatically controlled to maintain prespecified average active and reactive power injections to the system. This control scheme is considered the simplest for emulating a PQ bus, but it cannot guarantee either balanced voltages or currents at the PCC. The

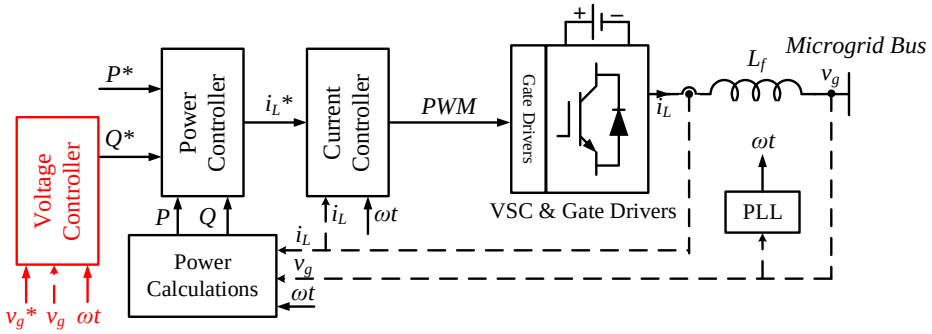


(a) CC-VSC

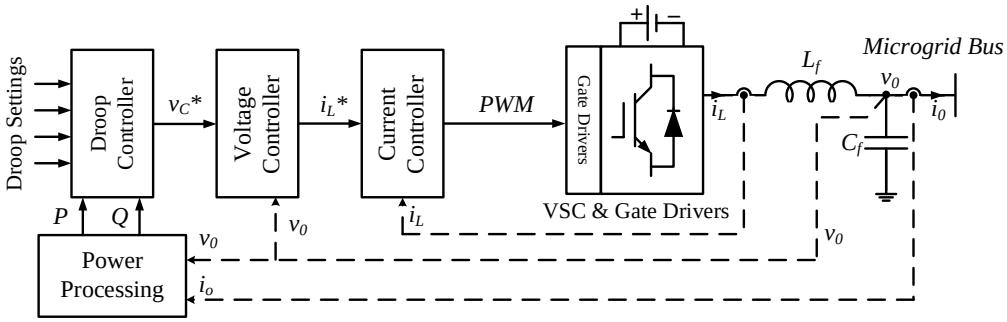


(b) droop-controlled VSC

Figure 3.1: Power circuits and control structures of electronically-interfaced DGs in ac microgrids.

mathematical modeling for this control topology is summarized as

$$P_{ac,G,i} = \sum_{x\in\{a,b,c\}} P^x_{ac,G,i} \tag{3.9}$$

$$Q_{ac,G,i} = \sum_{x\in\{a,b,c\}} Q^x_{ac,G,i} \tag{3.10}$$

$$P^x_{ac,G,i} = Y^x_{G,i} V_{ac,G,i} V^x_{ac,i} \sin(\delta^x_{V,G,i} - \delta^x_i) \tag{3.11}$$

$$Q^x_{ac,G,i} = Y^x_{G,i} V^*_{ac,G,i} V^x_{ac,i} \cos(\delta^x_{V,G,i} - \delta^x_i) - {V^*_{ac,i}}^2 \tag{3.12}$$

$$\delta^a_{V,G,i} = \delta^b_{V,G,i} + \frac{2}{3}\pi = \delta^c_{V,G,i} - \frac{2}{3}\pi \tag{3.13}$$

where $V_{ac,G,i}$ and $\delta^x_{V,G,i}$ are the converter output voltage magnitude and angle at phase $x \in \{a, b, c\}$, respectively, and $Y^x_{G,i}$ is the DG output admittance. The simple constant PQ

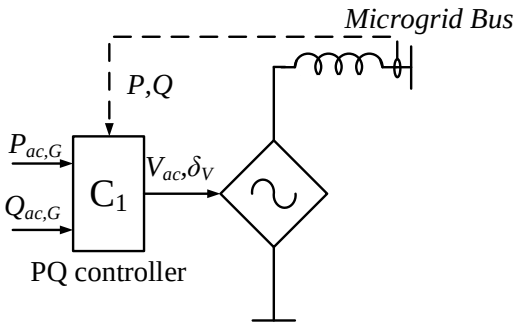


Figure 3.2: Simplified model of constant PQ AC DG.

topology can be represented as a controlled balanced voltage source behind the coupling impedance, as depicted in Figure 3.2. Note that the three-phase DG's reactive power is defined as the summation of the single-phase reactive powers at the three phases.

### Constant PQ DG with imbalance compensation

This control scheme is configured by implementing a current controller with imbalance compensation, therefore maintaining the output currents balanced under unbalanced terminal voltages. The control scheme still reflects the behavior of a PQ bus, which injects preset total active and reactive powers, and therefore (3.9) and (3.10) can still describe the DG's total power injections. However, since the DG's control topology maintains balanced current injections, the phase power injections and current phase angles are described by

$$P^x_{ac,G,i} = V^x_{ac,i} I_{ac,G,i} \cos(\delta^x_i - \delta^x_{I,G,i}) \tag{3.14}$$

$$Q^x_{ac,G,i} = V^x_{ac,i} I_{ac,G,i} \sin(\delta^x_i - \delta^x_{I,G,i}) \tag{3.15}$$

$$\delta^a_{I,G,i} = \delta^b_{I,G,i} + \frac{2}{3}\pi = \delta^c_{I,G,i} - \frac{2}{3}\pi \tag{3.16}$$

where $I_{ac,i}$ and $\delta^x_{I,G,i}$ are the converter output current magnitude and angle at phase $x \in \{a, b, c\}$, respectively. This DG can, thus, be represented as a controlled current source, as shown in Figure 3.3.

### Constant PV

This control topology replaces the reactive power controller with a voltage controller in the PQ control topology, as shown in red in Figure 3.1a. Furthermore, the voltage control

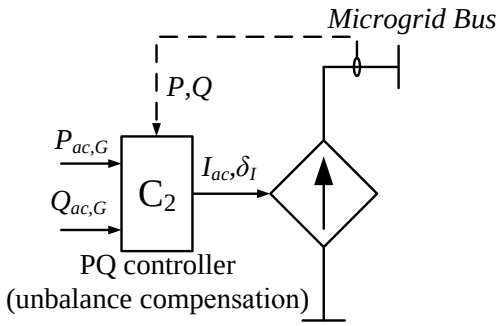


Figure 3.3: Simplified model of constant PQ AC DG with imbalance compensation.

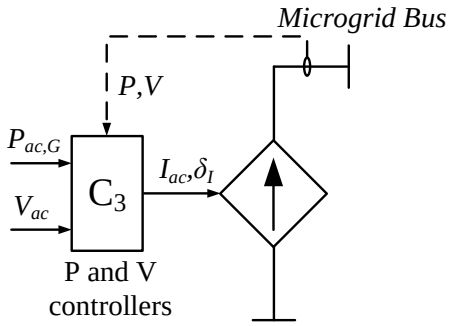


Figure 3.4: Simplified model of constant PV AC DG.

loop accommodates an imbalance compensation scheme to maintain controlled balanced voltages at the PCC. This control strategy emulates PV bus behavior, since the DG tightly controls the injected active power, whereas the reactive power injection adapts to maintain constant balanced voltages at the PCC. The PV control topology could be represented by a controlled current source that regulates the voltage magnitude and active power injection at its terminals, as presented in Figure 3.4. It can be mathematically modeled by (3.9) to describe the DG's three-phase active power in addition to the voltage magnitude and angle equations represented by

$$V_{ac,i}^{a} = V_{ac,i}^{b} = V_{ac,i}^{c} \tag{3.17}$$

$$\delta_{i}^{a} = \delta_{i}^{b} + \frac{2}{3}\pi = \delta_{i}^{c} - \frac{2}{3}\pi \tag{3.18}$$

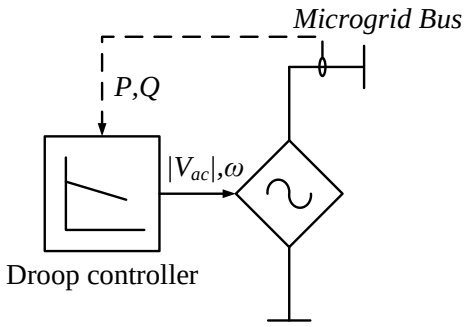


Figure 3.5: Simplified model of droop-controlled AC DG.

**Droop-controlled DGs**

This operational scheme is a key strategy for balancing the system loading and generation in islanded ac microgrids. Given the small installed DG capacities, the DGs share the responsibility of matching any change in the loading condition within permissible frequency and voltage deviation limits. Accordingly, some DGs follow droop characteristics given by (3.19) and (3.20) to collaboratively set the ac network's frequency and volt-age, thus attaining proportional active and reactive power sharing among the DGs [67]. The AC DG's active and reactive powers ($P_{ac,G,i}$ and $Q_{ac,G,i}$) can therefore be given as:

$$P_{ac,G,i} = \mu_i(\omega_{0,i} - \omega) \tag{3.19}$$

$$Q_{ac,G,i} = \eta_i(V_{ac,0,i} - |V_{ac,i}|) \tag{3.20}$$

In (3.19) and (3.20), $\omega_{0,i}$ and $V_{ac,0,i}$ are the no-load reference values for the DG output frequency and voltage, and $\mu_i$ and $\eta_i$ are the reciprocals of the DG droop gains. It is worth mentioning that this model assumes that the DG maintains balanced voltages at the PCC as previously presented in (3.17) and (3.18). Droop-controlled DGs can be simplified as controlled balanced voltage sources that autonomously change their output voltage magnitude and frequency based on their output powers, as illustrated in Figure 3.5.

## 3.3 DC Microgrid Modeling

This section demonstrates the modeling of dc microgrid components. For a dc subgrid comprised of a set $N_{dc}$ of buses, the power injected at any arbitrary bus $i \in N_{dc}$ ($P_{dc,i}$) can

be calculated as

$$P_{dc,i} = V_{dc,i} \sum_{j \in N_{dc}} V_{dc,j} G_{ij} \tag{3.21}$$

where $V_{dc,i}$ is the voltage of bus $i$, and $G_{ij}$ is the conductance matrix element.

### 3.3.1 DC Load Modeling

In general, constant-resistance, constant-power, and constant-current loads are the main load types in dc distribution networks. Constant-resistance model match various types of relays, heaters, and lamps. Constant-power loads are the most dominant because variable speed drives, dc motors, and dc power supplies demonstrate constant-power characteristic in a wide range of voltage. However, some motors draw almost the same current over a wide range of voltage and, thus, constant-current model is the best fit in this case. A generic model for an aggregated load can be represented as

$$P_{dc,L,i} = P^0_{dc,L,i} + V_{dc,i} I^0_{dc,L,i} \tag{3.22}$$

where $P^0_{dc,L,i}$ and $I^0_{dc,L,i}$ are the constant-power and constant-current portions of the aggregated load, respectively. It is noteworthy that the constant-resistance portion is not included in the model because this portion is incorporated directly into the system conductance matrix.

### 3.3.2 DC DG Modeling

DGs could follow either constant power or droop-based characteristics in a dc microgrid. Figure 3.6a illustrates the structure of constant-power DGs, for which current-controlled second-quadrant DC/DC converters are typically implemented if unidirectional power flow is always intended. The current control is typically realized using a PI-controller that sets the converter's duty cycle. The current reference is often set by maximum power point tracking (MPPT) algorithms, although external set points (red colored) can also be provided through power controllers in some scenarios.

As in ac microgrids, droop controls can be adopted to enhance power sharing among DGs in islanded dc microgrids, as illustrated in Figure 3.6b. This topology adopts nested current, voltage, and droop controllers to autonomously adjust the DG's output voltage according to the droop characteristics. This control topology can be realized via two main

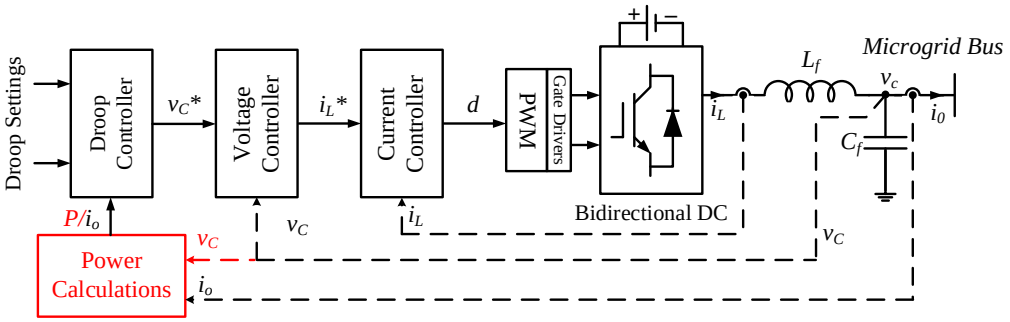


(a) Constant-power DC DG

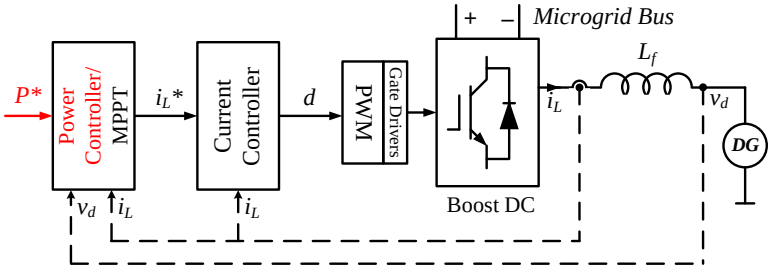


(b) Droop-controlled DC DG

Figure 3.6: Power circuits and control structures of electronically-interfaced DGs in dc microgrids.

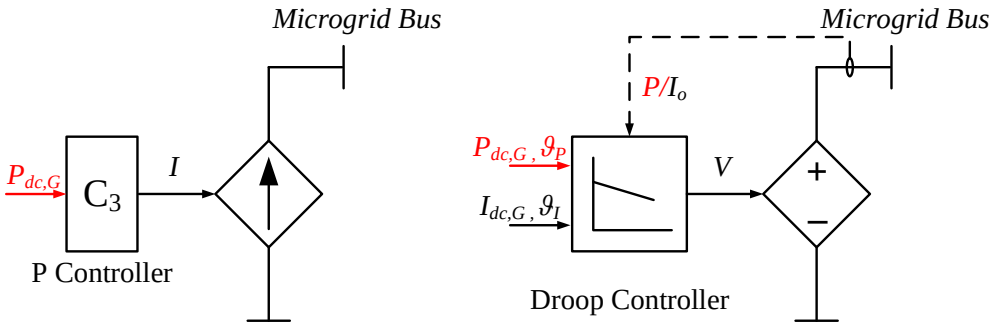


(a) Constant-power DC DG (b) Droop-controlled DC DG

Figure 3.7: Simplified models of electronically-interfaced DGs in dc microgrids.

control structures – namely, I-V and P-V (integrating red blocks). The droop operational characteristics are represented as

$$P_{dc,G,i} = \vartheta_{P,i}(V_{dc,0,i} - V_{dc,i}) \tag{3.23}$$

$$I_{dc,G,i} = \vartheta_{I,i}(V_{dc,0,i} - V_{dc,i}) \tag{3.24}$$

where $P_{dc,G,i}$ and $I_{dc,G,i}$ are the DG output power and current, $V_{dc,0,i}$ is the DG no-load reference voltage, and $\vartheta_{P,i}$ and $\vartheta_{I,i}$ are the droop gains for the DG output power and current, respectively. Figures 3.7a and 3.7b show the simplified models of constant power DGs (represented as a controlled current source) and droop-controlled DGs (represented as an autonomously controlled voltage source), respectively.

## 3.4 IC Modeling

ICs are essential components that connect ac and dc subgrids in a hybrid microgrid. As explained in subgrid modeling, droop-based DGs are implemented to share the load power within a single subgrid. Meanwhile, ICs between the ac and dc subgrids are responsible for sharing the overall load demand of the hybrid microgrid, regardless of the load location. ICs realize this objective by transferring active power from lightly loaded subgrids to heavily loaded ones. It is noteworthy that the relative loading of each sub-grid is inferred through a different variable depending on the subgrid type, i.e., frequency in ac subgrids and voltage in dc subgrids. Hence, ICs map these variables into a common normalized range to compare

the loading levels of unalike subgrids, following

$$\Delta\omega_{pu} = \frac{\omega - 0.5(\omega_{max} + \omega_{min})}{0.5(\omega_{max} - \omega_{min})} \tag{3.25}$$

$$\Delta V_{dc,pu,l} = \frac{V_{dc,l} - 0.5(V_{dc,max} + V_{dc,min})}{0.5(V_{dc,max} - V_{dc,min})} \tag{3.26}$$

where $\omega_{max}$ and $\omega_{min}$ are the maximum and minimum permissible values for the ac subgrid angular frequency, and$V_{dc,max}$ and $V_{dc,min}$ are the maximum and minimum allowable voltages in the dc subgrid. In this formulation, the loading conditions are normalized within the range 1 to 1 for both ac and dc subgrids; however, other normalizing ranges are also applicable. Hence, a single IC could transfer the appropriate amount of active power to equalize the normalized values of $\Delta\omega_{pu}$ and $\Delta V_{dc,pu,l}$, thus attaining proportional power sharing between the ac and dc subgrids. Alternatively, if multiple ICs are installed in the same hybrid microgrid, they employ a droop control scheme that allows active power sharing among the ICs. This droop scheme is realized by introducing an intentional error $e_{pu}$ between the normalized voltage and frequency, given by

$$e_{pu,l} = \Delta\omega_{pu} - \Delta V_{dc,pu,l} \tag{3.27}$$

This error is a variable that stimulates the ICs to share the active power transfer proportionally to their capacities according to

$$P_{ac,IC,l} = \sum_{x\in\{a,b,c\}} P^{x}_{ac,IC,l} = \frac{e_{pu,l}}{k_l} \tag{3.28}$$

where $P_{ac,IC,l}$ is the active power injected at the ac-side, and $k_l$ is an error coefficient inversely proportional to the IC capacity. However, proportional power sharing is not guaranteed if the ICs are installed at different dc buses, because, unlike the ac frequency, the dc voltage is not a global power flow variable in dc subgrids.

Moreover, the IC could provide reactive power support to the ac subgrid, which is adjusted via droop characteristics that function in the average three-phase terminal voltages while limited by the converter's capacity [22]. The reactive power $Q_{ac,IC,l}$ of an IC, injected at the ac-side bus $i \in N_{ac}$ can therefore be modeled as

$$Q_{ac,IC,l} = \sum_{x\in\{a,b,c\}} Q^{x}_{IC,l} = \eta_l(V_{ac,l,0} - \frac{1}{3}\sum_{x\in\{a,b,c\}} \left|V^{x}_{ac,l}\right|) \tag{3.29}$$

As shown in Figure 3.8a, ICs implement CC-VSCs with typical converter and control structures as explained in Section 3.2.2 , thus allowing for power exchange between ac and

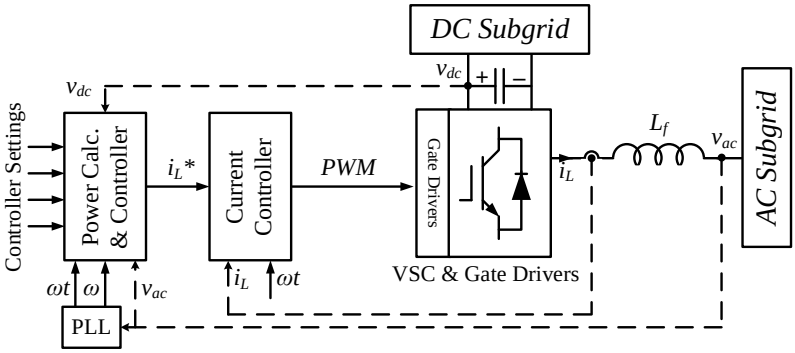


(a) Power circuit and control structure

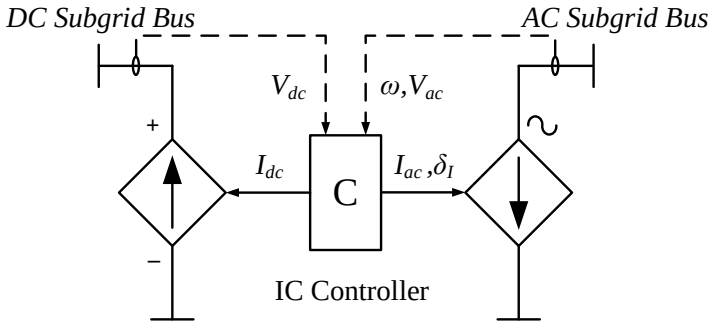


(b) Simplified model

Figure 3.8: Power circuit, control structure, and simplified model of IC in hybrid ac/dc microgrids.

dc subgrids. The IC's ac side is connected and synchronized to the ac subgrid while the dc terminals are connected to the dc subgrid. The voltages of the ac and dc subgrids are locally measured at the IC terminals and processed by the power controller to follow (3.25)-(3.29) in order to set the converter's active and reactive power references. ICs' controllers are assumed to account for ac subgrid's unbalanced voltages, and therefore they realize active power exchange and reactive power support by injecting balanced three-phase currents on the ac side, even with unbalanced terminal ac voltages. Hence, the phase active and reactive powers of the IC are described by

$$P^x_{ac,IC,l} = V^x_{ac,l}\, I_{ac,IC,l}\, \cos(\delta^x_l - \delta^x_{I,IC,l}) \tag{3.30}$$

$$Q^x_{ac,IC,l} = V^x_{ac,l}\, I_{ac,IC,l}\, \sin(\delta^x_l - \delta^x_{I,IC,l}) \tag{3.31}$$

$$\delta^a_{I,IC,l} = \delta^b_{I,IC,l} + \frac{2}{3}\pi = \delta^c_{I,IC,l} - \frac{2}{3}\pi \tag{3.32}$$

where $I_{ac,IC,l}$ and $\delta^x_{I,IC,l}$ are the converter output current magnitude and angle at phase $x \in \{a, b, c\}$, respectively.

To enhance the accuracy of the results, the generic power loss formula for the interlinking converter is adopted in this work [39], [118]:

$$P_{IC,loss,l} = C_0 + C_1 I_{ac,IC,l} + C_2 I^2_{ac,IC,l} \tag{3.33}$$

where $P_{IC,loss,l}$ is the converter power loss, $I_{ac,IC,l}$ is the injected current at the converter ac side, and $C_0$, $C_1$ and $C_2$ are the quadratic function coefficients. Figure 3.8b presents the IC's simplified model, implying that the IC is realized as a load for one subgrid while seen as a supply by the other. It is, however, represented as controlled current sources on both sides.

## 3.5 Power Flow Formulation

The power flow problem is the comprehensive formulation that defines the steady-state behavior of the entire system. The problem is formulated by identifying the minimum number of variables that could represent the system in the steady state. In order to have a well-defined system, the formulation must incorporate as many mismatch equations as power flow variables.

### 3.5.1 Mismatch Equations in an AC Subgrid

In steady-state analysis, a traditional ac power network could be represented by the values of the three-phase voltage magnitudes and angles at different buses. These power flow variables are extended to include the system frequency and additional variables based on the control strategy of the installed DGs. The active and reactive power balancing equations for each phase $x \in \{a, b, c\}$ are employed as key mismatch equations for each bus as

$$P^x_{ac,G,i} = P^x_{ac,L,i} + P^x_{ac,i} \tag{3.34}$$

$$Q^x_{ac,G,i} + Q^x_{ac,IC,l} = Q^x_{ac,L,i} + Q^x_{ac,i} \tag{3.35}$$

For a DG unit that implements constant PQ control without imbalance compensation, eight independent variables are defined:

$$x_{ac,PQ,i} = [V^{abc}_{ac,i} \quad \delta^{abc}_i \quad V_{ac,G,i} \quad \delta^a_{V,G,i}]^T \tag{3.36}$$

As demonstrated by (3.36), the converter output voltage angles at phases $\{b, c\}$ are not included, since the converter voltage is considered balanced. In this case, the eight corresponding mismatch equations are introduced by substituting (3.11) and (3.12) into (3.9), (3.10), (3.34), and (3.35), respectively. For a DG unit that adopts constant PQ scheme with imbalance compensation, the following eight independent variables are included in the problem.

$$x_{ac,\,comp,i} = [V^{abc}_{ac,i} \quad \delta^{abc}_i \quad I_{ac,G,i} \quad \delta^a_{I,G,i}]^T \tag{3.37}$$

Since the injected currents are balanced, the bus angles at phases b,c are dependent variables (3.18) and thus are not included in the formulation. The corresponding mismatch equations could be formulated using (3.9), (3.10), (3.34) and (3.35) after substituting the three-phase active and reactive powers modeled in (3.14) and (3.15). Further, a DG unit emulating a PV bus introduces only the phase angle of phase $\{a\}$ voltage as an independent power flow variable

$$x_{ac,PV,i} = [\delta^a_{I,G,i}]^T \tag{3.38}$$

The voltage magnitude is not included because it takes a pre-specified value in this control scheme. The voltage angles at phases $\{b, c\}$ are not considered due to their dependence on the voltage angle at phase $\{a\}$. Accordingly, the existence of a PV bus is handled by a single equation which is reached by substituting the injected three-phase active powers (3.9) into (3.34).

Moreover, for a droop-based DG, the voltage magnitude and angle at phase $\{a\}$ represent the independent power flow variables

$$x_{ac,droop,i} = [V_{ac,i}^{a} \quad \delta_i^a]^T \tag{3.39}$$

Two corresponding mismatch equations could be defined by substituting the total three-phase injected active and reactive powers (3.19) and (3.20) into (3.34) and (3.35), respectively. Finally, since the first bus voltage angle at phase $\{a\}$ is considered the reference angle ($\delta_1^a = 0$) while the system frequency is an unknown, the matching is maintained between the number of power flow variables and that of problem equations.

### 3.5.2 Mismatch Equations in an DC Subgrid

Compared to ac systems, the steady-state analysis of dc systems is much simpler, as the voltage values at different buses are sufficient to give a full steady-state representation of a dc system. Also, the mismatch equation is defined by directly combining the transferred, load, and generated powers (3.21)-(3.24) into the active power balancing equation (3.40) regardless of the DG type.

$$P_{dc,G,i} + V_{dc,G,i} I_{dc,G,i} = P_{dc,L,i} + P_{dc,i} \tag{3.40}$$

### 3.5.3 Mismatch Equations of the Interlinking Converter

For each ac bus connected to an interlinking converter, the power flow variables are augmented by eight variables:

$$x_{IC,l} = [V_{ac,l}^{abc} \quad \delta_i^{abc} \quad I_{ac,IC,l} \quad \delta_{I,IC,l}^{a}]^T \tag{3.41}$$

To handle these variables, (3.34), (3.35), (3.28) and (3.29) are added to the set of problem equations after substituting the three-phase active and reactive powers, as stated in (3.30) and (3.31). It is noteworthy that the active power injected at the dc-side is not an independent power flow variable, and is therefore not included in the problem, since it is a function of the active power injected in the ac-side as:

$$P_{dc,G,l} = -P_{ac,IC,l} + P_{IC,loss,l} \tag{3.42}$$

### 3.5.4 Newton-Trust Region

A set of non-linear equations representing the power flow problem is traditionally solved based on well-known Newton Raphson (NR) algorithms. In general, NR approaches illustrate quadratic rate of convergence in solving nonlinear problems. However, due to different factors associated with the power flow problem in unbalanced distribution systems, the NR algorithms may confront many challenges. Unlike transmission systems, distribution networks are characterized by predominantely resistive feeders in addition to the need of sparse Jacobian matrix inversion [28], [119]. Furthermore, with the added complexity associated with the integration of dc networks and their interactions with the unbalanced ac subgrid, the conventional NR methods could encounter further convergence issues. Accordingly, NR techniques may fail to successfully solve the power flow problem of the type of microgrid under investigation even with a flat start. This phenomenon is attributed to the narrow region of attraction while solving the formulated problem for such systems. In addition, the absence of a slack bus results in an operational state close to the boundary between the unsolvable and solvable regions. In this chapter, a Newton-Trust Region (NTR) approach is introduced, as an alternative, to avoid the common drawbacks of the NR methods. Trust-Region methods are considered effective, albeit simple, tools for solving larger-scale optimization problems and different sets of nonlinear equations. Furthermore, NTR approaches illustrate a quadratic rate of convergence similar to NR algorithms [120]; however, they belong to the gradient descent family, which guarantees conversion to the solution if it exists.

The set of nonlinear equations modeling the steady-state behavior of the islanded network can be formulated as a minimization problem:

$$\min \begin{cases} F_1(X) = & f_1(X) - A_1 \\ & \vdots \\ F_i(X) = & f_i(X) - A_i \\ & \vdots \\ F_n(X) = & f_n(X) - A_n \end{cases} \tag{3.43}$$

where$F_i(X)(i = 1, 2, \cdots, n)$ represents a set of equations that describe the network, $f_i(X)$ and $A_i$ are the variable dependent and independent terms, respectively, and $n$ is the number of variables. The proposed NTR algorithm starts by assuming an initial guess $X_0$ for the network variables. Then, at each iteration $k$, the algorithm calculates the suitable change in variables $\Delta_k$ that maintains $F_i(X_k + \Delta_k) < F_i(X_k)$. For this purpose, the original function $F_i(X_k)$ is approximated by a quadratic function $\tilde{F}_{i|k}(X_k)$ that demonstrates a

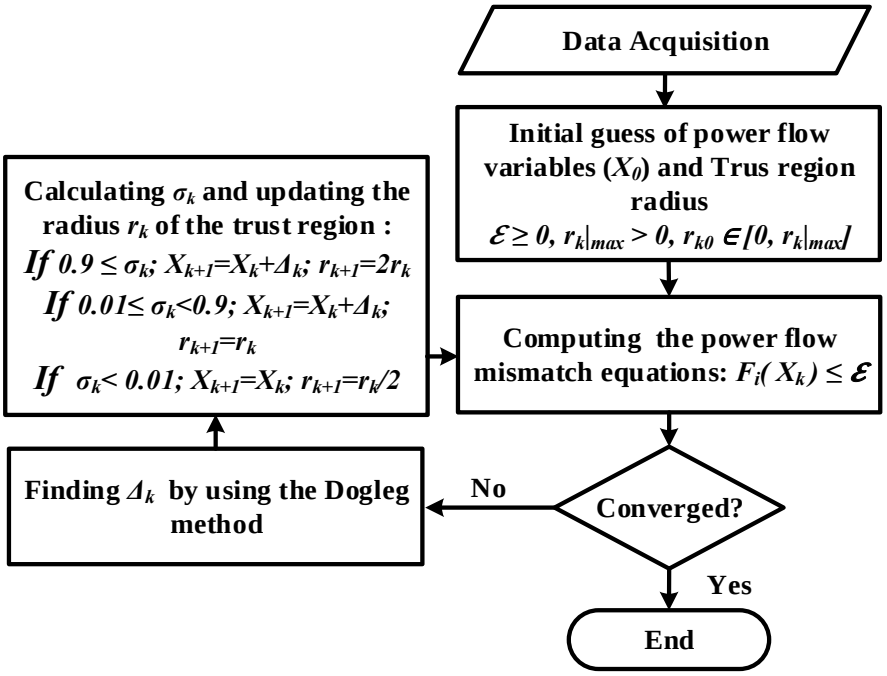


Figure 3.9: The power flow algorithm using NTR.

similar behavior in the neighborhood of $X_k$ and within a ball, a trust region, defined by a radius $r_k$:

$$\tilde{F}_{i|k}(X_k) = F_i(X) + \Delta_k^T \nabla F_i(X_k) + \frac{1}{2}\Delta_k^T \nabla^2 F_i(X_k)\Delta_k \tag{3.44}$$

where $\nabla F_i(X_k)$ and $\nabla^2 F_i(X_k)$ are the Jacobian and Hessian of the original function $F_i$ at $X_k$. Thus, $\Delta_k$ is solved as the minimizer of $\tilde{F}_{i|k}$ within the trust region:

$$\min \tilde{F}_{i|k}(X_k) \qquad \textit{subject to} \quad \|\Delta_k\| < r_k \tag{3.45}$$

The presentation of (3.45) is the standard form for the NTR algorithm. The solution mechanism of this representation includes two main steps: solving $\Delta_k$ and updating $r_k$. Both steps are explained in detail in the following subsections while Figure 3.9 highlights the steps of the proposed power flow in light of the NTR method.

**Updating variables (Dogleg Method)**

Using the Lagrangian Function, (3.46) can be solved in terms of a Lagrantian multiplier $\Lambda \geq 0$ [121]:

$$(\nabla^2 F_i(X_k) + \Lambda I)\Delta_k^* = -\nabla F_i(X_k) \tag{3.46}$$

If the solution lies inside the trust region, i.e., $\|\Delta_k\| > r_k$, then $\Lambda = 0$ and the problem is a simple unconstrained minimization:

$$\Delta_k^* = (\nabla^2 F_i(X_k))^{-1} - \nabla F_i(X_k) \tag{3.47}$$

Otherwise, the optimum solution can be calculated as

$$\Delta_k^* = -(\nabla^2 F_i(X_k)) + \Lambda I^{-1} - \nabla F_i(X_k) \tag{3.48}$$

Estimating $\Lambda$ can be achieved through Dogleg method which is efficient and entails low computational cost. Dogleg method approximates the function $\Delta_k()$ by a piecewise linear polygon $\tilde{\Delta(\tau)}$:

$$\tilde{\Delta(\tau)} = \begin{cases} \tau\Delta^u & 0 \leq \tau < 1 \\ \Delta^u + (\tau - 1)(\Delta^* - \Delta^u) & 1 \leq \tau \leq 2 \end{cases} \tag{3.49}$$

**Updating the trust regions radius**

The quality of the approximated function, $\tilde{F}_{i|k}$, in representing the original function, $F_i$, is the factor that determines the trust region radius $r_k$. The quality of the approximation is represented by ratio $\sigma_k$ calculated as:

$$\sigma_k = \frac{F_i(X_k) - F_i(X_k + \Delta_k)}{\tilde{F}_{i|k}(0) - \tilde{F}_{i|k}(X_k)} \tag{3.50}$$

High values of $\sigma_k$, i.e., $\sigma_k \geq 0.09$, reflects the good behavior of $\tilde{F}_{i|k}$, and thus the trust region is expanded ($r_{k+1} = 2r_k$) and the solution is updated ($X_{k+1} = X_k + \Delta_k$). For moderate values of $\sigma_k$, i.e., $\sigma_k \in [0.01, 0.09]$, $\tilde{F}_{i|k}$ is considered satisfactory and the solution is updated ($X_{k+1} = X_k + \Delta_k$), yet without changing the trust region radius ($r_{k+1} = r_k$). Finally, if $\sigma_k$ is found to be low, i.e., $\sigma_k < 0.01$, $\tilde{F}_{i|k}$ is not trusted to represent $F_i$ within the radius. Accordingly, the trust region $r_k$ is reduced to half and the new solution is rejected in this iteration ($X_{k+1} = X_k$).

It is worth mentioning that for each iteration, the active and reactive powers of DGs and ICs are calculated. If the output power of a droop-controlled DG exceeds its capacity limit, it is fixed at the maximum value, and the droop equations are overriden. Similarly, ICs' powers follow (3.28) and (3.29) only until they hit their maximum values. It is also noteworthy that the IC's active power transfer is given priority over its reactive power injection, which means that the reactive power limit depends on the available capacity after meeting the active power exchange requirements.

### 3.5.5 Initialization Procedure

For iterative solution methods, the initial variable assignment (i.e., the initial guess $X_0$) plays a vital role in the problem convergence. Typically, a flat start (i.e., the case with all bus voltages set to $1.00\angle 0.0^\circ$ pu) is utilized in balanced ac power flow algorithms, where the voltage magnitudes and angles are the unknown independent variables. On the other hand, the proposed algorithm solves for the three phase voltages of the ac subgrid's buses, the ac subgrid's frequency, the dc subgrid's voltages, and the ICs' currents/powers. In the proposed algorithm, a three-phase flat start is initially assigned to all ac buses (i.e., $V^a_{ac,i} = 1.0\angle 0.0^\circ$ pu, $V^b_{ac,i} = 1.0\angle -120.0^\circ$ pu, and $V^c_{ac,i} = 1.0\angle 120.0^\circ$ pu) while the ac subgrid's frequency is set to 1.0 p.u. The dc voltages are all set to 1.0 pu Furthermore, the ICs' active powers are initiated at zero values, which implies that the ICs' current magnitudes and angles are initially set to zero as well.

## 3.6 Case Studies

### 3.6.1 Model Validation

The accuracy of the power flow algorithm was verified through comparing its results with the steady-state results of detailed time-domain simulations performed in PSCAD/EMTDC software. This analysis was performed on a hybrid microgrid that combines ac and dc microgrids studied in [67], [122], respectively. Figure 3.10 shows the schematic diagram of the system under test. The subgrids have been deliberately selected with relatively small sizes to be suitable for time-domain simulations. The unbalanced behavior of the ac subgrid is provoked by replacing the loads defined in [67] with unbalanced constant PQ loads at buses 1 and 3. Two different operational scenarios are considered to highlight the generality and applicability of the presented models and the proposed power flow approach.

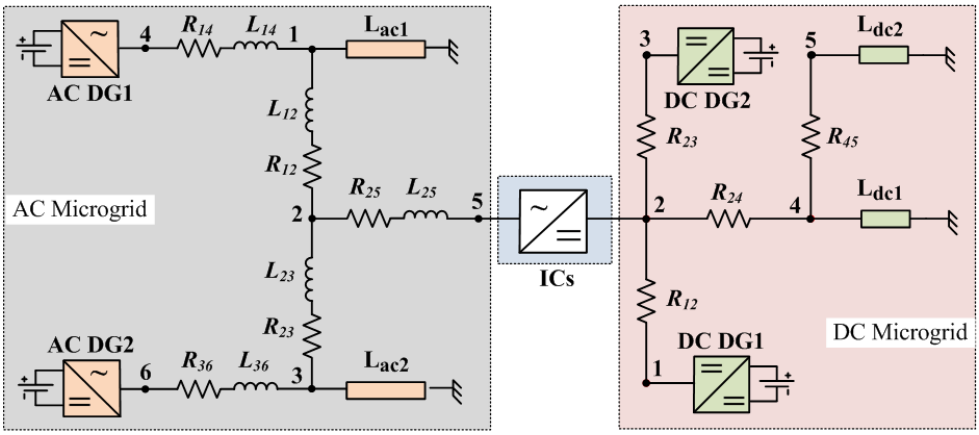


Figure 3.10: Test microgrid#3.1.

In the first operational scenario, the installed DGs in the ac subgrid are identical droop-based units with active power rating of 0.5 p.u, each. Similarly, two 0.25 p.u. droop-based DGs are placed at buses 1 and 3 of the dc subgrid. Two ICs connect buses 5 and 2 in the ac and dc subgrids, respectively, to allow power transfer/sharing between the two subgrids with an error coefficient $k_l$ of 0.1 p.u. Table 3.1 presents the steady-state results obtained from the proposed algorithm and the detailed time-domain simulation. The results indicate close agreement, with errors smaller than $4.7 \times 10^{-4}$ pu and $2.8 \times 10^{-4}$ rad for the voltage magnitudes and phase angles, respectively. These results highlight the high accuracy of the proposed modeling approach when used in unbalanced islanded hybrid ac/dc microgrids. It is worth mentioning that without power exchange between the subgrids, the ac subgrid incurs a higher loading ratio of 75% compared to 20.6% for the dc subgrid. However, with the frequency and voltage coupling principle in (3.28), the ICs equally share a total power transfer of 0.1497 p.u., yielding loading ratios of 59.8% and 56.8% in the ac and dc subgrids, respectively. Equal power sharing between the two ICs is achieved, since they are connected to the same dc bus, and therefore both measure the same dc voltage. Meanwhile, the approximate equality of the subgrid loading ratios is attained due to the system's small size. However, in larger-scale microgrids, the ICs power-sharing performance is quite different where a number of ICs connect various buses of the two subgrids. Thus, it should be given more attention, as discussed in Section 3.6.3.

Table 3.1: Validation results of test microgrid#3.1 (all DGs implement droop control)

**PSCAD\EMTDC**

| AC Bus# | $\lvert V_{ac}^{a}\rvert$ (pu) | $\delta^{a}$ (rad) | $\lvert V_{ac}^{b}\rvert$ (pu) | $\delta^{b}$ (rad) | $\lvert V_{ac}^{c}\rvert$ (pu) | $\delta^{c}$ (rad) | DC Bus# | $V_{dc}$ (pu) |
|---|---|---|---|---|---|---|---|---|
| 1 | 1.0074 | 0.0000 | 1.0038 | −2.0957 | 0.9998 | 2.0907 | 1 | 0.9917 |
| 2 | 1.0124 | −0.0011 | 1.0114 | −2.0978 | 1.0105 | 2.0874 | 2 | 0.9904 |
| 3 | 1.0117 | −0.0137 | 1.0113 | −2.1086 | 1.0099 | 2.0800 | 3 | 0.9945 |
| 4 | 1.0215 | 0.0067 | 1.0215 | −2.0876 | 1.0215 | 2.1011 | 4 | 0.9897 |
| 5 | 1.0194 | 0.0015 | 1.0181 | −2.0962 | 1.0171 | 2.0880 | 5 | 0.9887 |
| 6 | 1.0142 | −0.0134 | 1.0142 | −2.1078 | 1.0142 | 2.0810 | | |

$P_{ac,IC} = 0.1501$ pu

**Proposed method**

| AC Bus# | $\lvert V_{ac}^{a}\rvert$ (pu) | $\delta^{a}$ (rad) | $\lvert V_{ac}^{b}\rvert$ (pu) | $\delta^{b}$ (rad) | $\lvert V_{ac}^{c}\rvert$ (pu) | $\delta^{c}$ (rad) | DC Bus# | $V_{dc}$ (pu) |
|---|---|---|---|---|---|---|---|---|
| 1 | 1.0070 | 0.0000 | 1.0042 | −2.0958 | 1.0001 | 2.0908 | 1 | 0.9919 |
| 2 | 1.0128 | −0.0010 | 1.0118 | −2.0977 | 1.0102 | 2.0875 | 2 | 0.9904 |
| 3 | 1.0118 | −0.0138 | 1.0110 | −2.1084 | 1.0098 | 2.0801 | 3 | 0.9946 |
| 4 | 1.0216 | 0.0069 | 1.0216 | −2.0874 | 1.0216 | 2.1013 | 4 | 0.9894 |
| 5 | 1.0192 | 0.0012 | 1.0185 | −2.0962 | 1.0174 | 2.0881 | 5 | 0.9889 |
| 6 | 1.0141 | −0.0134 | 1.0141 | −2.1078 | 1.0141 | 2.0810 | | |

$P_{ac,IC} = 0.1497$ pu

In the second operational scenario, the DG units implement a mix of control strategies. This scenario is performed by changing the control strategy of the AC-DG2 to a constant PQ DG unit with current imbalance compensation ($P_{ac,G2} = 0.4$ pu, $Q_{G2} = 0.3$ pu), and DC-DG2 to a constant power DG ($P_{dc,G2} = 0.1$) pu, respectively. The results, shown in Table 3.2, confirm the good match between the proposed algorithm solution and the PSCAD/EMTDC output results, with a maximum error of $4.4 \times 10^{-4}$ pu and $2.6 \times 10^{-4}$ rad for the voltage magnitudes and phase angles, respectively. Therefore, the presented DG models and the proposed power flow algorithm can be utilized to analyze larger and more complicated systems, with high accuracy.

Table 3.2: Validation results of test microgrid#3.1 (DGs implement mixed control schemes)

**PSCAD\EMTDC**

| AC Bus# | $\lvert V_{ac}^{a}\rvert$ (pu) | $\delta^{a}$ (rad) | $\lvert V_{ac}^{b}\rvert$ (pu) | $\delta^{b}$ (rad) | $\lvert V_{ac}^{c}\rvert$ (pu) | $\delta^{c}$ (rad) | DC Bus# | $V_{dc}$ (pu) |
|---|---|---|---|---|---|---|---|---|
| 1 | 1.0202 | 0.0000 | 1.0155 | −2.1027 | 1.0079 | 2.0723 | 1 | 0.9978 |
| 2 | 1.0350 | 0.0063 | 1.0277 | −2.1068 | 1.0164 | 2.0524 | 2 | 0.9964 |
| 3 | 1.0749 | 0.0094 | 1.0648 | −2.1105 | 1.0490 | 2.0368 | 3 | 0.9994 |
| 4 | 1.0291 | 0.0010 | 1.0291 | −2.0939 | 1.0291 | 2.0952 | 4 | 0.9955 |
| 5 | 1.0332 | 0.0191 | 1.0286 | −2.0976 | 1.0200 | 2.0542 | 5 | 0.9948 |
| 6 | 1.0796 | 0.0082 | 1.0693 | −2.1121 | 1.0538 | 2.0351 | | |

$P_{ac,IC} = 0.0314$ pu

**Proposed method**

| AC Bus# | $\lvert V_{ac}^{a}\rvert$ (pu) | $\delta^{a}$ (rad) | $\lvert V_{ac}^{b}\rvert$ (pu) | $\delta^{b}$ (rad) | $\lvert V_{ac}^{c}\rvert$ (pu) | $\delta^{c}$ (rad) | DC Bus# | $V_{dc}$ (pu) |
|---|---|---|---|---|---|---|---|---|
| 1 | 1.0204 | 0.0000 | 1.0156 | −2.1028 | 1.0080 | 2.0724 | 1 | 0.9976 |
| 2 | 1.0351 | 0.0061 | 1.0279 | −2.1064 | 1.0164 | 2.0523 | 2 | 0.9963 |
| 3 | 1.0751 | 0.0096 | 1.0649 | −2.1106 | 1.0491 | 2.0366 | 3 | 0.9993 |
| 4 | 1.0291 | 0.0007 | 1.0291 | −2.0937 | 1.0291 | 2.0951 | 4 | 0.9953 |
| 5 | 1.0333 | 0.0192 | 1.0283 | −2.0978 | 1.0202 | 2.0543 | 5 | 0.9948 |
| 6 | 1.0799 | 0.0083 | 1.0697 | −2.1120 | 1.0541 | 2.0351 | | |

$P_{ac,IC} = 0.0314$ pu

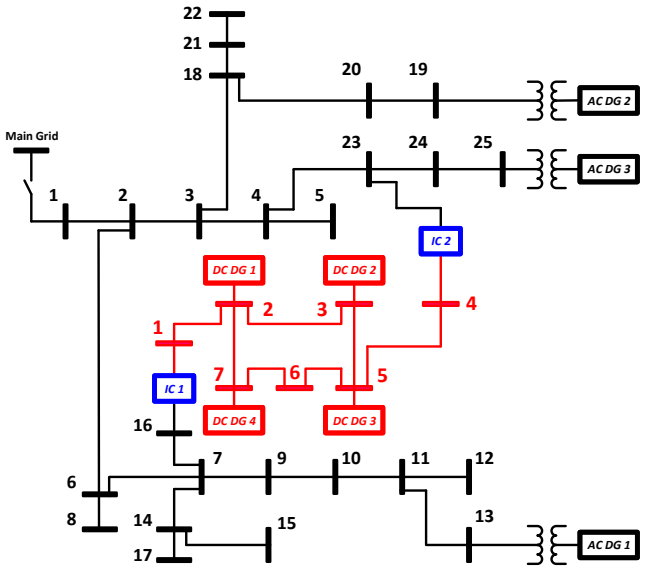


Figure 3.11: Test microgrid#3.2.

### 3.6.2 Effect of the Starting Point on Power Flow Convergence

As mentioned in Section 3.5.5, the starting point directly affects the power flow convergence. Therefore, this case study examines the proposed algorithm's convergence against changes in the starting point from the default values. This behavior is analyzed by incorporating the proposed steady-state models in a larger-scale hybrid microgrid. The microgrid under study is formed by connecting an unbalanced 25-bus ac subgrid [39] to a 7-bus dc subgrid [23], as shown in Figure 3.11.

The starting point of each variable group (i.e., ac voltages, dc voltages, ac frequency, and ICs' currents) were gradually changed, and the number of iterations needed to attain convergence for each case was accordingly recorded in Table 3.3. It is worth mentioning that only one variable group is changed at a time while the other groups are maintained at their default values. The results show that the algorithm convergence is most sensitive to the ac voltage starting point. However, it is fairly robust over a range of 35% around the rated value. On the other hand, the initial ac frequency guess has an insignificant effect on the solution convergence, even when it is set to zero. Furthermore, the starting dc voltage only affects the problem convergence at very low values, and leads to solution divergence as it approaches zero. Finally, as the ICs are initially set at any value within the ICs' rating of 0.25 pu in either direction, the algorithm is still able to converge with minimal

Table 3.3: Convergence results of test microgrid#3.1

| $V_{ac,0}$ (pu) | #iter. | $\omega_0$ (pu) | #iter. | $V_{dc,0}$ (pu) | #iter. | $P_{IC,0}$ (pu) | #iter. |
|---|---|---|---|---|---|---|---|
| 1.25 | Diverge | 2.0 | 6 | 2.0 | 5 | 0.25 | 4 |
| 1.20 | 5 | 1.8 | 4 | 1.8 | 5 | 0.20 | 4 |
| 1.15 | 5 | 1.6 | 4 | 1.6 | 4 | 0.15 | 4 |
| 1.10 | 4 | 1.4 | 4 | 1.4 | 4 | 0.10 | 4 |
| 1.05 | 4 | 1.2 | 4 | 1.2 | 4 | 0.05 | 4 |
| 1.00 | 4 | 1.0 | 4 | 1.0 | 4 | 0.00 | 4 |
| 0.95 | 4 | 0.8 | 4 | 0.8 | 5 | −0.05 | 3 |
| 0.90 | 4 | 0.6 | 4 | 0.6 | 5 | −0.10 | 3 |
| 0.85 | 5 | 0.4 | 4 | 0.4 | 12 | −0.15 | 3 |
| 0.80 | Diverge | 0.2 | 5 | 0.2 | 12 | −0.20 | 3 |
| 0.75 | Diverge | 0.0 | 6 | 0.0 | Diverge | −0.25 | 3 |

number of iterations. It is also observed that the number of iterations decreases when the ICs' active powers are initially set in the same direction (negative direction in this case) as their final values. Therefore, the proposed algorithm can generally be considered stable against initial point variations.

### 3.6.3 Active Power Sharing among ICs in Large-Scale Microgrids

According to [26], multiple ICs could be installed to increase system reliability. The implementation of (3.28) could maintain near-equal loading conditions at individual subgrids with the introduction of low error coefficient $k_l$. However, the ICs' active power transfer may differ based on the dc bus voltages at which the ICs are installed and the error coefficients $k_l$ of the ICs. It is worth mentioning that the two subgrids of test microgrid#3.2 are interlinked through two identical ICs, thus having the same $k_l$, but installed at two different locations. The analysis can be better understood by referring to Figures 3.12 and 3.13, which depict the effect of changing $k_l$ on the subgrids' percentage loadings, defined by (3.51), and the active power transfer through the ICs, respectively.

$$Subgrid's\ Percentage\ Loading\ = \frac{\sum_{i=1,2,\cdots} P_{G,i}}{\sum_{i=1,2,\cdots} P_{G,i}^{max}} \times 100 \tag{3.51}$$

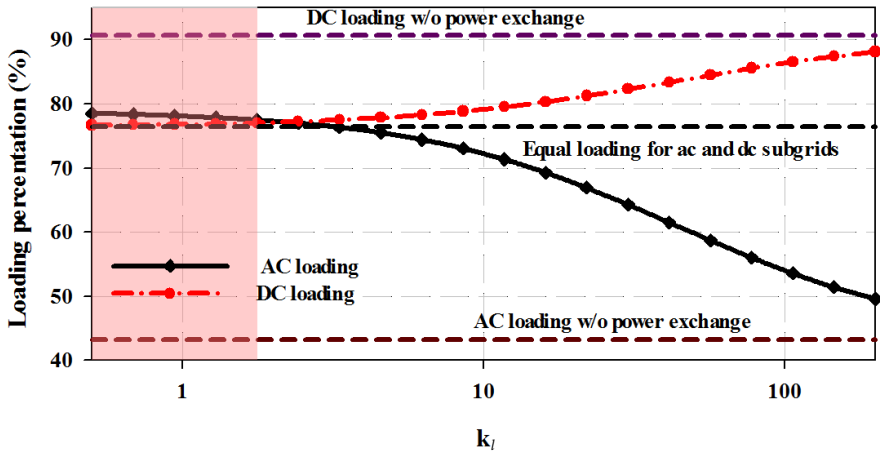


Figure 3.12: Subgrids' loading conditions under different error coefficients.

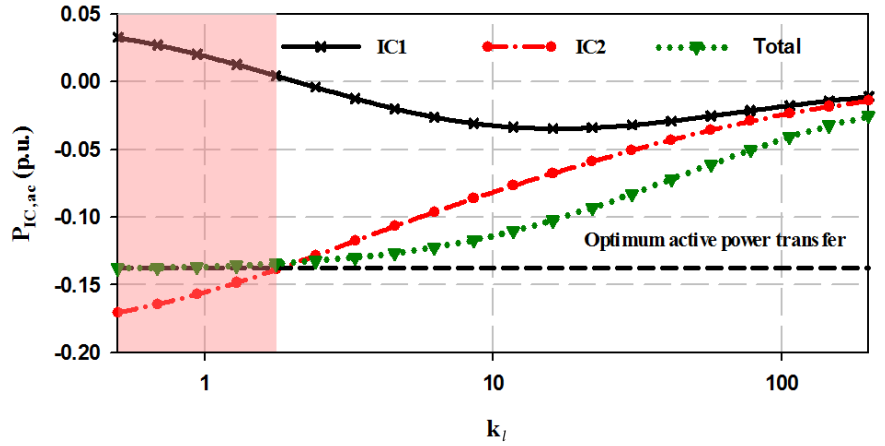


Figure 3.13: ICs' active power transfer under different error coefficients.

In (3.51), $P_{G,i}$ is the total active-power output of the DG (ac or dc) and $P_{G,i}^{max}$ the active-power capacity of the DG (ac or dc).

As demonstrated in Figures 3.12 and 3.13, there is a trade-off between the sharing accuracy of the overall system loading between the ac and dc subgrids and the sharing accuracy of the power transfer between the ICs. Lower values of $k_l$ lead to more even sharing of overall system loading between the ac and dc subgrids, as depicted in Figure 3.12. However, the plots in Figure 3.13 demonstrate that smaller error coefficient $k_l$ results in

increased mismatch between the ICs' active power transfers. For instance, although the total power transfer from the ac system to the dc system approaches the optimum value when $k_l$ is less than 1.3 p.u. (red shaded area), a hunting problem emerges (i.e., IC1 injects active power to the ac-side, while IC2 injects active power to the dc-side). On the other hand, high values of $k_l$ result in more even sharing of the active power transfer through the two ICs. However, less total active power is transferred to the heavily loaded dc subgrid in this case, thereby resulting in unequal loading of the subgrids. The optimal choice of IC locations, sizes, and parameters is a challenging point of research that may enable robust behavior of hybrid microgrids under different loading conditions.

### 3.6.4 The imbalance Effect on DG Phase-Loading

This case study highlights the importance of analyzing the unbalanced powers of DG phases in islanded hybrid microgrids. First, it is important to recall that droop-controlled DGs are introduced to increase system reliability by distributing load transients among all DGs. To minimize overall system operational cost, DG droop settings could be individually adjusted to dispatch the DG output powers [31]. This approach leads to higher loading of low-cost units compared to high-cost ones. According to models provided in [39], once the DG hits its maximum apparent-power limit, it switches to constant-PQ mode and maintains balanced voltages at its terminals. Although this model may be employed for steady-state studies of balanced microgrids, it cannot be generalized when analyzing unbalanced systems.

The aforementioned claim could be verified by applying the DG models of [39] while increasing the no-load reference values of one DG unit in test microgrid#3.2. In this example, the no-load reference values of AC-DG3 are increased, assuming it has the lowest operational cost. The apparent power of its phases as well as the total three-phase loading, defined by (3.52), would then be considered with the increase of the system ac loading.

$$Loading\ (\%) = \begin{cases} \dfrac{S^{x}_{ac,G,i}}{S^{ph,max}_{ac,G,i}} & \cdots (1-ph) \\ \\ \dfrac{\sum_{x\in\{a,b,c\}} S^{x}_{ac,G,i}}{3S^{ph,max}_{ac,G,i}} & \cdots (3-ph) \end{cases} \tag{3.52}$$

In (3.52), $S^{x}_{ac,G,i}$ and $S^{ph,max}_{ac,G,i}$ are the output phase apparent-power and the phase apparent-power capacity of the AC-DG, respectively. To control the ac loads, a loading factor $\lambda$ is

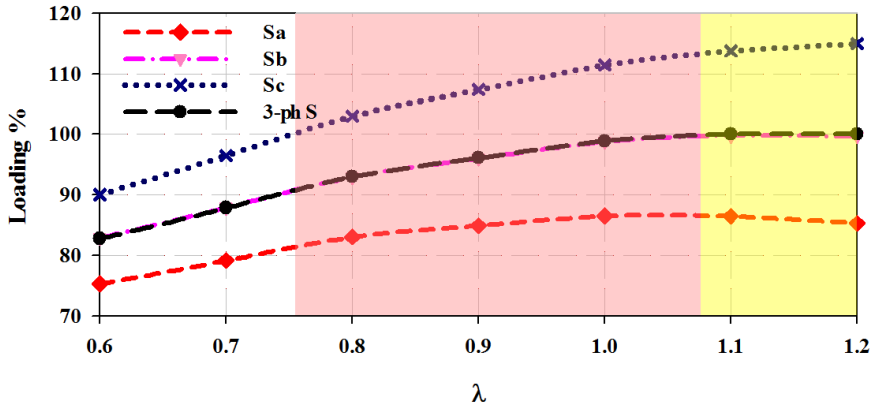


Figure 3.14: Loading percentage of AC-DG3 phases at different loading factors.

introduced such that

$$S_{ac,L,i} = \lambda S_{ac,L,base,i} \tag{3.53}$$

where $S_{ac,L,i}$ and $S_{ac,L,base,i}$ are the actual and base apparent powers of ac load $i$.

As demonstrated in Figure 3.14, as the loading factor increases above 0.76, the apparent power of phase $\{c\}$, $S^{c}_{ac,G}$, exceeds the phase capacity limit, while the overall DG loading is still below the DG's total three-phase capacity. At a loading factor of 1.08, AC-DG3 reaches its full-load three-phase capacity; however, phase $\{c\}$ is overloaded by 13.28% due to the ac subgrid's unbalanced loading. Moreover, the figure shows that for loading factors beyond 1.08, the droop-controlled DG switches to constant PQ mode to maintain the total DG power at its three-phase capacity limit. In general, exceeding the single-phase capacity of a DG unit has a severe impact on the power electronic converter. Therefore, the operation at high loading factors (e.g., loading factor higher than 0.76 in the case under study) is critical for electronically-interfaced DGs. Further research efforts should be conducted to develop advanced control schemes that accommodate unbalanced loading over the DG phases.

At the system level, injecting reactive power via ICs could replace a portion of the reactive power supplied by the AC DGs, thus relieving the stressed generation units. Figure 3.15 illustrates the percentage loading of phase $\{c\}$ of AC-DG3 for different reactive-power droop gains $\eta_l$ for the installed ICs. It is observed that for $\eta_l = 1.0$, the loading factor $\lambda$ can be increased up to 1.2 without overloading the DG's phase, whereas for $\eta_l = 0.0$ (i.e., no reactive power injection), the subgrid's load cannot be safely increased beyond 0.76, as the DG's phase loading exceeds its limit. In other words, increasing the reactive power droop gains implies more reactive power injection by the ICs, which enhances the system

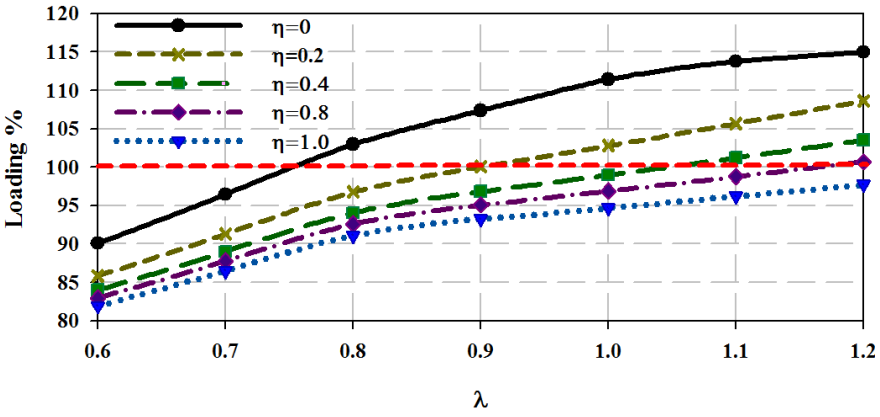


Figure 3.15: Loading percentage of AC-DG3 phases at different loading factors.

loadability. However, proper selection of the IC droop gains is necessary in order to avoid excessive reactive power injection by the ICs that may cause the AC DGs to operate at leading power factors.

## 3.7 Conclusions and Discussion

The sophisticated operational philosophy of islanded hybrid ac/dc microgrids entails a convenient steady-state tool for analyzing such evolving paradigm. Unlike grid-connected systems, islanded hybrid microgrids employ variables, yet linked, ac frequency and dc voltage to attain autonomous power sharing among ac and dc DGs. The lack of reported power flow methods that are capable of analyzing unbalanced hybrid ac/dc microgrids urged the development of a generic analysis tool that incorporates their modern operational aspects.

Accordingly, in this chapter, a novel power flow algorithm has been developed. The algorithm incorporates the models of different system components in phase coordinates, while considering various control schemes under unbalanced conditions, using the globally convergent NTR method. Time-domain simulations have been conducted to validate the accuracy of the introduced algorithm. In addition, the precision and effectiveness of the proposed analysis tool has been further verified by comparing the presented method's results with those of other methods reported in the literature. Furthermore, the robust convergence characteristics of the proposed approach have been confirmed by using different starting points. The algorithm was henceforth employed in different case studies

to highlight technical challenges confronting autonomous operation of hybrid microgrids. The first case demonstrated the effect of IC droop settings on power-sharing accuracy; the results revealed a trade-off between the load-sharing precision between the ac and dc subgrids, and the power-exchange sharing accuracy among ICs. Furthermore, the second case signified the importance of considering the critical effect of unbalanced operation on droop-controlled DGs. Additionally, the relieving impact of ICs' reactive power support on ac DGs was thoroughly discussed via the second case. The main merit of the proposed work, with respect to the approaches reported in the literature, is that it provides a generic platform that can be used for investigations on planning and operation of hybrid droop-controlled microgrids with unbalanced ac networks. Furthermore, it can be applied to more complicated systems comprising multiple interconnected ac and dc subgrids, with high accuracy of results.

# Chapter 4

# A Novel Adaptive Power Routing Scheme to Maximize Loadability of Islanded Hybrid AC/DC Microgrids

## 4.1 Introduction

As concluded in Chapter 2, the unbalanced operation of the ac subgrid in islanded hybrid ac/dc microgrids poses restrictions on loading of the microgrid, which directly affects the microgrid loadability. Taking into consideration the limited energy resources in islanded microgrids, allowing maximum use of the available resources becomes of great interest for microgrid planning and operation. Accordingly, this chapter thoroughly investigates the effect of unbalanced loading on the microgrid loadability and the necessity of load shedding under heavy loading conditions of autonomously-controlled microgrids. Furthermore, it explains the shortfalls of conventional supervisory controller in avoiding load shedding at heavily loaded phases. Thus, a novel adaptive power routing (APR) scheme is proposed to permit power routing among the unbalanced ac subgrid phases. The proposed APR scheme is incorporated into an optimal power flow (OPF) algorithm, which is executed through a supervisory controller with minimal communication requirements. The effectiveness of the proposed approach is verified through multiple case studies.

The remainder of the chapter is organized as follows: Section 4.2 provides a brief description of the imbalance problem in islanded microgrids. The proposed APR strategy is introduced in Section 4.3. Section 4.4 provides detailed steady-state models of the ac and dc subgrids and the ICs. In Section 4.5, the complete formulation of the proposed

APR-based OPF algorithm is presented in detail. Section 4.6 elaborates on the tackled problem and validates the proposed algorithm via several case studies, and Section 4.7 concludes the chapter.

## 4.2 Problem Description

Microgrids can be considered as electric regions with significant generation that could contribute to supplying the local power demand. Among the numerous features that microgrids should acquire, reliability, efficiency and resilience are the most salient. The reliability aspect is realized through sustaining power delivery to the local critical loads under system outages (i.e., disconnection from the utility grid). In balanced three-phase microgrids, the entire local loads could be served if the distributed generation satisfies

$$\sum_{i=1}^{N_{ac,DG}} P_{ac,G,i}^{max} \geq \sum_{j=1}^{N_{ac,L}} P_{ac,L,j} + \sum_{k=1}^{N_{ac,F}} P_{ac,loss,k} \tag{4.1}$$

$$\sum_{i=1}^{N_{ac,DG}} Q_{ac,G,i}^{max} \geq \sum_{j=1}^{N_{ac,L}} Q_{ac,L,j} + \sum_{k=1}^{N_{ac,F}} Q_{ac,loss,k} \tag{4.2}$$

where $P_{ac,G,i}^{max}$ and $Q_{ac,G,i}^{max}$ are the active and reactive power capacity of the $i$th DG, $P_{ac,L,j}$ and $Q_{ac,L,j}$ the active and reactive powers of the $j$th load, $P_{ac,loss,k}$ and $Q_{ac,loss,k}$ active and reactive power losses in the $k$th line, and $N_{ac,DG}$, $N_{ac,L}$, and $N_{ac,F}$ the total number of DGs, loads, and system feeders, respectively. If the aforementioned power adequacy constraints are not met, some of the uncritical loads have to be shed to maintain feeding of the critical ones.

On the other hand, in unbalanced three-phase microgrids, conditions (4.1) and (4.2) are not sufficient to represent the system's power adequacy criteria. In general, unbalanced loading is an intrinsic feature of ac microgrids due to the existence of single-phase loads. Furthermore, the network may comprise both three-phase and single-phase DGs. Although single-phase DGs typically have smaller ratings, their high penetration can result in significant generation capacity imbalance among the microgrid phases. This highly-unbalanced nature of the network imposes more challenges on the steady-state operation of the system in islanded mode of operation. Although the total installed DG capacity could be greater than the total three-phase demand and losses, the generation capacity of one phase may not be sufficient to supply the total demand connected to the same phase. This problem is anticipated to arise in heavily-loaded microgrids that normally import power from the

utility grid in grid-connected mode. In an islanding event, the total local generation could be critically sufficient to supply the total local loads, but insufficient to meet each phase's demand. Considering the structure of ac microgrids, the aforementioned power adequacy criteria can only be generalized if complemented by the single-phase adequacy criterion

$$\sum_{i=1}^{N_{ac,DG}} S_{ac,G,i}^{ph,max} \geq \sum_{j=1}^{N_{ac,L}} S_{ac,L,j}^{x} + \sum_{k=1}^{N_{ac,F}} S_{ac,loss,k}^{x} \qquad \forall\, x \in \{a,b,c\} \tag{4.3}$$

where $S_{ac,G,i}^{ph,max}$ is the phase apparent power capacity of the $i$th DG, $S_{ac,L,j}^{x}$ the phase apparent power demand of the $j$th load, and $S_{ac,loss,k}^{x}$ the phase apparent power loss of the $k$th distribution feeder. It is noteworthy that the apparent power is considered for the single-phase adequacy criterion rather than active or reactive powers. This criterion is used because the active and reactive power capacities of DGs are defined for the three phases combined, whereas the single-phase power limits are defined by the DG phase current/apparent power capabilities.

Moreover, droop controllers are typically adopted in microgrids to realize proportional active and reactive power sharing among DG units. The droop control in ac microgrids is achieved by defining

$$\omega = \omega_{0,i} - m_{p,i} P_{ac,G,i} \tag{4.4}$$

$$\left|V_{ac,i}\right| = V_{ac,0,i} - m_{q,i} Q_{ac,G,i} \tag{4.5}$$

where $\omega$ and $\omega_{0,i}$ are the DG output and no-load angular frequencies, $\left|V_{ac,i}\right|$ and $V_{ac,0,i}$ the DG output and no-load voltages, $m_p$ and $n_q$ the active power and reactive power droop gains, and $P_{ac,G,i}$ and $Q_{ac,G,i}$ the total DG output active and reactive powers, respectively. It is noteworthy that $P_{ac,G,i}$ and $Q_{ac,G,i}$ are the total active and reactive powers over the three phases of the DG unit. Therefore, if one phase of the DG unit is overloaded while the other two phases are not, the total DG power would conventionally be considered within limits. However, unlike conventional machine-based generators, overload capabilities of electronically-interfaced DGs are considerably limited [123]. Hence, a rather insignificant overload on one of the DG phases may result in the unit outage, and eventually microgrid collapse.

Load shedding is typically applied to relieve overloaded power systems to avert blackouts. Thus, shedding loads on overloaded phases could sustain the microgrid operation. Nonetheless, in the process, the customers' service reliability will be compromised. This chapter presents a novel APR scheme that utilizes the connection between the ac and dc subgrids to dynamically maximize the hybrid microgrid loadability under islanded mode of operation. A detailed description of the proposed method is explained in the next section.

## 4.3 Proposed Adaptive Power Routing Scheme

In hybrid ac/dc microgrids, the power flow between the ac and dc subgrids is typically realized through three-phase bidirectional ICs, thereby sharing the total load among all the DGs connected to both subgrids. The autonomous operation at the primary level of multiple ICs is attained by adopting droop controllers described by (4.6)-(4.9) for the $l$th IC [26].

$$\Delta\omega_{pu} = \frac{\omega - 0.5(\omega_{max} + \omega_{min})}{0.5(\omega_{max} - \omega_{min})} \tag{4.6}$$

$$\Delta V_{dc,pu,l} = \frac{V_{dc,l} - 0.5(V_{dc,max} + V_{dc,min})}{0.5(V_{dc,max} - V_{dc,min})} \tag{4.7}$$

$$P_{ac,IC,l} = \gamma_l(\Delta\omega_{pu} - \Delta V_{dc,pu,l}) \tag{4.8}$$

$$Q_{ac,IC,l} = \begin{cases} \eta_l(V_{ac,l,0} - \left|V_{ac,l}\right|) & if\ P_{ac,IC,l} \leq 0 \\ 0 & if\ P_{ac,IC,l} > 0 \end{cases} \tag{4.9}$$

In (4.6)-(4.9), $\Delta V_{dc,pu,l}$ is the per-unit dc voltage deviation, $V_{dc,l}$ the dc voltage at the IC's terminals, $V_{dc,max}$ and $V_{dc,min}$ the maximum and minimum allowed voltages of the dc subgrid, respectively, $\Delta\omega_{pu}$ the per-unit angular frequency deviation of the ac subgrid,$\omega_{max}$ and $\omega_{min}$ the maximum and minimum permissible angular frequencies of the ac subgrid, respectively, $P_{ac,IC,l}$ the three-phase active power transfer between the two subgrids, $Q_{ac,IC,l}$ the three-phase reactive power injected by the IC, $\gamma_l$ and $\eta_l$ the active- and reactive power coefficients, respectively, $V_{ac,l,0}$ the nominal ac subgrid voltage, and $\left|V_{ac,l}\right|$ the ac voltage magnitude at the IC's terminals. However, this control scheme realizes balanced power transfer through the three phases of the ICs, thus restricting the ICs to balanced operation. It is worth mentioning that according to (4.9), ICs can provide reactive power support only if active power is transferred from the dc to ac subgrids, implying that the local loading of the ac subgrid is relatively higher than that of the dc one [23], [26]. However, it could be beneficial to permit reactive power injection to support the ac subgrid even if the active power flows in the opposite direction.

In the proposed APR scheme, independent control of IC phases is considered. Hence, additional functionalities and auxiliary services can be provided through the links between the two subgrids. Many converter topologies and control schemes can be adopted to realize the connection between typical four-wire-ac and dc subgrids. For instance, three-phase four-leg voltage-source converters (VSCs) can provide compact transformer-less connections, while three-phase three-leg VSCs with delta/wye transformer is advantageous in

regard to voltage-level flexibility. Moreover, single-phase topologies can be adopted to flexibly provide interconnections at different locations of the hybrid microgrid, especially if the ac subgrid contains single- and/or two-phase laterals. Different configurations can be adopted in the same hybrid microgrid depending on various economic and technical aspects. It is worth mentioning that the proposed APR scheme is applicable to different system configurations [124]. In this study, three-phase three-leg ICs are assumed to be interfaced with the ac subgrid through delta/wye transformers.

### 4.3.1 Proposed IC Primary Control

At the IC primary control level, droop controls are still adopted to realize decentralized power sharing. However, the active power references of each phase are set independently. Furthermore, to provide reactive power support to the ac subgrid under heavy loading conditions, the reactive power injection to the ac subgrid is always allowed. Eliminating the restrictions on reactive power injection provides an additional degree of freedom to the microgrid supervisory controllers, thus allowing both active and reactive power routing. Reformulating (4.6)-(4.9) and applying the proposed changes, the IC's phase droop characteristics are obtained as

$$P^{x}_{ac,IC,l} = \gamma_l(\omega^{'} - V^{'}_{dc,l} - \varepsilon_p) \qquad \forall\, x \in \{a,b,c\} \tag{4.10}$$

$$Q^{x}_{ac,IC,l} = \eta_l(V_{ac,l,0} - \left|V^{x}_{ac,l}\right|) \qquad \forall\, x \in \{a,b,c\} \tag{4.11}$$

where

$$\omega^{'} = \frac{\omega}{0.5(\omega_{max} - \omega_{min})} \tag{4.12}$$

$$V^{'}_{dc,l} = \frac{V_{dc,l}}{0.5(V_{dc,max} - V_{dc,min})} \tag{4.13}$$

$$\varepsilon_p = \frac{V_{dc,max} + V_{dc,min}}{V_{dc,max} - V_{dc,min}} - \frac{\omega_{max} + \omega_{min}}{\omega_{max} - \omega_{min}} \tag{4.14}$$

Equation (4.11) implies that more reactive power will be injected to the ac subgrid phases with lower voltage magnitudes, thereby partially compensating for voltage (and reactive power) imbalance on the ac side.

### 4.3.2 Supervisory Control and Adaptive Power Routing

A secondary control layer with low communication requirements is introduced to attain more complex operational objectives. The supervisory controller communicates two control

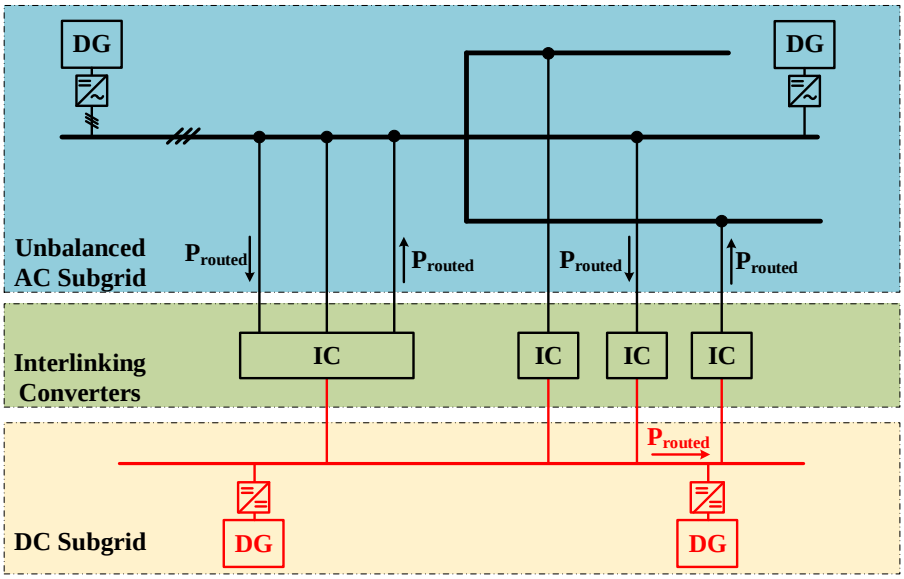


Figure 4.1: Graphical illustration of the proposed APR scheme.

signals $\delta\varepsilon_p^x$ and $\delta\varepsilon_q^x$ to the ICs' droop controllers in order to bias their active and reactive reference powers, respectively. Integrating the secondary signals into (4.10) and (4.11), the droop control equations can be rewritten as

$$P_{ac,IC,l}^x = \gamma_l(\omega^{'} - V_{dc,l}^{'} - \varepsilon_p + \delta\varepsilon_p^x) \qquad \forall\, x \in \{a,b,c\} \tag{4.15}$$

$$Q_{ac,IC,l}^x = \eta_l(V_{ac,l,0} - \left|V_{ac,l}^x\right| + \delta\varepsilon_q^x) \qquad \forall\, x \in \{a,b,c\} \tag{4.16}$$

Since the supervisory controller can bias the active and reactive power references of each phase individually, the power can be routed between the ac subgrid phases, as shown in Figure 4.1. In this case, the dc subgrid does not act only as an autonomous subgrid interfaced with the ac side in a hybrid structure, but also represents a dc energy pool providing an interfacing medium between the ac subgrid phases [125]. It is worth mentioning that the power routing can occur through different legs of three-phase converters, or via single-phase ICs connected at different locations. Furthermore, the routed power is superimposed on the power transferred between the ac and dc subgrids, maintaining the total ac-dc active power exchange at the desired value. The set points of each IC are optimally adjusted by the secondary controller in order to exploit the total available generation to supply the unbalanced ac subgrid loads; the optimization algorithm is discussed thoroughly in Section 4.6.

## 4.4 Hybrid Microgrid Steady-State Modeling

### 4.4.1 AC Microgrid Model

Modeling of unbalanced ac microgrids necessitates the development of single-phase representations for all steady-state mathematical formulations. This applies to the models of DGs, loads, and feeders, as well as the power flow equations.

#### AC DG Model

There are two major categories of DG units that can be integrated into an ac microgrid, namely, dispatchable and non-dispatchable DGs. Dispatchable DGs typically adopt droop controllers to proportionally share the load power at the primary control level, without the need for communication links. Furthermore, these DGs shape the ac subgrid voltage wave-form and collaboratively set the voltage magnitude and frequency, depending on the loading conditions. Since droop-controlled DGs follow the droop control characteristics in (4.4) and (4.5), the two equations can be reformulated to describe the DG generated active and reactive powers as

$$P_{ac,G,i} = \sum_{x\in\{a,b,c\}} P^{x}_{ac,G,i} = \mu_i(\omega_{0,i} - \omega + \delta\omega_{0,i}) \tag{4.17}$$

$$Q_{ac,G,i} = \sum_{x\in\{a,b,c\}} Q^{x}_{ac,G,i} = \eta_i(V_{ac,0,i} - \left|V_{ac,i}\right| + \delta V_{ac,0,i}) \tag{4.18}$$

where $P^{x}_{ac,G,i}$ and $Q^{x}_{ac,G,i}$ are the DG phase-x active and reactive powers, $\delta\omega_{0,i}$ and $\delta V_{ac,0,i}$ bias values that can be set by the supervisory controller, and $\mu_i$ and $\eta_i$ the reciprocals of the active- and reactive power droop gains, respectively. $\mu_i$ and $\eta_i$ are defined as

$$\mu_i = \frac{P^{max}_{ac,G,i}}{\omega_{max} - \omega_{min}} \tag{4.19}$$

$$\eta_i = \frac{Q^{max}_{ac,G,i}}{V_{ac,max} - V_{ac,min}} \tag{4.20}$$

where $V_{ac,max}$ and $V_{ac,min}$ are the maximum and minimum allowed voltage magnitudes for the ac subgrid, respectively.

The droop-controlled DGs are assumed to employ negative-sequence compensators that mitigate voltage unbalances at the DG terminals. Therefore, the three-phase voltages at

the DG bus are strictly balanced even under unbalanced loading. The voltages at the DG bus can then be described as

$$V_{ac,i}^{a} = V_{ac,i}^{b} = V_{ac,i}^{c} \tag{4.21}$$

$$\delta_{i}^{a} = \delta_{i}^{b} + \frac{2}{3}\pi = \delta_{i}^{c} - \frac{2}{3}\pi \tag{4.22}$$

where $V_{ac,i}^{a}$, $V_{ac,i}^{b}$, and $V_{ac,i}^{c}$ are the voltage magnitudes, and $\delta_{i}^{a}$, $\delta_{i}^{b}$, and $\delta_{i}^{c}$ the phase angles for the three phases at the DG bus.

On the other hand, non-dispatchable units inject constant active and reactive powers into the microgrid. However, they incorporate grid-following controllers that are incapable of independently forming the grid voltage. Therefore, they are often modeled as negative constant power loads.

### AC Load Model

The steady-state characteristics of ac loads is primarily dependent on their nature. The load frequency and voltage inherently affect the load behavior. Therefore, a generic static load model incorporating the voltage and frequency dependencies can be given by

$$P_{ac,L,i}^{x} = P_{ac,L,i}^{0,x}\left|V_{ac,i}^{x}\right|^{\alpha,x}(1 + K_{pf,i}^{x}\Delta\omega) \qquad \forall\, x \in \{a,b,c\} \tag{4.23}$$

$$Q_{ac,L,i}^{x} = Q_{ac,L,i}^{0,x}\left|V_{ac,i}^{x}\right|^{\beta,x}(1 + K_{qf,i}^{x}\Delta\omega) \qquad \forall\, x \in \{a,b,c\} \tag{4.24}$$

where $P_{ac,L,i}^{0,x}$ and $Q_{ac,L,i}^{0,x}$ are the nominal values of the load active and reactive powers, respectively, $\alpha$ and $\beta$ are the active and reactive power exponents, $\Delta\omega$ is the frequency deviation from the nominal value, and $K_{pf,i}^{x}$ and $K_{qf,i}^{x}$ are constants that define the load active and reactive power-frequency dependencies, respectively [117]. The values of the power exponents $\alpha$ and $\beta$ along with the two constants $K_{pf,i}^{x}$ and $K_{qf,i}^{x}$ define the types of individual loads in the ac subgrid.

### AC Feeders Model

In contrast with conventional power systems, the steady-state frequency of an islanded ac subgrid is load-dependent. Thus, the variation of the ac subgrid's line impedances, as the system frequency changes, should be taken into account. Applying Kron's reduction to

Carson's model of the three-phase four-wire grounded ac system, the following reduced 33 admittance matrix can be obtained.

$$Y_{ij}^{abc}(\omega) = \begin{bmatrix} Z_{ij}^{aa} & Z_{ij}^{ab} & Z_{ij}^{ac} \\ Z_{ij}^{ba} & Z_{ij}^{bb} & Z_{ij}^{bc} \\ Z_{ij}^{ca} & Z_{ij}^{cb} & Z_{ij}^{cc} \end{bmatrix}^{-1} \tag{4.25}$$

It is worth noting that the frequency-dependent admittance matrix implicitly include the neutral line admittance.

**AC Power Flow Equations**

For an unbalanced ac subgrid comprised of $N_{ac}$ set of buses, the phase active and reactive powers injected at any phase of an arbitrarily selected bus i can be given by (4.26) and (4.27), where $Y_{ij}^{xy}$ and $\theta_{ij}^{xy}$ are the Y-bus admittance matrix element's magnitude and angle, which vary with the ac subgrid's total loading.

$$\begin{aligned} P_{ac,i}^{x} = \sum_{j \in N_{ac} \setminus i} \sum_{y \in \{a,b,c\}} & \left|V_{ac,i}^{x}\right| \left|Y_{ij}^{xy}\right| \left|V_{ac,i}^{y}\right| \cos(\theta_{ij}^{xy} + \delta_{i}^{y} - \delta_{i}^{x}) \\ & - \left|V_{ac,i}^{x}\right| \left|Y_{ij}^{xy}\right| \left|V_{ac,j}^{y}\right| \cos(\theta_{ij}^{xy} + \delta_{j}^{y} - \delta_{i}^{x}) \end{aligned} \tag{4.26}$$

$$\begin{aligned} Q_{ac,i}^{x} = \sum_{j \in N_{ac} \setminus i} \sum_{y \in \{a,b,c\}} & \left|V_{ac,i}^{x}\right| \left|Y_{ij}^{xy}\right| \left|V_{ac,j}^{y}\right| \sin(\theta_{ij}^{xy} + \delta_{j}^{y} - \delta_{i}^{x}) \\ & - \left|V_{ac,i}^{x}\right| \left|Y_{ij}^{xy}\right| \left|V_{ac,i}^{y}\right| \sin(\theta_{ij}^{xy} + \delta_{i}^{y} - \delta_{i}^{x}) \end{aligned} \tag{4.27}$$

### 4.4.2 DC Microgrid Model

Dc microgrids may implement different configurations (e.g., unipolar or bipolar dc), various interface topologies (e.g., unidirectional and bidirectional power-electronic interface), and numerous control techniques (e.g., droop control, power control, or dc bus signaling) [18], [19], [126]. In this work, a unipolar dc microgrid with droop-controlled power-electronics-interfaced DGs is adopted. The dc subgrid may also include non-dispatchable power-controlled DGs represented as negative constant power loads.

### DC DG Model

Droop controlled generation units in dc microgrids can adopt either I-V or P-V droop controls in order to realize proportional power sharing among the connected DGs, as described by

$$P_{dc,G,i} = \vartheta_{P,i}(V_{dc,0,i} - V_{dc,i} + \delta V_{dc,0,i}) \tag{4.28}$$

$$I_{dc,G,i} = \vartheta_{I,i}(V_{dc,0,i} - V_{dc,i} + \delta V_{dc,0,i}) \tag{4.29}$$

where $P_{dc,G,i}$ and $I_{dc,G,i}$ are the DG output power and current, $V_{dc,0,i}$ and $V_{dc,i}$ the DG no-load and output voltages, respectively, $\delta V_{dc,0,i}$ a bias value adjusted by the secondary controller, and $\vartheta_{P,i}$ and $\vartheta_{I,i}$ the reciprocals of the droop gains for the DG output power and current, respectively. In hybrid ac/dc microgrids, P-V droops are commonly used to allow power sharing among the DGs integrated into both subgrids, and therefore (4.28) will be considered for this model. To attain proportional power sharing among the DGs in the dc subgrid, the droop gains are calculated as:

$$\vartheta_{P,i} = \frac{P_{dc,G,i}^{max}}{V_{dc,max} - V_{dc,min}} \tag{4.30}$$

where $P_{dc,G,i}^{max}$ is the maximum output power of the DG unit.

### DC Load Model

In order to account for all types of dc loads that can exist in dc distribution systems (e.g., constant power, constant-current, and constant-resistance loads), a generic load model is considered, which is described by

$$P_{dc,L,i} = P_{dc,L,i}^{0} + V_{dc,i} I_{dc,L,i}^{0} \tag{4.31}$$

where $P_{dc,L,i}$ and $I_{dc,L,i}^{0}$ are the load constant power and constant-current portions, respectively. It can be seen from (4.31) that the load model can represent any combination of constant power and constant-current loads connected to the same dc bus. Furthermore, constant-resistance loads can directly be integrated into the system conductance matrix.

### DC Feeders Model

Although dc feeders inherently contain inductances, these inductances may only affect the dynamic behavior of the network, whereas under steady-state conditions, the line is

represented only by its resistance [41], [127]. Therefore, the line conductance $g_{ij}$ between two arbitrary dc buses $i$ and $j$ is given as

$$g_{ij} = \frac{1}{r_{ij}} \tag{4.32}$$

where $r_{ij}$ is the line resistance.

**DC Power Flow Equations**

For a dc subgrid comprised of $N_{dc}$ buses, the power injected at any arbitrary bus $i$ can be obtained by

$$P_{dc,i} = V_{dc,i} \sum_{j \in N_{dc}} V_{dc,j} G_{ij} \tag{4.33}$$

where $V_{dc,i}$ is the dc bus $i$ voltage, and $G_{ij}$ is the conductance matrix element.

### 4.4.3 Interlinking Converter Model

The proposed APR strategy suggests that each phase of three-phase ICs be controlled independently; thus, the IC is modeled as three single-phase converters. Further, the mathematical model given by (4.12)-(4.16) is valid under all conditions, including when single-phase ICs are used. For improved modeling accuracy, the power losses for each IC phase is calculated as

$$P^x_{IC,loss,l} = C_0 + C_1 I^x_{ac,IC,l} + C_2 {I^x_{ac,IC,l}}^2 \qquad \forall\, x \in \{a, b, c\} \tag{4.34}$$

where $P^x_{IC,loss,l}$ is the converter phase power loss, $I^x_{ac,IC,l}$ the phase injected current at the converter ac-side, and $C_0$, $C_1$ and $C_2$ the quadratic function coefficients. It is worth mentioning that the power given by (4.15) is assumed at the IC's ac side; thus, the power losses are accounted for on the dc side.

## 4.5 Proposed Optimal Power Flow with Adaptive Power Routing

The highest priority in the operation of microgrids is to supply electrical power to the customers with minimal interruptions. Other lower-priority objectives (e.g., minimal operational cost) can be satisfied after meeting the customers' service continuity. Thus, this

chapter focuses on load shedding minimization, which is formulated as an OPF problem solved using an interior point method [53].

### 4.5.1 Objective Function

In grid-connected mode of operation, microgrids can avoid load shedding by importing power from the external utility grid. However, load shedding is essential in islanded microgrids under inadequate generation. Furthermore, load prioritization should be taken into consideration in order to maximize the microgrid's welfare. In [128], prioritization factors were introduced to classify the loads based on their respective criticalities and power ratings. The optimal power flow problem can then be mathematically formulated as

$$\min \sum_{i=1}^{N_{ac,L}} U_{L,i} \times W_{L,i} \tag{4.35}$$

where $U_{L,i}$ is a control variable that determines the state of the load $i$, with 1 meaning the load is shed, $W_{L,i}$ the priority factor for the load $i$, taking higher values as the load priority increases, and $N_{ac,L}$ the total number of loads. In this study, it is assumed that the loads' priority factors are dependent only on their respective powers implying that smaller loads are shed first. However, the loads' respective criticalities could also be considered if necessary.

### 4.5.2 Control Variables

The supervisory controller optimally sets the control parameters of all DGs installed in both ac and dc subgrids. Only set points $\delta\omega_0$, $\delta V_{ac}$, and $\delta V_{dc}$ are considered controllable in this work, while droop gains are kept constant. Furthermore, the two bias signals $\delta\varepsilon_p^x$ and $\delta\varepsilon_q^x$ for each IC phase are adjusted to attain the desired power routing and reactive power support, thereby minimizing load shedding on heavily-loaded phases.

### 4.5.3 Problem Constraints

The problem must satisfy the set of equations (4.12)-(4.34), which describe the IC, DG, and load models in addition to the power flow equations as equality constraints. Moreover,

the DG capacities for both ac and dc subgrids as well as the ac and dc lines' capacities must be accounted for by inequality constraints represented by

$$\sum_{x\in\{a,b,c\}} P^{x}_{ac,G,i} \leq P^{max}_{ac,G,i} \tag{4.36}$$

$$S^{x}_{ac,G,i} \leq S^{ph,max}_{ac,G,i} \qquad \forall\, x \in \{a,b,c\} \tag{4.37}$$

$$Q^{x}_{ac,G,i} \leq \sqrt{\left(S^{ph,max}_{ac,G,i}\right)^2 - \left(P^{x}_{ac,G,i}\right)^2} \qquad \forall\, x \in \{a,b,c\} \tag{4.38}$$

$$P_{dc,G,i} \leq P^{max}_{dc,G,i} \tag{4.39}$$

$$I^{x}_{ac,k} \leq I^{ph-max}_{ac,k} \tag{4.40}$$

$$I_{dc,k} \leq I^{max}_{dc,k} \tag{4.41}$$

where $S^{ph,max}_{ac,G,i}$ is the phase apparent power capacity of the DG's interfacing converter, $I^{x}_{ac,k}$ and $I^{ph-max}_{ac,k}$ the current and line capacities of the $k$th ac feeder, and $I_{dc,k}$ and $I^{max}_{dc,k}$ the current and line capacities of the $k$th dc feeder. It is noteworthy that for ac units, the total DG active power is limited by the energy source capacity, whereas the phase capacity $S^{ph,max}_{ac,G,i}$ is limited by the current rating of the DG's interfacing converter. Thus, the two constraints (4.36) and (4.37) are considered separately. To consider the IC power capacity limits, the active- and reactive power limits for any phase of converter $l$ are set according to

$$P^{x}_{ac,IC,l} \leq S^{ph-max}_{ac,IC,i} \qquad \forall\, x \in \{a,b,c\} \tag{4.42}$$

$$Q^{x}_{ac,IC,l} \leq \sqrt{\left(S^{ph-max}_{ac,IC,i}\right)^2 - \left(P^{x}_{ac,IC,i}\right)^2} \qquad \forall\, x \in \{a,b,c\} \tag{4.43}$$

where $S^{ph-max}_{ac,IC,i}$ is the IC's phase apparent power limit.

Moreover, since the set points of DGs will be controlled by the supervisory controller, the bus voltages and the ac subgrid frequency could largely deviate from their nominal values. Therefore, to ensure proper microgrid operation, both ac and dc bus voltages in addition to the ac subgrid frequency are constrained within the standard limits as follows

$$V_{ac,min} \leq V^{x}_{ac,i} \leq V_{ac,max} \qquad \forall\, x \in \{a,b,c\} \tag{4.44}$$

$$\omega_{min} \leq \omega \leq \omega_{max} \tag{4.45}$$

$$V_{dc,min} \leq V_{dc,i} \leq V_{dc,max} \tag{4.46}$$

Table 4.1: AC DG units' locations, ratings, and droop settings (test microgrid#4.1)

| DG# | Bus# | $\mu$ (pu) | $\eta$ (pu) | $\omega_0$ (pu) | $V_{ac,0}$ (pu) | $P_{ac,G}^{max}$ (pu) | $S_{ac,G}^{max}$ (pu) |
|---|---|---|---|---|---|---|---|
| 1 | 13 | 8.0 | 1.0 | 1.0083 | 1.05 | 0.16 | 0.185 |
| 2 | 19 | 4.0 | 0.5 | 1.0083 | 1.05 | 0.08 | 0.095 |
| 3 | 25 | 8.0 | 1.0 | 1.0083 | 1.05 | 0.16 | 0.185 |

## 4.6 Case Studies

In order to demonstrate the effectiveness and generality of the power management scheme in increasing the overall system loadability, the proposed approach has been applied on two test systems, incorporating the unbalanced 25-bus and the IEEE 123 node test feeder ac systems along with two dc systems. The 25-bus system is employed as a small test system to investigate the following points: loadability restrictions in heavily-loaded ac microgrids, as illustrated in Section 4.2, limitations of conventional droop settings in resolving the loadability problem, and the effectiveness of the installed ICs in increasing the system overall loadability by implementing the proposed APR scheme and reactive power support. On the other hand, the IEEE 123 bus system is simulated to shed light on the effects of the IC base loading on the proposed scheme.

### 4.6.1 Hybrid 25-Bus AC/7-Bus DC Microgrid

To introduce an unbalanced hybrid ac/dc microgrid, the 25-bus unbalanced ac test system [129] is interlinked with a 7-bus dc test system [130] through two ICs, as shown in Figure 4.2. Three ac DG units have been placed at different locations of the ac subgrid, while four dc DG units have been connected on the dc side. Tables 4.1 and 4.2 give the DG locations, ratings, and droop settings for the ac and dc subgrids, respectively. The base ac loads can be found in [39], while three constant power dc loads rated at 0.21, 0.14, and 0.16 p.u. are connected at buses 1, 4, and 6 of the dc subgrid, respectively. The two ICs are assumed identical with 0.2 p.u. power rating, and the active power coefficients for both converters, $\gamma_1$ and $\gamma_2$, are set to 10.

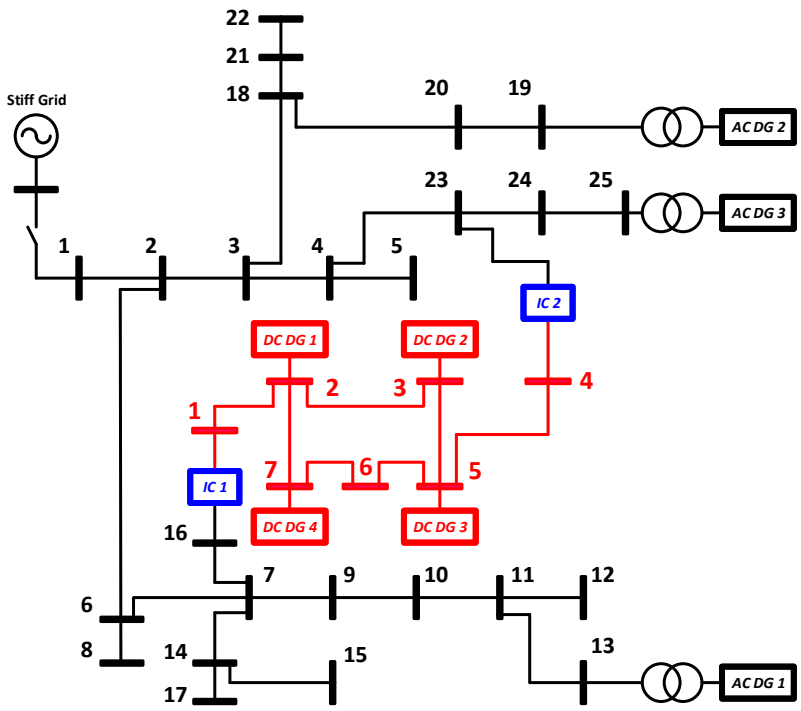


Figure 4.2: Test microgrid#4.1.

Table 4.2: DC DG units' locations, ratings, and droop settings (test microgrid#4.1)

| DG# | Bus# | $\vartheta_P$ (pu) | $V_{dc,0}$ (pu) | $P_{dc,G}^{max}$ (pu) |
|---|---|---|---|---|
| 1 | 2 | 1.25 | 1.05 | 0.125 |
| 2 | 3 | 1.25 | 1.05 | 0.125 |
| 3 | 5 | 1.25 | 1.05 | 0.125 |
| 4 | 7 | 1.25 | 1.05 | 0.125 |

**Case 1: Heavily-Loaded Microgrid with Autonomous Control**

This case study highlights the problem arisen due to unbalanced operation of ac subgrids in islanded hybrid microgrids under heavy loading conditions. The loads of the ac subgrid are controlled by defining

$$S_{ac,L,i} = \lambda S_{ac,L,base,i} \tag{4.47}$$

where $S_{ac,L,i}$ and $S_{ac,L,base,i}$ are the actual and base complex powers of ac load $i$, and $\lambda$ is the loading factor. The loading factor $\lambda$ is changed from 0.7 to 1.17 to examine the unbalanced microgrid loading effect on the DG phase loading. The system is autonomously operated as proposed by the authors in [26]. To highlight the technical problems associated with the autonomous operation, the DG apparent power limits defined by (4.37) are ignored, while the DGs' three-phase active power limits in (4.36) are considered. Therefore, the DGs can operate beyond their phase capacities for simulation purposes. The percentage loadings of some microgrid components (i.e., AC DG#1, ICs, ac subgrid, and dc subgrid), defined by (4.48), are plotted versus $\lambda$ to examine the autonomous microgrid control under unbalanced conditions.

$$Loading\ (\%) = \begin{cases} \dfrac{S^{x}_{ac,G/IC,i}}{S^{ph,max}_{ac,G/IC,i}} & \cdots (1-ph) \\ \dfrac{\sum_{x\in\{a,b,c\}} S^{x}_{ac,G/IC,i}}{3\ S^{ph,max}_{ac,G/IC,i}} & \cdots (3-ph) \\ \dfrac{\sum_{i=1}^{N_{DG}} P_{DG}}{\sum_{i=1}^{N_{DG}} P^{max}_{DG}} & \cdots (subgrid) \end{cases} \tag{4.48}$$

where $S^{x}_{ac,G/IC,i}$ is the phase apparent power of the AC DG or the IC, $S^{ph,max}_{ac,G/IC,i}$ the phase apparent power capacity of the AC DG or the IC, $P_{DG}$ the total active power output of the DG (ac or dc), and $P^{max}_{DG}$ the active power capacity of the DG (ac or dc). Table 4.3 summarizes the control variables used in each case study. Note that no control variables are introduced in this case study, as the microgrid is autonomously operated.

Table 4.3: Summary of control variables in different case studies (test microgrid#4.1)

| Case# | AC DGs | | DC DGs | ICs | | Loads |
|---|---|---|---|---|---|---|
| | $\delta\omega_0$ | $V_{ac,0}$ | $V_{ac,0}$ | $\varepsilon_p^x$ | $\varepsilon_p^x$ | $U_L$ |
| 1 | | | | | | |
| 2 | ✓ | ✓ | ✓ | | | ✓ |
| 3 | ✓ | ✓ | ✓ | ✓ | | ✓ |
| 4 | ✓ | ✓ | ✓ | ✓ | ✓ | ✓ |

As demonstrated in Figure 4.3a, the total three-phase apparent power of AC DG#1 reaches the DG capacity as $\lambda$ approaches 1.04. Nevertheless, as $\lambda$ increases beyond 0.79, phase $\{c\}$ exceeds the phase capacity, thereby constraining the DG's operation beyond this point. Furthermore, Figure 4.3b shows the percentage active power loadings of the ac and dc subgrids governed by the droop-controlled ICs as the ac load changes. As illustrated in the figure, although the installed energy sources can provide active power until the loading factor reaches 1.17, the DGs are restricted by the abovementioned lower limits.

Moreover, as shown in Figure 4.3c, as the ac load increases, the active powers exchanged through ICs decrease, thus allowing for power routing through different IC phases. Further, the ICs transfer unmatched powers due to different bus voltages at the dc side. Figure 4.3d depicts phase loading of the ac DGs and the ICs at $\lambda = 1.15$. It is noteworthy that ac DGs are loaded differently as a result of the unequal reactive power sharing. Furthermore, load shedding on overloaded DG phases becomes a necessity. The aforementioned shortcomings of autonomous control entail a secondary controller to supervise and optimize the microgrid operation.

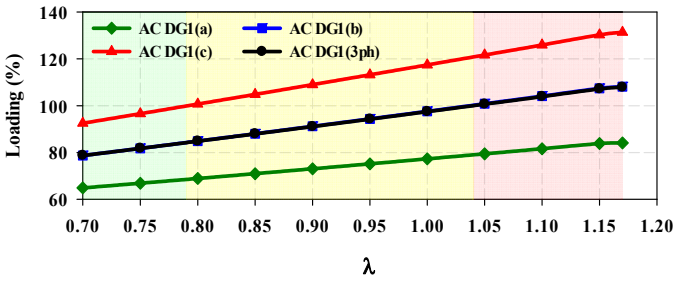


(a) Apparent power loading of AC DG1

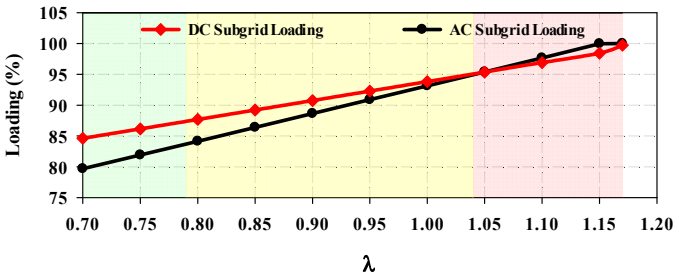


(b) Active power loading of ac and dc subgrids

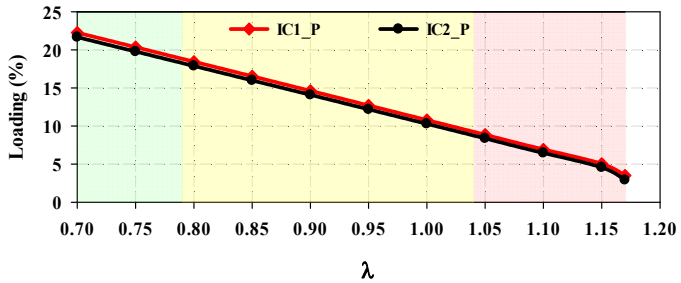


(c) Active power loading of ICs

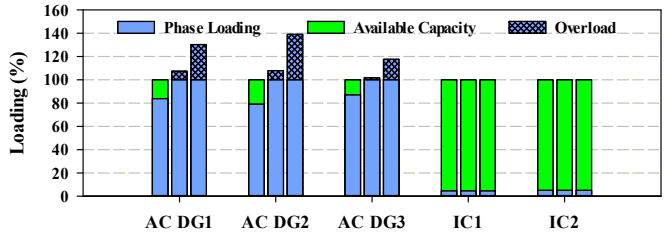


(d) Apparent power loading of DGs and ICs at $\lambda = 1.15$

Figure 4.3: Results of case 1.

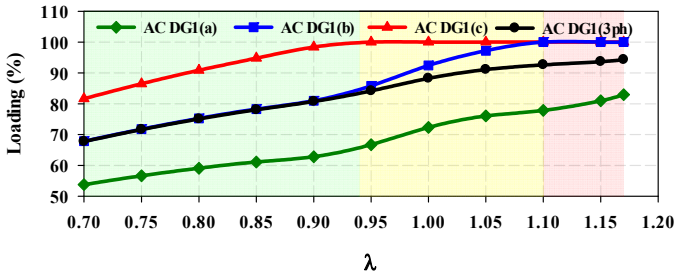


(a) Apparent power loading of AC DG1

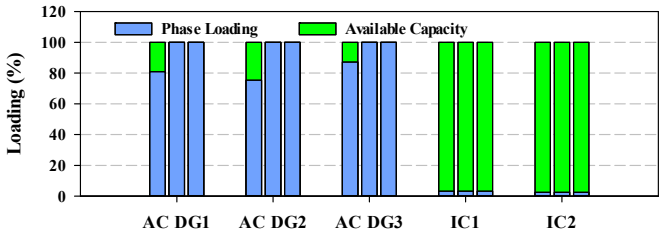


(b) Apparent power loading of DGs and ICs at $\lambda = 1.15$

Figure 4.4: Results of case 2.

### Case 2: Conventional Optimal DG Droop Settings

In this case study, the conventional supervisory control approach that optimizes DG droop settings is utilized to minimize load shedding. The ICs are autonomously controlled while the secondary controller is capable of shedding loads to protect DGs from phase overloading. Figure 4.4a shows that optimizing the DG droop settings could extend the microgrid loadability range to $\lambda = 0.94$. However, any further increase in the ac load cannot be fully accommodated since phase $\{c\}$ reaches the capacity limit. Furthermore, as the load factor exceeds 1.1, the secondary controller commences shedding phase b loads. Figure 4.4b shows the DG and IC percentage phase loadings at $\lambda = 1.15$. Due to the ac subgrid imbalance, DG phases $\{b\}$ and $\{c\}$ operate at their limits, whereas phase $\{a\}$ is underloaded. The results imply that loads are shed from heavily loaded phases despite the unused DG capacity on the lightly loaded ones. The shed ac loads are found to be 9% of the total ac demand. Therefore, power routing among ac subgrid phases would enhance the generation capacity utilization.

**Case 3: Adaptive Active Power Routing**

The proposed APR algorithm is employed in this case to permit active power exchange among the ac subgrid phases. Figure 4.5a demonstrates that APR tends to reduce the DG phase imbalance, thus avoiding load shedding up until $\lambda$ reaches 1.075. The APR algorithm could be better understood by referring to Figure 4.5b, which demonstrates the change of IC1 phase powers over the range of load variation. The figure shows that more power is routed between the lightly and heavily loaded phases $\{a\}$ and $\{c\}$ as the load increases, while slight change of phase $\{b\}$ power is observed. It is worth mentioning that in order to resolve the unequal IC power sharing problem, the optimizer constrains the total powers of the two ICs to be identical. Thus, the total IC 1 three-phase power is constant and equal to the total power through IC 2.

In contrast with the previous case considering the microgrid operation at $\lambda = 1.15$, the DG capacities are better exploited as illustrated in Figure 4.5c. Consequently, load shedding is reduced to 3%. Nevertheless, load shedding can further be diminished by allowing reactive power injection through ICs. Furthermore, operating the ac DGs at their limits might critically jeopardize the system stability. Hence, IC reactive power support will play a vital role in relieving the generation units.

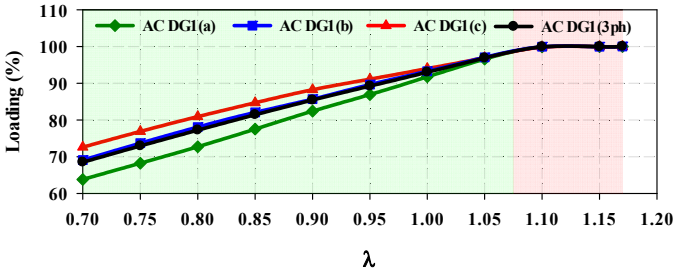


(a) Apparent power loading of AC DG1

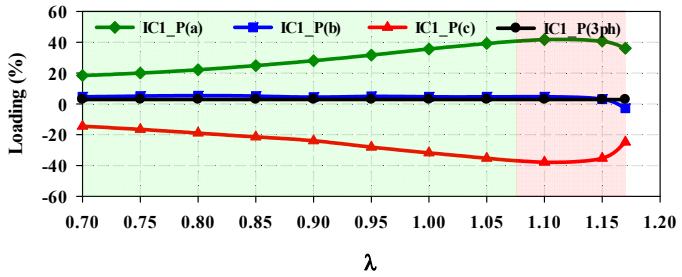


(b) Active power loading of IC1

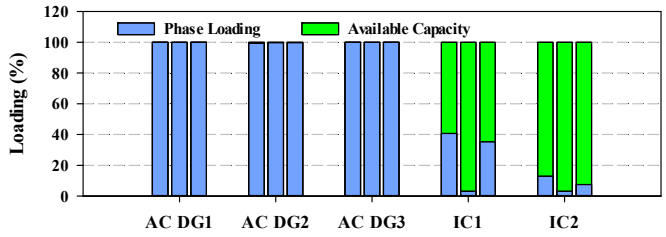


(c) Apparent power loading of DGs and ICs at $\lambda = 1.15$

Figure 4.5: Results of case 3.

**Case 4: Adaptive Power Routing with Reactive Power Injection**

This case sheds light on the significance of employing the unutilized IC capacities for reactive power support irrespective of the active power direction. Furthermore, in order to maximize the system flexibility, the reactive power of each IC phase is controlled independently. It can be observed in Figure 4.6a that the proposed algorithm renders the DG phases more balanced. Moreover, reactive power support mitigates the high DG loading, thereby granting higher loadability levels. Nonetheless, since the IC phases carry both active and reactive powers, higher IC apparent powers along with increased converter losses are anticipated, as demonstrated in Figure 4.6b. However, the relieved DGs, as shown in Figure 4.6c, could expand their active power contribution, thus entirely averting load shedding at $\lambda = 1.15$.

Figure 4.7 compares the percentage active power loading of the dc and ac subgrids for the three supervisory controllers deemed in the presented case studies. It is noticeable that all controllers force the DC DGs to generate their maximum powers, subsequently relieving the ac subgrid to minimize load shedding. The proposed APR-based controller with reactive power support has proved efficient to supply the linearly increasing load up until the DGs hit their limits. On the other hand, the other MGCCs fail to avoid shedding loads, although the total load is smaller than the system capacity. Disabling the IC reactive power support omits load shedding for $\lambda$ below 1.075 compared to 0.94 for the droop-setting-based control. It is noteworthy that, despite the differences, all types of supervisory control can maintain safe microgrid operation for loading levels higher than that of autonomous control, which is restricted to 0.74.

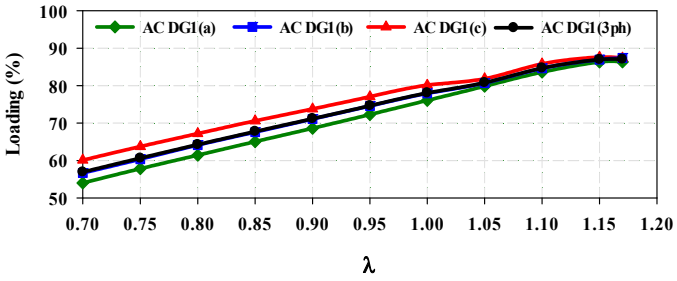


(a) Apparent power loading of AC DG1

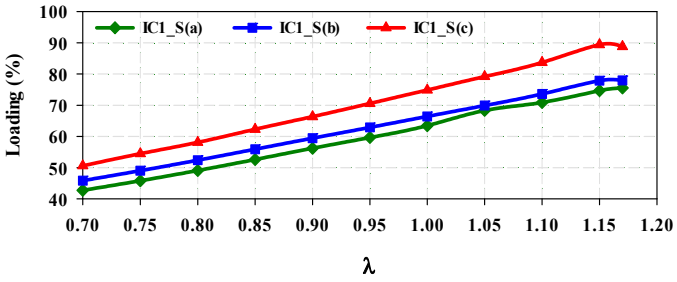


(b) Apparent power loading of IC1

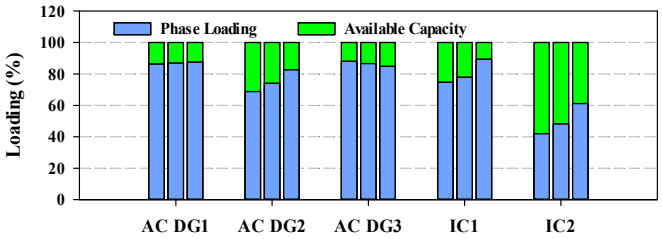


(c) Apparent power loading of DGs and ICs at $\lambda = 1.15$

Figure 4.6: Results of case 4.

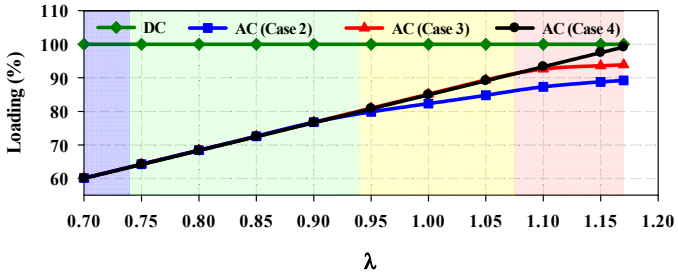


Figure 4.7: Loading of ac and dc subgrids for the different cases.

### 4.6.2 Hybrid IEEE 123-Node AC Test Feeder/22-Bus DC Microgrid

In the proposed APR scheme, the unused IC capacities play a vital role in determining the maximum amount of powers that can be routed among the ac subgrid's phases. The available unutilized IC capacities predominantly depend on the base power transferred through the ICs to supply the dc critical loads. Since the base power transfer changes with the generation and loading conditions of the subgrids, it becomes essential to take its effect into account when considering the application of the proposed scheme in practical systems with varying load and generation profiles. For example, when the two subgrids are heavily loaded, yet almost self-sufficient, the majority of the ICs' capacities are unoccupied, and therefore they can be fully employed in the APR scheme to avoid load shedding. On the other hand, under generation deficiency of either subgrid, the ICs transfer more base pow-er to supply the overloaded subgrid. Consequently, only the remaining IC capacities can be employed in routing the power among the ac subgrid's phases, which might restrict the system operation. This case study investigates the impact of the load and generation conditions on the proposed scheme, where a self-sufficient dc subgrid is first introduced, and then the dc generation is gradually reduced, which entails higher IC loading.

In this case study, the IEEE 123 node test feeder system [40] has been coupled to the 22-bus dc microgrid in [131] through two three-phase ICs to form a hybrid ac/dc microgrid, as shown in Figure 4.8. Three droop-controlled AC DGs have been connected to ac buses 149, 54, and 300, respectively. The AC DGs have active power/reactive power ratings of 0.35/0.1, 0.35/0.1, and 0.2/0.06 p.u., respectively. Furthermore, four droop-controlled DC DGs, rated at 0.1 p.u. each, are connected to dc buses 4, 8, 15, and 16, respectively. The dc load ratings and connections are defined in Table 4.4. The two ICs are rated at 0.21 p.u. each, which come to a total capacity slightly larger than the total dc load to be able to supply the dc loads in case of total loss of the dc generation. It is noteworthy that the dc subgrid is almost self-sufficient and the ac subgrid should theoretically be able to supply loads up to $\lambda$ equal to 1.24 under this condition. The DC DGs will then be sequentially disconnected in order to introduce different generation deficiency levels in the dc subgrid. The conventional and the proposed supervisory control schemes discussed in case studies 2 and 4 have been adopted to optimize the microgrid operation for each level of insufficiency. Note that disconnecting DC DGs reflects on the total microgrid capacity, which inherently means that the maximum possible ac load factor $\lambda$ becomes smaller as the deficiency level increases.

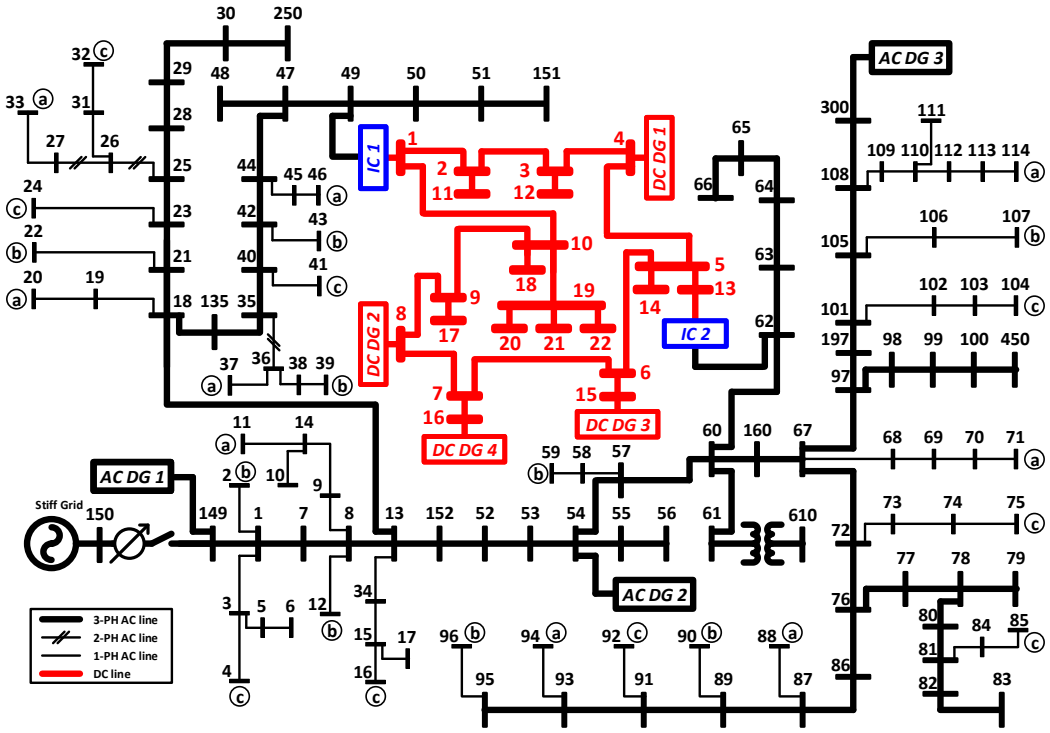


Figure 4.8: Test microgrid#4.2.

Table 4.4: DC loads of the 22-bus dc subgrid in test microgrid#4.2

| DC Bus# | 11 | 12 | 14 | 17 | 18 | 20 | 21 | 22 |
|---|---|---|---|---|---|---|---|---|
| Load Rating (pu) | 0.06 | 0.07 | 0.05 | 0.07 | 0.05 | 0.03 | 0.03 | 0.04 |

Table 4.5 shows the percentage loading levels of different ac microgrid components, as well as the percentage load shedding for each controller. The table also shows the loading factor $\lambda$ used for each case. The results reveal that the load shedding on heavily loaded phases is inevitable under the conventional supervisory control scheme for all deficiency levels, since the DGs' phases reach their limits, as expected. It can also be noticed that the base loading of the ICs gradually increase as the dc generation deficiency increases.

However, with the implementation of the proposed controller, the ac loads are diverted from the DGs' heavily loaded phases to the lightly loaded one, as long as the unemployed IC capacities are capable of providing power routing paths among the ac phases. It is noteworthy that the reduced system capacity resulting from disconnecting DC DGs entails reduced overall ac loading (i.e., $\lambda < 1.24$), which consequently decreases the total ac active and reactive power demands, and requires less capacity from the ICs for active power routing and reactive power support. This fact explains why the proposed APR-based supervisory controller succeeds in eliminating load shedding even with increased base power transfer through the ICs. Nevertheless, it is important to observe that the extreme case of total loss of all the DC DGs requires almost full occupancy of the IC capacities to supply the critical dc loads, thereby strictly limiting the available IC capacity for power routing.

However, the proposed scheme utilizes the remaining IC capacities to minimize, yet not to totally avoid, load shedding within the IC limits. In other words, the proposed APR scheme is effective even when the ICs transfer considerable base power, unless the ICs are fully loaded under extreme conditions (i.e., maximum dc load and zero dc generation). The results verify the generality and effectiveness of the proposed supervisory controller in maximizing the hybrid microgrid's loadability.

Table 4.5: Results of test microgrid#4.2

| DC generation deficiency (pu) | | | 0.0 ($\lambda = 1.24$) | | 0.1 ($\lambda = 1.10$) | | 0.2 ($\lambda = 0.95$) | | 0.3 ($\lambda = 0.81$) | | 0.4 ($\lambda = 0.67$) | |
|---|---|---|---|---|---|---|---|---|---|---|---|---|
| Supervisory controller | | | Conv. | Prop. | Conv. | Prop. | Conv. | Prop. | Conv. | Prop. | Conv. | Prop. |
| AC DG#1 | Load (%) | a | 100.0 | 97.0 | 100.0 | 96.8 | 100.0 | 95.7 | 100.0 | 95.6 | 100.0 | 100.0 |
| | | b | 85.0 | 95.2 | 87.9 | 95.6 | 89.6 | 95.6 | 91.7 | 95.6 | 95.3 | 96.2 |
| | | c | 100.0 | 96.6 | 100.0 | 96.4 | 98.8 | 95.4 | 98.4 | 95.4 | 99.2 | 98.4 |
| AC DG#2 | Load (%) | a | 100.0 | 96.0 | 100.0 | 96.2 | 100.0 | 95.6 | 100.0 | 96.0 | 100.0 | 100.0 |
| | | b | 72.4 | 96.6 | 72.4 | 96.3 | 72.7 | 95.6 | 74.6 | 94.9 | 75.9 | 81.3 |
| | | c | 98.7 | 96.2 | 96.6 | 96.2 | 94.6 | 95.6 | 93.9 | 95.9 | 93.0 | 97.1 |
| AC DG#3 | Load (%) | a | 100.0 | 95.7 | 100.0 | 94.9 | 100.0 | 92.9 | 100.0 | 92.6 | 100.0 | 100.0 |
| | | b | 90.7 | 93.4 | 91.2 | 93.3 | 89.5 | 91.8 | 89.5 | 92.4 | 88.3 | 90.4 |
| | | c | 100.0 | 94.8 | 99.5 | 94.1 | 96.8 | 92.2 | 96.3 | 92.3 | 94.4 | 97.3 |
| IC#1 | Load (%) | a | 1.4 | 97.4 | 28.9 | 81.7 | 56.5 | 77.3 | 73.7 | 78.7 | 96.1 | 100.0 |
| | | b | 1.4 | 61.1 | 28.9 | 69.6 | 56.5 | 89.3 | 73.7 | 99.9 | 96.1 | 100.0 |
| | | c | 1.4 | 61.5 | 28.9 | 62.8 | 56.5 | 75.7 | 73.7 | 86.7 | 96.1 | 100.0 |
| IC#2 | Load (%) | a | 1.0 | 97.4 | 19.1 | 81.3 | 43.7 | 74.4 | 69.2 | 73.5 | 94.5 | 100.0 |
| | | b | 1.0 | 75.9 | 19.1 | 86.2 | 43.7 | 99.6 | 69.2 | 99.2 | 94.5 | 100.0 |
| | | c | 1.0 | 62.1 | 19.1 | 63.3 | 43.7 | 74.2 | 69.2 | 86.5 | 94.5 | 100.0 |
| Load Shedding (%) | | | 7.7 | 0.0 | 7.3 | 0.0 | 6.7 | 0.0 | 5.9 | 0.0 | 5.0 | 3.1 |

## 4.7 Conclusions and Discussion

The unbalanced nature of hybrid ac/dc microgrids restricts autonomous system operation under islanded mode. A higher layer of control is typically provided to coordinate the DGs' operation. Under heavy loading conditions, conventional supervisory controllers fail to adequately supply loads on heavily loaded phases even if the three-phase generation sufficiency criteria are satisfied. This chapter introduced a supervisory controller, implementing a novel adaptive power routing (APR) technique that utilizes ICs to enable power routing among the ac subgrid's phases. Furthermore, the work proposed unrestricting IC reactive power support to relieve the ac subgrid, thus extending the system loadability. Various case studies were conducted to address the drawbacks of autonomous control, to demonstrate the performance of the proposed APR-based controller, and to compare its effectiveness against conventional approaches. The results demonstrate the ability of the pro-posed technique to better exploit the microgrid resources, thereby enhancing system reliability. The results also prove the proposed scheme generic and effective for different microgrid sizes, configurations, and loading conditions.

# Chapter 5

# A Generic Modeling and Power Flow Analysis Approach for Isochronous and Droop-Controlled AC Microgrids

## 5.1 Introduction

In Chapters 3 and 4, the ac subgrid was modeled in phase coordinates. Although the developed ac subgrid model provided an acceptable platform for steady-state analysis of unbalanced islanded hybrid ac/dc microgrids, there are some aspects that can be improved towards a more comprehensive, computationally-efficient, and accurate power flow approach. First, even though modeling in phase coordinates provides accurate models for EIDGs, it does not accurately represent the steady-state characteristics of SGDGs, due to the effect of their internal impedances on their terminal voltage unbalances. Second, interfacing transformers – typically used to connect 3-leg EIDGs to the 4-wire network – were not incorporated. Third, delta-connected loads were not considered in the models. Finally, in Chapter 3, the problem was formulated in a unified scheme and solved using a Newton-Trust Region (NTR) method. Nevertheless, other power flow methods could be employed to break down the system model into smaller subsystems, which will potentially enhance the power flow algorithms' performance. Therefore, an improved power flow approach for standalone hybrid ac/dc microgrids is developed over two stages for better readability and more detailed analysis. The first stage – presented in this chapter – provides a generic modeling and power flow approach for ac microgrids. The analysis incorporates the different ac microgrid's modes of operation, namely, isochronous and droop controls. The second

stage – presented in the next chapter – integrates the dc subgrid and ICs into the power flow algorithm to provide the complete framework, which can be used for both standalone unbalanced ac and hybrid ac/dc microgrids.

This chapter proposes a generic power flow algorithm for droop-controlled and isochronous microgrids under unbalanced conditions. The algorithm incorporates the sequence component models – rather than phase coordinate models used in [39] – of all system components, including various types of DG units with different steady-state characteristics. The adopted models allow for precise representations of SGDGs, as well as different configurations and controls of EIDGs [76]. The proposed algorithm utilizes these sequence component models to break down the steady-state analysis into three smaller independent, yet correlated, sub-problems. Accordingly, this method significantly reduces the power flow execution time with respect to NTR methods, as it deals with a set of small matrices rather than one large matrix representing the system as a whole.

The remainder of the chapter is organized as follows: Section 5.2 sheds lights on different operational modes of islanded and isolated microgrids. Section 5.3 describes the steady-state sequence-component mathematical modeling of microgrid elements. The proposed power flow algorithm is explained in Section 5.4. Section 5.5 attests to the validity of the proposed algorithm, and Section 5.6 investigates the introduced approach and the microgrid operation through case studies. Finally, Section 5.7 concludes the chapter.

## 5.2 Operational Modes of AC Microgrids

Numerous factors affect the operational mode of a microgrid, among which microgrid size, availability of RER, access to fuel, types of loads, and various economic considerations are significant [132]. A large DG may operate isochronously to set the microgrid's frequency, whereas a group of DGs with relatively similar capacities may employ droop controllers to collaboratively set the microgrid's voltage and frequency. Hence, microgrids can be categorized as droop-controlled and isochronously-controlled.

### 5.2.1 Droop-Controlled AC Microgrids

Droop controls are typically adopted to allow proportional power sharing among generators with comparable capacities. Thus, SGDGs could be droop-controlled at the primary level along with EIDGs in islanded microgrids if they have close capacities. In this context, the microgrid's voltage magnitude and frequency are load-dependent. It is worth mentioning

that a low-bandwidth supervisory controller is potentially required to monitor and regulate system variables (i.e., microgrid's voltage magnitude and frequency), especially if the microgrid supplies sensitive and critical loads. However, lack of a slack bus and proportional power sharing among the DGs eliminate system's dependence on one genera-tor, which potentially increases the microgrid's autonomy and reliability. This scheme could be desirable in islanded microgrids that normally operate in grid-connected mode.

### 5.2.2 Isochronously-Controlled AC Microgrids

In this mode, a dominant DG – typically SGDG – is operated in isochronous mode, thereby functioning as a slack bus (i.e., maintaining constant frequency and voltage at its terminals regardless of the connected load). Other DGs can inject active and reactive powers to the microgrid while following the main SGDG's frequency. It is noteworthy that this case is similar to the grid-connected mode of operation where the connection with the grid operates as a slack bus. However, the synchronous generator cannot keep its terminal voltages balanced under unbalanced loading due to its internal impedances, and thus it is not considered an ideal slack bus. Although the dominant SGDG forms the microgrid's voltage, other dispatchable DGs can still adopt droop control to sustain the microgrid operation in case of failure of the main SGDG. The output powers of these DGs are controlled by adjusting their droop settings, which is attainable through a higher level secondary controller. Non-dispatchable DGs – typically EIDGs – can inject powers to the microgrid; yet, they cannot form the microgrid voltage for proper operation if the main DG fails. This scheme is most suitable for isolated microgrids where DGs are to be integrated into existing gas- or diesel-powered networks.

## 5.3 AC Microgrid Modeling in Sequence Components

Unlike ac transmission systems, ac distribution networks are predominantly unbalanced due to the networks' intrinsic features, such as the existence of single-phase DGs and loads, feeder configurations, and single- and two-phase distribution laterals. This imbalance imposes further challenges on microgrids' modeling and analysis. A symmetrical sequence component analysis is therefore employed in this study for accurate representation of all microgrid components under unbalanced conditions.

### 5.3.1 AC Feeder Modeling

Distribution networks typically adopt 4-wire three-phase feeders, commonly unbalanced and untransposed, in addition to single- and/or two-phase laterals. Thus, the impedance matrix $Z_{ij}^{abc}$ between any two nodes $i$ and $j$, and the shunt admittance matrix $B_{i,j}^{abc}$ are asymmetrical in the phase form. The sequence component series admittance matrix $Y_{ij}^{012}$ can, hence, be calculated as

$$Y_{ij}^{012} = T^{-1} Z_{ij}^{abc^{-1}} T = \begin{bmatrix} y_{ij}^{00} & y_{ij}^{01} & y_{ij}^{02} \\ y_{ij}^{10} & y_{ij}^{11} & y_{ij}^{12} \\ y_{ij}^{20} & y_{ij}^{21} & y_{ij}^{22} \end{bmatrix} \tag{5.1}$$

where 0, 1 and 2 stand for zero-, positive- and negative-sequence components, respectively, and the transformation matrix $T$ is defined as

$$T = \begin{bmatrix} 1 & 1 & 1 \\ 1 & a^2 & a \\ 1 & a & a^2 \end{bmatrix} \qquad where \qquad a = 1\angle 120^\circ$$

Similarly, the shunt admittance matrix $B_{i,j}^{012}$ can be obtained in the sequence component frame as

$$B_{i,j}^{012} = T^{-1} B_{i,j}^{abc} T = \begin{bmatrix} b_{i,j}^{00} & b_{i,j}^{01} & b_{i,j}^{02} \\ b_{i,j}^{10} & b_{i,j}^{11} & b_{i,j}^{12} \\ b_{i,j}^{20} & b_{i,j}^{21} & b_{i,j}^{22} \end{bmatrix} \tag{5.2}$$

Since the phase matrices are asymmetrical, the sequence component admittance matrices are not symmetric diagonal, which implies that the three sequence components are coupled. Considering the series admittance matrix, given by (5.1), the sequence component currents $I_{ac,ij}^{012}$ flowing through the feeder connecting nodes $i$ and $j$ in terms of the sequence component voltages $V_{ac,i}^{012}$ are given by

$$\begin{bmatrix} I_{ac,ij}^{0} \\ I_{ac,ij}^{1} \\ I_{ac,ij}^{2} \end{bmatrix} = \begin{bmatrix} y_{ij}^{00} & y_{ij}^{01} & y_{ij}^{02} \\ y_{ij}^{10} & y_{ij}^{11} & y_{ij}^{12} \\ y_{ij}^{20} & y_{ij}^{21} & y_{ij}^{22} \end{bmatrix} \begin{bmatrix} V_{ac,i}^{0} - V_{ac,j}^{0} \\ V_{ac,i}^{1} - V_{ac,j}^{1} \\ V_{ac,i}^{2} - V_{ac,j}^{2} \end{bmatrix} \tag{5.3}$$

By introducing series admittance decoupling currents, $\Delta I_{ac,ij-se}^{012}$, defined by (5.4), the three

sequence currents can be decoupled as illustrated in (5.5).

$$\begin{bmatrix} I^0_{ac,ij-se} \\ I^1_{ac,ij-se} \\ I^2_{ac,ij-se} \end{bmatrix} = \begin{bmatrix} 0 & y^{01}_{ij} & y^{02}_{ij} \\ y^{10}_{ij} & 0 & y^{12}_{ij} \\ y^{20}_{ij} & y^{21}_{ij} & 0 \end{bmatrix} \begin{bmatrix} V^0_{ac,i} - V^0_{ac,j} \\ V^1_{ac,i} - V^1_{ac,j} \\ V^2_{ac,i} - V^2_{ac,j} \end{bmatrix} \tag{5.4}$$

$$\begin{bmatrix} I^0_{ac,ij} \\ I^1_{ac,ij} \\ I^2_{ac,ij} \end{bmatrix} = \begin{bmatrix} y^{00}_{ij} & 0 & 0 \\ 0 & y^{11}_{ij} & 0 \\ 0 & 0 & y^{22}_{ij} \end{bmatrix} \begin{bmatrix} I^0_{ac,ij-se} \\ I^1_{ac,ij-se} \\ I^2_{ac,ij-se} \end{bmatrix} \tag{5.5}$$

Similarly, the shunt admittance matrix, defined by (5.2), introduces coupled sequence component currents $I^{012}_{ac,ii}$ injected at node $i$ as

$$\begin{bmatrix} I^0_{ac,ii} \\ I^1_{ac,ii} \\ I^2_{ac,ii} \end{bmatrix} = \begin{bmatrix} b^{00}_{ij} & b^{01}_{ij} & b^{02}_{ij} \\ b^{10}_{ij} & b^{11}_{ij} & b^{12}_{ij} \\ b^{20}_{ij} & b^{21}_{ij} & b^{22}_{ij} \end{bmatrix} \begin{bmatrix} V^0_{ac,i} \\ V^1_{ac,i} \\ V^2_{ac,i} \end{bmatrix} \tag{5.6}$$

The shunt injected currents can also be decoupled if shunt decoupling currents, $\Delta I^{012}_{ac,ij-sh}$, are introduced as

$$\begin{bmatrix} I^0_{ac,ij-sh} \\ I^1_{ac,ij-sh} \\ I^2_{ac,ij-sh} \end{bmatrix} = \begin{bmatrix} 0 & b^{01}_{ij} & b^{02}_{ij} \\ b^{10}_{ij} & 0 & b^{12}_{ij} \\ b^{20}_{ij} & b^{21}_{ij} & 0 \end{bmatrix} \begin{bmatrix} V^0_{ac,i} \\ V^1_{ac,i} \\ V^2_{ac,i} \end{bmatrix} \tag{5.7}$$

Hence, the sequence currents injected due to the feeder shunt admittance can be decoupled using (5.8).

$$\begin{bmatrix} I^0_{ac,ii} \\ I^1_{ac,ii} \\ I^2_{ac,ii} \end{bmatrix} = \begin{bmatrix} b^{00}_{ij} & 0 & 0 \\ 0 & b^{11}_{ij} & 0 \\ 0 & 0 & b^{22}_{ij} \end{bmatrix} \begin{bmatrix} I^0_{ac,ij-sh} \\ I^1_{ac,ij-sh} \\ I^2_{ac,ij-sh} \end{bmatrix} \tag{5.8}$$

Therefore, complete decoupling of different sequence frames can be realized using current decoupling components, $\Delta I^{012}_{ac,i-j}$, that are comprised of both series and shunt decoupling currents, as given in (5.9).

$$\begin{bmatrix} I^0_{ac,i-j} \\ I^1_{ac,i-j} \\ I^2_{ac,i-j} \end{bmatrix} = \begin{bmatrix} I^0_{ac,ij-se} \\ I^1_{ac,ij-se} \\ I^2_{ac,ij-se} \end{bmatrix} \begin{bmatrix} I^0_{ac,ij-sh} \\ I^1_{ac,ij-sh} \\ I^2_{ac,ij-sh} \end{bmatrix} \tag{5.9}$$

Furthermore, since positive-sequence power flow analysis deals with active and reactive powers rather than currents, the positive-sequence decoupling component is transformed from current into active and reactive powers ($\Delta P^1_{ac,i-j}$ and $\Delta Q^1_{ac,i-j}$) by applying

$$\Delta P^1_{ac,i-j} + \Delta Q^1_{ac,i-j} = V^1_{ac,i}(I^1_{ac,i-j})^* \tag{5.10}$$

Finally, the decoupling current/power components can be formulated in their complete forms as

$$\Delta I^0_{ac,i-j} = y^{01}_{ij}(V^1_{ac,i} - V^1_{ac,j}) + y^{02}_{ij}(V^2_{ac,i} - V^2_{ac,j}) + b^{01}_{ij}V^1_{ac,i} + b^{02}_{ij}V^2_{ac,i} \tag{5.11}$$

$$\Delta P^1_{ac,i-j} + \Delta Q^1_{ac,i-j} = V^1_{ac,i}\Big[y^{10}_{ij}(V^0_{ac,i} - V^0_{ac,j}) + y^{12}_{ij}(V^2_{ac,i} - V^2_{ac,j}) + b^{10}_{ij}V^0_{ac,i} + b^{12}_{ij}V^2_{ac,i}\Big]^* \tag{5.12}$$

$$\Delta I^2_{ac,i-j} = y^{20}_{ij}(V^0_{ac,i} - V^0_{ac,j}) + y^{21}_{ij}(V^1_{ac,i} - V^1_{ac,j}) + b^{20}_{ij}V^0_{ac,i} + b^{21}_{ij}V^1_{ac,i} \tag{5.13}$$

Consequently, three decoupled Y-bus matrices – $Y^{00}$, $Y^{11}$, and $Y^{22}$ – can be constructed to formulate the three sequence component power flow problems independently. It is noteworthy that, unlike in grid-connected systems, the admittance matrices' parameters are load-dependent in droop controlled microgrids [39]. This fact necessitates updating the admittance matrices' elements according to the microgrid's frequency, which complicates the power flow problem.

### 5.3.2 AC DG Modeling

The physical structures of different DGs along with their various control schemes imply different mathematical models to precisely represent each DG type. DGs can mostly be classified into four categories as discussed in the following subsections. Note that other DG types can be modeled following the same approach.

#### Droop-controlled SGDG

Although various SGDGs adopt similar primary circuit configurations, as shown in Figure 5.1a, their models slightly vary based on their control schemes. Assuming that the SGDG regulates the positive sequence voltage at its terminals, the positive-sequence DG model can be represented as depicted in Figure 5.1b [36]. Furthermore, the negative and

zero sequence component circuits can be modeled as shown in Figures 5.1c and 5.1d, respectively, where the zero and negative-sequence admittances ($Y^0_{DG}$ and $Y^2_{DG}$) are obtained from the generator's datasheet or calculated using [133]

$$Y^0_{DG} = \left[ R_a + 3R_n + j \left( \frac{X''_{d-unsat} + X''_{q-unsat}}{2} + 3X_n \right) \right]^{-1} \tag{5.14}$$

$$Y^2_{DG} = \left[ R_a + j \frac{X''_{d-unsat} + X''_{q-unsat}}{2} \right]^{-1} \tag{5.15}$$

where $R_a$ is the armature resistance, $X''_{d-unsat}$ and $X''_{q-unsat}$ the unsaturated direct- and quadrature-axis sub-transient reactances respectively, and $R_n$ and $X_n$ the neutral resistance and reactance, respectively. Although SGDG generates balanced positive-sequence internal electromotive force (EMF), its terminal voltage undergoes unbalances under unequal phase loadings. The voltages across the negative and zero sequence admittances represent the voltage imbalance at the terminals.

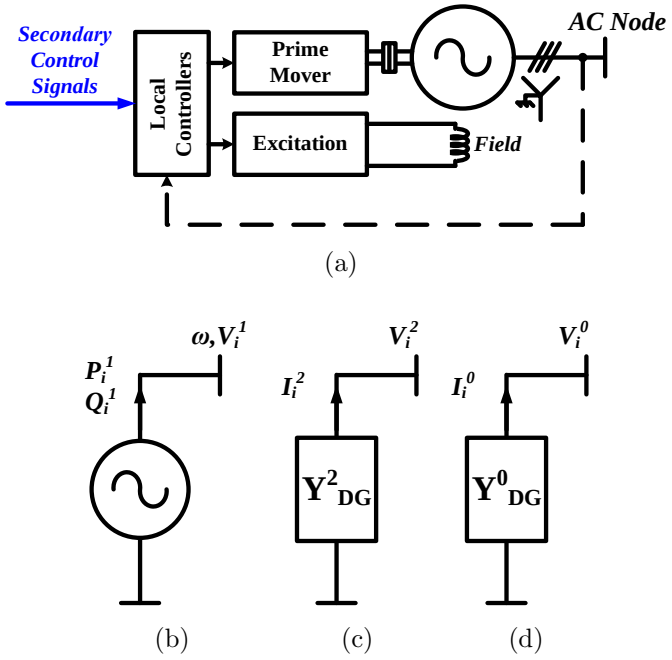


Figure 5.1: Structure and sequence component models of SGDG. (a) structure of SGDG, (b) positive-sequence model, (c) negative-sequence model, and (d) zero-sequence model.

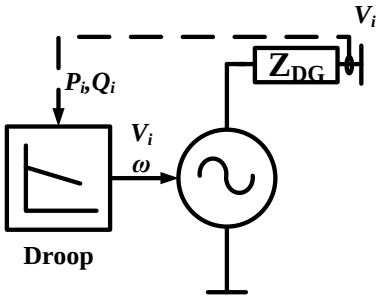


Figure 5.2: Simplified model of droop-controlled SGDG.

As shown in Figure 5.2, a droop-controlled SGDG's output voltage magnitude and frequency are dependent on the positive-sequence output active and reactive powers ($P^1_{ac,G,i}$ and $Q^1_{ac,G,i}$), as governed by the droop equations

$$P^1_{ac,G,i} = \frac{1}{3}\mu_i(\omega_{0,i} - \omega) \tag{5.16}$$

$$Q^1_{ac,G,i} = \frac{1}{3}\eta_i(V_{ac,0,i} - \left|V^1_{ac,i}\right|) \tag{5.17}$$

where the droop gains $\mu_i$ and $\eta_i$ are typically set as

$$\mu_i = \frac{P^{max}_{ac,G,i}}{\omega_{max} - \omega_{min}} \tag{5.18}$$

$$\eta_i = \frac{Q^{max}_{ac,G,i}}{V_{ac,max} - V_{ac,min}} \tag{5.19}$$

In (5.18) and (5.19), $P^{max}_{ac,G,i}$ and $Q^{max}_{ac,G,i}$ are the DG's maximum active and reactive powers, respectively, $\omega_{max}$ and $\omega_{min}$ the microgrid's maximum and minimum allowed frequencies, respectively, and $V_{ac,max}$ and $V_{ac,min}$ the DG's maximum and minimum positive-sequence terminal voltages, respectively. It is essential to mention that the SGDG's zero- and negative- sequence admittances, $Y^0_{DG}$ and $Y^2_{DG}$, are not constant, since the DGs' reactances are reliant on the load-dependent system frequency $\omega$.

### Isochronously-controlled SGDG

An isochronously-controlled SGDG is able to fix the microgrid's frequency while regulating the voltage at its terminals to a constant value. It can, thus, be considered a non-ideal slack bus. To model this DG, the same models and droop equations presented above can

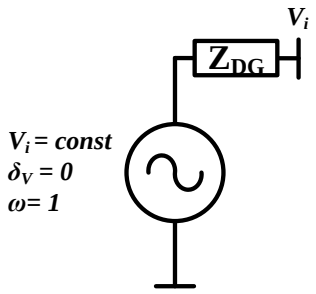


Figure 5.3: Simplified model of isochronous SGDG.

still be adopted by setting the droop gains to infinity. The SGDG's set-points (i.e., $\omega_{0,i}$ and $V^1_{ac,i}$) will determine the microgrid's frequency and the DG's terminal voltage, as shown in Figure 5.3. The SGDG's admittances are no longer variable in this case.

### Droop-controlled EIDG

Voltage-source converter (VSC)-based EIDGs, Figure 5.4a, can also implement droop controls to contribute in forming the microgrid voltage, as depicted in Figure 5.5. In general, EIDGs have positive-, negative-, and zero-sequence models similar to those of SGDGs, as depicted in Figures 5.4b to 5.4d. However, in contrast with SGDGs, they can suppress negative-sequence voltages at their terminals by implementing proper control loops, which denotes infinity negative-sequence admittance, as shown in Figure 5.4e [82]. However, other negative-sequence controls can also be adopted to realize negative-sequence current sharing among EIDGs [134]. Moreover, EIDGs can incorporate different circuit configurations, which primarily affect the DG's zero-sequence model. DGs that implement 3-leg VSCs do not provide a neutral current path; thus, they are represented as open circuit in the zero-sequence frame, as depicted in Figure 5.4f. However, 4-leg VSCs provide a neutral wire interfaced to the fourth leg through a filtering inductor. Therefore, their zero-sequence circuit is modeled as a short circuit if the VSC's controllers maintain balanced terminal voltages, or as a finite admittance otherwise, as shown in Figure 5.4d.

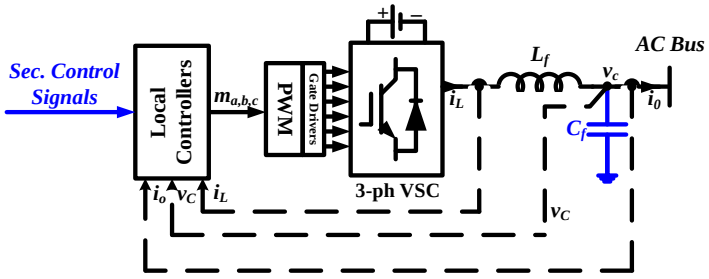


(a) Structure of EIDG

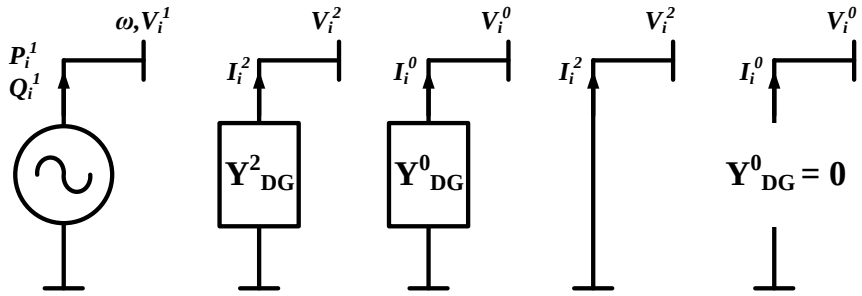


(b) (c) (d) (e) (f)

Figure 5.4: Structure and sequence component models of EIDG. (a) structure of EIDG, (b) positive-sequence model, (c) negative-sequence model, (d) zero-sequence model, (e) negative-sequence model as a short circuit, and (f) zero-sequence model as an open circuit.

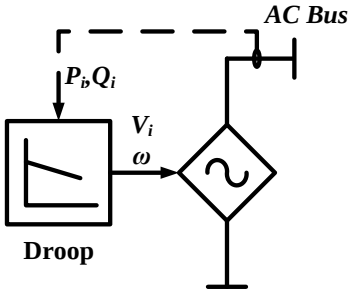


Figure 5.5: Simplified model of droop-controlled EIDG.

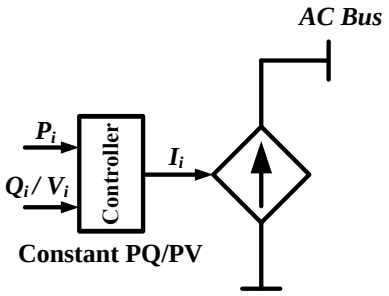


Figure 5.6: Simplified model of grid-tied EIDG.

It is worth mentioning that 3-leg VSCs are often interfaced to the 4-wire network through delta/grounded-wye transformers. With this configuration, the transformer's model, given by (5.20), must be integrated into the EIDG's model [135]. The previously presented droop equations (5.16)-(5.19) are valid for all discussed configurations of droop-controlled EIDGs.

$$\begin{bmatrix} I_\Delta^0 \\ I_\Delta^1 \\ I_\Delta^2 \\ I_Y^0 \\ I_Y^1 \\ I_Y^2 \end{bmatrix} = \begin{bmatrix} 0 & 0 & 0 & 0 & 0 & 0 \\ 0 & Y_{s.c} & 0 & 0 & -Y_{s.c}\angle -30^\circ & 0 \\ 0 & 0 & Y_{s.c} & 0 & 0 & -Y_{s.c}\angle 30^\circ \\ 0 & 0 & 0 & Y_{s.c} & 0 & 0 \\ 0 & -Y_{s.c}\angle 30^\circ & 0 & 0 & Y_{s.c} & 0 \\ 0 & 0 & -Y_{s.c}\angle -30^\circ & 0 & 0 & Y_{s.c} \end{bmatrix} \begin{bmatrix} V_\Delta^0 \\ V_\Delta^1 \\ V_\Delta^2 \\ V_Y^0 \\ V_Y^1 \\ V_Y^2 \end{bmatrix} \tag{5.20}$$

### Grid-Tied EIDG (Constant PQ/PV EIDG)

EIDGs may employ a grid-tied control scheme, which is typical for intermittent and non-dispatchable sources. In this control topology, the EIDG often employs a current-controlled VSC that does not contribute to forming the grid voltage; instead, it synchronizes to the existing grid and acts as a grid-follower (i.e., grid-tied) [76]. The EIDG injects controlled currents, as illustrated in Figure 5.6, to follow the DG's power or voltage references.

In the positive-sequence frame, a constant PQ EIDG is modeled as constant active and reactive power source, given by

$$P_{ac,G,i}^1 = \frac{1}{3} P_{ac,G,sp,i} \tag{5.21}$$

$$Q_{ac,G,i}^1 = \frac{1}{3} Q_{ac,G,sp,i} \tag{5.22}$$

where $P_{ac,G,sp,i}$ and $Q_{ac,G,sp,i}$ are the EIDG's specified active and reactive powers. Alternatively, a constant PV EIDG can fix the node voltage, rather than injecting constant reactive power, and henceforth it can be represented by (5.21) and (5.23).

$$V^1_{ac,i} = V_{sp,i} \tag{5.23}$$

Other grid-tied EIDG control schemes can also be represented by introducing minor modifications to (5.21) and (5.22).

On the other hand, the EIDG is represented as admittances in the zero- and negative-sequence models, as shown in Figures 5.4c and 5.4d, respectively. The zero- and negative sequence admittances can have zero, infinite, or finite nonzero values. Such values are dependent on the converter's structure (i.e., 3-leg or 4-leg), output filter configuration, and EIDG's control scheme, as detailed in [36] and [136]. It is noteworthy that although the same EIDG models for grid-connected microgrids in [36] and [136] can be adopted in the proposed work, the frequency dependency of the EIDGs' admittances has to be taken into consideration in this study.

### 5.3.3 AC Load Modeling

The steady-state model of loads is primarily dependent on their type. Loads are affected differently by voltage and frequency deviations that typically occur in droop-controlled microgrids. The load's features are incorporated in this study through a generic static load model that reflects the load's dependency on voltage and frequency [117]:

$$P^x_{ac,L,i} = P^{0,x}_{ac,L,i} \left| V^x_{ac,i} \right|^{\alpha,x} (1 + K^x_{pf,i} \Delta\omega) \tag{5.24}$$

$$Q^x_{ac,L,i} = Q^{0,x}_{ac,L,i} \left| V^x_{ac,i} \right|^{\beta,x} (1 + K^x_{qf,i} \Delta\omega) \tag{5.25}$$

$$\forall\, x \in \begin{cases} \{a,b,c\} & for\ Y\ loads \\ \{ab,bc,ca\} & for\ \Delta\ loads \end{cases}$$

where $P^{0,x}_{ac,L,i}$ and $Q^{0,x}_{ac,L,i}$ are the nominal load active and reactive powers, $\alpha$ and $\beta$ the active and reactive power exponents, $\Delta\omega$ the frequency deviation, and $K^x_{pf,i}$ and $K^x_{qf,i}$ the constants defining the load dependency on frequency deviations [117]. The values of the power exponents are sometimes equal, and take the values of 0, 1, or 2 for constant-power, constant-current, and constant-impedance loads, respectively. They, however, may be assigned different values to represent other load types if needed. On the other hand, the

values of $K^x_{pf,i}$ and $K^x_{qf,i}$ vary with the load class (i.e., residential, commercial, etc.) and season (i.e., summer, winter, etc.). At the lower power level, the load components (i.e., air conditioner, heater, television set, etc.) contribute to these values. Further details on various load types and their dependencies on voltage and frequency can be found in [117] and [137].

Since loads in distribution systems are typically unbalanced, the currents of load phases must be calculated individually:

$$I^x_{ac,L,i} = \frac{P^x_{ac,L,i} - jQ^x_{ac,L,i}}{V^x_{ac,L,i}} \qquad \forall\, x \in \begin{cases} \{a,b,c\} & for\ Y\ loads \\ \{ab,bc,ca\} & for\ \Delta\ loads \end{cases} \tag{5.26}$$

The load currents can, then, be transformed into their respective sequence components ($I^{012}_{ac,L,i}$) by applying

$$I^{012}_{ac,L,i} = T^{-1} I^{abc}_{ac,L,i} \tag{5.27}$$

The positive-sequence load active and reactive powers ($P^1_{ac,L,i}$ and $Q^1_{ac,L,i}$) can, therefore, be calculated as

$$P^1_{ac,L,i} + Q^1_{ac,L,i} = V^1_{ac,i}(I^1_{ac,L,i})^* \tag{5.28}$$

While (5.26)-(5.28) can directly be applied to $Y$-connected loads, $\Delta$-connected loads require more attention, as they encounter line voltages. Conversions between line and phase quantities, through (5.29) and (5.30), are necessary before substituting into (5.26)-(5.28).

$$\begin{bmatrix} V^{ab}_{ac,L,i} \\ V^{bc}_{ac,L,i} \\ V^{ca}_{ac,L,i} \end{bmatrix} = \begin{bmatrix} 1 & -1 & 0 \\ 0 & 1 & -1 \\ -1 & 0 & 1 \end{bmatrix} \begin{bmatrix} V^{a}_{ac,L,i} \\ V^{b}_{ac,L,i} \\ V^{c}_{ac,L,i} \end{bmatrix} \tag{5.29}$$

$$\begin{bmatrix} I^{a}_{ac,L,i} \\ I^{b}_{ac,L,i} \\ I^{c}_{ac,L,i} \end{bmatrix} = \begin{bmatrix} 1 & 0 & -1 \\ -1 & 1 & 0 \\ 0 & -1 & 1 \end{bmatrix} \begin{bmatrix} I^{ab}_{ac,L,i} \\ I^{bc}_{ac,L,i} \\ I^{ca}_{ac,L,i} \end{bmatrix} \tag{5.30}$$

## 5.4 Proposed AC Power Flow Algorithm

Obtaining a generic and accurate steady-state solution for droop-controlled microgrids is cumbersome if the problem is formulated in phase-coordinates. The decomposition into sequence components provides a more flexible and accurate alternative for modeling different operational modes of DGs and the inherent unbalanced feature of microgrids. In this

work, the sequence component approach is adopted to solve the power flow of microgrids that comprise different DG types. As illustrated in Figure 5.7, the algorithm starts by ac-quiring the system data and applying per unit conversions. Then, the admittance matrices are constructed and factorized, and the load sequence component currents/powers are calculated. Consequently, the sequence component voltages and system frequency are solved for. The load flow variables are then updated and the phase node voltages are calculated. To take the DGs' capacity limits into account, the output powers of all DGs are evaluated at each iteration. If a DG's power limit is exceeded, the output power is fixed at the maximum value, and the DG no longer follows the droop characteristics. The iteration is repeated until the results converge. It is worth noting that the loads, sequence load currents, decoupling components, and admittance matrices are updated at each iteration, as the microgrid's voltage magnitude and frequency change. The remainder of this section explains the subroutines in the proposed algorithm.

### 5.4.1 Positive-Sequence Power Flow

Decoupling sequence-component circuits allows independent, yet correlated, solutions of the three subsystems. The positive sequence power flow problem can be solved using the well-known NR method with some modifications. For a microgrid comprised of $N_{ac}$ buses, $2N_{ac}$ positive-sequence mismatch equations are defined for active and reactive powers at all buses. Assuming that all nodes integrate a DG and a load, generic active and reactive power mismatch equations can be formulated at an arbitrary bus $i$ as

$$\Gamma_{ac,P,i} = P^1_{ac,G,i} - P^1_{ac,L,i} - P^1_{ac,i} - \sum_{j \in N_{ac} \backslash i} \Delta P^1_{ac,i-j} \tag{5.31}$$

$$\Gamma_{ac,Q,i} = Q^1_{ac,G,i} - Q^1_{ac,L,i} - Q^1_{ac,i} - \sum_{j \in N_{ac} \backslash i} \Delta Q^1_{ac,i-j} \tag{5.32}$$

where $P^1_{ac,i}$ and $Q^1_{ac,i}$ are the active and reactive power injections at the bus $i$, which are defined by

$$P^1_{ac,i} = \sum_{j \in N_{ac}} \left|V^1_{ac,i}\right| \left|V^1_{ac,j}\right| \left|Y^{11}_{ij}\right| \cos\left(\delta^1_i - \delta^1_j - \theta^{11}_{ij}\right) \tag{5.33}$$

$$Q^1_{ac,i} = \sum_{j \in N_{ac}} \left|V^1_{ac,i}\right| \left|V^1_{ac,j}\right| \left|Y^{11}_{ij}\right| \sin\left(\delta^1_i - \delta^1_j - \theta^{11}_{ij}\right) \tag{5.34}$$

In (5.33) and (5.34), $|V^1_{ac,i}|$ and $\left|V^1_{ac,j}\right|$, and $\delta^1_i$ and $\delta^1_j$ are the positive-sequence voltage magnitudes and angles at nodes $i$ and $j$, respectively, and $|Y^{11}_{ij}|$ and $\theta^{11}_{ij}$ the magnitude and

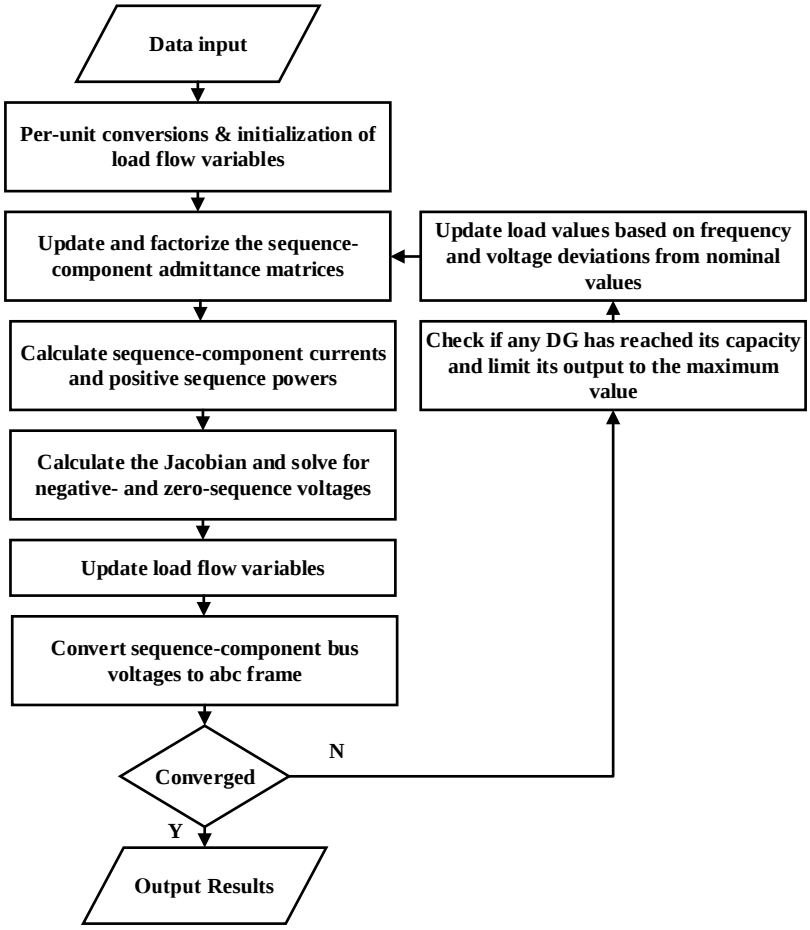


Figure 5.7: Flow chart of the proposed power flow algorithm.

angle of the positive-sequence Y-bus matrix element, respectively. Note that the absence of generation and/or load at a bus translates to substituting their powers with zeros.

Considering that the microgrid frequency is primarily dependent on the positive-sequence power flow, and by choosing the first bus's angle as a reference (i.e., $\delta_1^1 = 0.0$), $2N_{ac}$ unknowns have to be solved for: $N_{ac}$ node voltages, the microgrid's frequency $\omega$, and $N_{ac} - 1$ node angles. Thus, the positive-sequence voltage magnitudes ($|\mathbf{V_{ac}^1}|$), angles ($\delta^{\mathbf{1}}$), and frequency ($\omega$) for iteration $(k+1)$ in terms of the variables of iteration $(k)$ are obtained as

$$\begin{bmatrix} \left|\mathbf{V_{ac}^1}\right|_{(k+1)} \\ \delta^{\mathbf{1}}{}_{(k+1)} \\ \omega_{(k+1)} \end{bmatrix} = \begin{bmatrix} \left|\mathbf{V_{ac}^1}\right|_{(k)} \\ \delta^{\mathbf{1}}{}_{(k)} \\ \omega_{(k)} \end{bmatrix} - J_{ac}^{-1} \begin{bmatrix} \Gamma_{\mathbf{ac,P}(k)} \\ \\ \Gamma_{\mathbf{ac,Q}(k)} \end{bmatrix} \tag{5.35}$$

where the Jacobian matrix $J_{ac}$ is formed as

$$J_{ac} = \begin{bmatrix} \dfrac{\partial \Gamma_{\mathbf{ac,P}}}{\partial |\mathbf{V_{ac}^1}|} & \dfrac{\partial \Gamma_{\mathbf{ac,P}}}{\partial \delta^{\mathbf{1}}} & \dfrac{\partial \Gamma_{\mathbf{ac,P}}}{\partial \omega} \\ \\ \dfrac{\partial \Gamma_{\mathbf{ac,Q}}}{\partial |\mathbf{V_{ac}^1}|} & \dfrac{\partial \Gamma_{\mathbf{ac,Q}}}{\partial \delta^{\mathbf{1}}} & \dfrac{\partial \Gamma_{\mathbf{ac,Q}}}{\partial \omega} \end{bmatrix} \tag{5.36}$$

Due to the microgrid's droop characteristics, the Jacobean matrix elements are not exactly the same as those of conventional systems. By substituting from (5.12), (5.16), (5.17), (5.24), (5.25), (5.33), and (5.34) into (5.31) and (5.32), the matrix elements are obtained as (5.37)-(5.42).

$$\frac{\partial \Gamma_{ac,P,i}}{\partial \left|V_{ac}^{1}\right|} = \begin{cases} \dfrac{\partial \Gamma_{ac,P,i}}{\partial \left|V_{ac,i}^{1}\right|} = -\sum\limits_{j \in N_{ac}} \left|V_{ac,j}^{1}\right| \left|Y_{ij}^{11}\right| \cos\left(\delta_i^1 - \delta_j^1 - \theta_{ij}^{11}\right) \\ \qquad\qquad - 2\left|V_{ac,i}^{1}\right| \left|Y_{ij}^{11}\right| \cos\left(\theta_{ii}^{11}\right) \\ \qquad\qquad - \bar{\alpha_i} P_{ac,L,i}^{1} \left|V_{ac,i}^{1}\right|^{\bar{\alpha_i}-1} \left(1 + \bar{K_{pf,i}} \Delta\omega\right) \\ \dfrac{\partial \Gamma_{ac,P,i}}{\partial \left|V_{ac,j}^{1}\right|} = -\sum\limits_{j \in N_{ac}} \left|V_{ac,i}^{1}\right| \left|Y_{ij}^{11}\right| \cos\left(\delta_i^1 - \delta_j^1 - \theta_{ij}^{11}\right) \end{cases} \tag{5.37}$$

$$\frac{\partial \Gamma_{ac,Q,i}}{\partial \left|V_{ac}^{1}\right|} = \begin{cases} \dfrac{\partial \Gamma_{ac,Q,i}}{\partial \left|V_{ac,i}^{1}\right|} = -\sum\limits_{j \in N_{ac}} \left|V_{ac,j}^{1}\right| \left|Y_{ij}^{11}\right| \sin\left(\delta_i^1 - \delta_j^1 - \theta_{ij}^{11}\right) \\ \qquad\qquad - 2\left|V_{ac,i}^{1}\right| \left|Y_{ij}^{11}\right| \sin\left(\theta_{ii}^{11}\right) \\ \qquad\qquad - \bar{\beta_i} Q_{ac,L,i}^{1} \left|V_{ac,i}^{1}\right|^{\bar{\beta_i}-1} \left(1 + \bar{K_{qf,i}} \Delta\omega\right) \\ \dfrac{\partial \Gamma_{ac,Q,i}}{\partial \left|V_{ac,j}^{1}\right|} = -\sum\limits_{j \in N_{ac}} \left|V_{ac,i}^{1}\right| \left|Y_{ij}^{11}\right| \sin\left(\delta_i^1 - \delta_j^1 - \theta_{ij}^{11}\right) \end{cases} \tag{5.38}$$

$$\frac{\partial \Gamma_{ac,P,i}}{\partial \delta^1} = \begin{cases} \dfrac{\partial \Gamma_{ac,P,i}}{\partial \delta_i^1} = \sum\limits_{j \in N_{ac}} \left|V_{ac,i}^{1}\right| \left|V_{ac,j}^{1}\right| \left|Y_{ij}^{11}\right| \sin\left(\delta_i^1 - \delta_j^1 - \theta_{ij}^{11}\right) \\ \dfrac{\partial \Gamma_{ac,P,i}}{\partial \delta_j^1} = -\left|V_{ac,i}^{1}\right| \left|V_{ac,j}^{1}\right| \left|Y_{ij}^{11}\right| \sin\left(\delta_i^1 - \delta_j^1 - \theta_{ij}^{11}\right) \end{cases} \tag{5.39}$$

$$\frac{\partial \Gamma_{ac,Q,i}}{\partial \delta^1} = \begin{cases} \dfrac{\partial \Gamma_{ac,Q,i}}{\partial \delta_i^1} = -\sum\limits_{j \in N_{ac}} \left|V_{ac,i}^{1}\right| \left|V_{ac,j}^{1}\right| \left|Y_{ij}^{11}\right| \cos\left(\delta_i^1 - \delta_j^1 - \theta_{ij}^{11}\right) \\ \dfrac{\partial \Gamma_{ac,Q,i}}{\partial \delta_j^1} = \left|V_{ac,i}^{1}\right| \left|V_{ac,j}^{1}\right| \left|Y_{ij}^{11}\right| \cos\left(\delta_i^1 - \delta_j^1 - \theta_{ij}^{11}\right) \end{cases} \tag{5.40}$$

$$\frac{\partial \Gamma_{ac,P,i}}{\partial \omega} \approxeq -\frac{1}{3}\mu_i - P_{ac,L,i}^{1} \left|V_{ac,i}^{1}\right|^{\bar{\alpha_i}} \bar{K_{pf,i}} \tag{5.41}$$

$$\frac{\partial \Gamma_{ac,Q,i}}{\partial \omega} \approxeq -\frac{1}{3}\eta_i - Q_{ac,L,i}^{1} \left|V_{ac,i}^{1}\right|^{\bar{\beta} i} \bar{K_{qf,i}} \tag{5.42}$$

The bars above load parameters (i.e., $\alpha$, $\beta$, $K_{pf}$, and $K_{qf}$) in (5.37), (5.38), (5.41), and (5.42) denote their averaged values over the unbalanced loads at node $i$.

It is worth mentioning that for the derivatives with respect to the microgrid's frequency, the admittance is assumed constant, as its change has insignificant contribution to the Jacobian elements' values. However, the admittance variation is considered when calculating the mismatch equations to ensure accurate results.

### 5.4.2 Negative- and Zero-Sequence Power Flows

The negative and zero-sequence voltages ($|\mathbf{V^2_{ac}}|$ and $|\mathbf{V^0_{ac}}|$) for the same iteration $(k+1)$ can be directly calculated by solving

$$\mathbf{V^0_{ac}}_{(k+1)} = \left[Y^{00}_{(k+1)}\right]^{-1} \left[-\mathbf{I^0_{ac,L}}_{(k+1)} - \mathbf{\Delta I^0_{ac}}_{(k+1)}\right] \tag{5.43}$$

$$\mathbf{V^2_{ac}}_{(k+1)} = \left[Y^{22}_{(k+1)}\right]^{-1} \left[-\mathbf{I^2_{ac,L}}_{(k+1)} - \mathbf{\Delta I^2_{ac}}_{(k+1)}\right] \tag{5.44}$$

where $\mathbf{I^0_{ac,L}}$ and $\mathbf{I^2_{ac,L}}$ are zero- and negative-sequence the load current vectors, respectively, and the decoupling current vectors $\mathbf{\Delta I^0_{ac}}$ and $\mathbf{\Delta I^2_{ac}}$ are constructed by calculating the total decoupling currents at each bus $i$ as

$$\Delta I^0_{ac,i} = \sum_{j \in N_{ac}} \Delta I^0_{ac,i-j} \tag{5.45}$$

$$\Delta I^2_{ac,i} = \sum_{j \in N_{ac}} \Delta I^2_{ac,i-j} \tag{5.46}$$

Furthermore, since equations (5.31) and (5.32) assume three-phase feeders and Y-connected loads, all delta-connected loads must be pre-processed using (5.29) and (5.30) at each iteration.

### 5.4.3 Comparison with the Problem Formulation of the NTR method

The NTR-based approach, reported in [39], formulates the unbalanced power flow problem in phase coordinates. Accordingly, the power flow problem comprises 6 equations at each node to represent the active and reactive power mismatches for the three phases, leading to a problem size of $(6N_{ac} \times 6N_{ac})$. Furthermore, the adopted NTR solution method is

formulated as an optimization algorithm to minimize the mismatch powers (ideally to zero). Although this method demonstrates good convergence performance in terms of robustness and number of iterations, its computational cost is significantly high due to the problem's large size. On the other hand, as per (5.35), (5.43), and (5.44), the proposed approach breaks down the power flow problem into three independent sub-problems of sizes ($2N_{ac} \times 2N_{ac}$), ($N_{ac} \times N_{ac}$), and ($N_{ac} \times N_{ac}$), for the decoupled positive-, negative-, and zero-sequence subsystems, respectively. Such reduction in problem size results in substantial decrease in computational and memory requirements of the problem solution, even when including the decoupling computational overhead in the proposed method [138]. Meanwhile, the proposed approach allows parallel solution of the sub-problems, which leads to further reduction in the algorithm's execution time. Additionally, the NTR method evaluates the gradient and Hessian matrices numerically, thus adding considerable computational burden on the algorithm; this burden significantly escalates as the microgrid size increases. On the contrary, the Jacobian matrix elements are directly calculated through (5.37)-(5.42) in the proposed approach, thereby resulting in minimal computational effort. Altogether, these factors remarkably advantage the proposed approach's performance over that of its NTR-based counterpart.

## 5.5 Performance Validation of the Proposed Approach

The performance of the proposed modeling and power flow algorithm was validated through comparison of accuracy and computational time against time-domain simulations and a traditional NTR-based algorithm.

### 5.5.1 Comparison with time-domain simulations

The power flow algorithm was tested on a modified IEEE 13-node test feeder [40], shown in Figure 5.8. Three droop-controlled DGs of different types, sizes, and settings, presented in Table 5.1, were connected to buses 650, 681, and 692. The SGDG's ratings and parameters can be found in [139]. Furthermore, a 2.5 MVA delta-wye transformer interfaces the 3-leg EIDG to the 4-wire network; its short-circuit resistance and reactance at 60 Hz are 1% and 6%, respectively. Although the system is relatively small, it includes all different components of distribution systems, namely, untransposed feeders, unbalanced loads, different load connections, distribution transformers, and single- and two-phase laterals and loads. The microgrid's small size allows conducting detailed time-domain simulations for model validation.

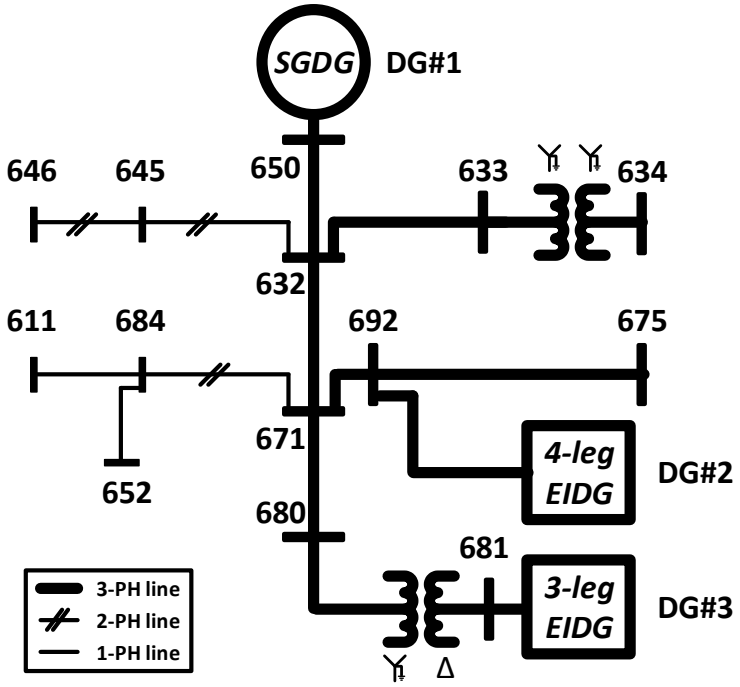


Figure 5.8: Test microgrid#5.1: modified IEEE 13-node test feeder

Table 5.1: DG ratings and droop settings (test microgrid#5.1)

| DG# | DG Type | $\mu$ (pu) | $\eta$ (pu) | $\omega_0$ (pu) | $V_{ac,0}$ (pu) | $P_{ac,G}^{max}$ (pu) | $S_{ac,G}^{max}$ (pu) |
|---|---|---|---|---|---|---|---|
| 1 | SGDG | 25.2 | 7.56 | 1.00 | 1.00 | 0.504 | 0.630 |
| 2 | 4-leg EIDG | 18.0 | 5.40 | 1.00 | 1.00 | 0.360 | 0.450 |
| 3 | 3-leg EIDG | 20.0 | 6.00 | 1.00 | 1.00 | 0.400 | 0.500 |

A complete time-domain model of the test microgrid was constructed and run in MATLAB/Simulink environment until it converged to a steady state. The proposed algorithm, implemented in MATLAB, was also executed to solve the same power flow problem. Table 5.2 demonstrates close agreement between the power flow results obtained based on the proposed models and solution algorithm and those of the time-domain simulations. The mismatches are smaller than $6.06 \times 10^{-4}$ pu, $0.13^{\circ}$ ($2.36 \times 10^{-3}$ rad), and $5.72 \times 10^{-5}$ pu for the voltage magnitude, angle, and frequency, respectively, validating the accuracy of the proposed method.

### 5.5.2 Robustness of the Proposed Approach

It is important to ensure that a power flow algorithm is robust and able to converge under various conditions. Therefore, the robustness of the proposed approach was examined under light and heavy microgrid loading conditions, which may result in over- and under-voltages, respectively. The loads of test microgrid#5.1 were multiplied by a factor $\lambda$ to change the microgrid loading, as per

$$P^{0,x}_{ac,L,i} + jQ^{0,x}_{ac,L,i} = \lambda \left( P^{0,x}_{ac,L,base,i} + jQ^{0,x}_{ac,L,base,i} \right) \tag{5.47}$$

where $P^{0,x}_{ac,L,base,i}$ and $Q^{0,x}_{ac,L,base,i}$ are the base load active and reactive powers, respectively.

Table 5.3 shows the maximum and minimum observed voltages of the microgrid under each loading condition. Furthermore, for a power mismatch tolerance of $1.0 \times 10^{-6}$, the table shows the number of iterations for convergence in each case. The results demonstrate that for the no-load condition (i.e., $\lambda = 0$), the connected capacitors boost the microgrid voltage above the DG's set points. On the contrary, heavy loading condition (i.e., $\lambda = 1.5$) results in under-voltages at some microgrid nodes. In all cases, the proposed algorithm converges in 7 or 8 iterations, proving the robustness of the proposed approach under different loading and voltage conditions.

### 5.5.3 Performance Comparison with the NTR-based approach

To further validate the accuracy and performance of the proposed approach, a performance comparison against the NTR method was performed through solving the power flow of the 25-node microgrid in [12], which considered the integration of three identical droop-controlled DGs. Both algorithms were executed on a PC with a 64-bit Intel Core i7 @3.4 GHz CPU and 16 GB of RAM. The two methods were initialized at a three-phase flat start:

Table 5.2: Power-flow results of test microgrid#5.1

**MATLAB/Simulink**

| Bus# | $\lvert V_{ac}^{a}\rvert$ (pu) | $\delta^{a}$ (deg) | $\lvert V_{ac}^{b}\rvert$ (pu) | $\delta^{b}$ (deg) | $\lvert V_{ac}^{c}\rvert$ (pu) | $\delta^{c}$ (deg) |
|---|---|---|---|---|---|---|
| **650** | 0.9921 | 0.00 | 0.9845 | −120.30 | 0.9863 | 120.13 |
| 632 | 0.9802 | − 0.65 | 0.9709 | −121.43 | 0.9765 | 119.08 |
| 633 | 0.9772 | − 0.72 | 0.9691 | −121.48 | 0.9740 | 119.08 |
| 634 | 0.9546 | − 1.38 | 0.9514 | −121.95 | 0.9561 | 118.60 |
| 645 | | | 0.9620 | −121.62 | 0.9747 | 119.10 |
| 646 | | | 0.9604 | −121.55 | 0.9727 | 119.15 |
| 671 | 0.9760 | − 1.43 | 0.9759 | −121.41 | 0.9763 | 118.58 |
| 680 | 0.9804 | − 1.06 | 0.9791 | −121.01 | 0.9804 | 118.98 |
| **681** | 0.9906 | −29.62 | 0.9906 | −149.63 | 0.9906 | 90.37 |
| 684 | 0.9740 | − 1.46 | | | 0.9743 | 118.48 |
| 611 | | | | | 0.9724 | 118.34 |
| 652 | 0.9685 | − 1.38 | | | | |
| **692** | 0.9760 | − 1.43 | 0.9759 | −121.41 | 0.9763 | 118.58 |
| 675 | 0.9700 | − 1.67 | 0.9781 | −121.58 | 0.9742 | 118.60 |

$\omega = 0.98951$ pu

**Proposed Method**

| Bus# | $\lvert V_{ac}^{a}\rvert$ (pu) | $\delta^{a}$ (deg) | $\lvert V_{ac}^{b}\rvert$ (pu) | $\delta^{b}$ (deg) | $\lvert V_{ac}^{c}\rvert$ (pu) | $\delta^{c}$ (deg) |
|---|---|---|---|---|---|---|
| **650** | 0.9920 | 0.00 | 0.9839 | −120.25 | 0.9866 | 120.19 |
| 632 | 0.9803 | − 0.57 | 0.9709 | −121.34 | 0.9765 | 119.17 |
| 633 | 0.9774 | − 0.63 | 0.9690 | −121.38 | 0.9740 | 119.16 |
| 634 | 0.9548 | − 1.29 | 0.9513 | −121.85 | 0.9562 | 118.70 |
| 645 | | | 0.9620 | −121.52 | 0.9747 | 119.19 |
| 646 | | | 0.9604 | −121.60 | 0.9728 | 119.24 |
| 671 | 0.9762 | − 1.30 | 0.9762 | −121.30 | 0.9762 | 118.70 |
| 680 | 0.9804 | − 0.96 | 0.9791 | −121.92 | 0.9803 | 119.09 |
| **681** | 0.9906 | −29.54 | 0.9906 | −149.54 | 0.9906 | 90.46 |
| 684 | 0.9742 | − 1.32 | | | 0.9742 | 118.60 |
| 611 | | | | | 0.9723 | 118.46 |
| 652 | 0.9688 | − 1.25 | | | | |
| **692** | 0.9762 | − 1.30 | 0.9762 | −121.30 | 0.9762 | 118.70 |
| 675 | 0.9701 | − 1.54 | 0.9783 | −121.47 | 0.9743 | 118.70 |

$\omega = 0.98957$ pu

Table 5.3: Robustness results (test microgrid#5.1)

| $\lambda$ | 0.0 | 0.5 | 1.0 | 1.5 |
|---|---|---|---|---|
| Max. node voltage | 1.0143 | 0.9990 | 0.9920 | 0.9852 |
| Min. node voltage | 1.0054 | 0.9793 | 0.9513 | 0.9246 |
| #iterations | 8 | 7 | 8 | 8 |

Table 5.4: Performance comparison (25-node microgrid)

| | Proposed method | | NTR [39] | |
|---|---|---|---|---|
| Tolerance | $1.0 \times 10^{-6}$ | $1.0 \times 10^{-12}$ | $1.0 \times 10^{-6}$ | $1.0 \times 10^{-12}$ |
| Solution time (ms) | 75 | 108 | 3,220 | 3,893 |
| #iterations | 3 | 7 | 3 | 4 |

the NTR method adopted a flat start in phase coordinates (i.e., all nodes were assigned $V^a_{ac,i} = 1.0\angle 0.0^\circ$ pu, $V^b_{ac,i} = 1.0\angle -120.0^\circ$ pu, and $V^c_{ac,i} = 1.0\angle 120.0^\circ$ pu), while the proposed method was initialized in symmetrical sequence components (i.e., all nodes were assigned $V^0_{ac,i} = 0.0$ pu, $V^1_{ac,i} = 1.0\angle 0.0^\circ$ pu, and $V^2_{ac,i} = 0.0$ pu). The microgrid's frequency was assumed to be initially 1.0 pu for both methods. The stopping criterion was unified and selected such that the gradient norm did not exceed the specified tolerance value. The two approaches produced similar results if directly-connected 4-leg EIDGs were assumed in the proposed method. However, the NTR-based approach failed to produce accurate results when the transformers' effects and/or other types of DGs were considered. The reason for this inaccuracy is neglecting the interfacing transformers' effects and assuming that all DG types can maintain balanced terminal voltages. Furthermore, the proposed algorithm demonstrated considerably improved solution time, as shown in Table 5.4, for two tolerance values. The results prove that the proposed approach outperforms its NTR-based counterpart not only in accuracy, but also in computational-efficiency.

## 5.6 Case Studies

The following case studies highlight the effectiveness of the proposed algorithm in solving larger and more complex microgrids. The modified IEEE 123-node test feeder has been adopted to form a test microgrid by adding three DG units to nodes 149, 251, and 300, as shown in Figure 5.9. While the system structure remained the same, the two micro-

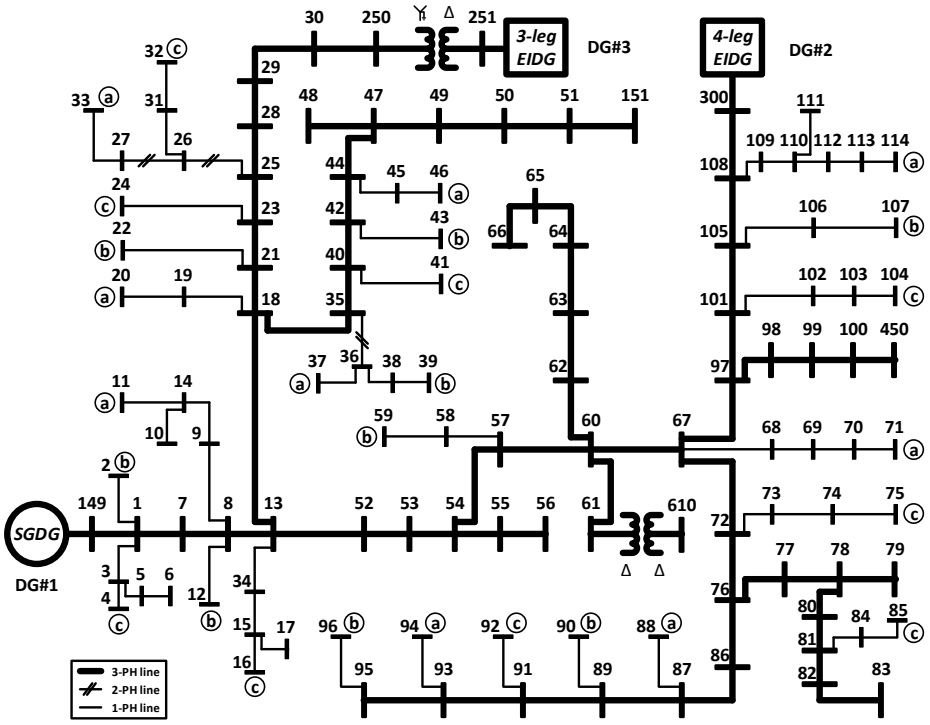


Figure 5.9: Test microgrid#5.2: modified IEEE 123-node test feeder

grid operational control modes (i.e., droop and isochronous) were investigated in the two following subsections.

### 5.6.1 Droop-Controlled Microgrid

In this analysis, the DGs implement droop characteristics according to the parameters stated in Table 5.1. The voltage magnitudes and angles of all buses are presented in Table 5.5. The DGs collaboratively set the steady-state frequency to 0.98905 pu. The results demonstrate key aspects pertaining to the behaviors of different types of DGs under unbalanced operation. While the 4-leg EIDG with negative- and zero-sequence voltage compensation maintains balanced voltages at its terminals (node#300), the 3-wire EIDG cannot compensate for zero-sequence voltages behind the interfacing transformers, as observed at node#250. Furthermore, the SGDG encounters unbalanced terminal voltages (node#149) due to its internal impedances.

Table 5.5: Power flow results of test microgrid#5.2

| Bus# | $\lvert V_{ac}^{a}\rvert$ (pu) | $\delta^{a}$ (deg) | $\lvert V_{ac}^{b}\rvert$ (pu) | $\delta^{b}$ (deg) | $\lvert V_{ac}^{c}\rvert$ (pu) | $\delta^{c}$ (deg) |
|---|---|---|---|---|---|---|
| 149 | 0.9815 | 0.00 | 0.9861 | −119.49 | 0.9868 | 120.17 |
| 1 | 0.9770 | − 0.25 | 0.9846 | −119.63 | 0.9826 | 120.02 |
| 2 | | | 0.9844 | −119.63 | | |
| 3 | | | | | 0.9809 | 119.99 |
| 4 | | | | | 0.9804 | 119.98 |
| 5 | | | | | 0.9797 | 119.97 |
| 6 | | | | | 0.9790 | 119.96 |
| 7 | 0.9736 | − 0.42 | 0.9836 | −119.74 | 0.9803 | 119.95 |
| 8 | 0.9715 | − 0.53 | 0.9828 | −119.82 | 0.9788 | 119.90 |
| 9 | 0.9700 | − 0.56 | | | | |
| 10 | 0.9681 | − 0.60 | | | | |
| 11 | 0.9678 | − 0.60 | | | | |
| 12 | | | 0.9825 | −119.83 | | |
| 13 | 0.9694 | − 0.65 | 0.9813 | −119.92 | 0.9765 | 119.80 |
| 14 | 0.9684 | − 0.59 | | | | |
| 15 | | | | | 0.9751 | 119.77 |
| 16 | | | | | 0.9741 | 119.75 |
| 17 | | | | | 0.9746 | 119.76 |
| 18 | 0.9661 | − 0.63 | 0.9789 | −119.89 | 0.9746 | 119.97 |
| 19 | 0.9648 | − 0.66 | | | | |
| 20 | 0.9639 | − 0.68 | | | | |
| 21 | 0.9676 | − 0.52 | 0.9795 | −119.79 | 0.9755 | 120.04 |
| 22 | | | 0.9782 | −119.82 | | |
| 23 | 0.9689 | − 0.44 | 0.9804 | −119.69 | 0.9761 | 120.10 |
| 24 | | | | | 0.9746 | 120.07 |
| 25 | 0.9701 | − 0.35 | 0.9814 | −119.59 | 0.9771 | 120.18 |
| 26 | 0.9699 | − 0.37 | | | 0.9766 | 120.16 |
| 27 | 0.9695 | − 0.39 | | | 0.9766 | 120.16 |
| 28 | 0.9711 | − 0.27 | 0.9820 | −119.52 | 0.9781 | 120.25 |
| 29 | 0.9730 | − 0.12 | 0.9827 | −119.41 | 0.9798 | 120.33 |
| 30 | 0.9757 | 0.06 | 0.9834 | −119.29 | 0.9817 | 120.41 |
| 250 | 0.9770 | 0.17 | 0.9838 | −119.22 | 0.9831 | 120.47 |

| Bus# | $\lvert V_{ac}^{a}\rvert$ (pu) | $\delta^{a}$ (deg) | $\lvert V_{ac}^{b}\rvert$ (pu) | $\delta^{b}$ (deg) | $\lvert V_{ac}^{c}\rvert$ (pu) | $\delta^{c}$ (deg) |
|---|---|---|---|---|---|---|
| 251 | 0.9915 | −28.05 | 0.9915 | −148.05 | 0.9915 | 91.95 |
| 31 | | | | | 0.9760 | 120.15 |
| 32 | | | | | 0.9756 | 120.14 |
| 33 | 0.9682 | − 0.42 | | | | |
| 34 | | | | | 0.9755 | 119.78 |
| 35 | 0.9633 | − 0.72 | 0.9764 | −119.98 | 0.9735 | 119.91 |
| 36 | 0.9624 | − 0.74 | 0.9759 | −120.03 | | |
| 37 | 0.9617 | | | | | |
| 38 | | | 0.9752 | −120.04 | | |
| 39 | | | 0.9748 | −120.05 | | |
| 40 | 0.9618 | − 0.76 | 0.9752 | −120.03 | 0.9725 | 119.86 |
| 41 | | | | | 0.9721 | 119.85 |
| 42 | 0.9603 | − 0.80 | 0.9741 | −120.08 | 0.9716 | 119.82 |
| 43 | | | 0.9729 | −120.10 | | |
| 44 | 0.9592 | − 0.83 | 0.9734 | −120.11 | 0.9708 | 119.79 |
| 45 | 0.9586 | − 0.84 | | | | |
| 46 | 0.9582 | − 0.85 | | | | |
| 47 | 0.9582 | − 0.85 | 0.9724 | −120.14 | 0.9698 | 119.74 |
| 48 | 0.9579 | − 0.86 | 0.9721 | −120.15 | 0.9696 | 119.74 |
| 49 | 0.9579 | − 0.86 | 0.9718 | −120.15 | 0.9695 | 119.72 |
| 50 | 0.9579 | − 0.87 | 0.9718 | −120.14 | 0.9691 | 119.71 |
| 51 | 0.9577 | − 0.88 | 0.9719 | −120.14 | 0.9691 | 119.71 |
| 52 | 0.9676 | − 0.82 | 0.9804 | −120.09 | 0.9757 | 119.65 |
| 53 | 0.9670 | − 0.89 | 0.9799 | −120.18 | 0.9753 | 119.57 |
| 54 | 0.9668 | − 0.93 | 0.9794 | −120.23 | 0.9751 | 119.52 |
| 55 | 0.9666 | − 0.93 | 0.9793 | −120.24 | 0.9752 | 119.52 |
| 56 | 0.9665 | − 0.93 | 0.9791 | −120.25 | 0.9752 | 119.52 |
| 57 | 0.9669 | − 1.04 | 0.9778 | −120.38 | 0.9745 | 119.38 |
| 58 | | | 0.9771 | −120.39 | | |
| 59 | | | 0.9768 | −120.40 | | |
| 60 | 0.9674 | − 1.29 | 0.9754 | −120.65 | 0.9727 | 119.09 |
| 61 | 0.9674 | − 1.29 | 0.9754 | −120.65 | 0.9727 | 119.09 |
| 610 | 0.9674 | − 1.29 | 0.9754 | −120.65 | 0.9727 | 119.09 |

| Bus# | $\lvert V_{ac}^{a}\rvert$ (pu) | $\delta^{a}$ (deg) | $\lvert V_{ac}^{b}\rvert$ (pu) | $\delta^{b}$ (deg) | $\lvert V_{ac}^{c}\rvert$ (pu) | $\delta^{c}$ (deg) |
|---|---|---|---|---|---|---|
| 62 | 0.9666 | − 1.29 | 0.9743 | −120.63 | 0.9706 | 119.08 |
| 63 | 0.9660 | − 1.28 | 0.9734 | −120.61 | 0.9696 | 119.07 |
| 64 | 0.9657 | − 1.26 | 0.9716 | −120.58 | 0.9674 | 119.04 |
| 65 | 0.9651 | − 1.27 | 0.9713 | −120.53 | 0.9644 | 119.03 |
| 66 | 0.9653 | − 1.29 | 0.9715 | −120.50 | 0.9629 | 119.03 |
| 67 | 0.9683 | − 1.37 | 0.9754 | −120.76 | 0.9728 | 119.01 |
| 68 | 0.9667 | − 1.40 | | | | |
| 69 | 0.9648 | − 1.44 | | | | |
| 70 | 0.9635 | − 1.47 | | | | |
| 71 | 0.9627 | − 1.48 | | | | |
| 72 | 0.9686 | − 1.47 | 0.9744 | −120.87 | 0.9725 | 118.88 |
| 73 | | | | | 0.9703 | 118.84 |
| 74 | | | | | 0.9685 | 118.80 |
| 75 | | | | | 0.9674 | 118.78 |
| 76 | 0.9684 | − 1.53 | 0.9737 | −120.97 | 0.9731 | 118.83 |
| 77 | 0.9695 | − 1.60 | 0.9747 | −121.05 | 0.9738 | 118.75 |
| 78 | 0.9698 | − 1.62 | 0.9751 | −121.06 | 0.9739 | 118.73 |
| 79 | 0.9695 | − 1.63 | 0.9752 | −121.07 | 0.9739 | 118.74 |
| 80 | 0.9717 | − 1.68 | 0.9766 | −121.12 | 0.9746 | 118.62 |
| 81 | 0.9737 | − 1.76 | 0.9787 | −121.15 | 0.9750 | 118.51 |
| 82 | 0.9745 | − 1.80 | 0.9799 | −121.18 | 0.9757 | 118.48 |
| 83 | 0.9756 | − 1.82 | 0.9809 | −121.21 | 0.9765 | 118.43 |
| 84 | | | | | 0.9723 | 118.46 |
| 85 | | | | | 0.9710 | 118.43 |
| 86 | 0.9674 | − 1.57 | 0.9718 | −121.14 | 0.9744 | 118.80 |
| 87 | 0.9668 | − 1.59 | 0.9710 | −121.24 | 0.9749 | 118.78 |
| 88 | 0.9667 | − 1.62 | | | | |
| 89 | 0.9664 | − 1.59 | 0.9707 | −121.28 | 0.9753 | 118.76 |
| 90 | | | 0.9706 | −121.32 | | |
| 91 | 0.9662 | − 1.59 | 0.9704 | −121.30 | 0.9754 | 118.75 |
| 92 | | | | | 0.9753 | 118.69 |
| 93 | 0.9658 | − 1.59 | 0.9702 | −121.32 | 0.9755 | 118.75 |
| 94 | 0.9651 | − 1.61 | | | | |
| 95 | 0.9658 | − 1.58 | 0.9698 | −121.34 | 0.9757 | 118.75 |

| Bus# | $\lvert V_{ac}^{a}\rvert$ (pu) | $\delta^{a}$ (deg) | $\lvert V_{ac}^{b}\rvert$ (pu) | $\delta^{b}$ (deg) | $\lvert V_{ac}^{c}\rvert$ (pu) | $\delta^{c}$ (deg) |
|---|---|---|---|---|---|---|
| 96 | | | 0.9695 | −121.34 | | |
| 97 | 0.9697 | − 1.29 | 0.9759 | −120.74 | 0.9735 | 119.05 |
| 98 | 0.9694 | − 1.30 | 0.9757 | −120.75 | 0.9734 | 119.04 |
| 99 | 0.9697 | − 1.29 | 0.9748 | −120.76 | 0.9731 | 119.00 |
| 100 | 0.9699 | − 1.29 | 0.9748 | −120.75 | 0.9727 | 118.98 |
| 450 | 0.9699 | − 1.29 | 0.9748 | −120.75 | 0.9727 | 118.98 |
| 101 | 0.9713 | − 1.20 | 0.9767 | −120.71 | 0.9744 | 119.09 |
| 102 | | | | | 0.9729 | 119.06 |
| 103 | | | | | 0.9714 | 119.03 |
| 104 | | | | | 0.9695 | 118.99 |
| 105 | 0.9726 | − 1.10 | 0.9776 | −120.71 | 0.9763 | 119.18 |
| 106 | | | 0.9764 | −120.73 | | |
| 107 | | | 0.9749 | −120.76 | | |
| 108 | 0.9742 | − 1.00 | 0.9797 | −120.66 | 0.9780 | 119.30 |
| 300 | 0.9838 | − 0.47 | 0.9838 | −120.47 | 0.9838 | 119.53 |
| 109 | 0.9700 | − 1.08 | | | | |
| 110 | 0.9680 | − 1.12 | | | | |
| 111 | 0.9673 | − 1.14 | | | | |
| 112 | 0.9674 | − 1.13 | | | | |
| 113 | 0.9654 | − 1.17 | | | | |
| 114 | 0.9649 | − 1.18 | | | | |

Moreover, the effect of the transformer delta-wye connection on the DG phase loading can be concluded from the results in Table 5.6. It is observed that not only the total DG active and reactive powers are higher at the DG terminals (node#251) than those at the microgrid's bus (node#250) due to the transformer impedance, but also the power unbalances among the three phases are different at the two nodes because of the transformer delta-wye connection. This analysis is critical, in particular, for microgrids' loadability studies [1], [2]. The proposed method accounts for various system components and their different characteristics, ensuring more accurate analysis compared to other methods.

To further investigate the robustness and performance of the proposed approach in solving larger-scale microgrids, the analysis performed in Sections 5.5.2 and 5.5.3 were repeated for test microgrid#5.2. Table 5.7 presents the maximum and minimum microgrid

Table 5.6: DG output phase powers for test microgrid#5.2

| DG# | Node# | $P^a_{ac,G}$ (pu) | $P^b_{ac,G}$ (pu) | $P^c_{ac,G}$ (pu) | $Q^a_{ac,G}$ (pu) | $Q^b_{ac,G}$ (pu) | $Q^c_{ac,G}$ (pu) |
|---|---|---|---|---|---|---|---|
| 1 | 149 | 0.1042 | 0.0817 | 0.0902 | 0.0390 | 0.0310 | 0.0448 |
| 2 | 300 | 0.0855 | 0.0467 | 0.0649 | 0.0425 | 0.0243 | 0.0207 |
| 3 | 250 | 0.0883 | 0.0576 | 0.0721 | 0.0235 | 0.0110 | 0.0101 |
| 4 | 251 | 0.0849 | 0.0692 | 0.0650 | 0.0146 | 0.0284 | 0.0079 |

Table 5.7: Robustness results (test microgrid#5.2)

| $\lambda$ | 0.0 | 0.5 | 1.0 | 1.5 |
|---|---|---|---|---|
| Max. node voltage | 1.0284 | 1.0048 | 0.9915 | 0.9844 |
| Min. node voltage | 1.0046 | 0.9840 | 0.9577 | 0.9308 |
| #iterations | 8 | 7 | 7 | 7 |

voltages as well as the number of iterations for the algorithm to converge. Meanwhile, Table 5.8 compares the proposed approach's performance against that of the NTR method. It is noteworthy that since the NTR approach does not model delta-connected loads, the microgrid loads were all converted to wye-connection, for the sake of performance comparison. As seen in Table 5.8, the performance superiority of the proposed algorithm becomes more evident with the increase in the microgrid size. Overall, the results solidify the previously obtained ones for test microgrid#5.1, and therefore they confirm the approach's robustness and enhanced performance over the conventional one.

Table 5.8: Performance comparison (test microgrid#5.2)

| | Proposed method | | NTR [12] | |
|---|---|---|---|---|
| Tolerance | $1.0 \times 10^{-6}$ | $1.0 \times 10^{-12}$ | $1.0 \times 10^{-6}$ | $1.0 \times 10^{-12}$ |
| Solution time (ms) | 467 | 1,009 | 111,849 | 144,827 |
| #iterations | 3 | 10 | 3 | 4 |

### 5.6.2 Isochronously-Controlled Microgrid

This case studies the microgrid's isochronous operation. The active and reactive power ratings of SGDG (DG#1) are increased to 4.0 and 5.0 pu, respectively, allowing it to dominate the microgrid's operation. Furthermore, its droop gains $\mu$ and $\eta$ are set to infinity, resulting in tight regulation of microgrid's frequency at its reference value of $\omega = 1.00$ pu. On the other hand, DG#2 and DG#3 are droop-controlled and their droop set-points, $\omega_0$ and $V_{ac,0}$, can be adjusted to control their output powers.

To examine the effect of changing the frequency set-point on the microgrid operation, DG#2's frequency set-point $\omega_0$ was gradually changed from 0.975 to 1.025 pu, while DG#3's was kept constant at 1.00 pu. Figure 5.10a depicts the changes of the output active power of the three phases of DG#2, while Figure 5.10b shows the total output power of the three DGs. Although the output power of the three-phases are unequal due to the system unbalances, it can generally be observed that the phase active powers proportionally increase with the frequency set-point if set above the microgrid frequency (i.e., $\omega_0 > 1.00$ pu). Furthermore, as the set-point is decreased below the microgrid frequency (i.e., $\omega_0 < 1.00$ pu), the active power reverses direction meaning that the DG absorbs power, which can be desirable for ESSs. Moreover, as DG#2 approaches its active power capacity in either direction (i.e., $\omega_0 < 0.98$ pu or $\omega_0 > 1.02$ pu), the power is limited to the maximum value, which verifies the effectiveness of the proposed algorithm in enforcing DG limits in the solution. Note that, as illustrated in Figure 5.10b, the total output active power of DG#3 is zero regardless of the set-point of DG#2 because its set-point is fixed at the microgrid's frequency. However, as DG#2's active power changes, the isochronous DG autonomously adjusts its power to maintain successful microgrid operation, since it acts as a non-ideal slack bus.

Similarly, DG#2's voltage set-point $V_{ac,0}$ was gradually changed from 0.825 to 1.100 pu. The corresponding phase reactive powers are plotted in Figure 5.11a. Unlike the microgrid frequency, the voltage is not a global variable, and thus the DG injects reactive power at $V_{ac,0} = 1.00$ pu due to voltage drops across the feeders. Nevertheless, the DG's reactive power approaches zero at $V_{ac,0} \approxeq 0.96$ pu where the set-point is almost equal to the DG's positive-sequence terminal voltage. Below this value, DG#2 absorbs reactive power from the microgrid. The algorithm is also capable of limiting the DG's reactive power as it approaches its maximum value in either direction. The effect of changing DG#2's voltage set-point on other DGs is demonstrated in Figure 5.11b. The figure shows that, due to different deviations in bus voltages, DG#3's reactive power is neither zero nor constant as DG#2's voltage set-point is being changed. However, the significant reactive power changes are observed in the controlled DG (i.e., DG#2) and the isochronous SGDG, as it

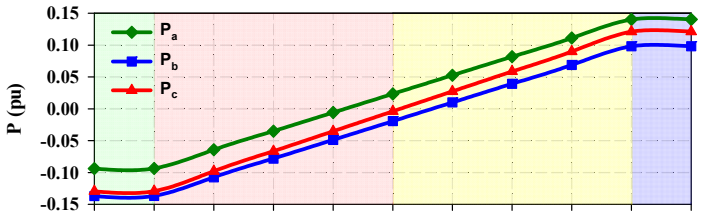


(a) DG#2 phase active powers

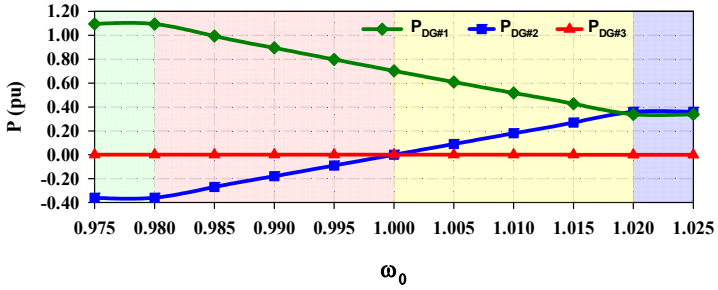


(b) Active powers of all DGs

Figure 5.10: Effects of changing the droop frequency set-point on active powers.

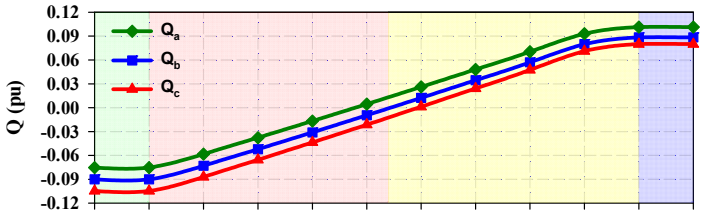


(a) DG#2 phase reactive powers

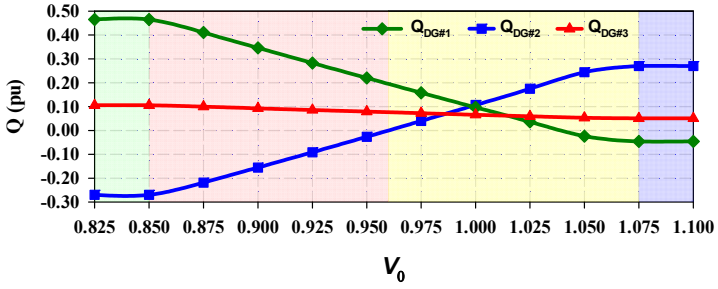


(b) Reactive powers of all DGs

Figure 5.11: Effects of changing the droop voltage set-point on reactive powers.

maintains the reactive power balance of the microgrid.

It is worth mentioning that the results also confirm the algorithm's robustness when solving isochronous microgrids, as it converged under a wide range of DG settings. Although the microgrid's node voltages varied from values as low as 0.9016 p.u at $V_{ac,0} = 0.825$ pu to values as high as 1.0093 pu at $V_{ac,0} = 1.10$ pu, the algorithm successfully converged under both normal and extreme operational conditions.

## 5.7 Conclusions and Discussion

Steady-state analysis is crucial for planning and operation studies of microgrids. Since microgrids can be controlled in either droop or isochronous modes, the development of a generic, accurate, and computationally-efficient power flow analysis approach becomes essential. The unbalanced nature of distribution networks and the possibility of the coexistence of SGDGs and EIDGs entail precise modeling of their different characteristics. In this chapter, a generalized methodology based on symmetrical sequence component analysis of microgrids was developed. The models of different DG types were presented and integrated into the power flow formulation. An NR algorithm was used to solve the power flow problem while taking the DG droop characteristics and power limits into consideration.

The IEEE 13-node test feeder was modified to form a droop-controlled microgrid for model and algorithm validation. The detailed time-domain model of the test system was built and simulated in MATLAB/Simulink. The close match between the results of the algorithm and time-domain simulations proves the accuracy of the developed method. Furthermore, two case studies, incorporating a modified IEEE 123-node test microgrid, were introduced to examine the effectiveness of the proposed method in analyzing more complex microgrids, and to study the operation of droop-based DGs in isochronous microgrids. The results shed light on the use of droop settings for 4-quadrant control of dispatchable units in isochronous microgrids. They also show the effectiveness of the proposed algorithm in limiting the DGs' powers, in both directions, as they approach their limits.

Moreover, the robustness of the proposed algorithm was tested through changing the test microgrids' operational conditions from light to heavy loading, and from droop to isochronous modes of operation. The algorithm demonstrated solid convergence characteristics under various testing conditions. Furthermore, the algorithm showed superior performance, in terms of accuracy and execution time, when compared to the reported NTR approach.

# Chapter 6

# An Improved Modeling and Power Flow Analysis Approach for Unbalanced Islanded Hybrid AC/DC Microgrids

## 6.1 Introduction

In Chapter 5, a comprehensive modeling and power flow analysis approach for standalone unbalanced ac microgrids was developed. In this chapter, the work is extended to include the dc subgrid and ICs to provide a complete, accurate, and efficient platform for steady-state analysis of hybrid ac/dc microgrids. Accordingly, this chapter proposes an enhanced sequential power flow algorithm – as compared with the unified power flow algorithm previously developed in Chapter 3 – that takes the features of islanded hybrid ac/dc microgrids into consideration. First, an NR method is adopted to solve for the decoupled symmetrical components of the unbalanced ac subgrid. Subsequently, the coupling parameters between the ac and dc subgrids are updated; henceforth, the dc subgrid is solved. The algorithm exhibits three main merits over the one based on NTR [1]

1. *Generality* – the approach considers the unbalanced features of ac subgrids, integration and coexistence of various DG types, and parallel operation of ICs.

2. *Computational efficiency* – the algorithm breaks down the system model into smaller decoupled ac and dc sets of equations, and further divides the ac system into smaller

symmetrical component models that are solved independently, thereby significantly reducing the computational requirements [41], [35].

3. *Accuracy* – different models are adopted to represent the features of different DG types (i.e., SGDG and EIDG) in symmetrical components, rather than one inaccurate unified model in phase coordinates [36].

The remainder of the chapter is organized as follows: Section 6.2 illustrates the core differences between the conventional unified and the proposed sequential power flow approaches. Section 6.3 reviews the steady-state modeling of the ac subgrid based on symmetrical component analysis. Section 6.4 describes the dc subgrid's steady-state modeling. ICs' models, considering their different control schemes, are presented in Section 6.5. The proposed power flow algorithm is thoroughly explained in Section 6.6. Section 6.7 validates the proposed algorithm through comparisons with time-domain simulations. The algorithm's computational efficiency and limit-enforcement capabilities are examined, through further case studies, in Section 6.8. Finally, Section 6.9 concludes the chapter.

## 6.2 Sequential versus Unified Power Flow Approaches for Unbalanced Hybrid AC/DC Microgrids

Computational and memory requirements are crucial factors in defining the computational efficiency of power flow algorithms. In conventional unified power flow approaches for hybrid ac/dc microgrids, the ac and dc power flow problems, in addition to the coupling between the two through ICs, are integrated into one problem. Accordingly, the unbalanced ac subgrid comprising $N_{ac}$ nodes introduces $6N_{ac}$ equations for the active and reactive powers of the three phases at each node. Additionally, the dc subgrid with $N_{dc}$ nodes introduces $N_{dc}$ power flow equations. Finally, if the two subgrids are coupled through $N_{IC}$ ICs, their active power equations are added to the problem. Altogether, the microgrid components result in a problem of size $(6N_{ac} + N_{dc} + N_{IC})$. Considering the dramatic nonlinear increase in the memory and computational requirements of matrix operations – typically used in power flow algorithms – with the matrix size, solving such a problem becomes computationally inefficient, especially for online and large-scale microgrid applications.

In this work, a sequential approach is proposed to break down the system model into smaller subsystems, thus resulting in considerable reduction in the problem solution requirements. The proposed approach constructs the ac and dc power flow problems separately. The ac subproblem solves only for the ac variables. In addition, instead of formulating the ac problem in phase coordinates leading to a problem size of $6N_{ac}$, decoupled

sequence component analysis is adopted to break down the ac subgrid into smaller subsystems of sizes $2N_{ac}$, $N_{ac}$, and $N_{ac}$ for the positive-, negative-, and zero-sequence subsystems, respectively. These decoupled ac subsystems can be solved in parallel, leading to significant improvement in the ac subproblem solution time. On the other hand, the dc power flow subproblem – of size $(N_{dc} + N_{IC})$ – incorporates the dc subgrid power flow as well as the IC equations. The correlation between the ac and dc subproblems is conserved by updating the dc power flow variables based on the ac power flow results in a sequential manner. These multiple reductions in the problem size extensively enhance the algorithm performance as compared to conventional unified approaches.

## 6.3 AC Subgrid Modeling in Sequence Components

The complete ac subgrid modeling is identical to the unbalanced ac microgrid modeling presented earlier in Section 5.3.

## 6.4 DC subgrid Modeling

Steady-state modeling of dc microgrids is simpler than that of their ac counterparts, since they do not include complex impedances, reactive powers, and unbalances. This section describes the steady-state models of the dc subgrid's main components.

### 6.4.1 DC DG Modeling

Modern dc microgrids adopt droop-controlled dc generation to partially or fully feed the local dc loads, and to exchange power with external systems. Droop-controlled dc DGs employ dc/dc converters and local controllers, as shown in Figure 6.1a. Thus, a droop-controlled dc DG can be simplified as in Figure 6.1b. Droop control allows proportional power sharing among dc DGs, which is mathematically represented, for a DG at an arbitrary dc bus $i$, as

$$P_{dc,G,i} = \vartheta_{P,i} \left( V_{dc,0,i} - V_{dc,i} \right) \tag{6.1}$$

where $P_{dc,G,i}$ is the dc DG's output power,$V_{dc,0,i}$ and $V_{dc,i}$ the DG's output voltages at no-load and under load, respectively, and $\vartheta_{P,i}$ the droop gain. The droop gain is set according

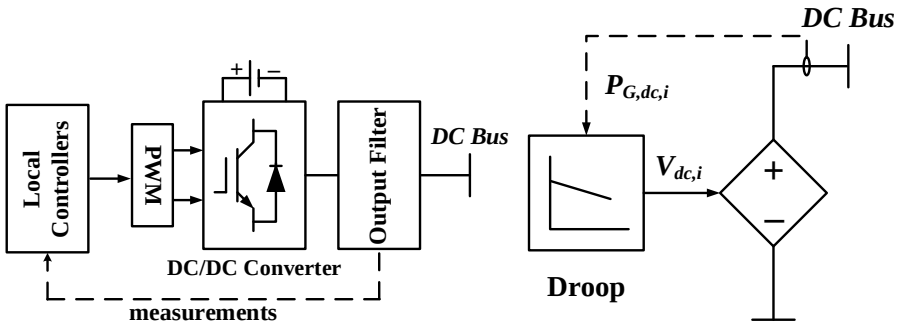


(a) Schematic diagram (b) Simplified model

Figure 6.1: Schematic diagram and simplified model of droop-controlled DC DG.

to (6.2) to attain the desired proportional power sharing, yet with some inevitable error due to voltage mismatches among dc buses.

$$\vartheta_{P,i} = \frac{P_{dc,G,i}^{max}}{V_{dc,max} - V_{dc,min}} \tag{6.2}$$

In (6.2) $P_{dc,G,i}^{max}$ is the maximum DG power, and $V_{dc,max}$ and $V_{dc,min}$ the maximum and minimum allowed dc voltages, respectively.

### 6.4.2 DC Feeder Modeling

Line resistance is the only parameter representing dc feeders at steady-state. Thus, for any feeder connecting dc nodes $i$ and $j$, conductance can be given in terms of the total line resistance $r_{ij}$ as

$$g_{ij} = \frac{1}{r_{ij}} \tag{6.3}$$

### 6.4.3 DC Load Modeling

Similar to ac loads, a generic dc load model, given by (6.4), is used to describe the load power as a function of the dc voltage.

$$P_{dc,L,i} = P_{dc,L,i}^{0}(V_{dc,i})^{\varrho} \tag{6.4}$$

In (6.4), $P_{dc,L,i}^{0}$ is the load rated-power and $\varrho$ the power exponent that is assigned a value of 0, 1, or 2 for constant-power, constant-current, or constant-impedance loads, respectively.

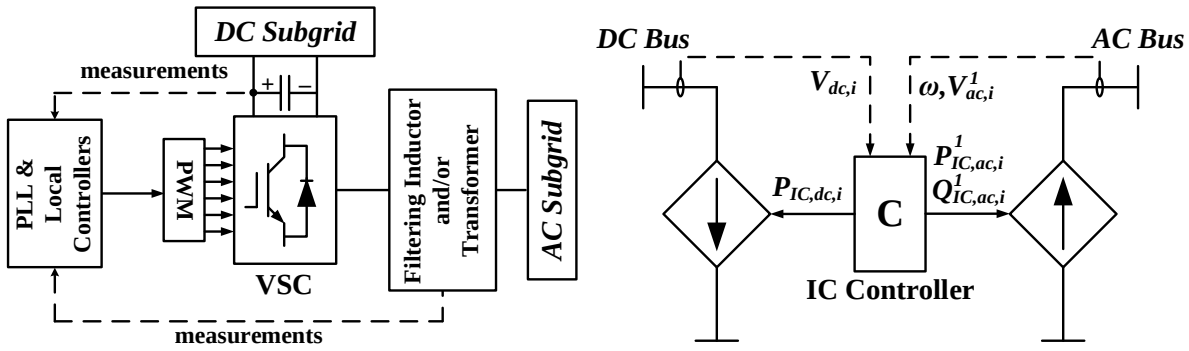


(a) Schematic diagram (b) Simplified model

Figure 6.2: Schematic diagram and simplified model of IC.

## 6.5 Interlinking Converter Modeling in Sequence Components

Typically, ICs implement three-phase bidirectional current-controlled VSCs that inject/absorb balanced three-phase currents to/from the ac subgrid and absorb/inject dc current from/to the dc subgrid, as shown in Figure 6.2a. Therefore, the converter is seen from the ac side as a power source/load in the positive-sequence frame, whereas it is represented as open circuits for negative- and zero-sequence models. At the dc side, the converter is seen as a dc load/source, as depicted in the simplified model in Figure 6.2b.

The amount of power transferred through an IC depends on the adopted IC control scheme, which is also related to the microgrid configuration. To attain generality, ac and dc subgrids are assumed droop-controlled, and are interlinked through multiple droop-controlled ICs to share the power exchanged between the subgrids. For autonomous operation, the $l$th IC locally measures the ac subgrid's frequency, $\omega$, and the dc subgrid's voltage at its terminal, $V_{dc,l}$, and calculates their per-unit deviations as

$$\Delta\omega_{pu} = \frac{\omega - 0.5(\omega_{max} + \omega_{min})}{0.5(\omega_{max} - \omega_{min})} \tag{6.5}$$

$$\Delta V_{dc,pu,l} = \frac{V_{dc,l} - 0.5(V_{dc,max} + V_{dc,min})}{0.5(V_{dc,max} - V_{dc,min})} \tag{6.6}$$

Then, the IC implements (6.7) to autonomously determine its share of the active power

$P^1_{ac,IC,l}$ transferred between the two subgrids.

$$P^1_{ac,IC,l} = \frac{1}{3}\gamma_l(\Delta\omega_{pu} - \Delta V_{dc,pu,l}) \tag{6.7}$$

In (6.7), the IC droop gain $\gamma_l$ is set according to (6.8) to attain proportional power sharing, where $S^{max}_{IC,l}$ is the IC's rated power and $e_{ac-dc,max}$ the globally defined difference between $\Delta\omega_{pu}$ and $\Delta V_{dc,pu,l}$ at, or beyond, which all ICs should ideally transfer their maximum powers. It is worth mentioning that inaccuracies in proportional power sharing among ICs are expected due to unequal dc voltages at different ICs' dc terminals [1], [26].

$$\gamma_l = \frac{S^{max}_{IC,l}}{e_{ac-dc,max}} \tag{6.8}$$

Moreover, an IC usually provides reactive power support to the ac subgrid as long as its capacity, $S^{max}_{IC,l}$, is not fully occupied by the prioritized active power. Therefore, bound by the maximum value given by (6.9), ICs inject reactive power $Q^1_{ac,IC,l}$ following the droop characteristics in (6.10). The droop gain $\eta_l$ is calculated using (6.11), where the constant $\rho$ is unified for all ICs.

$$Q^1_{ac,IC,max,l} = \sqrt{\left(S^{max}_{IC,i}\right)^2 - \left(P^1_{ac,G,i}\right)^2} \tag{6.9}$$

$$Q^1_{ac,IC,l} = \eta_l \left(V_{ac,l,0} - \left|V^1_{ac,l}\right|\right) \tag{6.10}$$

$$\eta_l = \rho \, \frac{S^{max}_{IC,l}}{V_{ac,max} - V_{ac,min}} \qquad 0 < \rho \leq 1 \tag{6.11}$$

For a hybrid ac/dc microgrid integrating a single IC, a tighter control scheme, using a PI controller, can be adopted to achieve

$$\Delta\omega_{pu} = \Delta V_{dc,pu,l} \tag{6.12}$$

Mathematically, equation (6.12) can be deduced from the general formula (6.7) by setting $e_{ac-dc,max}$ to zero in (6.8). Similarly, other control schemes for ICs can be deduced from (6.7) by applying minor modifications, which renders the proposed approach generic.

## 6.6 Proposed AC/DC Microgrid Power Flow Algorithm

For minimized computational requirements, this work proposes a sequential power flow algorithm, illustrated in Figure 6.3, which sequentially solves the decoupled ac and dc subgrid equations, while maintaining the correlation between the two, according to the IC control scheme. The independent solution of each subgrid's set of equations considerably reduces the algorithm's execution time as compared to those in unified approaches, because it allows conducting mathematical operations on smaller matrices, instead of one large matrix describing the entire system. Besides, the symmetrical component method further reduces the ac power flow subroutine's execution time, as it permits parallel solution of the symmetrical component models. The following subsections explain the algorithm's subroutines in detail.

### 6.6.1 AC Power Flow

The positive-sequence power flow is solved using a modified NR method to accommodate the ac subgrid's droop-characteristics. For an ac subgrid comprising $N_{ac}$ buses, the total injected active and reactive powers at any node $i$ can be described as

$$P^1_{ac,i} = \sum_{j \in N_{ac}} \left|V^1_{ac,i}\right| \left|V^1_{ac,j}\right| \left|Y^{11}_{ij}\right| \cos\left(\delta^1_i - \delta^1_j - \theta^{11}_{ij}\right) \tag{6.13}$$

$$Q^1_{ac,i} = \sum_{j \in N_{ac}} \left|V^1_{ac,i}\right| \left|V^1_{ac,j}\right| \left|Y^{11}_{ij}\right| \sin\left(\delta^1_i - \delta^1_j - \theta^{11}_{ij}\right) \tag{6.14}$$

where $\left(\left|V^1_{ac,i}\right| \text{ and} \left|V^1_{ac,j}\right|\right)$ and $(\delta^1_i \text{ and } \delta^1_j)$ are the positive-sequence voltage magnitudes and angles at nodes $i$ and $j$, respectively, and $\left|Y^{11}_{ij}\right|$ and $\theta^{11}_{ij}$ the positive-sequence Y-bus matrix element's magnitude and angle, respectively. Accordingly, the node's power mismatch equations can be formulated as

$$\Gamma_{ac,P,i} = P^1_{ac,G,i} + P^1_{ac,IC,l} - P^1_{ac,L,i} - P^1_{ac,i} - \sum_{j \in N_{ac} \setminus i} \Delta P^1_{ac,i-j} \tag{6.15}$$

$$\Gamma_{ac,Q,i} = Q^1_{ac,G,i} + Q^1_{ac,IC,l} - Q^1_{ac,L,i} - Q^1_{ac,i} - \sum_{j \in N_{ac} \setminus i} \Delta Q^1_{ac,i-j} \tag{6.16}$$

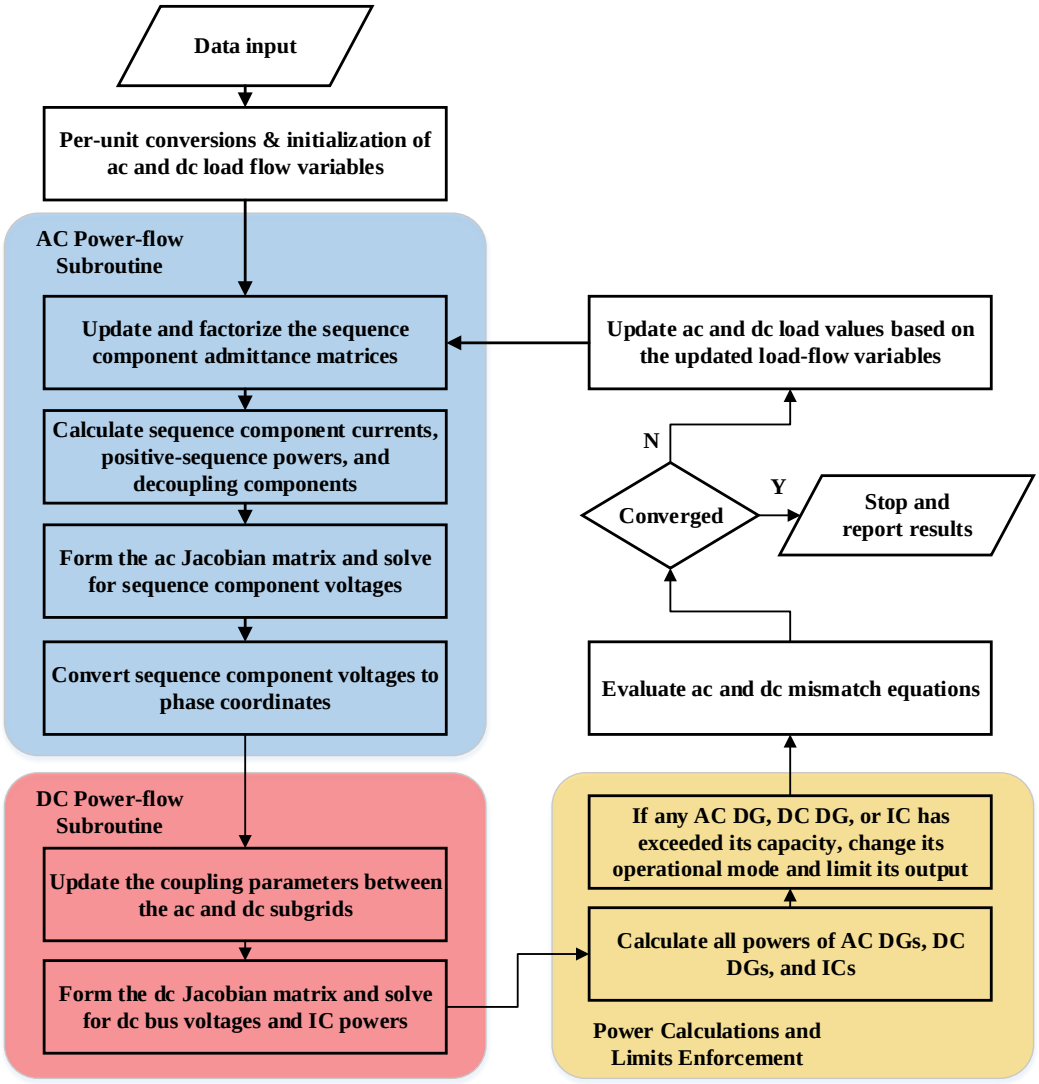


Figure 6.3: Flow chart of the proposed hybrid ac/dc power flow algorithm

In (6.15) and (6.16), the IC's active and reactive powers ($P^1_{ac,IC,l}$ and $Q^1_{ac,IC,l}$) are assumed constant with values based on the results of the preceding iteration. They are set to zero at the initialization stage or if no IC is connected to bus $i$.

Considering that the ac subgrid's frequency is a power flow variable, the ac Jacobian matrix $J_{ac}$ can be defined as

$$J_{ac} = \begin{bmatrix} \dfrac{\partial \Gamma_{\mathbf{ac,P}}}{\partial |\mathbf{V^1_{ac}}|} & \dfrac{\partial \Gamma_{\mathbf{ac,P}}}{\partial \delta^{\mathbf{1}}} & \dfrac{\partial \Gamma_{\mathbf{ac,P}}}{\partial \omega} \\ \dfrac{\partial \Gamma_{\mathbf{ac,Q}}}{\partial |\mathbf{V^1_{ac}}|} & \dfrac{\partial \Gamma_{\mathbf{ac,Q}}}{\partial \delta^{\mathbf{1}}} & \dfrac{\partial \Gamma_{\mathbf{ac,Q}}}{\partial \omega} \end{bmatrix} \tag{6.17}$$

where $\left|\mathbf{V^1_{ac}}\right|$ and $\delta^{\mathbf{1}}$ are the positive-sequence node voltage magnitude and angle vectors, respectively. At iteration $(k+1)$, the positive-sequence voltage magnitudes, frequency, and angles are calculated, in terms of their values at iteration $(k)$, as

$$\begin{bmatrix} \left|\mathbf{V^1_{ac}}\right|_{(k+1)} \\ \delta^{\mathbf{1}}{}_{(k+1)} \\ \omega_{(k+1)} \end{bmatrix} = \begin{bmatrix} \left|\mathbf{V^1_{ac}}\right|_{(k)} \\ \delta^{\mathbf{1}}{}_{(k)} \\ \omega_{(k)} \end{bmatrix} - J_{ac}^{-1} \begin{bmatrix} \Gamma_{\mathbf{ac,P}(k)} \\ \\ \Gamma_{\mathbf{ac,Q}(k)} \end{bmatrix} \tag{6.18}$$

It is worth mentioning that although the ac subgrid lacks a slack bus, the first bus's angle $\delta^1_1$ is set to zero, so that the number of ac unknowns, $2N_{ac}$, is equal to the number of system equations.

The negative- and zero-sequence complex node voltage vectors can be directly calculated from the linear relations

$$\mathbf{V^0_{ac}}_{(k+1)} = \left[Y^{00}_{(k+1)}\right]^{-1} \left[-\mathbf{I^0_{ac,L}}_{(k+1)} - \mathbf{\Delta I^0_{ac}}_{(k+1)}\right] \tag{6.19}$$

$$\mathbf{V^2_{ac}}_{(k+1)} = \left[Y^{22}_{(k+1)}\right]^{-1} \left[-\mathbf{I^2_{ac,L}}_{(k+1)} - \mathbf{\Delta I^2_{ac}}_{(k+1)}\right] \tag{6.20}$$

where $Y^{00}$ and $Y^{22}$ are the zero- and negative-sequence Y-bus matrices, and $\mathbf{\Delta I^0_{ac}}$ and $\mathbf{\Delta I^2_{ac}}$ the decoupling current vectors comprising the total decoupling currents at each node $i$, given as

$$\Delta I^0_{ac,i} = \sum_{j \in N_{ac}} \Delta I^0_{ac,i-j} \tag{6.21}$$

$$\Delta I^2_{ac,i} = \sum_{j \in N_{ac}} \Delta I^2_{ac,i-j} \tag{6.22}$$

### 6.6.2 Correlation between AC and DC Subgrids

To allow independent solutions of the power flow problems of the ac and dc subgrids, while maintaining the correlation between them, the mutual effects between the subgrids have to be integrated into the algorithm. Considering the ac subgrid, the total power transferred through the ICs can be represented as a dummy DG with the following droop characteristic [23]

$$P^1_{IC,total} = \sum P^1_{ac,IC,l} = \frac{1}{3}\mu_{ac}(\omega_{0,ac} - \omega) \tag{6.23}$$

where the virtual droop gain $\mu_{ac}$ and no-load frequency $\omega_{0,ac}$ are defined by

$$\mu_{ac} = -\frac{\partial P^1_{IC,total}}{\partial \omega} \tag{6.24a}$$

$$\omega_{0,ac} = \omega + \frac{P^1_{IC,total}}{\mu_{ac}} \tag{6.24b}$$

Note that the values of $\mu_{ac}$ and $\omega_{0,ac}$ are not fixed, and are updated at each power flow algorithm iteration.

On the other hand, to decouple ICs' powers at the dc side from the ac subgrid's variables, the frequency  is substituted from (6.23) in (6.7). Consequently, the ICs' active power mismatch equation can be formulated as a function of the dc voltages as

$$\mathit{\Gamma}_{IC,P,l} = P^1_{ac,IC,l} + a^{-}_{V,l} V_{dc,l} + a_{PV,l} + a_{ac,l} \sum_{j \neq l} P^1_{ac,IC,j} \tag{6.25}$$

where

$$\begin{aligned}
a^{-}_{V,l} &= \frac{a_V \mu_{ac} \gamma_l}{3\left(a_\omega \gamma_l + \mu_{ac}\right)} \\
a_{PV,l} &= \frac{\mu_{ac}\gamma_l \left(a_{\omega V} - a_\omega \omega_{0,ac}\right)}{3\left(a_\omega \gamma_l + \mu_{ac}\right)} \\
a_{ac,l} &= \frac{a_\omega \gamma_l}{a_\omega \gamma_l + \mu_{ac}} \\
a_V &= \frac{2}{V_{dc,max} - V_{dc,min}} \\
a_\omega &= \frac{2}{\omega_{max} - \omega_{min}} \\
a_{\omega V} &= \frac{\omega_{max} + \omega_{min}}{\omega_{max} - \omega_{min}} - \frac{V_{dc,max} + V_{dc,min}}{V_{dc,max} - V_{dc,min}}
\end{aligned}$$

Hence, the ICs' mismatch power equations, given by (6.25), can be integrated into the independent dc power flow subroutine. It is worth noting that if a microgrid implements a single IC, the droop gain $\gamma_l$ is set to infinity, and all the other ICs' powers $P^1_{ac,IC,j}$ in (6.25) are set to zero, which leads to the same formulas presented in [23].

### 6.6.3 DC Power Flow

The dc power flow solves for the dc bus voltages as well as the ICs' active powers. Assuming a dc subgrid with $N_{dc}$ nodes, the dc power injected at any node $i \in N_{dc}$ is given by

$$P_{dc,i} = V_{dc,i} \sum_{j \in N_{dc}} V_{dc,j} G_{ij} \tag{6.26}$$

where $G_{ij}$ is the conductance matrix element. Thus, the node's power mismatch equation is formulated as

$$\Gamma_{dc,P,i} = P_{dc,G,i} + P_{dc,IC,l} - P_{dc,L,i} - P_{dc,i} \tag{6.27}$$

where $P_{dc,IC,l}$ is the IC's power at the dc side, which is related to the IC's power at the ac side, $P^1_{ac,IC,l}$, and the IC's losses, $P^1_{loss,IC,l}$, by

$$P_{dc,IC,l} = -3P^1_{ac,IC,l} + P^1_{loss,IC,l} \tag{6.28}$$

By integrating the ICs' power mismatch equations into the dc power flow, the dc Jacobian matrix $J_{dc}$ can be defined as

$$J_{dc} = \begin{bmatrix} \dfrac{\partial \Gamma_{\mathbf{dc,P}}}{\partial \mathbf{V_{dc}}} & \dfrac{\partial \Gamma_{\mathbf{dc,P}}}{\partial \mathbf{P_{IC}}} \\ \dfrac{\partial \Gamma_{\mathbf{IC,P}}}{\partial \mathbf{V_{dc}}} & \dfrac{\partial \Gamma_{\mathbf{IC,P}}}{\partial \mathbf{P_{IC}}} \end{bmatrix} \tag{6.29}$$

where $\mathbf{V_{dc}}$ and $\mathbf{P_{IC}}$ are the dc bus voltage and IC active power vectors, respectively. Similar to ac subgrids, the dc bus voltages and ICs' active powers can be calculated at iteration $(k+1)$, in terms of the variables at iteration $(k)$, using

$$\begin{bmatrix} \mathbf{V_{dc}}_{(k+1)} \\ \mathbf{P_{IC}}_{(k+1)} \end{bmatrix} = \begin{bmatrix} \mathbf{V_{dc}}_{(k)} \\ \mathbf{P_{IC}}_{(k)} \end{bmatrix} - J_{dc}^{-1} \begin{bmatrix} \Gamma_{\mathbf{dc,P}(k)} \\ \\ \Gamma_{\mathbf{IC,P}(k)} \end{bmatrix} \tag{6.30}$$

Finally, the output powers of all DGs and ICs are calculated. If any DG or IC exceeds its capacity, its power is restricted to the maximum value and its operational mode is changed from droop to constant-power.

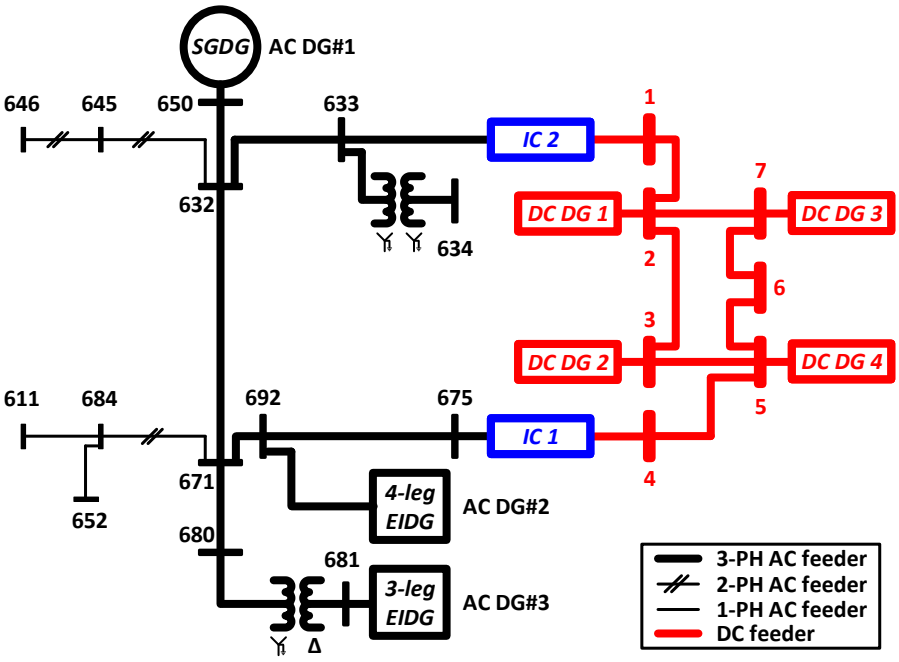


Figure 6.4: Test microgrid#6.1: modified IEEE 13-node ac/7-node dc microgrid.

## 6.7 Approach Validation

In order to verify the accuracy of the proposed models and power flow algorithm, a test hybrid ac/dc microgrid, shown in Figure 6.4, comprising a modified IEEE 13-node ac sub-grid [40] and a 7-node dc subgrid [130], was used. The ac subgrid integrates three droop-controlled AC DGs of various types, ratings, and droop settings, given in Table 6.1. The SGDG's data were obtained from a commercial generator's datasheet [139]. On the other hand, four DC DGs are connected to the dc subgrid, with their ratings and droop settings given in Table 6.2. The dc subgrid integrates three constant-power loads rated at 0.15, 0.10, and 0.08 pu, and connected to dc nodes 1, 4, and 6, respectively. The microgrid's size is relatively small to facilitate conducting time-domain simulations necessary for model and algorithm validation. Despite its small size, the ac subgrid integrates various components found in standard distribution systems, such as unbalanced feeders, unbalanced loads with various configurations, and distribution transformers with different connections. To render the validation procedure comprehensive, two cases were studied to verify the proposed approach's accuracy in solving hybrid ac/dc microgrids with single and multiple ICs, respectively. The ICs' data is given in Table 6.3.

Table 6.1: AC DGs' ratings and droop settings (test microgrid#6.1)

| DG# | DG Type | $\mu$ (pu) | $\eta$ (pu) | $\omega_0$ (pu) | $V_{ac,0}$ (pu) | $P_{ac,G}^{max}$ (pu) | $S_{ac,G}^{max}$ (pu) |
|---|---|---|---|---|---|---|---|
| 1 | SGDG | 25.2 | 7.56 | 1.00833 | 1.01 | 0.504 | 0.630 |
| 2 | 4-leg EIDG | 18.0 | 5.40 | 1.00833 | 1.01 | 0.360 | 0.450 |
| 3 | 3-leg EIDG | 20.0 | 6.00 | 1.00833 | 1.01 | 0.400 | 0.500 |

Table 6.2: DC DGs' ratings and droop settings (test microgrid#6.1)

| DG# | $\vartheta_P$ (pu) | $V_{dc,0}$ (pu) | $P_{dc,G}^{max}$ (pu) |
|---|---|---|---|
| 1,3 | 2.00 | 1.05 | 0.200 |
| 2,4 | 2.50 | 1.05 | 0.250 |

Table 6.3: ICs' ratings and reactive power droop settings (test microgrid#6.1)

| IC# | $\eta$ (pu) | $V_{ac,0}$ (pu) | $S_{IC}^{max}$ (pu) |
|---|---|---|---|
| 1 | 1.00 | 1.01 | 0.100 |
| 2 | 0.50 | 1.01 | 0.050 |

### 6.7.1 A Hybrid Microgrid with a Single IC

In this case, only IC1 is employed to interlink the two subgrids, and therefore it follows the control scheme in (6.12). In Table 6.4, , the power flow results obtained by implementing the proposed approach are compared with the steady-state results of the MATLAB/Simulink time-domain model of the same system. The close agreement of the results of the two methods proves that the proposed approach is accurate for steady-state analysis of hybrid ac/dc microgrids incorporating a single IC.

### 6.7.2 A Hybrid Microgrid with Multiple Droop-Controlled ICs

This case tests the proposed approach's validity for hybrid ac/dc microgrids with multiple droop-controlled ICs. The two ICs (IC1 and IC2) are connected to interface the two subgrids. The ICs' active powers follow the droop characteristics described by (6.7), while the global IC parameter $e_{ac-dc,max}$ is set to 3%. The results of the proposed method are contrasted against those obtained through MATAB/Simulink simulations in Table 6.5. The proposed approach solves for this configuration with high precision, which indicates its validity for different system configurations and IC control schemes. Tables 6.6 and 6.7 summarize the maximum per-unit and relative/percentage mismatches between the power flow variables obtained by the two methods (i.e., proposed and time-domain simulations) for the two cases (i.e., single and multiple ICs).

Table 6.4: Power flow results of test microgrid#6.1 (case#1 – single IC)

**MATLAB/Simulink**

| AC Bus# | $\lvert V_{ac}^{a}\rvert$ (pu) | $\delta^a$ (deg) | $\lvert V_{ac}^{b}\rvert$ (pu) | $\delta^b$ (deg) | $\lvert V_{ac}^{c}\rvert$ (pu) | $\delta^c$ (deg) | DC Bus# | $V_{dc}$ (pu) |
|---|---|---|---|---|---|---|---|---|
| 650 | 1.0025 | 0.00 | 0.9951 | −120.31 | 0.9966 | 120.11 | 1 | 1.0039 |
| 632 | 0.9913 | − 0.56 | 0.9820 | −121.35 | 0.9876 | 119.15 | 2 | 1.0054 |
| 633 | 0.9883 | − 0.63 | 0.9802 | −121.40 | 0.9850 | 119.16 | 3 | 1.0080 |
| 634 | 0.9653 | − 1.30 | 0.9622 | −121.87 | 0.9669 | 118.68 | 4 | 1.0018 |
| 645 | | | 0.9730 | −121.54 | 0.9857 | 119.18 | 5 | 1.0035 |
| 646 | | | 0.9714 | −121.61 | 0.9838 | 119.22 | 6 | 1.0040 |
| 671 | 0.9880 | − 1.26 | 0.9879 | −121.23 | 0.9883 | 118.76 | 7 | 1.0060 |
| 680 | 0.9920 | − 0.91 | 0.9908 | −120.87 | 0.9920 | 119.12 | | |
| 681 | 1.0014 | −29.61 | 1.0014 | −149.61 | 1.0014 | 090.39 | | |
| 684 | 0.9860 | − 1.28 | | | 0.9863 | 118.66 | | |
| 611 | | | | | 0.9844 | 118.52 | | |
| 652 | 0.9804 | − 1.21 | | | | | | |
| 692 | 0.9880 | − 1.26 | 0.9879 | −121.23 | 0.9883 | 118.76 | | |
| 675 | 0.9831 | − 1.47 | 0.9912 | −121.38 | 0.9874 | 118.80 | | |

$\omega = 0.998697$ pu $\qquad S_{IC,1} = 0.06607 + j0.02266$ pu

**Proposed method**

| AC Bus# | $\lvert V_{ac}^{a}\rvert$ (pu) | $\delta^a$ (deg) | $\lvert V_{ac}^{b}\rvert$ (pu) | $\delta^b$ (deg) | $\lvert V_{ac}^{c}\rvert$ (pu) | $\delta^c$ (deg) | DC Bus# | $V_{dc}$ (pu) |
|---|---|---|---|---|---|---|---|---|
| 650 | 1.0023 | 0.00 | 0.9946 | −120.27 | 0.9969 | 120.16 | 1 | 1.0039 |
| 632 | 0.9914 | − 0.49 | 0.9821 | −121.27 | 0.9875 | 119.23 | 2 | 1.0054 |
| 633 | 0.9885 | − 0.55 | 0.9802 | −121.32 | 0.9850 | 119.22 | 3 | 1.0080 |
| 634 | 0.9655 | − 1.22 | 0.9622 | −121.79 | 0.9669 | 118.75 | 4 | 1.0018 |
| 645 | | | 0.9731 | −121.46 | 0.9857 | 119.25 | 5 | 1.0035 |
| 646 | | | 0.9714 | −121.54 | 0.9837 | 119.30 | 6 | 1.0040 |
| 671 | 0.9881 | − 1.14 | 0.9881 | −121.14 | 0.9881 | 118.86 | 7 | 1.0060 |
| 680 | 0.9920 | − 0.84 | 0.9908 | −120.80 | 0.9920 | 119.21 | | |
| 681 | 1.0014 | −29.54 | 1.0014 | −149.54 | 1.0014 | 090.46 | | |
| 684 | 0.9862 | − 1.17 | | | 0.9862 | 118.76 | | |
| 611 | | | | | 0.9842 | 118.61 | | |
| 652 | 0.9806 | − 1.09 | | | | | | |
| 692 | 0.9881 | − 1.14 | 0.9881 | −121.14 | 0.9881 | 118.86 | | |
| 675 | 0.9832 | − 1.54 | 0.9914 | −121.47 | 0.9874 | 118.70 | | |

$\omega = 0.998703$ pu $\qquad S_{IC,1} = 0.06603 + j0.02264$ pu

Table 6.5: Power flow results of test microgrid#6.1 (case#2 – two ICs)

**MATLAB/Simulink**

| AC Bus# | $\lvert V_{ac}^{a}\rvert$ (pu) | $\delta^a$ (deg) | $\lvert V_{ac}^{b}\rvert$ (pu) | $\delta^b$ (deg) | $\lvert V_{ac}^{c}\rvert$ (pu) | $\delta^c$ (deg) | DC Bus# | $V_{dc}$ (pu) |
|---|---|---|---|---|---|---|---|---|
| 650 | 1.0035 | 0.00 | 0.9958 | −120.31 | 0.9975 | 120.12 | 1 | 1.0034 |
| 632 | 0.9927 | − 0.58 | 0.9831 | −121.36 | 0.9889 | 119.15 | 2 | 1.0051 |
| 633 | 0.9903 | − 0.63 | 0.9819 | −121.39 | 0.9870 | 119.16 | 3 | 1.0083 |
| 634 | 0.9673 | − 1.30 | 0.9639 | −121.86 | 0.9689 | 118.68 | 4 | 1.0033 |
| 645 | | | 0.9742 | −121.54 | 0.9871 | 119.17 | 5 | 1.0047 |
| 646 | | | 0.9725 | −121.62 | 0.9851 | 119.21 | 6 | 1.0049 |
| 671 | 0.9884 | − 1.35 | 0.9884 | −121.33 | 0.9887 | 118.66 | 7 | 1.0067 |
| 680 | 0.9925 | − 1.00 | 0.9912 | −120.96 | 0.9924 | 119.03 | | |
| 681 | 1.0017 | −29.69 | 1.0017 | −149.69 | 1.0017 | 090.31 | | |
| 684 | 0.9865 | − 1.38 | | | 0.9868 | 118.57 | | |
| 611 | | | | | 0.9849 | 118.42 | | |
| 652 | 0.9809 | − 1.30 | | | | | | |
| 692 | 0.9884 | − 1.35 | 0.9884 | −121.33 | 0.9887 | 118.66 | | |
| 675 | 0.9832 | − 1.58 | 0.9914 | −121.49 | 0.9875 | 118.69 | | |

$\omega = 0.998618$ pu, $S_{IC,1} = 0.04069 + j0.02252$ pu, $S_{IC,2} = 0.02140 + j0.01180$ pu

**Proposed method**

| AC Bus# | $\lvert V_{ac}^{a}\rvert$ (pu) | $\delta^a$ (deg) | $\lvert V_{ac}^{b}\rvert$ (pu) | $\delta^b$ (deg) | $\lvert V_{ac}^{c}\rvert$ (pu) | $\delta^c$ (deg) | DC Bus# | $V_{dc}$ (pu) |
|---|---|---|---|---|---|---|---|---|
| 650 | 1.0033 | 0.00 | 0.9953 | −120.27 | 0.9978 | 120.17 | 1 | 1.0034 |
| 632 | 0.9928 | − 0.51 | 0.9832 | −121.28 | 0.9889 | 119.23 | 2 | 1.0051 |
| 633 | 0.9904 | − 0.56 | 0.9819 | −121.31 | 0.9870 | 119.23 | 3 | 1.0083 |
| 634 | 0.9674 | − 1.22 | 0.9638 | −121.78 | 0.9689 | 118.76 | 4 | 1.0033 |
| 645 | | | 0.9741 | −121.46 | 0.9871 | 119.25 | 5 | 1.0047 |
| 646 | | | 0.9725 | −121.54 | 0.9851 | 119.29 | 6 | 1.0049 |
| 671 | 0.9886 | − 1.14 | 0.9886 | −121.14 | 0.9886 | 118.86 | 7 | 1.0067 |
| 680 | 0.9925 | − 0.84 | 0.9913 | −120.80 | 0.9924 | 119.21 | | |
| 681 | 1.0017 | −29.61 | 1.0017 | −149.61 | 1.0017 | 090.39 | | |
| 684 | 0.9867 | − 1.26 | | | 0.9867 | 118.67 | | |
| 611 | | | | | 0.9847 | 118.52 | | |
| 652 | 0.9811 | − 1.18 | | | | | | |
| 692 | 0.9886 | − 1.14 | 0.9886 | −121.14 | 0.9886 | 118.86 | | |
| 675 | 0.9833 | − 1.47 | 0.9916 | −121.39 | 0.9876 | 118.79 | | |

$\omega = 0.998624$ pu, $S_{IC,1} = 0.04066 + j0.02250$ pu, $S_{IC,2} = 0.02138 + j0.01179$ pu

Table 6.6: Maximum per-unit mismatches of power flow variables (test microgrid#6.1)

| Case# | $\|V_{ac}\|$ (pu) | $\delta$ (rad) | $V_{dc}$ (pu) | $P_{IC}$ (pu) |
|---|---|---|---|---|
| 1 | $5.0 \times 10^{-4}$ | $2.0 \times 10^{-3}$ | $5.6 \times 10^{-6}$ | $3.9 \times 10^{-5}$ |
| 2 | $5.3 \times 10^{-4}$ | $3.6 \times 10^{-3}$ | $5.1 \times 10^{-6}$ | $2.4 \times 10^{-5}$ |

Table 6.7: Maximum relative/percentage mismatches of power flow variables (test microgrid#6.1)

| Case# | $\|V_{ac}\|$ (%) | $V_{dc}$ (%) | $P_{IC}$ (%) |
|---|---|---|---|
| 1 | 0.0499 | 0.0006 | 0.0593 |
| 2 | 0.0534 | 0.0005 | 0.0774 |

## 6.8 Case Studies

The developed algorithm is employed to solve the power flow of a larger and more complicated microgrid to further investigate its effectiveness. The test microgrid#6.2 is constructed by interlinking the modified 25-node ac subgrid in [129] and the 22-node dc subgrid in [131] through two ICs, as shown in Figure 6.5. The $e_{ac-dc,max}$ for the two ICs is set to 3%. The same DG and IC data given in Tables 6.1 to 6.3 are used, while the dc loads are defined in Table 6.8 as constant-power loads.

### 6.8.1 Microgrid Power Flow

The proposed algorithm is utilized to produce the power flow results of test microgrid#6.2. As seen in Table 6.9, various AC DG types encounter different terminal voltage unbalances. In contrast with the SGDG, the 4-leg EIDG maintains balanced terminal voltages under

Table 6.8: DC loads of test microgrid#6.2

| DC Bus# | 6 | 7 | 8 | 11 | 12 | 14 | 15 | 16 | 17 | 20 | 21 | 22 |
|---|---|---|---|---|---|---|---|---|---|---|---|---|
| $P_{dc,L}$ (pu) | 0.03 | 0.05 | 0.04 | 0.02 | 0.01 | 0.02 | 0.02 | 0.05 | 0.06 | 0.02 | 0.02 | 0.03 |

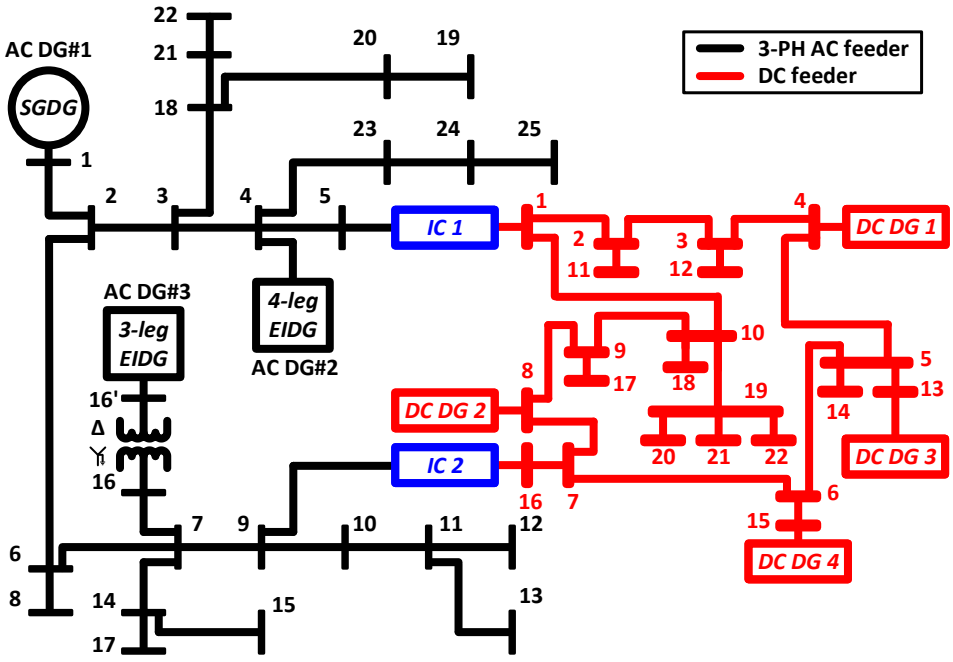


Figure 6.5: Test microgrid#6.2: 25-node ac/22-node dc microgrid.

unbalanced loading. In addition, the delta-wye transformer shifts the 3-leg EIDG's terminal voltages by 30 degrees (node#16′), yet it introduces voltage unbalances to the subgrid's node (node#16). As anticipated, the results show that the ICs do not accurately share the transferred power in proportion to their capacities, due to the different voltages at their dc terminals. Likewise, the DC DGs encounter inaccurate power sharing, as observed in Table 6.10. Furthermore, the ac subgrid's unbalanced active and reactive powers are shared among AC DG phases differently depending on their type and location, as observed in Table 6.11. Collectively, the proposed algorithm successfully models and solves for the different system components on both ac and dc sides.

Table 6.9: Power flow results of test microgrid#6.2

| AC Bus# | $\lvert V_{ac}^{a}\rvert$ (pu) | $\delta^{a}$ (deg) | $\lvert V_{ac}^{b}\rvert$ (pu) | $\delta^{b}$ (deg) | $\lvert V_{ac}^{c}\rvert$ (pu) | $\delta^{c}$ (deg) | DC Bus# | $V_{dc}$ (pu) |
|---|---|---|---|---|---|---|---|---|
| 1 | 0.9893 | 0.00 | 0.9887 | −120.08 | 0.9874 | 119.99 | 1 | 1.0024 |
| 2 | 0.9791 | − 0.24 | 0.9789 | −120.25 | 0.9788 | 119.73 | 2 | 1.0030 |
| 3 | 0.9775 | − 0.32 | 0.9774 | −120.31 | 0.9775 | 119.65 | 3 | 1.0039 |
| 4 | 0.9794 | − 0.33 | 0.9794 | −120.33 | 0.9794 | 119.67 | 4 | 1.0049 |
| 5 | 0.9797 | − 0.35 | 0.9797 | −120.35 | 0.9797 | 119.66 | 5 | 1.0053 |
| 6 | 0.9727 | − 0.20 | 0.9723 | −120.19 | 0.9728 | 119.76 | 6 | 1.0045 |
| 7 | 0.9683 | − 0.16 | 0.9680 | −120.13 | 0.9685 | 119.80 | 7 | 1.0025 |
| 8 | 0.9706 | − 0.20 | 0.9703 | −120.18 | 0.9709 | 119.76 | 8 | 1.0026 |
| 9 | 0.9634 | − 0.18 | 0.9628 | −120.13 | 0.9640 | 119.77 | 9 | 1.0018 |
| 10 | 0.9591 | − 0.18 | 0.9581 | −120.11 | 0.9598 | 119.76 | 10 | 1.0017 |
| 11 | 0.9571 | − 0.18 | 0.9560 | −120.11 | 0.9579 | 119.76 | 11 | 1.0030 |
| 12 | 0.9561 | − 0.18 | 0.9548 | −120.10 | 0.9569 | 119.77 | 12 | 1.0039 |
| 13 | 0.9564 | − 0.18 | 0.9551 | −120.11 | 0.9572 | 119.76 | 13 | 1.0054 |
| 14 | 0.9625 | − 0.15 | 0.9623 | −120.10 | 0.9628 | 119.79 | 14 | 1.0052 |
| 15 | 0.9604 | − 0.15 | 0.9602 | −120.09 | 0.9609 | 119.78 | 15 | 1.0046 |
| 16 | 0.9747 | − 0.10 | 0.9744 | −120.09 | 0.9745 | 119.87 | 16 | 1.0024 |
| 16′ | 0.9916 | −28.85 | 0.9916 | −148.85 | 0.9916 | 91.15 | 17 | 1.0018 |
| 17 | 0.9614 | − 0.15 | 0.9613 | −120.10 | 0.9614 | 119.79 | 18 | 1.0017 |
| 18 | 0.9717 | − 0.32 | 0.9717 | −120.29 | 0.9720 | 119.65 | 19 | 1.0014 |
| 19 | 0.9669 | − 0.31 | 0.9675 | −120.29 | 0.9677 | 119.66 | 20 | 1.0014 |
| 20 | 0.9692 | − 0.32 | 0.9694 | −120.29 | 0.9698 | 119.65 | 21 | 1.0014 |
| 21 | 0.9682 | − 0.31 | 0.9679 | −120.29 | 0.9683 | 119.66 | 22 | 1.0013 |
| 22 | 0.9663 | − 0.31 | 0.9656 | −120.28 | 0.9663 | 119.67 | | |
| 23 | 0.9761 | − 0.33 | 0.9765 | −120.33 | 0.9768 | 119.67 | | |
| 24 | 0.9741 | − 0.33 | 0.9747 | −120.33 | 0.9751 | 119.66 | | |
| 25 | 0.9718 | − 0.32 | 0.9729 | −120.33 | 0.9732 | 119.67 | | |
| $\omega = 0.998572$ pu, $S_{IC,1} = 0.02687 + j0.03032$ pu, $S_{IC,2} = 0.01381 + j0.02331$ pu | | | | | | | | |

Table 6.10: DC DG output phase powers for test microgrid#6.2

| DC DG# | 1 | 2 | 3 | 4 |
|---|---|---|---|---|
| $P_{dc,G}$ (pu) | 0.0902 | 0.1185 | 0.0892 | 0.1134 |

Table 6.11: AC DG output phase powers for test microgrid#6.2

| AC DG# | $P^a_{ac,G}$ (pu) | $P^b_{ac,G}$ (pu) | $P^c_{ac,G}$ (pu) | $Q^a_{ac,G}$ (pu) | $Q^b_{ac,G}$ (pu) | $Q^c_{ac,G}$ (pu) |
|---|---|---|---|---|---|---|
| 1 | 0.0822 | 0.0822 | 0.0816 | 0.0532 | 0.0536 | 0.0560 |
| 2 | 0.0576 | 0.0599 | 0.0582 | 0.0556 | 0.0559 | 0.0539 |
| 3 | 0.0652 | 0.0648 | 0.0652 | 0.0371 | 0.0368 | 0.0365 |

### 6.8.2 Proposed Algorithm's Performance Evaluation

#### Limits-Enforcement and Operational Modes

To examine the proposed algorithm's capability of enforcing DG and IC limits and the respective changes in their operational modes, the dc loads were gradually changed by multiplying them by a factor $\lambda_{dc}$ ranging from 0.20 to 2.83. Figures 6.6a to 6.6c demonstrate the changes in the ICs' active and reactive powers, the DC DGs' powers, and the AC DGs' active and reactive powers, respectively. It is observed that for $\lambda_{dc}$ below 0.40, the two ICs are operating at their limits, thus not following (6.7), and injecting only active powers to the ac subgrid. Therefore, the changes in the dc loads are only reflected on the DC DGs, whereas the AC DGs undergo constant loading. For $\lambda_{dc}$ between 0.40/0.50 and 2.05/1.90, IC1/IC2 operates in droop-control mode, as per (6.7), and transfers power between the subgrids depending on their relative loadings. For this range of $\lambda_{dc}$, the ac and dc subgrids are coupled, thus the changes in dc loads are reflected on the AC DGs' active powers. It is noteworthy that the ICs reverse their active power direction as $\lambda_{dc}$ exceeds 1.25 and 1.20 for IC1 and IC2, respectively, as the dc subgrid's loading increases. Besides, as ICs transfer active powers below their capacity limits, they inject reactive powers into the ac subgrid, which directly affects the AC DGs' reactive powers. Note that the ICs' reactive powers are independent of their active power directions. As $\lambda_{dc}$ exceeds 2.05, the ICs inject their maximum powers, in constant-power mode, to the dc subgrid. Therefore, the further increase in dc loads is supplied solely by the DC DGs. Note that DC DG#2's limit is enforced for $\lambda_{dc} \geq 2.75$. Furthermore, all the DC DGs approach their limits at $\lambda_{dc} = 2.83$, beyond which no feasible solution exists. Overall, the results prove the algorithm's effectiveness in enforcing ICs' and DGs' power limits, as well as in changing their operational modes accordingly.

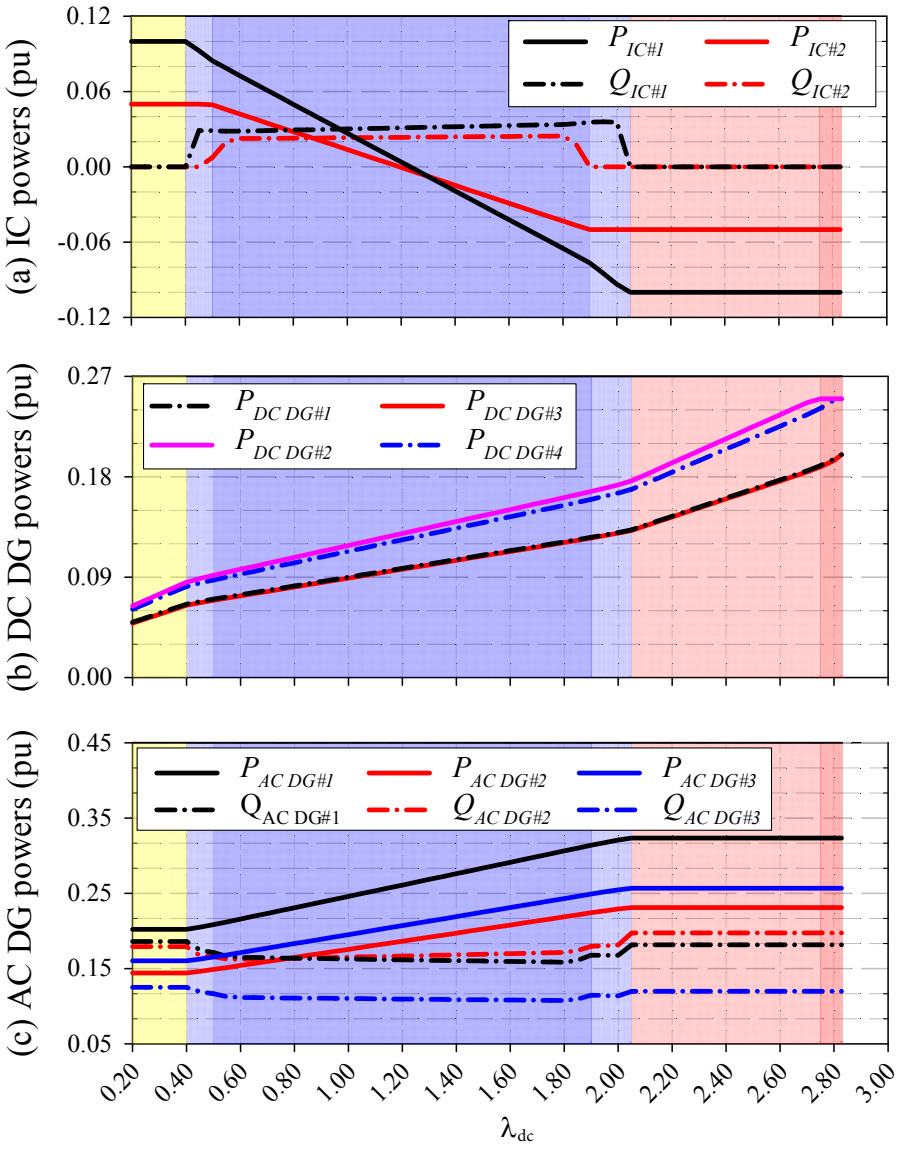


Figure 6.6: Effects of changing the dc loads on the microgrid operation.

### Convergence Characteristics

To highlight the proposed algorithms convergence characteristics under different loading and operating conditions, the number of iterations needed for convergence is examined for $\lambda_{dc}$ between 0.2 and 2.8. Figure 6.7 shows the number of iterations until the algorithm

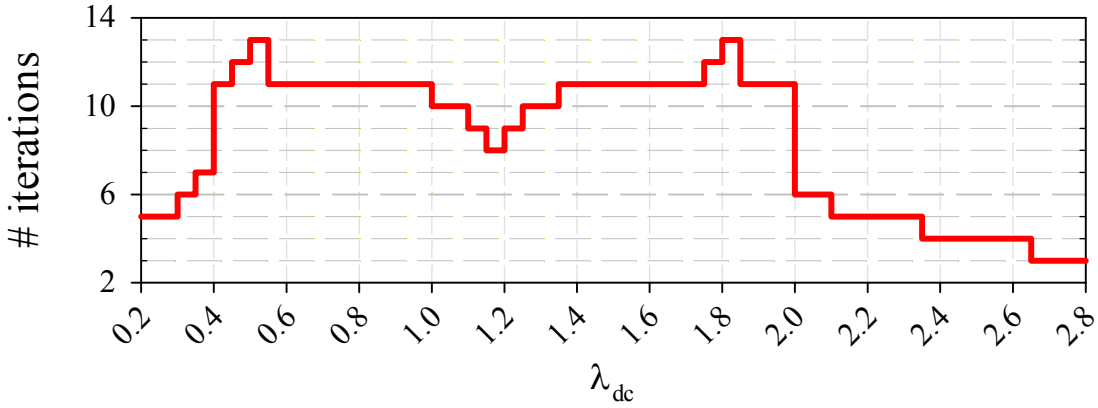


Figure 6.7: Number of iterations under different loading conditions

converges to a solution within a tolerance of $1.0 \times 10^{-6}$. It is noteworthy that the algorithm generally converges faster when ICs are operating at their limits, which occurs when $\lambda_{dc}$ is either low or high, as previously discussed. The reduction in the number of iterations can be attributed to elimination of the coupling between the ac frequency and dc voltage, due to ICs injecting/absorbing constant powers at their limits, thus reducing the problem size and resulting in faster convergence. Similarly, when a DG operates at its limits, it follows constant power, rather than droop characteristics, which results in problem simplification and faster convergence to the solution. Overall, the proposed algorithm demonstrated robust convergence characteristics for microgrids of different sizes and under various loading conditions.

### Accuracy and Computational-Efficiency

To evaluate the proposed algorithm's performance in comparison with the unified NTR-based approach in [1], both algorithms were employed to solve the same power flow problem of test microgrid#6.2. Since the NTR-based approach assumes one model for all AC DGs, all the employed AC DGs had to be changed to 4-leg EIDGs. Note that this assumption had to be made for the sake of performance comparison due to the modeling inaccuracies/shortcomings of the reported NTR-based method. The algorithms were executed using a PC with a 64-bit Intel Core i7 @3.4 GHz CPU and 16 GB of RAM, with the same convergence criterion, i.e., tolerance of $1.0 \times 10^{-6}$. The proposed NR-based algorithm demonstrated substantial reduction in execution time as compared to the NTR-based approach, as they converged in 162.5 and 3,803.6 ms, respectively. This significant decrease in computational cost is primarily due to the multiple reductions in problem size

attained through the proposed approach, as explained in Section 6.2. Additionally, the proposed algorithm calculates the Jacobian matrix elements by direct substitution in the power mismatch derivative equations, whereas the NTR algorithm evaluates the gradient and Hessian matrices using numerical methods with added computational cost. It is worth noting that the proposed algorithms enhanced performance becomes more apparent as the microgrid size increases.

## 6.9 Conclusions and Discussion

Developing generalized, computationally-efficient and accurate power flow algorithms is vital for steady-state analysis of hybrid ac/dc microgrids. This chapter proposes a sequential power flow algorithm based on symmetrical component analysis of the unbalanced ac subgrid's components. In comparison with the methodology developed in Chapter 3, the adopted modeling method guarantees more precise representation of different AC DG types, while the sequential scheme permits faster algorithm execution. The proposed approach was first validated by comparing its results with those obtained through MATLAB/Simulink time-domain simulations. For this purpose, a hybrid ac/dc microgrid, comprising a modified IEEE 13-node ac subgrid, a 7-node dc subgrid, and two interlinking converters (ICs), was constructed. The two sets of results obtained through the two methods were in close agreement, for the test microgrid under two cases – single and two ICs. Furthermore, the proposed algorithm was utilized to solve the power flow problem of a larger system composed of a 25-node ac and 22-node dc subgrids, interfaced through two ICs. The algorithm did not only prove effective in solving such complicated microgrid structure, but also demonstrated superior performance, in terms of execution time, with respect to the NTR-based approach. Moreover, the limit-enforcement ability of the power flow algorithm was investigated by forcing the converters to reach their capacity limits due to dc load changes.

# Chapter 7

# Conclusions, Contributions, and Future Work

This chapter summarizes the research work presented in the thesis. It also highlights the main contributions and the directions for future work.

## 7.1 Thesis Summary and Conclusions

Chapter 1 presented the motivations behind the work developed in this thesis. Based on these motivations, a comprehensive literature survey was conducted to identify the gaps, the potential contributions, and the technical challenges in the reported research work. Accordingly, the research objectives were set, and an overview of the thesis organization was presented.

Chapter 2 presented a comprehensive background review on the structure and control of ac, dc, and hybrid ac/dc microgrids. The review covered the hierarchical control of each microgrid type, and highlighted the control schemes and functionalities of each level of control (i.e., primary, secondary, and tertiary control levels). Furthermore, the different types of control of ICs for autonomous operation of hybrid ac/dc microgrids were discussed. Moreover, the power flow and optimal power flow analyses were briefly reviewed. The fundamentals of each type of analysis were discussed to lay a basis for steady-state analysis of hybrid ac/dc microgrids. The chapter also explained that the conventional method were not suitable for microgrid applications, concluding that novel approaches that incorporate the microgrids' characteristics needed to be developed.

Chapter 3 provided a novel power flow algorithm as a viable tool to accurately analyze the steady-state behavior of islanded hybrid ac/dc microgrids. The operational philosophy of these networks is sophisticated since both the ac frequency and dc voltage are variable, coupled, and sensitive to the control schemes of the DGs and ICs. In order to render the analysis generic, mathematical models were developed for control schemes of the DGs and ICs under unbalanced conditions. The presented models were then incorporated into an optimized power flow formulation and the solution was found using the globally convergent NTR method. The algorithm's accuracy was verified using detailed time-domain simulations in PSCAD/EMTDC environment. The effectiveness of the introduced power flow algorithm was illustrated via two case studies. The first case investigated parallel operation of droop-controlled ICs and highlighted the effects of IC settings on load sharing among subgrids and power-transfer sharing through installed ICs. The performed analysis demonstrated the trade-off between accurate load sharing between the ac and dc subgrids on the one hand, and proportional power-transfer sharing among ICs on the other hand. This analysis led to the conclusion that attention should be paid when designing the ICs' set points to guarantee optimal microgrid operation. The second case revealed the significance of analyzing the loading condition for each phase of the DGs rather than for the total three-phase power generation, which was commonly followed in steady-state analysis in the reported literature. The results of this case study showed that the microgrid operational limits of unbalanced hybrid ac/dc microgrids may be restricted to a value lower than the total generation capacity due to overloading of DG phases due to unbalanced loads.

Chapter 4 proposed a novel APR scheme for hybrid ac/dc microgrids operating in islanded mode, where unlike in grid-connected microgrids, local generation adequacy is crucial for proper system operation. As identified in Chapter 3, the unbalanced nature of ac distribution networks limits the microgrid loadability in the sense that loads must be shed from heavily loaded phases, even if the connected DGs have not reached their total three-phase capacity limits. The main challenge was to exploit the available resources by routing the power between the ac subgrid phases, thereby minimizing load shedding. The proposed method utilized the ICs between the ac and dc sides of hybrid ac/dc microgrids to provide this functionality. A supervisory controller with minimal communication requirements was proposed to implement a APR-based OPF algorithm to allow full loadability of the islanded network. The formulated OPF problem was solved analytically using an interior point method. Many case studies were conducted to address the imbalance problem and to validate the effectiveness of the proposed strategy against conventional methods, which were based solely on optimal DG droop settings. The first case illustrated the imbalance problem and the imposed limits on the microgrid operation under heavy loading. It also identified the potential use of ICs for APR under heavy loadings of both ac and dc

subgrids. The second case verified the limitations on the conventional optimal droop setting approach, and its ineffectiveness in dealing with the imbalance problem under heavy loading. The third and fourth cases tested the effectiveness of the proposed scheme and its ability to maximize the microgrid loadability. An additional case – involving the IEEE 123-node ac subgrid and a 22-node dc subgrid – was conducted to approve the proposed scheme's validity for larger-scale microgrids.

Chapter 5 introduced a generic steady-state modeling and power flow analysis approach for droop- and isochronously-controlled ac microgrids. The proposed framework adopted symmetrical sequence component models, rather than phase-coordinate models, of microgrid elements. Such approach immensely reduced the power flow execution time, as it broke down the system model into independent equation sets with considerably reduced sizes. To render the proposed approach practical and generic, it integrated different types and control schemes of DGs, including SGDG and EIDG units. Furthermore, it incorporated unbalanced loads and feeders, transformer connections, different load characteristics and configurations, as well as microgrid droop features. A novel power flow algorithm based on a modified NR method was proposed to solve for the microgrid steady-state voltage magnitudes, angles, and frequency. The accuracy of the models and algorithm was verified through comparison with detailed time-domain simulations in MATALB/Simulink. Additionally, the proposed approach was shown to outperform the reported NTR approach in generality, accuracy, and performance. Two case studies – incorporating IEEE 123-node test microgrid – were further performed to examine the effectiveness of the proposed approach in solving complicated droop-controlled microgrids, and to examine the behavior of droop-controlled DGs in isochronous microgrids. The proposed approach successfully and efficiently solved for the IEEE 123-node test microgrid under droop and isochronous modes of operation. Furthermore, it showed that the active and reactive powers of droop-controlled DGs can be controlled in isochronous microgrids by adjusting the frequency and voltage droop settings, respectively. However, the total power balance of the microgrid was always maintained by the large isochronous generator. The results also demonstrated that these droop-controlled DGs injected unbalanced phase powers to the microgrid.

Chapter 6 proposed a generalized and efficient power flow algorithm for islanded hybrid ac/dc microgrids. The algorithm extended the work proposed in Chapter 5 to include the dc subgrid and the different configurations and control schemes of ICs. The algorithm considered the various microgrid operational aspects, i.e., absence of a slack bus, unbalanced ac subgrid, droop-controlled ac and dc voltages and ac frequency, and coupling between the ac frequency and dc voltage through ICs. To attain high computational efficiency, the algorithm adopted three features. First, it modeled the ac subgrid elements in sequence components, thereby dividing the subgrid's set of equations into three smaller

sets for faster parallel solution. This approach also accurately represented different types of ac DGs. Second, the algorithm sequentially solved for the power flow variables of the ac and dc subgrids, thus reducing number of equations to be solved simultaneously, once again for further computational cost alleviation. Third, the algorithm implemented the quadratically-convergent Newton-Raphson technique – rather than the computationally-inefficient NTR method that was previously adopted in Chapter 3 – to solve the decoupled sets of equations. The proposed algorithm was validated through comparisons with time-domain simulations, in MATLAB/Simulink, for test hybrid ac/dc microgrids of different configurations, featuring single and multiple ICs. Moreover, three case studies – adopting a 25-node unbalanced ac/22-node dc hybrid microgrid – were introduced to examine the proposed algorithm's effectiveness in solving larger-scale microgrids, to investigate its limit-enforcement capabilities, and to evaluate its performance as compared to the method developed in Chapter 3. The proposed algorithm successfully solved for the larger-scale hybrid microgrid and enforced the DGs' and ICs' capacity limits under various loading conditions. Furthermore, the results showed that the proposed algorithm was not only more accurate than its NTR-based counterpart, but it was also substantially more efficient in terms of computational requirements.

## 7.2 Contributions

The main contributions of this research can be summarized as follows:

- Developing a steady-state analysis tool for droop-controlled unbalanced hybrid ac/dc microgrids. The developed tool modeled different components of the unbalanced droop-controlled ac subgrid, the droop-controlled dc subgrid, and the interlinking converters considering their various control schemes. The microgrid's nonlinear equations were formulated in a unified form, and solved using a Newton-Trust Region method.

- Identifying the technical challenges associated with operating islanded hybrid ac/dc microgrids under unbalanced loadings. First, the IC settings have to be adjusted carefully to maintain proper microgrids operation given the trade-off between the power sharing of the ac and dc subgrids and the proportional power sharing among ICs. Second, the DGs on the ac side are limited by their phase apparent power capacity, rather than the total three-phase capacity, which imposes further limits on heavy loading of such microgrids.

- Proposing a novel adaptive power routing scheme and implementing an optimal power flow algorithm based on it to maximize the loadability of islanded unbalanced hybrid ac/dc microgrids.

- Developing a generic and efficient modeling and power flow analysis approach for unbalanced ac microgrids based on symmetrical sequence component analysis of the microgrid components. The developed approach accurately modeled different types of DGs, and included transformers, unbalanced feeders, and unbalanced loads with various configurations.

- Developing an improved power flow algorithm for unbalanced hybrid ac/dc microgrids, which extended the developed sequence-component-based ac power flow analysis approach to include dc subgrids and interlinking converters. The created platform allows for more accurate and faster steady-state analysis of hybrid ac/dc microgrids as compared to conventional approaches. Therefore, it can be used for steady-state microgrid studies, such as planning, stability, and optimal operation.

## 7.3 Directions for Future Work

The developed research work can be extended to include:

- Developing a platform to optimally set the ICs' settings to attain specific microgrid planning and/or operation objectives, subject to the various hybrid ac/dc microgrid constraints.

- Employing the proposed adaptive power routing scheme and the developed sequence-component-based power flow approach into one framework to optimize the operation of hybrid ac/dc microgrids that incorporate both SGDGs and EIDGs, distribution transformers, and unbalanced loads with different configurations.

- Experimentally implementing and investigating the effects of the developed adaptive power routing scheme on the microgrid stability and operation.

- Incorporating the developed power flow analysis approaches in microgrid planning studies pertaining to DG and IC sizing and siting.

# References


[1] R. E. P. N. for the 21st Century, "Renewables 2014 global status report," REN21, Tech. Rep., 2014.

[2] C. Hernandez-Aramburo, T. Green, and N. Mugniot, "Fuel consumption minimization of a microgrid," *IEEE Transactions on Industry Applications*, vol. 41, no. 3, pp. 673–681, May 2005.

[3] P. Dondi, D. Bayoumi, C. Haederli, D. Julian, and M. Suter, "Network integration of distributed power generation," *Journal of Power Sources*, vol. 106, no. 12, pp. 1 – 9, 2002, proceedings of the Seventh Grove Fuel Cell Symposium.

[4] J. P. Lopes, N. Hatziargyriou, J. Mutale, P. Djapic, and N. Jenkins, "Integrating distributed generation into electric power systems: A review of drivers, challenges and opportunities," *Electric Power Systems Research*, vol. 77, no. 9, pp. 1189 – 1203, 2007, distributed Generation.

[5] C. Chakraborty, H. H.-C. Iu, and D. D.-C. Lu, "Power Converters , Control , and Energy Management for Distributed Generation," *IEEE Transactions on Industrial Electronics*, vol. 62, no. 7, pp. 4466–4470, 2015.

[6] B. Lasseter, "Microgrids [distributed power generation]," in *Proceedings of 2001 IEEE Power Engineering Society Winter Meeting.*, vol. 1. IEEE, 2001, pp. 146–149.

[7] R. Lasseter, "Microgrids," in *Proc. IEEE Power Eng. Soc.*, 2002, pp. 305–308.

[8] R. Panora, J. E. Gehret, M. M. Furse, R. H. Lasseter, and L. Fellow, "Real-World Performance of a CERTS Microgrid in Manhattan," *IEEE Transactions on Sustainable Energy*, vol. 5, no. 4, pp. 1356–1360, 2014.

[9] N. Hatziargyriou, H. Asano, R. Iravani, and C. Marnay, "Microgrids: An Overview of Ongoing Research, Development, and Demonstration Projects," *IEEE Power & Energy Magazine*, no. August, pp. 78–94, 2007.

[10] S. Parhizi, H. Lotfi, A. Khodaei, and S. Bahramirad, "State of the Art in Research on Microgrids: A Review," *IEEE Access*, vol. 3, pp. 890–925, 2015.

[11] R. Lasseter and P. Paigi, "Microgrid: a conceptual solution," *Proceedings of IEEE 35th Annual Power Electronics Specialists Conference PESC 04*, pp. 4285–4290, 2004.

[12] P. Piagi and R. Lasseter, "Autonomous control of microgrids," in *2006 IEEE Power Engineering Society General Meeting.* IEEE, 2006, p. 8 pp.

[13] J. M. Guerrero, J. C. Vasquez, J. Matas, L. G. De Vicuña, and M. Castilla, "Hierarchical control of droop-controlled AC and DC microgrids - A general approach toward standardization," *IEEE Trans. Ind. Electron.*, vol. 58, no. 1, pp. 158–172, 2011.

[14] M. Arriaga, C. A. Canizares, and M. Kazerani, "Long-Term Renewable Energy Planning Model for Remote Communities," *IEEE Trans. Sustain. Energy*, vol. 7, no. 1, pp. 221–231, 2016.

[15] L. Che and M. Shahidehpour, "DC Microgrids : Economic Operation and Enhancement of Resilience by Hierarchical Control," *IEEE Trans. Smart Grid*, vol. 5, no. 5, pp. 2517–2526, 2014.

[16] P. Karlsson and J. Svensson, "DC bus voltage control for a distributed power system," *IEEE Trans. Power Electron.*, vol. 18, no. 6, pp. 1405–1412, 2003.

[17] A. A. Hamad, M. A. Azzouz, and E. F. El-Saadany, "Multiagent Supervisory Control for Power Management in DC Microgrids," *IEEE Transactions on Smart Grid*, vol. 7, no. 2, pp. 1057–1068, 2016.

[18] T. Dragicevic, X. Lu, J. Vasquez, and J. Guerrero, "DC MicrogridsPart I: A Review of Control Strategies and Stabilization Techniques," *IEEE Trans. Power Electron.*, vol. 8993, no. c, pp. 1–1, 2015. [Online]. Available: http://ieeexplore.ieee.org/lpdocs/epic03/wrapper.htm?arnumber=7268934

[19] T. Dragicevic, X. Lu, J. Vasquez, and J. Guerrero, "DC MicrogridsPart II: A Review of Power Architectures, Applications and Standardization Issues," *IEEE Trans. Power Electron.*, vol. 8993, no. c, pp. 1–1, 2015.

[20] F. Nejabatkhah and Y. W. Li, "Overview of Power Management Strategies of Hybrid AC/DC Microgrid," *IEEE Trans. Power Electron.*, vol. 30, no. 12, pp. 7072–7089, 2015.

[21] A. Gupta, S. Doolla, and K. Chatterjee, "Hybrid AC-DC Microgrid: Systematic Evaluation of Control Strategies," *IEEE Trans. Smart Grid*, vol. PP, no. 99, pp. 1–1, 2017.

[22] N. Eghtedarpour and E. Farjah, "Power Control and Management in a Hybrid AC / DC Microgrid," *IEEE Transactions on Smart Grid*, vol. 5, no. 3, pp. 1494–1505, 2014.

[23] A. A. Hamad, M. A. Azzouz, and E. F. El Saadany, "A Sequential Power Flow Algorithm for Islanded Hybrid AC/DC Microgrids," *IEEE Trans. Power Syst.*, vol. 31, no. 5, pp. 3961–3970, 2016.

[24] X. Lu, J. M. Guerrero, K. Sun, J. C. Vasquez, R. Teodorescu, and L. Huang, "Hierarchical control of parallel AC-DC converter interfaces for hybrid microgrids," *IEEE Trans. Smart Grid*, vol. 5, no. 2, pp. 683–692, 2014.

[25] P. C. Loh, D. Li, Y. K. Chai, and F. Blaabjerg, "Autonomous Control of Interlinking Converter with Energy Storage in Hybrid AC-DC Microgrid," *IEEE Trans. Ind. Appl.*, vol. 49, no. 3, pp. 1374–1382, 2013.

[26] P. C. Loh, D. Li, Y. K. Chai, and F. Blaabjerg, "Autonomous Operation of Hybrid Microgrid with AC and DC Subgrids," *IEEE Trans. Power Electron.*, vol. 28, no. 5, pp. 2214–2223, may 2013.

[27] J. M. Guerrero, P. C. Loh, T.-L. Lee, and M. Chandorkar, "Advanced Control Architectures for Intelligent Microgrids Part II : Power Quality , Energy Storage, and AC/DC Microgrids," *IEEE Trans. Ind. Electron.*, vol. 60, no. 4, pp. 1263–1270, 2013.

[28] C. Cheng and D. Shirmohammadi, "A three-phase power flow method for real-time distribution system analysis," *IEEE Trans. Power Syst.*, vol. 10, no. 2, pp. 671–679, may 1995.

[29] S. Moghaddas-Tafreshi and E. Mashhour, "Distributed generation modeling for power flow studies and a three-phase unbalanced power flow solution for radial distribution systems considering distributed generation," *Electric Power Systems Research*, vol. 79, no. 4, pp. 680–686, apr 2009.

[30] A. M. Vural, "Interior point-based slack-bus free-power flow solution for balanced islanded microgrids," *International Transactions on Electrical Energy Systems*, pp. n/a–n/a, jul 2015.

[31] M. M. Abdelaziz and E. El-Saadany, "Maximum loadability consideration in droop-controlled islanded microgrids optimal power flow," *Electric Power Systems Research*, vol. 106, pp. 168–179, 2014.

[32] F. Katiraei, R. Iravani, N. Hatziargyriou, and A. Dimeas, "Microgrids Management: Controls and Operation Aspects of Microgrids," *IEEE Power & Energy Magazine*, no. June, pp. 54–65, 2008.

[33] Z. Miao, A. Domijan, and L. Fan, "Investigation of microgrids with both inverter interfaced and direct AC-connected distributed energy resources," *IEEE Trans. Power Del.*, vol. 26, no. 3, pp. 1634–1642, 2011.

[34] A. R. Bergen and V. Vittal, *Power Systems Analysis*, 2nd ed. New Jersey: Prentice Hall, 2000.

[35] M. Abdel-Akher, K. M. Nor, and A. H. A. Rashid, "Improved three-phase power-flow methods using sequence components," *IEEE Trans. Power Syst.*, vol. 20, no. 3, pp. 1389–1397, 2005.

[36] M. Z. Kamh and R. Iravani, "Unbalanced model and power-flow analysis of microgrids and active distribution systems," *IEEE Trans. Power Del.*, vol. 25, no. 4, pp. 2851–2858, 2010.

[37] F. Mumtaz, M. H. Syed, M. A. Hosani, and H. H. Zeineldin, "A Novel Approach to Solve Power Flow for Islanded Microgrids Using Modified Newton Raphson with Droop Control of DG," *IEEE Trans. Sustain. Energy*, vol. 7, no. 2, pp. 493–503, 2016.

[38] M. E. Nassar and M. M. Salama, "A novel branch-based power flow algorithm for islanded AC microgrids," *Elect. Power Syst. Res.*, vol. 146, pp. 51–62, 2017.

[39] M. M. A. Abdelaziz, H. E. Farag, E. F. El-Saadany, and Y. A. R. I. Mohamed, "A Novel and Generalized Three-Phase Power Flow Algorithm for Islanded Microgrids Using a Newton Trust Region Method," *IEEE Trans. Power Syst.*, vol. 28, no. 1, pp. 190–201, 2013.

[40] W. H. Kersting, "Radial distribution test feeders," *IEEE Trans. Power Syst.*, vol. 6, no. 3, pp. 975–985, 1991.

[41] J. Beerten, S. Cole, and R. Belmans, "Generalized steady-state VSC MTDC model for sequential AC/DC power flow algorithms," *IEEE Trans. Power Syst.*, vol. 27, no. 2, pp. 821–829, 2012.

[42] W. Wang and M. Barnes, "Power Flow Algorithms for Multi-Terminal VSC-HVDC With Droop Control," *IEEE Transactions on Power Systems*, vol. 29, no. 4, pp. 1721–1730, jul 2014.

[43] A. A. Eajal, M. A. Abdelwahed, E. F. El-Saadany, and K. Ponnambalam, "A Unified Approach to the Power Flow Analysis of AC/DC Hybrid Microgrids," *IEEE Trans. Sustain. Energy*, vol. 7, no. 3, pp. 1145–1158, 2016.

[44] E. Aprilia, K. Meng, M. Hosani, H. Zeineldin, and Z. Dong, "Unified Power Flow Algorithm for Standalone AC/DC Hybrid Microgrids," *IEEE Trans. Smart Grid*, vol. 3053, no. c, pp. 1–11, 2017.

[45] H. M. A. Ahmed, A. B. Eltantawy, and M. Salama, "A Generalized Approach to the Load Flow Analysis of AC-DC Hybrid Distribution Systems," *IEEE Trans. Power Syst.*, vol. 8950, no. c, pp. 1–1, 2017.

[46] D. E. Olivares, A. Mehrizi-Sani, A. H. Etemadi, C. A. Canizares, R. Iravani, M. Kazerani, A. H. Hajimiragha, O. Gomis-Bellmunt, M. Saeedifard, R. Palma-Behnke, G. A. Jimenez-Estevez, and N. D. Hatziargyriou, "Trends in Microgrid Control," *IEEE Trans. Smart Grid*, vol. 5, no. 4, pp. 1905–1919, jul 2014.

[47] A. Bidram and A. Davoudi, "Hierarchical structure of microgrids control system," *IEEE Trans. Smart Grid*, vol. 3, no. 4, pp. 1963–1976, 2012.

[48] H. Han, X. Hou, J. Yang, J. Wu, M. Su, and J. M. Guerrero, "Review of Power Sharing Control Strategies for Islanding Operation of AC Microgrids," *IEEE Trans. Smart Grid*, vol. PP, no. 99, p. 1, 2015.

[49] a. Micallef, M. Apap, C. Spiteri-Staines, and J. Guerrero, "Single-Phase Microgrid With Seamless Transition Capabilities Between Modes of Operation," *IEEE Trans. Smart Grid*, vol. PP, no. 99, p. 1, 2015.

[50] J. Lopes, C. Moreira, and A. Madureira, "Defining Control Strategies for MicroGrids Islanded Operation," *IEEE Trans. Power Syst.*, vol. 21, no. 2, pp. 916–924, may 2006.

[51] Q. Shafiee, J. M. Guerrero, and J. C. Vasquez, "Distributed Secondary Control for Islanded Microgrids A Novel Approach," *IEEE Trans. Power Electron.*, vol. 29, no. 2, pp. 1018–1031, 2014.

[52] H. E. Farag, M. M. A. Abdelaziz, and E. F. El-Saadany, "Voltage and reactive power impacts on successful operation of islanded microgrids," *IEEE Trans. Power Syst.*, vol. 28, no. 2, pp. 1716–1727, 2013.

[53] M. M. A. Abdelaziz, H. E. Farag, and E. F. El-Saadany, "Optimum Droop Parameter Settings of Islanded Microgrids With Renewable Energy Resources," *IEEE Trans. Sustain. Energy*, vol. 5, no. 2, pp. 434–445, 2014.

[54] Y. Han, P. Shen, X. Zhao, and J. M. Guerrero, "An Enhanced Power Sharing Scheme for Voltage Unbalance and Harmonics Compensation in an Islanded Microgrid," *IEEE Trans. Energy Convers.*, vol. 31, no. 3, pp. 1037–1050, 2016.

[55] M. Hamzeh, H. Karimi, and H. Mokhtari, "A new control strategy for a multi-bus MV microgrid under unbalanced conditions," *IEEE Trans. Power Syst.*, vol. 27, no. 4, pp. 2225–2232, 2012.

[56] M. Savaghebi, A. Jalilian, J. C. Vasquez, and J. M. Guerrero, "Secondary Control Scheme for Voltage Unbalance Compensation in an Islanded Droop-Controlled Microgrid," *IEEE Trans. Smart Grid*, vol. 3, no. 2, pp. 797–807, 2012.

[57] C. H. Lin, C. S. Chen, H. J. Chuang, M. Y. Huang, and C. W. Huang, "An expert system for three-phase balancing of distribution feeders," *IEEE Trans. Power Syst.*, vol. 23, no. 3, pp. 1488–1496, 2008.

[58] H. A. Mostafa, R. El-Shatshat, and M. M. A. Salama, "Multi-Objective Optimization for the Operation of an Electric Distribution System With a Large Number of," *IEEE Trans. Smart Grid*, vol. 4, no. 2, pp. 1038–1047, 2013.

[59] M. Shukla and A. Sekar, "Study of the effect of X/R ratio of lines on voltage stability," in *Proceedings of the Annual Southeastern Symposium on System Theory*, 2003, pp. 93–97.

[60] B. M. Eid, N. A. Rahim, J. Selvaraj, and A. H. El Khateb, "Control Methods and Objectives for Electronically Coupled Distributed Energy Resources in Microgrids: A Review," *IEEE Systems Journal*, pp. 1–13, 2014.

[61] J. C. Vasquez, J. M. Guerrero, J. Miret, M. Castilla, and L. G. D. Vicuña, "Hierachial Control of Intelligent Microgrids," *IEEE Industrial Electronics Maganize*, no. December 2010, pp. 23–29, 2010.

[62] O. Palizban, K. Kauhaniemi, and J. M. Guerrero, "Microgrids in active network management  part II: System operation, power quality and protection," *Renewable and Sustainable Energy Reviews*, vol. 36, pp. 440–451, 2014.

[63] O. Palizban, K. Kauhaniemi, and J. M. Guerrero, "Microgrids in active network management  part II: System operation, power quality and protection," *Renewable and Sustainable Energy Reviews*, vol. 36, pp. 440–451, 2014.

[64] J. M. Guerrero, M. Chandorkar, T.-l. Lee, and P. C. Loh, "Advanced Control Architectures for Intelligent Microgrids  Part I : Decentralized and Hierarchical Control," *IEEE Transactions on Industrial Electronics*, vol. 60, no. 4, pp. 1254–1262, 2013.

[65] M. Rashid, *Power Electronics: Circuits, Devices, and Applications*. Pearson Education, 2003.

[66] N. Mohan and T. Undeland, *Power electronics: converters, applications, and design*. Wiley India, 2007.

[67] N. Pogaku, S. Member, M. Prodanovic, T. C. Green, and S. Member, "Modeling , Analysis and Testing of Autonomous Operation of an Inverter-Based Microgrid," *IEEE Trans. Power Electron.*, vol. 22, no. 2, pp. 613–625, 2007.

[68] Y. A.-R. I. Mohamed, "New control algorithms for the distributed generation interface in grid-connected and micro-grid systems," Ph.D. dissertation, University of Waterloo, 2008.

[69] H. Nikkhajoei and R. H. Lasseter, "Distributed Generation Interface to the CERTS Microgrid," *IEEE Transactions on Power Delivery*, vol. 24, no. 3, pp. 1598–1608, 2009.

[70] R. H. Lasseter, J. H. Eto, B. Schenkman, J. Stevens, H. Vollkommer, D. Klapp, E. Linton, H. Hurtado, and J. Roy, "CERTS microgrid laboratory test bed," *IEEE Transactions on Power Delivery*, vol. 26, no. 1, pp. 325–332, 2011.

[71] A. Yazdani and R. Iravani, *Voltage-Sourced Converters in Power Systems: Modeling, Control, and Applications*. Wiley, 2010.

[72] Y. Mohamed and E. El-Saadany, "Adaptive Decentralized Droop Controller to Preserve Power Sharing Stability of Paralleled Inverters in Distributed Generation Microgrids," *IEEE Transactions on Power Electronics*, vol. 23, no. 6, pp. 2806–2816, November 2008.

[73] E. Barklund, N. Pogaku, M. Prodanovic, C. Hernandez-Aramburo, and T. Green, "Energy Management in Autonomous Microgrid Using Stability-Constrained Droop Control of Inverters," *IEEE Transactions on Power Electronics*, vol. 23, no. 5, pp. 2346–2352, September 2008.

[74] I. U. Nutkani, P. C. Loh, and F. Blaabjerg, "Droop scheme with consideration of operating costs," *IEEE Transactions on Power Electronics*, vol. 29, no. 3, pp. 1047–1052, 2014.

[75] J. M. Guerrero, L. G. De Vicuña, J. Matas, J. Miret, and M. Castilla, "Output impedance design of parallel-connected UPS inverters," *IEEE International Symposium on Industrial Electronics*, vol. 2, no. 4, pp. 1123–1128, 2004.

[76] J. Rocabert, A. Luna, F. Blaabjerg, and P. Rodriguez, "Control of power converters in AC microgrids," *IEEE Trans. Power Electron.*, vol. 27, no. 11, pp. 4734–4749, 2012.

[77] K. D. Brabandere, B. Bolsens, J. V. den Keybus, A. Woyte, J. Driesen, and R. Belmans, "A Voltage and Frequency Droop Control Method for Parallel Inverters," *IEEE Transactions on Power Electronics*, vol. 22, no. 4, pp. 1107–1115, apr 2007.

[78] Y. Li and Y. W. Li, "Power management of inverter interfaced autonomous microgrid based on virtual frequency-voltage frame," *IEEE Transactions on Smart Grid*, vol. 2, no. 1, pp. 18–28, 2011.

[79] Q. Zhong and T. Hornik, *Control of Power Inverters for Distributed Generation and Renewable Energy*, ser. Wiley - IEEE. John Wiley and Sons, 2011.

[80] P. Wang, C. Jin, D. Zhu, Y. Tang, P. C. Loh, and F. H. Choo, "Distributed Control for Autonomous Operation of a Three-Port AC/DC/DS Hybrid Microgrid," *IEEE Transactions on Industrial Electronics*, vol. 62, no. 2, pp. 1279–1290, 2015.

[81] J. He and Y. W. Li, "Analysis, design, and implementation of virtual impedance for power electronics interfaced distributed generation," *IEEE Transactions on Industry Applications*, vol. 47, no. 6, pp. 2525–2538, 2011.

[82] J. C. Vasquez, J. M. Guerrero, M. Savaghebi, J. Eloy-garcia, and R. Teodorescu, "Modeling , Analysis , and Design of Parallel Three-Phase Voltage Source Inverters," *IEEE Trans. Ind. Electron.*, vol. 60, no. 4, pp. 1271–1280, 2013.

[83] J. Guerrero, J. Vasquez, J. Matas, M. Castilla, and L. de Vicuna, "Control Strategy for Flexible Microgrid Based on Parallel Line-Interactive UPS Systems," *IEEE Trans. Ind. Electron.*, vol. 56, no. 3, pp. 726–736, March 2009.

[84] Q. Shafiee, T. Dragicevic, J. C. Vasquez, and J. M. Guerrero, "Hierarchical Control for Multiple DC-Microgrids Clusters," *IEEE Transactions on Energy Conversion*, vol. 29, no. 4, pp. 922–933, 2014.

[85] M. Savaghebi, A. Jalilian, J. C. Vasquez, and J. M. Guerrero, "Secondary Control for Voltage Quality Enhancement in Microgrids," *IEEE Trans. Smart Grid*, vol. 3, no. 4, pp. 1893–1902, 2012.

[86] L. Meng, T. Dragicevic, J. M. Guerrero, and J. C. Vasquez, "Dynamic consensus algorithm based distributed global efficiency optimization of a droop controlled DC microgrid," *ENERGYCON 2014 - IEEE International Energy Conference*, pp. 1276–1283, 2014.

[87] T. Dragicevic, J. Vasquez, J. Guerrero, and D. Škrlec, "Advanced LVDC Electrical Power Architectures and Microgrids," *IEEE Electrification Magazine*, vol. 2, no. 1, pp. 54–65, 2014.

[88] D. Salomonsson, S. Member, L. Söder, and A. Sannino, "An Adaptive Control System for a DC Microgrid for Data Centers," *IEEE Transactions on Industry Applications*, vol. 44, no. 6, pp. 1910–1917, 2008.

[89] H. Kakigano, Y. Miura, and T. Ise, "Distribution voltage control for DC microgrids using fuzzy control and gain-scheduling technique," *IEEE Transactions on Power Electronics*, vol. 28, no. 5, pp. 2246–2258, 2013.

[90] K. Sun, L. Zhang, Y. Xing, and J. Guerrero, "A Distributed Control Strategy Based on DC Bus Signaling for Modular Photovoltaic Generation Systems With Battery Energy Storage," *IEEE Transactions on Power Electronics*, vol. 26, no. 10, pp. 3032–3045, 2011.

[91] J. Schönberger, R. Duke, and S. D. Round, "DC-bus signaling: A distributed control strategy for a hybrid renewable nanogrid," *IEEE Transactions on Industrial Electronics*, vol. 53, no. 5, pp. 1453–1460, 2006.

[92] R. S. Balog and P. T. Krein, "Bus selection in multibus DC microgrids," *IEEE Transactions on Power Electronics*, vol. 26, no. 3, pp. 860–867, 2011.

[93] B. K. Johnson, R. H. Lasseter, F. L. Alvarado, and R. Adapa, "Expandable multiterminal dc systems based on voltage droop," *IEEE Transactions on Power Delivery*, vol. 8, no. 4, pp. 1926–1932, 1993.

[94] A. M. Rahimi and A. Emadi, "Active damping in DC/DC power electronic converters: A novel method to overcome the problems of constant power loads," *IEEE Transactions on Industrial Electronics*, vol. 56, no. 5, pp. 1428–1439, 2009.

[95] V. Nasirian, S. Moayedi, A. Davoudi, and F. Lewis, "Distributed Cooperative Control of DC Microgrids," *IEEE Transactions on Power Electronics*, vol. 8993, no. c, pp. 1–1, 2014.

[96] X. Lu, J. M. Guerrero, K. Sun, and J. C. Vasquez, "An improved droop control method for dc microgrids based on low bandwidth communication with dc bus voltage restoration and enhanced current sharing accuracy," *IEEE Trans. Power Electron.*, vol. 29, no. 4, pp. 1800–1812, 2014.

[97] C. Jin, P. Wang, J. Xiao, Y. Tang, and F. H. Choo, "Implementation of hierarchical control in DC microgrids," *IEEE Transactions on Industrial Electronics*, vol. 61, no. 8, pp. 4032–4042, 2014.

[98] Q. Shafiee, C. Stefanovic, T. Dragicevic, P. Popovski, J. C. Vasquez, and J. M. Guerrero, "Robust networked control scheme for distributed secondary control of islanded microgrids," *IEEE Trans. Ind. Electron.*, vol. 61, no. 10, pp. 5363–5374, 2014.

[99] L. Meng, J. M. Guerrero, J. C. Vasquez, F. Tang, and M. Savaghebi, "Tertiary control for optimal unbalance compensation in islanded microgrids," *2014 IEEE 11th International Multi-Conference on Systems, Signals and Devices, SSD 2014*, 2014.

[100] C. Jin, P. C. Loh, P. Wang, Y. Mi, and F. Blaabjerg, "Autonomous operation of hybrid AC-DC microgrids," *2010 IEEE International Conference on Sustainable Energy Technologies, ICSET 2010*, 2010.

[101] F. Blaabjerg, P. C. Loh, D. Li, and Y. K. Chai, "Autonomous operation of acdc microgrids with minimised interlinking energy flow," *IET Power Electronics*, vol. 6, no. 8, pp. 1650–1657, 2013.

[102] P. C. Loh, D. Li, Y. K. Chai, and F. Blaabjerg, "Hybrid AC-DC microgrids with energy storages and progressive energy flow tuning," *IEEE Transactions on Power Electronics*, vol. 28, no. 4, pp. 1533–1543, 2013.

[103] A. A. a. Radwan and Y. A. R. I. Mohamed, "Stabilization of medium-frequency modes in isolated microgrids supplying direct online induction motor loads," *IEEE Transactions on Smart Grid*, vol. 5, no. 1, pp. 358–370, 2014.

[104] A. A. a. Radwan, S. Member, Y. A.-r. I. Mohamed, and S. Member, "Bidirectional Power Management in Hybrid AC-DC Islanded Microgrid System," pp. 1–5, 2014.

[105] M. Davari and Y. A. R. I. Mohamed, "Robust multi-objective control of VSC-based DC-voltage power port in hybrid AC/DC multi-terminal micro-grids," *IEEE Transactions on Smart Grid*, vol. 4, no. 3, pp. 1597–1612, 2013.

[106] J. J. Grainger and W. D. Stevenson, *Power System Analysis*. New York: McGraw-Hill, 1994.

[107] H. Saadat, *Power System Analysis*, 2nd ed. New York: McGraw-Hill, 2009.

[108] H. Dommel and W. Tinney, "Optimal Power Flow Solutions," *IEEE Transactions on Power Apparatus and Systems*, vol. PAS-87, no. 10, pp. 1866–1876, 1968.

[109] J. A. Momoh, M. E. El-Hawary, and R. Adapa, "A review of selected optimal power flow literature to 1993 part i: nonlinear and quadratic Programming Approaches," *IEEE Transactions on Power Systems*, vol. 14, no. 1, pp. 96–103, 1999.

[110] J. A. Momoh, M. E. Ei-Hawary, and R. Adapa, "A review of selected optimal power flow literature to 1993 part ii: newton, linear programming and Interior Point Methods," *IEEE Transactions on Power Systems*, vol. 14, no. 1, pp. 105–111, 1999.

[111] M. Huneault and F. Galiana, "A survey of the optimal power flow literature," *IEEE Transactions on Power Systems*, vol. 6, no. 2, pp. 762–770, 1991. [Online]. Available: http://ieeexplore.ieee.org/document/76723/

[112] G. Opoku, "OPl IMAL POWER SVSl EM VAR PLANNING," *IEEE Trans. Power Syst.*, vol. 5, no. 1, pp. 53–60, 1990.

[113] Y.-T. Hsiao, C.-C. Liu, H.-D. Chiang, and Y.-L. Chen, "A new approach for optimal VAr sources planning in large scale electric power systems," *IEEE Transactions on Power Systems*, vol. 8, no. 3, pp. 988–996, 1993.

[114] M. Bjelogrlic, M. S. Calovic, P. Ristanovic, and B. S. Babic, "Application of Newton's optimal power flow in voltage/reactive power control," *IEEE Transactions on Power Systems*, vol. 5, no. 4, pp. 1447–1454, 1990.

[115] J. Zhu, *Optimization of Power System Operation*. Hoboken, NJ, USA: Wiley-IEEE Press, 2009.

[116] W. H. Kersting, *Distribution System Modeling and Analysis, Second Edition*. vol. 15, CRC Press, 2006.

[117] P. Kundur, *Power System Stability and Control*. New York: McGraw-Hill, 1994.

[118] G. Daelemans, "VSC HVDC in meshed networks," Ph.D. dissertation, K.U.Leuven, Leuven, Belgium, 2008.

[119] G. X. Luo and A. Semlyen, "Efficient load flow for large weakly meshed networks," *IEEE Transactions on Power Systems*, vol. 5, no. 4, pp. 1309–1316, 1990.

[120] A. R. Conn, N. I. M. Gould, and P. L. Toint, *Trust Region Methods*. SIAM, 2000.

[121] J. J. Moré and D. C. Sorensen, "Computing a Trust Region Step," *SIAM Journal on Scientific and Statistical Computing*, vol. 4, no. 3, pp. 553–572, sep 1983.

[122] H. Mohsenian-Rad and A. Davoudi, "Towards Building an Optimal Demand Response Framework for DC Distribution Networks," *IEEE Transactions on Smart Grid*, vol. 5, no. 5, pp. 2626–2634, sep 2014.

[123] R. C. Dugan, T. S. Key, and G. J. Ball, "Distributed Resources Standards," *IEEE Ind. Appl. Mag.*, vol. 12, no. 1, pp. 27–34, 2006.

[124] A. Hintz, U. R. Prasanna, and K. Rajashekara, "Comparative Study of Three-phase Grid Connected Inverter Sharing Unbalanced Three-phase and / or Single-phase systems," *IEEE Trans. Ind. Appl.*, vol. PP, no. 99, pp. 1–1, 2016.

[125] M. Davari and Y. A. R. I. Mohamed, "Variable-structure-based nonlinear control for the master VSC in DC-energy-pool multiterminal grids," *IEEE Transactions on Power Electronics*, vol. 29, no. 11, pp. 6196–6213, 2014.

[126] D. Wu, F. Tang, T. Dragicevic, J. M. Guerrero, and J. C. Vasquez, "Coordinated Control Based on Bus-Signaling and Virtual Inertia for Islanded DC Microgrids," pp. 1–12, 2015.

[127] J. Lei, T. An, Z. Du, and Z. Yuan, "A General Unified AC / DC Power Flow Algorithm with MTDC," *IEEE Trans. Power Syst.*, vol. PP, no. 99, pp. 1–1, 2016.

[128] R. Faranda, A. Pievatolo, and E. Tironi, "Load Shedding: A New Proposal," *IEEE Trans. Power Syst.*, vol. 22, no. 4, pp. 2086–2093, 2007.

[129] P. R. Raju, G. K. V. ;Bijwe, "Efficient reconfiguration of balanced and unbalanced distribution systems for loss minimisation," *IET Gen., Transm., Distrib*, vol. 2, no. 1, pp. 7–12, 2008.

[130] P. Kankanala, S. C. Srivastava, A. K. Srivastava, and N. N. Schulz, "Optimal control of voltage and power in a multi-zonal MVDC shipboard power system," *IEEE Trans. Power Syst.*, vol. 27, no. 2, pp. 642–650, 2012.

[131] J. Ma, G. Geng, and Q. Jiang, "Two-Time-Scale Coordinated Energy Management for Medium-Voltage DC Systems," *IEEE Trans. Power Syst.*, vol. 31, no. 5, pp. 3971–3983, 2016.

[132] M. Arriaga, C. Cañizares, and M. Kazerani, "Renewable energy alternatives for remote communities in Northern Ontario, Canada," *IEEE Trans. Sustain. Energy*, vol. 4, no. 3, pp. 661–670, 2013.

[133] Y. S. Tamura J, Takeda I, Kimura M, UENO M, "A synchronous machine model for unbalanced analysis," *Elect. Eng. Jpn.*, vol. 119, no. 2, pp. 46–59, 1997.

[134] P. T. Cheng, C. A. Chen, T. L. Lee, and S. Y. Kuo, "A cooperative imbalance compensation method for distributed-generation interface converters," *IEEE Trans. Ind. Appl.*, vol. 45, no. 2, pp. 805–815, 2009.

[135] J. Arrillaga and N. R. Watson, *Computer modeling of electrical power systems*, 2nd ed. New York: Wiley, 2001.

[136] M. Z. Kamh and R. Iravani, "A unified three-phase power-flow analysis model for electronically coupled distributed energy resources," *IEEE Trans. Power Del.*, vol. 26, no. 2, pp. 899–909, 2011.

[137] C. Concordia and S. Ihara, "Load Representation in Power System Stability Studies," *IEEE Trans. Power App. Syst.*, vol. PAS-101, no. 4, pp. 969–977, 1982.

[138] X. P. Zhang, "Fast three phase load flow methods," *IEEE Trans. Power Syst.*, vol. 11, no. 3, pp. 1547–1554, 1996.

[139] "STAMFORD Gennerator Technical Datasheet." [Online]. Available: https://stamford-avk.com/sites/default/files/literature/all/MVSI804RWdg51.pdf

[140] M. Allam, A. Hamad, M. Kazerani, and E. El-Saadany, "A steady-state analysis tool for unbalanced islanded hybrid AC/DC microgrids," *Elect. Power Syst. Res.*, vol. 152, pp. 71–83, 2017.

[141] M. A. Allam, A. A. Said, M. Kazerani, and E. F. El Saadany, "A Novel Dynamic Power Routing Scheme to Maximize Loadability of Islanded Hybrid AC/DC Microgrids under Unbalanced AC Loading," *IEEE Trans. Smart Grid*, to be published.

[142] A. Clark-Ginsberg, "What's the Difference between Reliability and Resilience?" Tech. Rep. [Online]. Available: https://ics-cert.us-cert.gov/sites/default/files/ICSJWG-Archive/QNL_MAR_16/reliability%20and%20resilience%20pdf.pdf

[143] "The Authoritative Dictionary of IEEE Standards Terms, Seventh Edition," in *IEEE Std 100-2000*, 2000, pp. 1–1362.

[144] NATIONAL INFRASTRUCTURE ADVISORY COUNCIL, "CRITICAL INFRASTRUCTURE RESILIENCE FINAL REPORT AND RECOMMENDATIONS," Tech. Rep., 2009. [Online]. Available: https://www.dhs.gov/sites/default/files/publications/niac-critical-infrastructure-resilience-final-report-09-08-09-508.pdf

# Appendix List of Publications


[1] M. A. Allam, A. A. Hamad, M. Kazerani, and E. F. El Saadany, "A steady-state analysis tool for unbalanced islanded hybrid AC/DC microgrids," *Elect. Power Syst. Res.*, vol. 152, pp. 71–83, 2017.

[2] M. A. Allam, A. A. Hamad, M. Kazerani, and E. F. El Saadany, "A Novel Dynamic Power Routing Scheme to Maximize Loadability of Islanded Hybrid AC/DC Microgrids under Unbalanced AC Loading," *IEEE Trans. Smart Grid*, to be published (Early Access).

[3] M. A. Allam, A. A. Hamad, and M. Kazerani, "A Generic Modeling and Power-Flow Analysis Approach for Isochronous and Droop-Controlled Microgrids," *IEEE Trans. Power Syst.*, to be published (Early Access).

[4] M. A. Allam, A. A. Hamad, and M. Kazerani, "A Sequence-Component-Based Power-Flow Analysis for Unbalanced Droop-Controlled Hybrid AC/DC Microgrids," *IEEE Trans. Sustain. Energy*, under review.

[5] M. Pape, M. A. Allam, and M. Kazerani, "Design and implementation of a highly reconfigurable microgrid test bed platform," in *2016 IEEE Canadian Conference on Electrical and Computer Engineering (CCECE)*, Vancouver, BC, 2016, pp. 1–6.

# Glossary

The following are definitions of terms used in the thesis.

| | |
|---|---|
| **System Reliability** | The ability of the power system to deliver electricity in the quantity and with the quality demanded by users. Reliability is generally measured by interruption indices defined by the IEEE Standard 1366 [142], [143] |
| **System Resilience** | The ability of a system to recover and, in some cases, transform from adversity. The National Infrastructure Advisory Council defines critical infrastructure resilience as: *"The ability to reduce the magnitude and/or duration of disruptive events. The effectiveness of a resilient infrastructure or enterprise depends upon its ability to anticipate, absorb, adapt to, and/or rapidly recover from a potentially disruptive event."* [142]–[144] |
| **System Security** | The ability of the power system to remain secure without serious consequences to any pre-selected list of credible contingencies. [143] |
| **Loadability** | The maximum load that a microgrid can supply constantly. |
| **Algorithm Robustness** | The ability of an algorithm to converge under various conditions. |